Atomic Oxygen Densities in Pulsed Inductively Coupled Plasmas: — Laser Spectroscopy and — Energy Resolved Actinometry

Michael Kin Ting Mo

Doctor of Philosophy

University of York

Physics

July 2022

Abstract

Plasma processing of semiconductors allows high-precision etching of nanoscale-sized features and as a result the computational power of devices has continued to increase. However, defects that arise during manufacturing greatly impact their performance. Better control over the plasma species is desired to reduce these, and active monitoring of the plasma during manufacturing will lead to improved optimisation over the production of key reactive species as well as early detection of process drift. While Two-photon Absorption Laser Induced Fluorescence (TALIF) spectroscopy can accurately measure atomic densities with high spatial and temporal resolution, implementing it as a routine industrial method is challenging. As such, this thesis was motivated by the need to develop compatible diagnostics for practical use within the semiconductor manufacturing industry. Energy Resolved Actinometry (ERA) is a passive approach and has previously been used to provide reliable information in atmospheric and capacitively-coupled plasmas. Consequently, its viability was further tested under a different operating regime in a low pressure, pulsed inductively coupled plasma at high powers to recreate processing conditions of interest in a modified Gaseous Electronics Conference reference cell.

This thesis studies the production of atomic oxygen since it is chemically similar to commonly used etch gases, but is much easier to model and use experimentally. TALIF was used to first determine these densities over a range of pressures (10-50 Pa), applied powers (400-1000 W), helium-oxygen admixtures (10-20%), and pure O_2 to provide benchmark values. Moreover, it was also used to determine the gas temperature over these conditions through comparison of the fluorescence between the $O(^3P_J)$ levels, and was necessary for calculations used in ERA. Consequently, the passive optical method was employed to also measure these values, with helium emission investigated to provide an alternative line-ratio giving more reliable measurements. As a result, good qualitative and quantitative agreement were found between the two diagnostics, with the potential to be more easily implemented onto various industrial plasma sources for better characterisation of the plasma during processing.

List of Publications and Contributed Presentations

Publications

Michael Mo, Kari Niemi, Timo Gans, *The dynamics of atomic oxygen densities and gas temperatures in the afterglow of a pulsed, inductively coupled oxygen plasma: two-photon absorption laser induced fluorescence spectroscopy.* In preparation.

Michael Mo, Kari Niemi, Andrew R. Gibson, Chris Bowman, Deborah O'Connell, Timo Gans, *Two-gas energy resolved actinometry in a pulsed, inductively coupled oxygen plasma.* In preparation.

Contributed Presentations

Michael Mo, Kari Niemi, Andrew R. Gibson, Chris Bowman, Deborah O'Connell, Timo Gans. Oral presentation: *Atomic oxygen densities in pulsed inductively-coupled plasmas: Laser spectroscopy and energy resolved actinometry.* Gaseous Electronics Conference 2021.

Michael Mo, Andrew R. Gibson, Chris Bowman, Deborah O'Connell, Timo Gans. Poster presentation: *Applying Bayesian analysis with optical emission spectroscopy to obtain plasma parameters.* Technological Plasma Workshop 2019, Coventry, UK.

Michael Mo, Martin Blake, Andrew R. Gibson, Timo Gans, Deborah O'Connell. Poster presentation: *Metrology for in-situ industrial plasma processing.* Data driven plasma science conference 2018, University of York, UK.

List of Symbols and Abbreviations

η	Detector quantum efficiency
Γ	Gamma function
κ	Thermal conductivity
λ	Wavelength
$\langle\epsilon\rangle$	Mean electron energy
$\langle\nu\rangle$	Mean collision velocity
μ	Reduced mass, Mean value
ν	Electromagnetic frequency
Ω	Collision strength
σ	Collision cross-section, uncertainty
$\sigma^{(2)}$	Two-photon excitation cross-section
τ_{eff}	Effective lifetime
τ_{nat}	Natural lifetime
θ	Probability parameter
A	Einstein coefficient, Fitting parameter
a	Branching ratio
a_0	Hydrogen atom radius
C	Capacitor
c	Speed of light in a vacuum
D	Measured data, Diffusion coefficient
d	Direct excitation
de	Dissociative excitation
E	Energy, Effective excitation
e	Elementary charge
$f(\epsilon)$	Electron energy distribution function
$f(x,\theta)$	Forward model
F	Fluorescence
f	Gas fraction
g	Statistical weight, Normalised line profile
h	Planck constant
I	Intensity
i	Excited level
J	Total angular momentum quantum number
k	Rate coefficient, Lower excited state
k_B	Boltzmann's constant
k_q	Quenching coefficient
ln	Natural logarithm
m	Mass, Metastable species
n	Number density

n_q	Quenching partner number density
P	Probability
Q	Quenching
r_O	Dissociation degree
R_y	Rydberg energy
S	Signal
T	Filter transmission efficiency, Trigger event
t	Time
T_e	Electron temperature
T_g	Gas temperature
x	Collisionality parameter, Parameter value, Energy ratio
ASE	Amplified Stimulated Emission
CCD	Charge-Coupled Device
CCP	Capacitively Coupled Plasma
DDG	Digital Delay Generator
EEDF	Electron Energy Distribution Function
ERA	Energy Resolved Actinometry

ETI	Equal Tail Interval
GEC	Gaseous Electronics Conference
HDI	Highest Density Interval
HERA	Helium Energy Resolved Actinometry
ICCD	Intensified Charge-Coupled Device
ICP	Inductively Coupled Plasma
LTP	Low Temperature Plasma
MCP	Micro-Channel Plate
OES	Optical Emission Spectroscopy
OPO	Optical Parametric Oscillator
PDF	Probability Distribution Function
PID	Proportional, Integral, Derivative
PROES	Phase-Resolved Optical Emission Spectroscopy
RF	Radio-Frequency
ROI	Region of Interest
TALIF	Two-photon Absorption Laser Induced Fluorescence
TTL	Transistor-Transistor Logic

Contents

List of Tables

List of Figures

Acknowledgments

Embarking on this PhD journey has led to many highs and lows. Over these past five years, I have met many characters who have made the adventure an enjoyable one. For this, I would firstly like to express my gratitude to everyone who has been there with me along the way.

I would like to thank my supervisors, Deborah O'Connell and Timo Gans for giving me the opportunity to carry out this PhD, and for their support and guidance throughout the project. Also to James Dedrick for helping to get this thesis over the finish line. To my undergraduate supervisors back in Bristol, Paul Harper, Byung Chul Kim, and Chris Allen who helped write the letters of recommendation in the first place.

Special thanks to Kari Niemi who has been a key pillar of support with both the experimental and theoretical aspects, and being the first point of contact for all the laboratory mishaps and queries. To the low-temperature plasma group for welcoming me into their fold and all of their encouragement. To Andrew Gibson and Chris Bowman who took their time to teach me the skills used in this thesis. And to James Ellis, Dave Meehan and Scott Doyle who helped me get up and running with the experimental equipment.

I have had the pleasure of sharing my time at York with my fellow PhD and masters students, post-docs, and the rest of the YPI family. To all those at the fencing club, the DnD crew, and the lads at football. The friends who I had spent countless hours gaming with when I certainly should have been doing work. Thanks to Joce, James, Dave and Sarah who allayed the worries I had with the thesis writing.

Timeline shout-out to COVID-19 and the pandemic for altering the course of the project and giving me a renewed perspective on life. Thanks to Hololive and Achievement Hunter for keeping me preoccupied and cheering me up in the low times, and being a source of entertainment and inspiration. I am thankful for the free lunches, legendary chicken goujons,

and delicious cakes kindly offered by the talented bakers of the YPI, all of which have helped to provide sustenance and boost morale.

Last, but not least, my mum, dad, my brother and his family, and the rest of my family who have been there to support me every step of the way. And to all who believed in me, thank you.

Declaration

I declare that this thesis is a presentation of original work, and it has not previously been presented for an award at this, or any other, University. This thesis is the result of my own investigations, except where otherwise stated. All other sources are acknowledged as References.

All of the experiments and analyses presented in this thesis was carried out by the author. The results of which are in preparation to be published, with some of this work previously presented at conferences. All of these details are given in the "List of Publications and Contributed Presentations" section.

The original data acquisition and analysis scripts for the TALIF measurements were received from then-PhD student James Ellis, but the latter was written by Dr. Jérôme Bredin who also developed the script used for the laser attenuation feedback control scheme. The acquisition script for the camera was modified by the author for pulsed measurements. The analysis script was edited for evaluation of oxygen and xenon fluorescence. The TALIF apparatus was largely already in place when the author was carrying out their measurements. Previous users were PhD users: James Ellis and Martin Blake who accredited the set-up to Dr. Jérôme Bredin and Dr. Kari Niemi.

The original data acquisition, cross section data, and analysis scripts for the energy resolved actinometry measurements were received from Dr. Andrew R. Gibson. The analysis script was subsequently modified and re-made to be adapted for helium energy resolved actinometry as well as easier user-functionality. A script from then-PhD Frederik Riedel supplied a script to calculate errors from optical emission measurements that was also modified by the author to be compatible with input data.

This work was been funded by the Engineering and Physical Sciences Research Council, grant reference numbers EP/K018388/1 and EP/S022430/1.

Chapter 1

Introduction

This introduction first introduces how plasma is used in the semiconductor manufacturing process and the issues that arise from this. It then covers various plasma operating aspects that relate this work to industrially relevant interests. Lastly, it introduces diagnostics and underlines the inherent difficulties associated with each. Emphasis is placed on two particular techniques where this work aims to address these, ending with motivations and an outline of the thesis.

1.1 Low-temperature plasmas

Plasma is a gaseous matter that can be created by depositing sufficient energy into a gas to overcome the force of attraction between charged species. Thus, forming positively and negatively-charged particles in a cloud of free electrons. These can be manipulated using external electromagnetic fields. A plasma can be categorised depending on its plasma density and electron temperature [1, 2]. A low temperature plasma is a subset of plasma with a key characteristic being that the charged species are not in thermal equilibrium with each other. The heavy species i.e. ions and neutrals can remain at room temperature, $\sim$1/40 electronvolts, whereas the electrons possess can possess several. For reference, 1 eV is equivalent to 11,600 K. So, the electrons are very energetic, responsible for sustaining the plasma as well as driving key processes of interest to industry.

1.2 Applications of Low Temperature Plasmas

Low Temperature Plasmas (LTPs) have potential in a wide range of actively researched technological applications [3], from biomedical [4,5] to spacecraft propulsion [6,7]. One already well-established field is in the semiconductor manufacturing industry. Plasma processing has been extensively used in the production of microelectronics, and an example of this is a transistor seen in figure 1.1. Notably, it has facilitated the continuation of Moore's Law which states that the computing power of microelectronics roughly double every two years. The mechanisms behind how the plasma species are involved in the surface modification is covered extensively in [1,8,9]. Briefly, neutral radicals and positively charged ions are both capable of etching and sputtering away material to form tiny structures, namely transistors. When applied in tandem, the surface modification is significantly enhanced [10]. Further advancements in the field have enabled the feature sizes of microelectronics to reach the order of nanometres [9,11].

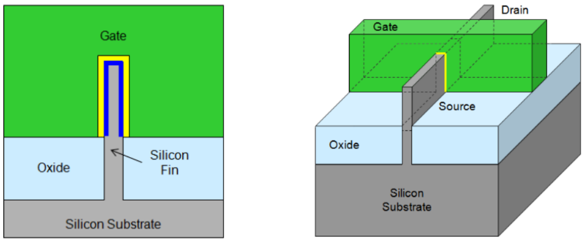

Figure 1.1: An example of a 3D transistor. Silicon wafers are used as the base material to make integrated circuits. The ideal 3D transistor profile has high-aspect ratio trench depth versus width with straight sidewalls, producing the fins. As a result, having multiple fins as close to each other as possible, that is increasing the packing density, results in improved computing power. The first step in its lay-up is to use plasma species to etch away substrate material to form these structures. Figure adapted from ref. [12]

However, this length scale entails stricter manufacturing precision for satisfactory device performance. Minute variations in the fabrication process affect the end product [13,14], with tolerances as tight as a few atoms [15]. Thus, it is these very same species that also cause defects, such as undercutting or notching [16–18].

Examples of these are illustrated in figure 1.2. Going clockwise from the top-left are bowing, microtrenching, undercutting, overcutting, notching and tapering. Most of these cases are intrinsically linked with the chemistry of the plasma. Etching via reactive neutrals isotropically removes material and causes undercutting. However, a by-product in the etching of silicon with fluorine is the production of C_xF_y polymers. This sticks to the sidewalls and may produce a thin film, termed passivation. This layer prevents further etching and many of the defective profiles mentioned, enabling formation of deep trenches with straight sidewalls. However, too much of this results in greater difficulty in the removal of material, and as a result leads to tapering. The amount of passivation can be controlled through the addition of oxygen whereby oxygen atoms prevents this polymer build-up [19]. Moreover, atomic oxygen helps to increase the etchant density and therefore increase etch rate [8]. Consequently, controlling the amount of reactive species is critical to the quality of the treated surface and speed of manufacturing. This may be achieved by adjusting input parameters during the plasma process to fine-tune the plasma as needed, such as introducing more or less of a particular gas.

Moreover, another parameter of interest is the mean electron energy. Energetic electrons are responsible for driving the chemistry of the plasma since these are able to produce reactive species through electron impact dissociation. Such reactions require a certain threshold energy, and so measuring the mean electron energy gives an idea of what reactions are present, and ideally promoted or reduced as needed. Moreover, high mean electron energies as found in capacitively-coupled plasmas tend to produce energetic ions that actually cause damage to the substrate.

This thesis looks at how further improvements can be achieved in this area, both through development of in-situ diagnostics to measure plasma parameters that influence the etching process, and study how these respond to various input conditions.

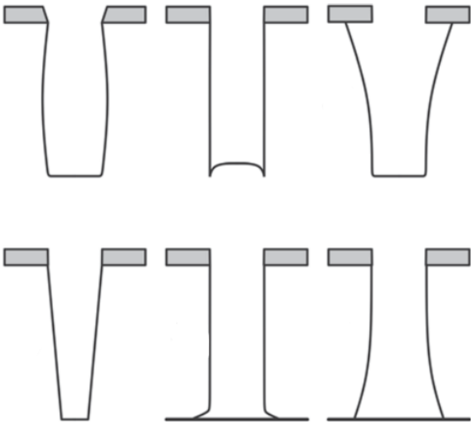

Figure 1.2: Plasma-induced manufacturing defects caused by plasma species. While structures have reached the nanoscale thanks to these, various examples of imperfections are also caused by them and are shown here. Better control of these is deemed to be necessary for improved consistency in device quality. Figure adapted from ref. [20]

1.3 Interest in using high density plasmas

High density plasmas are desirable to increase the rate at which a product is processed. One source in particular is an Inductively Coupled Plasma (ICP); a sketch of an experimental reactor that emulates an industrial device is seen in figure 1.3 and is capable of achieving electron densities of up to $n_e \sim 10^{12}$ cm^{-3} [1]. For comparison, this is an order of magnitude greater than Capacitively Coupled Plasmas (CCPs), so the prospect of manufacturing ten times faster is attractive to maximise output. It has additional advantages over CCPs, including lower sheath potentials [21] as well as the ability to control the impinging ion energy by separately biasing the substrate electrode [22]. As a result, there is greater control over damage from high energy ions. Thus, ICPs are an attractive plasma source for plasma processing.

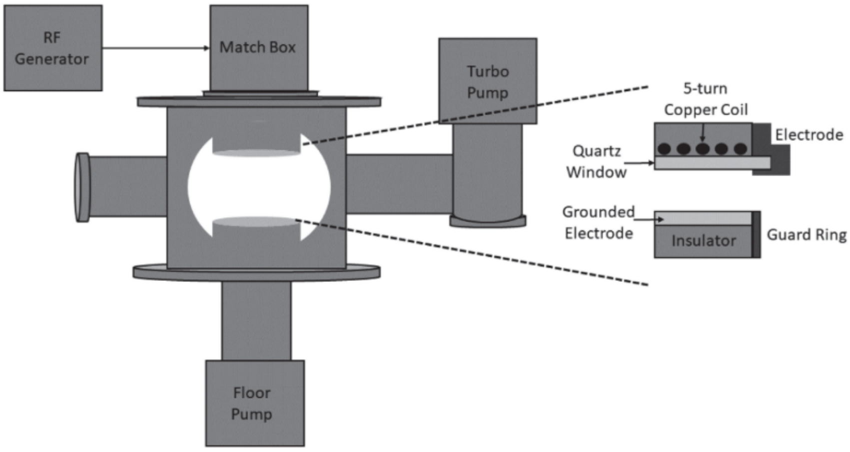

Figure 1.3: A sketch of a modified GEC experimental reactor configured for inductive coupling capable of producing high plasma densities used in later experiments. Figure taken from [23].

A brief introduction of how an ICP operates is given here, with further details covered by [1,24,25]. As its name suggests, power is transferred to the electrons in the plasma through time-varying induced fields. Current flowing through a metal coil generates an electric field that in turn makes an alternating magnetic field. Both of these can be experienced by the electrons at different powers. This leads to a characteristic feature of ICPs where they are able to operate in two distinct modes. At low powers, the electrostatic forces are dominant and so electrons gain energy from a moving sheath, similar to CCPs. Hence, this lends its name to the E-mode. With increasing applied power, more electrons are produced.

Additionally, the induced magnetic field from the coil becomes stronger, which in turn begins to induce a current in the plasma. With sufficient electron density, the induced current from the electrons dominates ionisation process [24, 26] and so is known as the H-mode. As seen in figure 1.4 this operating regime is visually very bright, has much higher electron densities than the E-mode, and also has lower sheath potentials - another benefit of this mode. While not explored here, there is a transition regime in between these where the plasma is not stable.

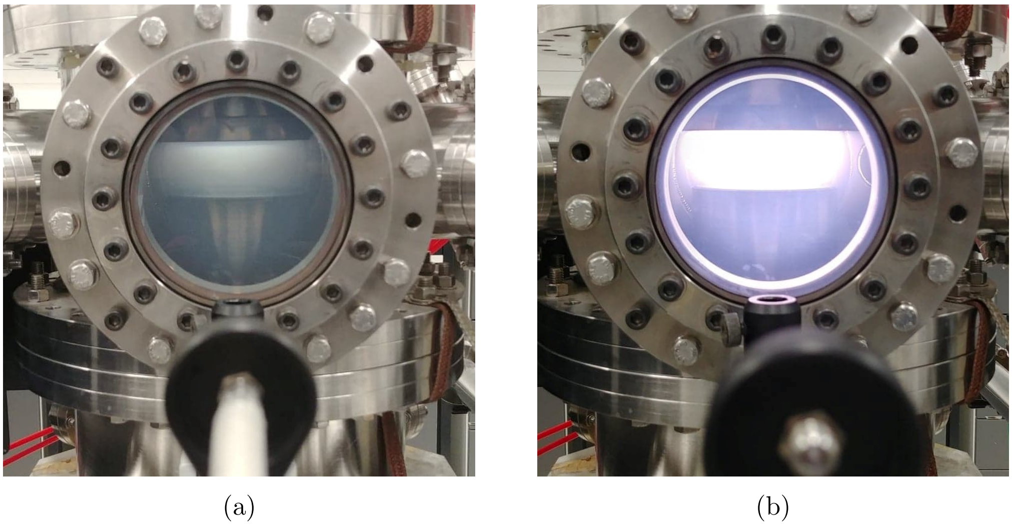
(a) (b)

Figure 1.4: An inductively coupled plasma containing oxygen is operated in a) low and b) high power modes on the GEC reactor. The latter is much brighter and has higher plasma density which is attractive for rapid surface modification. Plasma parameters that influence this are sought through the passive capture and analysis from its optical emission.

1.4 Benefits of pulsed Inductively Coupled Plasmas

Continuous operation of an ICP in H-mode causes significant gas heating. In molecular gas mixtures, this is due to increased amount of heat released upon dissociation [27, 28]. Moreover, this has additional effects on the substrate [27], the chemistry which has a temperature dependence [28], the uniformity of the plasma [28–30], and the longevity of the reactor. Thus, pulsing allows the gas temperature to return to background [29] and consequently reduces the time-averaged heat loads [31]. This opens up the potential modification of materials that have lower heat-thresholds, i.e. plastics.

In addition to this, operating in this mode has other advantages of interest in industrial applications including better selectivity [32, 33], etch rates [34] and lower wafer damage [1, 3, 35]. Further in-depth reviews of the benefits of pulsed plasma covering these topics include [34, 36]. Earlier, defects such as notching and micro-trenching were mentioned. These are typically as a result of build-up of charge from positively bombarding ions at the bottom of the trench causing subsequent ions to be repelled. By briefly extinguishing the plasma, electrons and negative ions are able to escape and neutralise the surfaces. As such, commonly observed defects are deemed preventable by modulating the power.

Another potential advantage is the ability to shape the electron energy distribution that dictates the composition of the plasma. Upon ignition, high energy electrons are produced before settling into a steady state, with higher electron temperatures achievable at lower duty cycles [37]. Hence, control over production of particular radicals may be possible, such as the case with production of atomic fluorine and oxygen mixtures; the dissociative excitation energies to produce these atoms are are 9.6 [38] and 16 eV [39] for SF_6 and O_2 respectively. Selection of pulse frequency and duty cycle would tailor the production of specific species depending on the amount of etching needed.

Pulsing is achieved through temporally modulating the power at an electrode. Depending on the particular desired effect, this can either be the main coil for ICP, at the target substrate or both. The pulse frequency and duration are additional variables for greater fidelity over plasma parameters, such as the electron energies [40], or adjusting the pulse-timings between the two electrodes for increased ion flux and energies [41].

When pulsing an ICP, the plasma always ignites in the E-mode since it has to build up sufficient electron density for H-mode transition. Then, it operates in the high-power mode as normal once steady state is achieved. The time to reach this is affected by factors such as pressure [40,42]. Once the power is off, the electrons no longer have an external heating source. So, electron-impact mechanisms and subsequently the plasma sustainment quickly subside. This is the off-time and, as there is little plasma emission, active diagnostics can be applied to probe the species' dynamics during this period.

Conversely to the electrons, the heavy particle species live on a much longer timescale and can remain in the plasma afterglow. These may further interact with the surface modification. Indeed, the etch rate was found to be similar for both pulsed and continuous operation [43]. Subsequently, for heat-sensitive treatments, high amounts of radical species can be generated during the pulse while minimising continuous exposure to elevated temperatures. Therefore, it is worthwhile to study pulsed plasmas where possible as it holds much potential over continuous. Others have studied the evolution of the atomic oxygen species in the afterglow in pyrex discharge tubes using a diagnostic electrical pulse [44,45] or resonant vacuum absorption spectroscopy [46]. Using an alternative technique can better compare and contrast its behaviour, particularly in a plasma source more relevant for semiconductor processing.

1.5 The role of oxygen plasmas

Oxygen plasmas have a wide range of applications and are particularly used to remove polymer films produced during the etching process [19,47]. Mixing it with other etch gases increases the etchant density as well [19,48]. Ultimately, atomic oxygen is a potent and versatile species that has great importance in the manufacture of integrated circuits. Thus, knowing how it can be effectively produced is of interest to optimise surface modification.

It is both electronegative and chemically reactive - properties exhibited by etch gases used in semiconductor manufacturing, such as CF_4 and SF_6. In particular, oxygen's electronegativity is comparable with fluorine and therefore displays similar chemistry [49]. Since typical etch gases mentioned earlier are more complex molecules, they therefore have a myriad of chemical pathways, especially within gas mixtures. So, accurately modelling the entire gas chemistry in a plasma is challenging, especially where data is limited such as cross-sections and reaction rates. Instead, given its much simpler structure and properties, studying oxygen may lead to a similar reflection of etching characteristics. There is already a wealth of literature regarding its cross-sections [39,50], recombination probabilities [51], etc. Consequently, models will be more considerate of all possible interactions, as exemplified by [52–55].

From an experimental point of view, it is a much easier gas to obtain and use in experiments given that the alternative themselves may cause unwanted etching of apparatus. This facilitates easier comparison between experiments and theory, and can therefore improve our understanding of the model system. For example, how ion-ion recombination affect negative ion loss [56] or how an oxygen metastable further contributes to an oxygen emission line that is used for actinometry [57].

One parameter of interest is the atomic oxygen density - radical species provide reactive chemistry that enables surface modification. It is desirable to measure these to have better control during plasma processing. For example, addition of oxygen feed gas to etch mixtures has the ability to increase the etchant density [8, 19, 48]. Yet, both this and the etch rate do not linearly scale with increased oxygen content, and too much can lower these parameters [48]. Thus, optimising the manufacturing process requires careful monitoring of the plasma species.

Consequently, given its importance, the atomic oxygen densities have been measured extensively through various means, including actinometry [58], laser spectroscopy [59,60], and relatively recently Energy Resolved Actinometry (ERA) [61, 62]. These measurements have been carried out in all manner of plasma sources. As such, a greater understanding of how it behaves under various conditions ensures confidence in development of newer diagnostics, which will be discussed later.

1.6 The Gaseous Electronics Conference reference cell

The Gaseous Electronics Conference (GEC) reference cell is an experimental reactor with an internationally agreed upon design. So, measurements carried out in this are more easily comparable between research groups [63, 64]. Moreover, closely mimicking the conditions of an industrial device allow observations to be of practical benefits for industrial purposes [65]. In contrast to plasma processing machines, it was designed to enable easy access including large quartz windows. This allows the use of optical diagnostics, in this case, laser spectroscopy and phase-resolved optical emission spectroscopy, to be employed. These are preferable since this does not require insertion of probes or titration gases into the plasma that could introduce asymmetries in the processing. These can be divided into active or passive techniques as described earlier.

Although the original design was a parallel-plate geometry [64], a modified inductively coupled version has also since been developed [66]. Consequently, investigations using a more practically relevant high density plasma are able to be carried out. Despite the existence of other high density plasma sources, such as Electron Cyclotron Resonance, measurements using a common reference helps to identify discrepancies or similarities of the plasma's behaviour. Therefore, this aids in contributing to a knowledge base to control a plasma in the future.

1.7 Diagnostics used in determination of atomic densities

Real time monitoring of a plasma during processing is a pinnacle aim for active feedback control. By doing so, drifts in processing or malfunctions are identified early and avoid costly post-process inspections and corrections. However, development of compatible diagnostics are still needed. On one hand, laser diagnostics are complex to use and difficult to implement as routine in industry, but require less analysis to obtain good quality information.

On the other hand, spectrometers for optical emission spectroscopy (OES) are much simpler and are already used for detecting end-point etching [19]. Another advantage of OES is that obtaining spectral data is very quick. Consequently, real-time measurements of the electron temperature and densities [67], with feedback control of the manufacturing process over these plasma parameters from recorded spectral data [68] and process monitoring [69,70] has been researched. OES has also been investigated to determine atomic oxygen negative ion densities [71], possible fault detection [72], predicting plasma etch characteristics [73] and monitoring the plasma species [74, 75]. Yet, its functionality regarding this last application is so far limited to qualitative descriptions of the presence of a species. Ideally, it would be utilised to get the same information as laser spectroscopy from the passive emission, that is, absolute number densities.

Analysing these spectra is a major challenge as there are many processes that contributes to emission. Figure 1.5 illustrates these contrasting diagnostics. ERA is investigated as a balance between the two where it is much less complicated to carry out experimentally than laser methods, while only needing slightly more processing of the data.

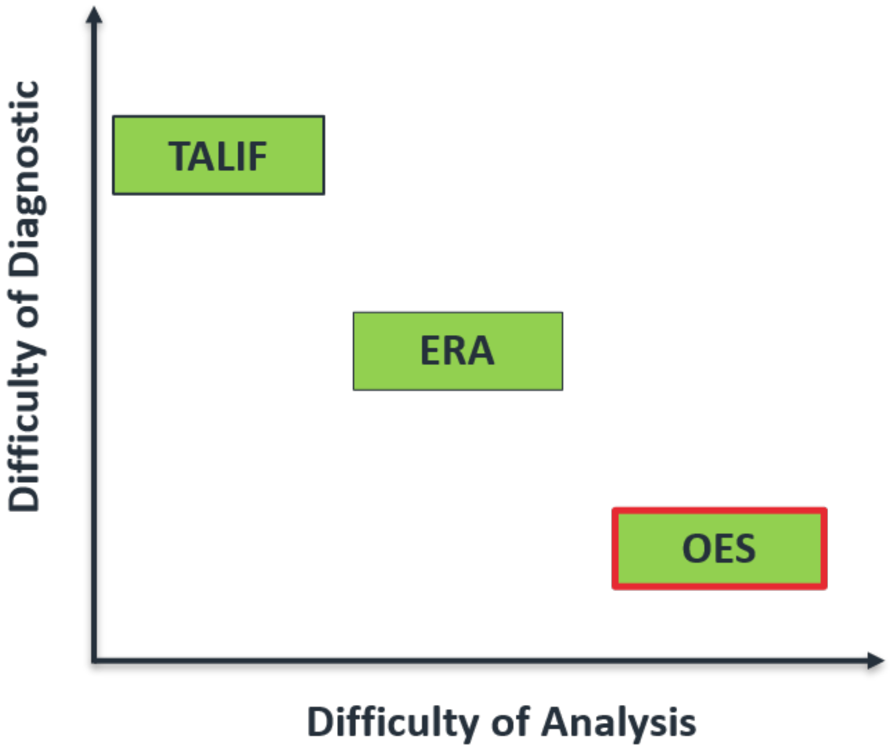

Figure 1.5: Representation of diagnostic complexity versus ease of analysis. There are many diagnostic techniques available for laboratory use, but few compatible with industrial devices. Ideally, real-time information is gathered from simple methods like optical emission spectroscopy outlined in red, but with the ease of analysis and quality of information as laser spectroscopy. ERA aims towards bridging the gap between these.

1.7.1 Active techniques: Two-photon Absorption Laser Induced Fluorescence

Laser-based techniques are active methods that externally stimulate the species of interest to generate emission. In-depth discussion of these have been covered by [76, 77]. This thesis looks at Two-photon Absorption Laser Induced Fluorescence (TALIF) which is capable of obtaining absolute atomic oxygen densities when properly calibrated. As this quantity is of great interest in various applications, TALIF has been employed in many other plasma sources [59, 78–84]. Though of these, only a few studies have used the technique in low pressure, inductive plasmas [56, 85]. Overall, it is a well-practised technique and has served as a useful benchmark for the passive diagnostic, ERA [61, 86] which this thesis investigates in a different plasma regime.

Although it is able to obtain absolute atomic densities, its accuracy is dependent on the calibration which leads to great uncertainty in the final result. As such, others have instead favoured alternative techniques, such as Cavity Ringdown Spectroscopy [87], or Resonant Absorption Spectroscopy [47]. The strength of the TALIF signal correlates to the number density of the species of interest, and calibrating this against a known source gives absolute number density. Titration involves an appropriate gas to react with the atomic species, though this would not be suitable for industrial purposes as this can introduce unwanted chemistry. That aside, it also requires additional components compatible with existing set-ups and therefore adds more complexity. Alternatively, absolute densities are attainable through calibration using noble gases and have been benchmarked against the titration method [60]. However, this requires knowledge of two-photon excitation cross-section ratios. Moreover, the reported uncertainty in these measurements are as large as a factor of 2 [88] and will affect the reported magnitude. Nonetheless, it still gives both qualitative and quantitative information about the plasma behaviour. Plus, it is able to study the afterglow dynamics with good temporal resolution.

TALIF is seldom used for determining gas temperatures, which can be inferred through the Doppler broadening profile of the excitation wavelength [89, 90]. However, this very much needs high resolution of the laser output, and so it is not possible to carry out this technique on oxygen unless highly specialised apparatus are used [90]. Alternatively, for the case of atomic oxygen, the relative fluorescence from its ground state sub-levels can also give the gas temperature from Boltzmann plots [60, 91]. Regarding the latter case, these were for atmospheric pressure plasmas. On the other hand, this method has not yet been tried in low-pressure, ICPs where heating is prominent and influences reaction rates. Gas temperatures of oxygen plasmas in a pulsed ICP has been carried out using other well-known methods, but inevitably required nitrogen or argon [92]. Obtaining this through just the oxygen species offers an independent way, one without resorting to gases that may provide unwanted reactions.

1.7.2 Passive techniques: Energy Resolved Actinometry

Plasma naturally gives off light that contains a wealth of information. Species generate characteristic wavelengths which aids in identifying the composition of the plasma. Obviously, this passive emission should be taken advantage of as much as possible in place of active methods that risk perturbing the plasma. This can be done through ERA that builds on the conventional actinometry approach.

Conventional actinometry is a simple way of obtaining the densities of species through comparing the strengths of particular lines against one another. However, it is based on several assumptions that are often not met. Firstly, emission comes not only from direct impact with atomic ground state species, but also from dissociative excitation. Without considering this, atomic densities can be overestimated [59, 78]. It also requires knowledge about the electron energies to compare the intensities against the excitation rates. It may be supplemented with Langmuir probes [93, 94] but this is invasive. Otherwise, it has to be assumed [59] which introduces more uncertainties. Lastly, the excitation cross-sections are energy dependent and so the excitation rates are susceptible to changes in the electron energy distribution which will occur with varying conditions [95, 96].

On the other hand, ERA circumvents these issues by utilising a second line ratio to simultaneously solve the two unknown parameters, mean electron energy and atomic number density. Thus, compared to TALIF, additional practical information is obtained through this method. Moreover, it compares excitation ratios rather than emission intensity ratios where the latter is also susceptible to additional contributions from metastable and cascades. ERA utilises phase-resolved optical emission spectroscopy which minimises these [97].

The technique was first applied in an atmospheric pressure plasma jet and showed good agreement with TALIF [61]. It was further used in a capacitively coupled system [62]. Lastly, it was tested in the low powered mode of an ICP and again showed similarities with TALIF [86]. However, it found difficulty with determining plasma parameters when applied to the high powered mode [86]. As such, it has yet to be fully realised for the inductively coupled regime of an ICP.

However, ERA only studied simple gas mixtures, namely oxygen and argon. For more industrially relevant applications, the introduction of etch gases would be more beneficial in directly studying the effects on atomic oxygen density with changing input conditions. Alternatively, since excitation ratios between oxygen and argon are studied to obtain plasma parameters of interest, the same practice could be extended using fluorine emission. Actinometry of this gas has been investigated [98,99], and the latter found good agreement in the density of F atoms, but required the use of Langmuir probes. As such, application of ERA would be of interest in further work as it is able to simultaneous determine these parameters passively from the plasma emission.

1.8 Using helium as a diagnostic tool

Helium gas is traditionally used to cool the substrate owing to its good thermal conductivity [20]. It is also inert which makes it ideal for avoiding unwanted induced chemistries. Even though it has emission lines at 706 nm and 728 nm, these have not been well-investigated whether they can be exploited to obtain plasma parameters in a low-pressure discharge. Albeit, the threshold energies to enter these excited states are rather high, ~23 eV and are susceptible to quenching, so may be difficult to detect. Nonetheless, this may also be exploited if compared against argon emission that has lower threshold excitation energies ~13 eV. The sampling of two different energy populations would enable greater sensitivity in measurements, especially since changes in electron temperatures of less than 1 eV can adversely impact wafer quality [100]. Trace rare gas OES was used to determine electron temperatures, but despite including helium, it was not observable in Cl_2 plasmas [100]. Similarly, its emission was not used in determination of electron temperature in oxygen plasmas [101]. This was also likely due to it constituting 1% of the gas mixture in both cases and giving negligible signal. In contrast, mean electron energies were able to be deduced with sufficient helium in an atmospheric plasma [102]. As such, it is of interest if there are ideal conditions where these emission lines can be of use in diagnostics, i.e. adjusting the gas composition so helium emission is strong enough to be more easily compared against argon [103].

1.9 Motivation

To recap the motivations behind this thesis:

1. Development of compatible diagnostics for use in industry is needed to better understand plasma behaviour and identify key process parameters that affect the quality of semiconductors during manufacturing. ERA is a passive technique able to determine atomic oxygen densities and the mean electron energy. Moreover, it is much simpler to use than two-photon laser spectroscopy in obtaining the former quantity. However, it has yet to be successfully employed in the inductive regime of an ICP. Implementing Bayesian methods and helium emission is explored to allow greater flexibility and sensitivity in the determination of these plasma parameters. Consequently, verifying the measurements of atomic oxygen under varying plasma conditions is equally as important. Hence, the established method of TALIF is also used to independently benchmark these.

2. While gas temperature has an influence on, for example the plasma uniformity, obtaining absolute atomic densities using both TALIF and ERA require knowledge of this. It will particularly affect the calculated densities through the latter method. However, gas heating is prevalent in inductively coupled plasmas operated in the high power mode. As a result, unlike capacitively or atmospheric plasmas, the gas temperature cannot be easily assumed. This is made more complex when working with gas mixtures which will have varying levels of contribution from different heating mechanisms. Therefore, T_g must be determined in order to provide more accurate calculations in the analysis. This is also achievable using TALIF by comparing the relative fluorescence from each of the atomic oxygen ground state sub-levels, and only requires little adjustment to the experimental set-up.

1.10 Thesis outline

In this thesis, the atomic oxygen densities, gas temperatures, and mean electron energies of a pulsed, ICP operated in the high-power regime are investigated using two optical-based diagnostics. The outline of the thesis is as follows:

Chapter 2 covers the theory behind the diagnostic techniques, including how observed emission arises and analysed to determine plasma parameters.

Chapter 3 covers the experimental set-up and how the measurements were taken for both TALIF and ERA.

Chapter 4 contains the results from TALIF under a range of varying plasma conditions of power, pressure, and gas composition in order to obtain benchmark values of atomic oxygen densities. These were taken in the afterglow of the pulse to achieve better signal-to-noise of the detected fluorescence signal.

Chapter 5 extends the use of the laser to probe other ground state sub-levels in order to determine the gas temperature. The relative fluorescence from each are compared and plotted on Boltzmann plots, with the slope giving the gas temperature. Moreover, the temporal evolution of these sub-levels in the afterglow are discussed.

Chapter 6 extends the use of ERA in the high-powered mode of a pulsed, ICP in order to assess its applicability in this regime. High electron temperatures were found which raised doubts over the accuracy of the measured plasma parameters. Investigations into the cause for this pointed to the use of the 777 nm emission line giving ambiguous results due to the high dissociative excitation contribution.

Chapter 7 builds on the principles of ERA using helium in an alternative line ratio to overcome ambiguity found in the original method. More consistent electron temperatures were obtained and results show good agreement with TALIF, both qualitatively and quantitatively, over the studied plasma conditions.

Chapter 8 summarises the main findings and future work is outlined.

Chapter 2

Background theory

The theory for how both diagnostics used in this thesis, Two-photon Absorption Laser Induced Fluorescence (TALIF) and Energy Resolved Actinometry (ERA), obtain plasma parameters are described in this chapter. Both of these are able to determine atomic oxygen densities, but through alternative methods. Therefore, this section discusses how the emission from the plasma is interpreted to obtain this as well as other parameters of interest.

2.1 Two-photon Absorption Laser Induced Fluorescence

2.1.1 Excitation scheme and fluorescence

Whenever excitation is caused by photon absorption that results in emission of a different wavelength during subsequent de-excitation, this phenomenon is termed fluorescence. The amount of resulting emission observed is proportional to the number density of the species in the initial level that the incoming photons interact with. Furthermore, transitions between particular levels are achievable by the use of lasers since these are able to provide mono-energetic photons. Hence, laser diagnostics are able to directly access information about specific species in this manner.

A single photon can be absorbed, as in normal Laser Induced Fluorescence (LIF). However, this often requires vacuum ultraviolet (VUV) wavelengths if exciting directly from the ground state. These wavelengths are challenging to produce and also entails additional experimental complexities, such as requiring measurements to take place under vacuum. On the other hand, multiple photons can be simultaneously absorbed to reach the excited state. Thus, two photons with the same energy and using a laser with high enough intensity, two-photon absorption can be achieved. In TALIF, the transition to the upper level may be different than the single photon case, allowing for alternate emission lines to be observed.

Figure 2.1 is a reproduction of the two-photon excitation scheme for atomic oxygen and the noble gas calibration, xenon [60]. The simultaneous absorption of two photons to the excited state requires wavelengths of 225.65 nm and 224.31 nm, and the resulting fluorescence are 844.87 nm and 834.91 nm for atomic oxygen and xenon, respectively.

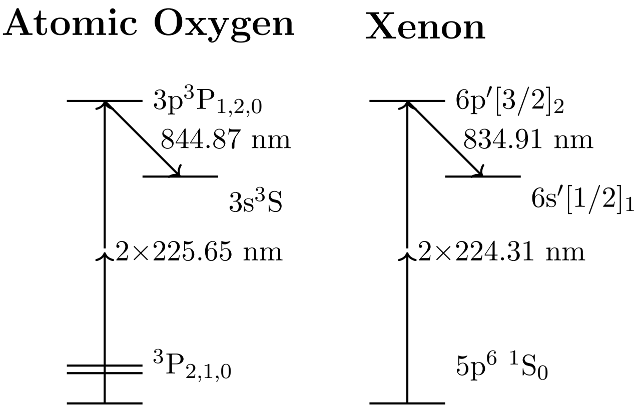

Figure 2.1: Two-photon excitation scheme for atomic oxygen and xenon recreated from [60].

The relative fluorescence between the species investigated, in this case atomic oxygen, and a noble gas, xenon can be compared in order to obtain the absolute atomic densities of the desired species. Also, it is important to differentiate between the origin of the observed emission from other sources, such as plasma-induced, as this will affect the calculation of the atomic oxygen density - only photons due to excitation from the laser should be counted.

2.1.2 Obtaining absolute atomic densities

A full treatment of the TALIF methodology and treatment can be found elsewhere [104,105]. Nonetheless, the key equations used are included here for easier reference. In particular, the absolute atomic state densities can be determined from equation (2.1), and involves calibration with a noble gas, where the subscripts R and X denote the reference gas and the species of interest, respectively.

$$n_X = \frac{T_R}{T_X}\frac{\eta_R}{\eta_X}\frac{\sigma_R^{(2)}}{\sigma_X^{(2)}}\frac{a_R}{a_X}\left(\frac{h\nu_X}{h\nu_R}\right)^2\left(\frac{E_R}{E_X}\right)^2\frac{S_X}{S_R}n_R \tag{2.1}$$

T is the transmission value of the optical filter; η the quantum efficiency of the detector; $\frac{\sigma_R^{(2)}}{\sigma_X^{(2)}}$ is the two-photon cross-section ratio; a is the effective branching ratio of the excited state; $h\nu$ the laser photon energy; E the laser pulse energy; S the integrated signal of the fluorescence, and n the atomic number density.

T and η are constant values that depend on the optics used. Similarly, the two-photon cross-section ratio and $h\nu$ values are also constants, the former of which is taken from literature. The other terms are determined experimentally. Firstly, E can vary from day-to-day operation of the laser. Determination of a involves lifetime scans where the intensity of the fluorescence is measured over time, and similarly for S but with varying excitation laser wavelength. Lastly, the reference species' density n_R can be determined through the ideal gas law, $n = p/(k_B T_g)$. Subsequently, absolute densities are obtained through this calibration of the fluorescence signal intensity with the known reference amounts.

2.1.3 Fluorescence signal intensity

The intensity of the fluorescence depends on both the laser energy and also excitation wavelength. As the former increases, it produces a much more intense beam, and so the likelihood of interaction between photons and species is greater. For two-photon processes, the signal intensity is proportional to the square of the laser energy. Yet, care must be taken to avoid saturation effects where loss of signal i.e. excited states can occur through Amplified Stimulated Emission (ASE) and photoionisation. This can be avoided by operating the laser below energies where these become prominent, and onset of these effects are determined by observation of non-linearity on an energy saturation curve.

Moreover, fluorescence is not strictly limited to the single excitation wavelengths mentioned previously - a small range of neighbouring wavelengths can also induce fluorescence due to equipment limitations and natural phenomena, namely Doppler broadening effects [106].

The normalised line profile, $g(\lambda)$ is a convolution of the laser line profile and other broadening mechanisms that affect the emission line [104]. However, the laser line profile is assumed to be the most dominant in the experimental system, and has a Gaussian profile. Consequently, Gaussian fits are applied to the resulting fluorescence when carrying out the spectral scan.

Equations (2.2) and (2.3) show that the integrated emission over a range of excitation wavelengths has a response that is a convolution between the normalised line profile and an intensity value. Thus, if the line profiles are the same for both species i.e. oxygen and xenon, then the total integrated intensity value scales with a single value, I_0 which is the maximum intensity at the central excitation wavelength. However, this may not be the case, and so the entire spectral profile has to be integrated over the range of excitation wavelengths that return fluorescence. This gives the total signal, S.

$$\int_{\lambda_1}^{\lambda_2} I_f(\lambda) d\lambda = \int_{\lambda_1}^{\lambda_2} g(\lambda) d\lambda \cdot I_0 \tag{2.2}$$

Where

$$\int g(\lambda) d\lambda = 1 \tag{2.3}$$

The two-photon scheme only excites atomic oxygen's lowest ground state sub-level, $O(^3P_2)$. Thus, the absolute densities correspond as such. The total n_O value can be obtained through using the Boltzmann fraction assuming that each of the sub-levels are in thermal equilibrium and a gas temperature is known.

2.1.4 Branching ratio calculation

The branching ratio, a_{23}, can be calculated by equation (2.4) and represents the fraction of excited atomic species that spontaneously emits photons of interest. The remaining fraction either decays and produces other wavelengths or is quenched by other particles before they are able to do so. A_{23} is the Einstein coefficient i.e. the probability that an excited state will decay from the upper state '2' into a lower, third state '3'. These transition probabilities are well documented in the NIST atomic spectra database [107]. A_2 is the sum of all possible transitions from the upper state to lower states. The reciprocal of this gives the natural lifetime, τ_{nat} which is the time it can remain in this excited state before spontaneous decay. In the absence of quenching, equation (2.5) gives the pure branching ratio for the transition of interest. For oxygen, the branching ratio is 1.000 whereas for xenon it is 0.733 [60].

$$a_{23} = \frac{A_{23}}{A_2 + Q} \tag{2.4}$$

$$a'_{23} = \frac{A_{23}}{A_2} \tag{2.5}$$

$$Q = \Sigma\, k_q n_q \tag{2.6}$$

However, quenching is likely to be present for the pressures investigated. Consequently, Q is the total quenching rate given by equation (2.6), and is the sum of the products of quenching partner density n_q and their corresponding quenching coefficient, k_q. The quenching rate may also be affected by the gas temperature and the effects are further discussed later. The main quenching partner is assumed to be molecular oxygen - compared to monatomic particles, it has both translational and rotational degrees of freedom, allowing it to store more potential energy and is reflected in having higher quenching coefficient. Finally, other species present (He, Ar) may provide negligible quenching, and the degree of self-quenching of excited oxygen by atomic oxygen is uncertain as its density is unknown. Ultimately, direct calculation of the total quenching rate is challenging given it is dependent on many factors.

Nevertheless, since the denominator of equation (2.4), i.e. $\frac{1}{A_2+Q}$ is equivalent to the effective lifetime τ_{eff}, it can be experimentally obtained by fitting the decay of the fluorescence signal at increasing delay times from the initial laser stimulus.

$$\tau_{eff} = \frac{1}{A_2 + Q} \tag{2.7}$$

In addition, equations (2.4) and (2.5) can be combined to give equation (2.8) where the branching ratio of the experimental condition is from the pure branching ratio value, the natural lifetime, and the fitted effective lifetime.

$$a_{23} = a'_{23} \frac{A_2}{A_2 + Q} \tag{2.8}$$

Thus, the value of the branching ratio for a given experimental condition can be used in equation (2.1) to calculate the density of the investigated species.

2.1.5 Effective lifetimes

2.1.5.1 Experimental Effective Lifetime

The effective lifetime can be determined experimentally by fitting the exponential decay of the recorded intensity over time. Figure 2.2 shows an exponentially decaying signal from an experimental dataset for atomic oxygen as the camera is variably triggered from a fixed laser arrival time. The laser pulse is assumed to be Gaussian (max. 5 ns FWHM) and its arrival time approximated by matching the peak intensity with the maximum fluorescence, both normalised for comparison. The x-axis relates to the camera trigger timing; it is first triggered at a time t=0 ns so that the initial measurement is prior to any observed fluorescence. The laser pulse arrives a few nanoseconds later. Therefore, this trigger time is increasingly delayed in nanosecond timesteps to obtain the time-dependent signal. The camera gatewidth is represented by the red rectangle and chosen to optimise enough signal-to-noise ratio from the experimental measurements. However, often this gatewidth is a few nanoseconds longer than the timesteps of 1 or 2 ns. As such, there may be some double-counting of the fluorescence. Ideally, the gatewidth should be the same as the timestep to only capture the fluorescence within this increment. Nonetheless, the choice of camera gate width was found not to affect the measured lifetimes [108].

Once the background signal is removed, an exponential decay function is fitted to the data using equation (2.9); a is the fitted amplitude, and the negative reciprocal of b gives the effective lifetime that is subsequently used in equation (2.8) and in turn the absolute density calculations. However, care must be taken to account for the laser pulse width since it does not instantaneously excite the species i.e. the edges of the main pulse also cause fluorescence. The dotted vertical line shows approximately when there is no more possible fluorescence from the laser pulse. The measured lifetime does depend on whether the fitting starts at the peak fluorescence signal or at the estimated end of the laser pulse as seen by the two exponential fits. This thesis assumes that the pulse is instantaneous and fitting starts at the maximum signal. The effects on the observed lifetimes will be discussed in chapter 4.

$$I = a \exp\left(-\frac{t}{b}\right) \tag{2.9}$$

$$\tau_{eff} = -\frac{1}{b} \tag{2.10}$$

2.1.5.2 Theoretical Effective Lifetime

The effective lifetimes of the excited atomic oxygen state derived from the TALIF measurements can be compared to the theoretical calculation using equation (2.11). $A_i = \tau_{nat}^{-1}$ is the reciprocal of the natural lifetime, and the total quenching is given by $Q_i = \Sigma\ n_q k_q$. n_q is the density of the quenching partner and k_q the quenching coefficient. Molecular oxygen is assumed to dominate the overall quenching rate as the other species (He, Ar, O) have much smaller quenching coefficients compared to O_2.

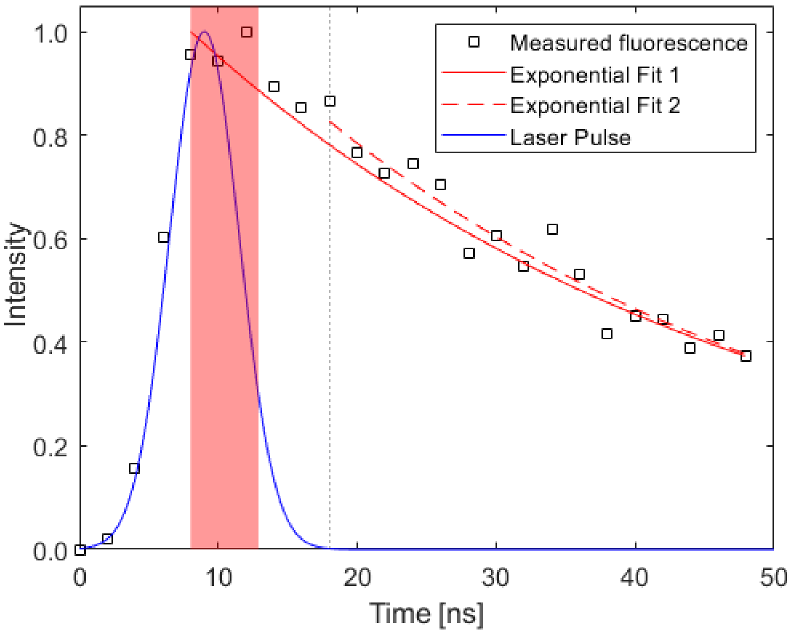

Figure 2.2: Example fitting of an exponential decay curve to a fluorescence signal. Determining the effective lifetime of the excited state from the decay constant is needed for calculation of the branching ratio and by extent the atomic densities of interest.

$$\tau_{eff} = \frac{1}{A_i + Q_i} \tag{2.11}$$

The natural lifetime value of the $O(3p^3P)$ state and its quenching coefficient with O_2 can be found from literature, leaving n_q to be calculated. Nonetheless, both components of the quenching rate are affected by the gas temperature. Since the inductive mode has substantial gas heating, it is important to consider this effect. Firstly, quenching coefficients are typically evaluated at 300 K, but can scale as $k_q \propto \sqrt{T_g}$ in equation (2.12) since higher temperatures promote frequency of collisions. Subsequently, this coefficient can be modified to scale with elevated temperatures, given by equation (2.13).

$$k_q^i = \sigma_q^i \langle \nu \rangle = \sigma_q^i \sqrt{\frac{8k_B T_g}{\pi \mu}} \tag{2.12}$$

$$k_q^i(T_g) = k_q^i(300)\sqrt{\frac{T_g}{300}} \tag{2.13}$$

Conversely, due to the ideal gas law, p/k_BT_g, for a given pressure, the neutral gas density is expected to change with gas temperature such that $n_q \propto 1/T_g$. Thus, the overall scaling of the quenching rate with changing temperature is $1/\sqrt{T_g}$. Although, the gas temperatures for these conditions are unknown until they are measured. Nonetheless, the effective lifetimes can be estimated by varying this parameter, and later compare them to the experimental results.

Moreover, the density of molecular oxygen, n_{O2} in the plasma will change once atomic oxygen is produced during the pulse. The significance will depend on the degree of dissociation, but generally it is expected that the loss of the main quenching partner, O_2 will reduce the quenching. To calculate the possible effective lifetimes, the dissociation degree is also varied to observe its impact.

The feed molecular oxygen density is given by equation (2.14) and given the superscript, 0 to denote densities before dissociation by the plasma pulse. Then, the molecular oxygen quenching density in the afterglow, n^1_{O2} (superscript of 1 for after the pulse) is calculated as the feed molecular oxygen density minus the equivalent amount assumed to be directly converted into atomic oxygen, n_O, equation (2.15). The factor of 2 in the denominator is related to the fact that one oxygen molecule produces two oxygen atoms. There is the possibility that not all these will be probed due to loss reactions with the chamber walls. The effects of the wall recombination coefficient on n_O was studied at various pressures in a stainless steel chamber and found to have a non-linear effect [53]. From this same paper, the recombination coefficient may be taken as 0.15 for the pressures investigated here. However, it could be lower as seen in [109] where it was observed to decrease with pressure. Overall, if this is accounted for, then the measured n_O would correspond to at least 85% of the total after losses. A range of n_O values are calculated using the dissociation degree definition $r_O = n_O/n^0_{O2}$. Ultimately, equation (2.17) gives the total quenching of $O(3p^3P)$ with O_2 with the consideration of various gas temperatures and dissociation degrees.

$$n^0_{O2} = \frac{p}{k_B T_g} \tag{2.14}$$

$$n^1_{O2} = n^0_{O2} - \frac{n_O}{2} \tag{2.15}$$

$$r_O = n_O / n^0_{O2} \tag{2.16}$$

$$Q_i = n^1_{O2}\, k_q^{O2} \tag{2.17}$$

Figure 2.3a shows the range of theoretical effective lifetime values for a range of dissociation degrees and gas temperatures in a pure oxygen plasma at 20 and 50 Pa. In the higher pressure case, the effective lifetime is lower due to greater amount of molecular oxygen. It is further reduced at lower gas temperatures - although quenching increases with temperature, the plasma becomes less dense due to the ideal gas law and so there would be fewer collisions.

Figure 2.3b shows that in mainly helium mixtures the effective lifetimes increase as there is less of the main quenching partner, O_2. In the 10% case, there is minimal variation whereas in the pure O_2 case it differs by 3 ns over the range of temperatures and dissociation degrees.

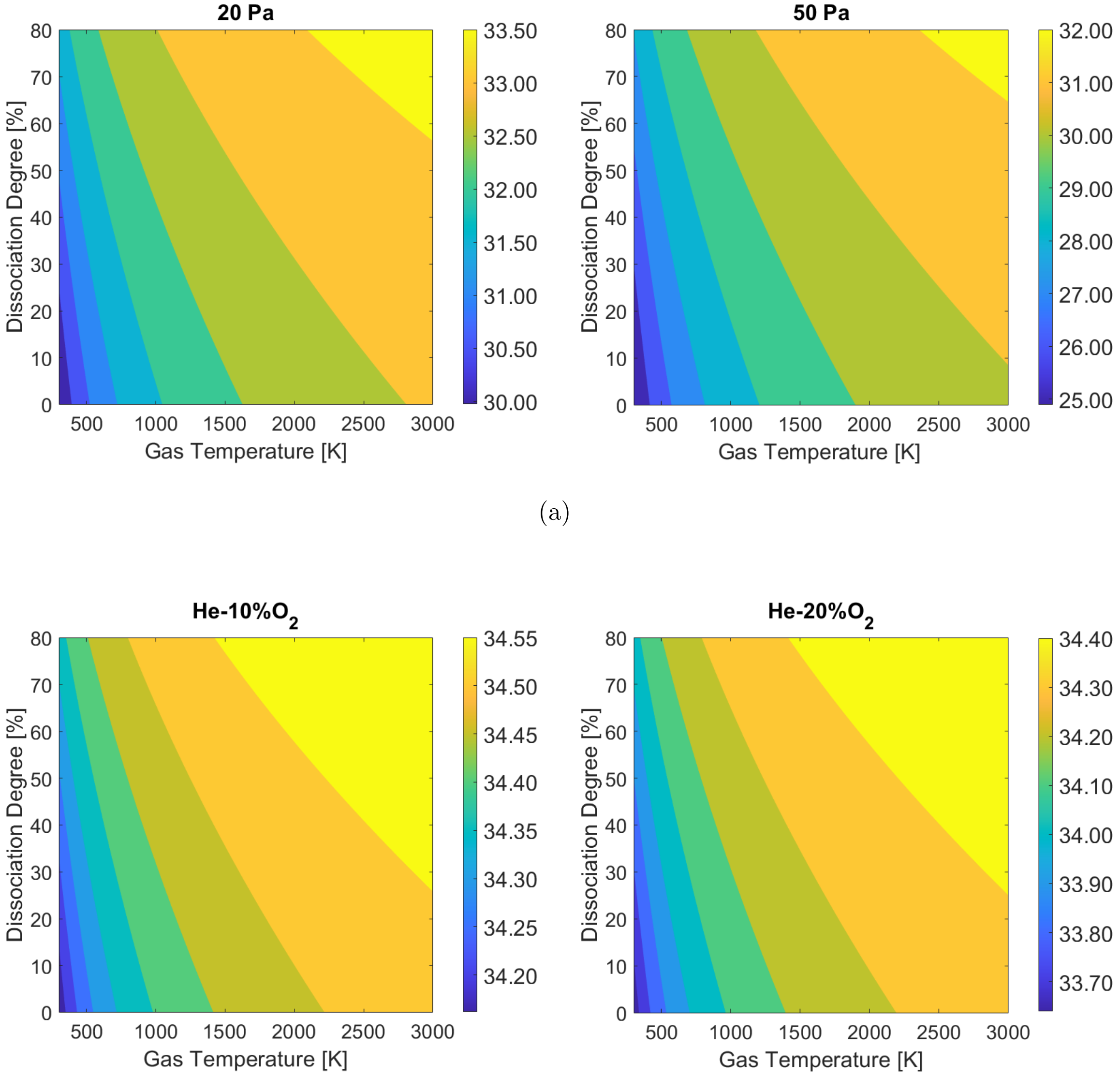

(a)

(b)

Figure 2.3: Theoretical effective lifetimes for $O(3p^3P)$ a) in pure O_2 at 20 Pa and 50 Pa, and b) in helium with 10 and 20% O_2 at 20 Pa. The colour bars correspond to the value of τ_{eff} in ns. These values are calculated with varying dissociation degrees and gas temperatures across different pressures and oxygen contents assuming only quenching by O_2. Low dissociation degrees and gas temperatures, and higher molecular oxygen contents reduce the effective lifetimes. This was done to verify experimentally obtained τ_{eff}.

2.1.6 Gas temperatures

Both the ground state $O(^3P_J)$ and the upper level $O(3p^3P_J)$ are triplet states, that is, it has fine-splitting into three sub-energy levels. Excitation to a specific upper level, $O(3p^3P_J)$, is only possible if the laser wavelength has high enough resolution, as carried out by [60, 91]. Nonetheless, since the ground state $O(^3P_J)$ is more distinctly split, it is possible to excite each sub-level in the ground state to the upper state - the latter is assumed to be indistinguishable, so this triplet is treated as a just a single state, $O(3p^3P)$.

However, the excitation wavelengths for each transition will result in a slightly different output energy, such as from transmission efficiencies in the optics. Therefore, comparison between the fluorescence should be carried out using the normalised values. Equation (2.18) shows that fluorescence is proportional to the branching ratio, a_{23}, the two-photon cross-section, $\sigma^{(2)}$, the population density in the target state, n_O, and the square of the laser output energy, E_L. The two-photon excitation cross-section ratio can be taken to be the same for each sub-level and has been shown to be the case by [110,111]. The branching ratio from the $O(3p^3P)$ level will also be the same. Ultimately, the normalised fluorescence signal given by equation (2.19) observed from an excitation wavelength will be proportional to the population of the ground state of a particular sub-level - equation (2.20).

$$I_F \propto a_{23}\sigma^{(2)}n_O E_L^2 \tag{2.18}$$

$$I^* = \frac{I_F}{E_L^2} \tag{2.19}$$

$$I^* \propto n_O \tag{2.20}$$

Consequently, the intensity of the fluorescence generated by the laser is synonymous with the population density of the sub-level.

2.1.6.1 Gas temperature via slope of Boltzmann plot

The gas temperature can then be determined from the slope of a Boltzmann plot of the normalised fluorescence against the energy level of each sub-level. This method has been used in atmospheric pressure plasma jets [60, 91].

$$\frac{n_J}{\Sigma n_J} = \frac{(2J+1)\exp(-E_J/k_BT_g)}{\Sigma(2J+1)\exp(-E_J/k_BT_g)} \tag{2.21}$$

The Boltzmann fraction, equation (2.21) can be re-arranged into the form $y = mx + c$ as in equation (2.22):

$$\ln\left(\frac{n_J}{2J+1}\right) = -(1/k_BT_g)E_J + \ln\left(\frac{\Sigma_J\, n_J}{\Sigma_J(2J+1)\exp(-E_J/k_BT_g)}\right) \tag{2.22}$$

The gradient is equal to $-(1/k_BT_g)$, so T_g is obtained from the fitting coefficients for a straight line. Figure 2.4 shows that the slope can be fitted using either the lowest two energy levels where there is greater signal, or all three. The highest energy level may cause the fits to deviate from each other due to its expected low signal quality, and therefore result in differing gas temperatures. In this case, a steeper downward slope will have cooler T_g.

The definition of gas temperature, T_g is described as follows. Atomic oxygen has fine structure splitting in the ground state level, and the energy difference between these can be expressed in terms of wavenumbers, $\sigma = 1/\lambda$. These are at 0, 158.26 and 226.98 cm^{-1}. The energies of these is obtained by equation (2.23):

$$E = hc\sigma \tag{2.23}$$

This can also be expressed as thermal energy with temperature, T using equation (2.24) for 3 degrees of translation freedom: x, y, and z. Therefore, temperature T will correspond to the mean kinetic energy of a neutral particle.

$$E = \frac{3}{2}k_BT \tag{2.24}$$

If the plasma has enough collisions to provide thermalisation, then this will result in a gas temperature. This will be the case if the collision frequency between background collisions is greater than the collision frequency of steady state atomic oxygen production and losses. Alternatively, since the measurements are made in the afterglow, there will be a thermalisation process. The reciprocal of collision frequency, ν gives the mean collision time, and if this is much less than the time between the plasma shut-off and the time the laser measurements are made, then the particles will have thermalised.

The aforementioned would require cross sections and calculation of reaction rates. Instead, albeit at slightly different repetition rate and duty cycle, Meehan et al. showed that steady state gas temperature was reached within the first few milliseconds of the plasma pulse [92]. Thus, it is believed that the plasma is collisional enough so that atomic oxygen species are already in thermal equilibrium with the background species as well as each other during the end of the pulse and afterglow period.

Therefore, by comparing equations (2.23) and (2.24), if $T = T_g$ and is sufficient enough to overcome the energy difference, then there will be mixing of the populations. As such, if this is at 400 K, then $k_B T_g = 277.5$ cm^{-1}. Since the wavenumber is greater than the energy difference between the sub-levels, a distribution can be produced between the $O(^3P_J)$. Thus, measuring the relative population in each sub-level will return T_g.

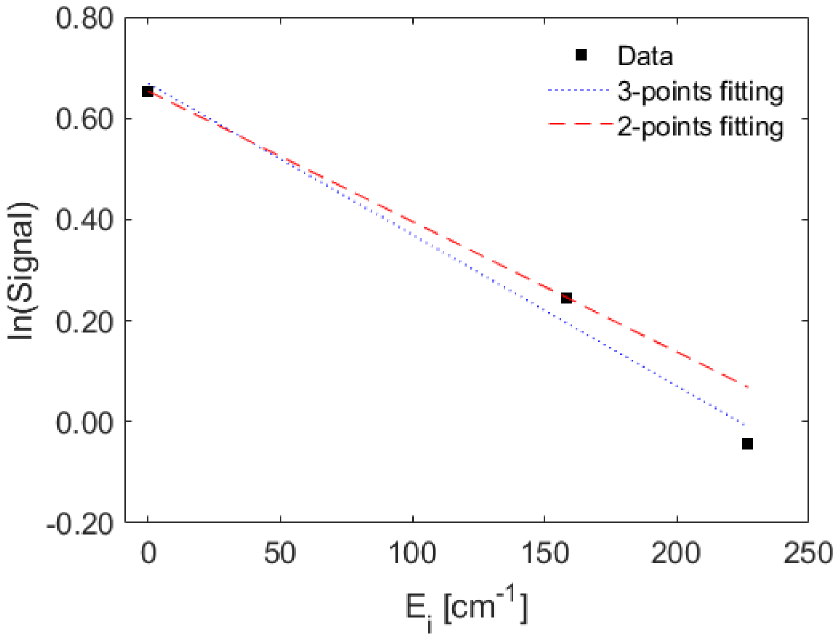

Figure 2.4: Example of determining gas temperature via Boltzmann plot. The natural logarithm of the fluorescence intensity excited from the target state is plotted against its energy level. The slope from the linear fit can be used to determine the gas temperature where the gradient is equal to $-(1/k_B T_g)$. The signal-to-noise ratio of the highest energy level may lead to uncertainties. Therefore, the fitting can be carried out using the other two more populated levels.

2.1.6.2 Gas temperature via Boltzmann fraction

The integration of the full line profile and subsequent fitting analysis to determine gas temperatures is a time-consuming process. Instead, it is investigated whether taking gas temperature measurements at a single excitation wavelength that gives maximum fluorescence for each of the sub-levels and directly comparing the ratio of these intensities with a theoretical Boltzmann fraction distribution would enable swifter measurements with more time resolution in the afterglow.

For a range of input T_g, the value that minimised the difference with the experimental ratio is taken to be the gas temperature. Equation (2.21) is used to produce figure 2.5 where the population fraction $n_J/\Sigma n_J$ is a function of T_g. This method shows greater sensitivity at gas temperatures below 1500 K - there is little variation above this and approaches a finite value of 0.56.

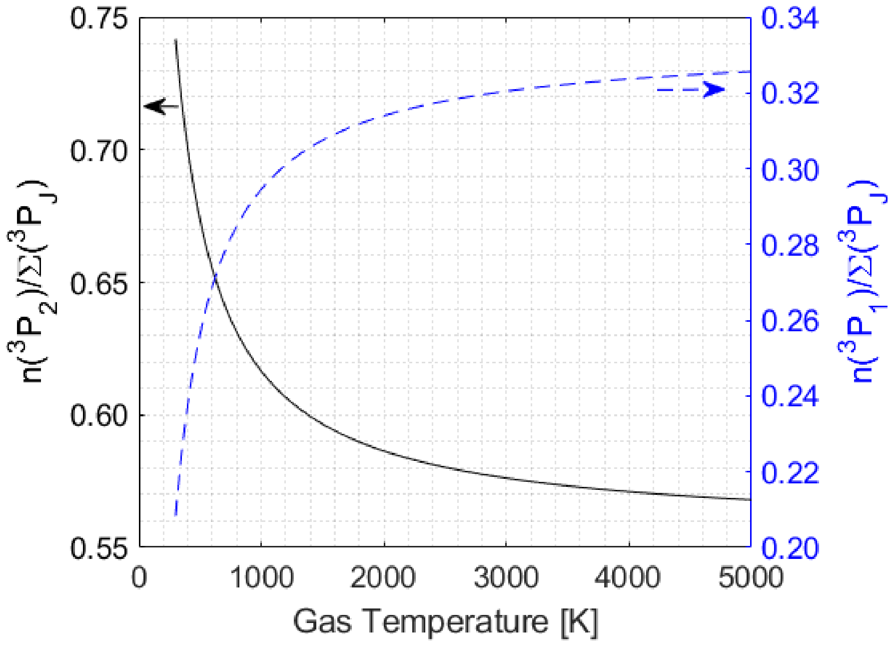

Figure 2.5: Theoretical Boltzmann fractions as function of gas temperature. The fluorescence intensity excited from the target state is compared against the sum from all states, and the input gas temperature that is closest to the theoretical value is taken as the measured value. Here, the two most populated states are depicted.

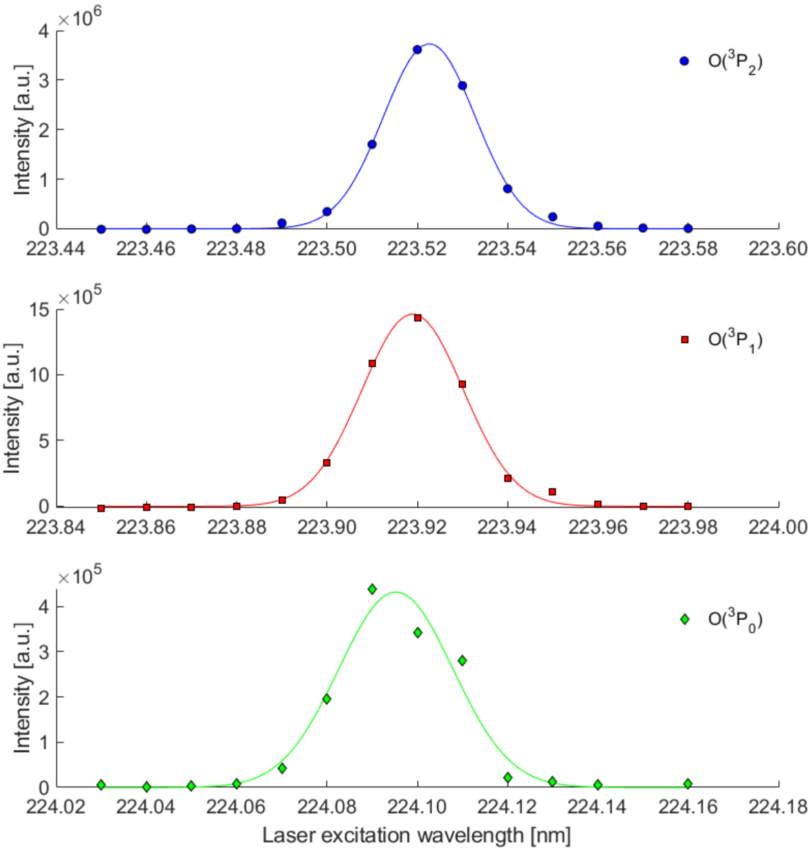

Figure 2.6: Comparison of experimental versus fitted wavelengths. Peak excitation wavelength from experimental measurements may not align with the maximum from the fitted Gaussian, and will introduce uncertainty in the evaluation of T_g.

This approach has two assumptions. Firstly, the normalised line profiles are the same for all of the excitations, and so only the peak excitation wavelength value is needed to determine the gas temperature. Thus, the normalised line profiles from each of the sublevels were checked to ensure that they were the same i.e. all followed a laser-broadening dominated Gaussian profile. Secondly, this experimental peak fluorescence is the same as the fitted peak value. This is due to the limitations of the laser system's output resolution - the actual peak wavelength may reside between two values. Hence, comparing the peak value of a Gaussian fit over the resonance wavelength with the single excitation wavelength can give an estimated uncertainty.

Figure 2.6 shows this is the case. Nonetheless, the difference between the peak excitation and fitted values were no more than 6%, with the largest discrepancy for the $O(^3P_2)$ state. Also, the experimental case always had a lower value than the fitted value for this and the $O(^3P_1)$ state. Additionally, the fitting for the $O(^3P_0)$ state is rather poor. Regardless, as this is the lowest populated state, it did not dramatically impact the determination of the gas temperature. A few sets of conditions were taken to check how much difference there was and whether the conditions affected the uncertainty. These are tabulated in table 2.1 and showed little difference overall in the experimental and fitted peak values.

	Peak value differences [%]			Total uncertainty [%]
Condition	$O(^3P_2)$	$O(^3P_1)$	$O(^3P_0)$	
Pure O_2, 20 Pa, 600 W	-5.5197	-0.2628	-4.8536	7.35
Pure O_2, 20 Pa, 1000 W	-4.6093	-0.7787	2.1549	5.15
Pure O_2, 50 Pa, 600 W	-3.7798	-0.2351	-0.5182	3.82
He-20%O_2, 20 Pa, 600 W	-3.1506	-1.8743	1.7211	4.05

Table 2.1: The calculated uncertainties for a variety of conditions. The peak excitation value is compared against the fitted value for the full line profiles. The experiment values tended to be smaller than the fitted values. The total uncertainty is from these percentage differences added in quadrature.

As one last confirmation, the obtained gas temperatures from the Boltzmann fraction method are compared through using both the entire integrated spectral line profile for all three sub-levels versus the just the peak excitation fluorescence values under several plasma conditions.

2.2 Energy Resolved Actinometry

The second diagnostic method of interest employed in this thesis is ERA. It uses Phase-Resolved Optical Emission Spectroscopy (PROES) in which the emission captured within an rf cycle is processed to determine excitation phenomena from which it originates. This timescale is when electron species can respond to the rf frequency, and therefore its dynamics during plasma heating can be captured.

2.2.1 Distinction between plasma-induced emission and fluorescence

In laser-induced fluorescence, photons were absorbed by ground state species and emitted a different wavelength of light upon relaxation. Electrons are able to play a similar role where excited states are produced through collisions. Thus, the emission can be passively measured without needing an external stimulus, and is the subject of optical emission studies, such as [94, 112–114] to name a few. As with any excitation process, there needs to be a certain amount of electron energy to enable the transition from the ground state species into a higher level. Moreover, the excitation rate is dependent on an energy-dependent cross-section between the electron and target.

2.2.2 Electron Energy Distribution Function

Electrons gain energy from the rf power supplied from the coil as they are able to respond to the induced time-varying fields at this frequency [18]. Electrons undergo heating through ohmic and collisionless processes from the electromagnetic fields from the coil [1]. They gain more energy as they accelerate from these fields, and lose energy through collisions with each other and with species in the plasma. Eventually, the electrons will reach a steady state where they have a range of energies. Hence, the electron energy distribution function (EEDF) describes the proportion of electrons that possess a certain amount of energy. Since only electrons that have sufficient amount of energy are able to drive processes, namely excitation and dissociation, it is useful to assess how this distribution responds to changing plasma conditions to maximise for example, the production of radical species.

There are several factors that can influence the shape of this EEDF. The first is related to how collisional the plasma is. Higher pressures evoke greater amount of collisions due to the shorter mean free path of the electrons [115] and also higher rate of inelastic electron-heavy particle collisions [56]. Next, the species present can also affect the distribution. Molecular plasmas are able to take energy away via inelastic collisions and have been taken into consideration on the excitation rates in actinometry [58]. The ionization threshold of the gas species also has an influence - sufficient production of electrons are needed to sustain the plasma through ionization. It is easier for argon as it has a low ionization threshold (15.8 eV) and in contrast, helium is much higher (24.6 eV). This leads to differing electron temperatures where pure argon is lower than pure helium [116]. Lastly, the plasma source, for example, capacitively coupled plasmas have been reported to show bi-Maxwellian distributions [99, 117, 118].

Equations (2.25-2.27) are mathematical descriptions of the EEDF and are dependent on both the collisionality parameter, x and the mean electron energy, $\langle\epsilon\rangle$. Γ is the gamma function [119]. $x = 0.5$, 1 or 2 corresponds to a bi-Maxwellian, Maxwellian or Druyvesteyn distribution, respectively. When the distribution is Maxwellian, the mean electron energy may be referred to as an electron temperature, T_e. Higher T_e will flatten the EEDF and shift the curve so that there is a greater bulk of low energy electrons and also have higher population in the energetic tail region as can be seen in the left side panel of figure 2.7, resulting in more emission.

This collisionality parameter is particularly important to take into account for modelling. Bi-Maxwellian distributions have been observed in capacitively-coupled plasmas [117, 118] and the low-power mode of an ICP [120], and is described by two electron temperatures. On the other hand, inelastic collision processes can remove the number of high energy electrons and are characteristic of Druyvesteyns, as can be seen in the right side panel of figure 2.7; molecular oxygen in particular can cause this depletion in the tail. As a result, this can drastically reduce the amount of observable excitation and would require higher $\langle\epsilon\rangle$ for a comparable T_e. Some have reported Maxwellian distributions with growing pressure in oxygen CCP [99], or evolution upon transition into the H-mode of an ICP [120, 121].

$$f(\epsilon) = c_1 \epsilon^{1/2} \mathrm{exp}(-c_2 \epsilon^x) \tag{2.25}$$

$$c_1 = \frac{x}{\langle\epsilon\rangle^{3/2}} \frac{[\Gamma(\zeta_2)]^{3/2}}{[\Gamma(\zeta_1)]^{5/2}} \tag{2.26}$$

$$c_2 = \frac{1}{\langle\epsilon\rangle^{x}} \left[\frac{\Gamma(\zeta_2)}{\Gamma(\zeta_1)}\right]^{x} \tag{2.27}$$

Where $\zeta_1 = 3/2x$ and $\zeta_2 = 5/2x$.

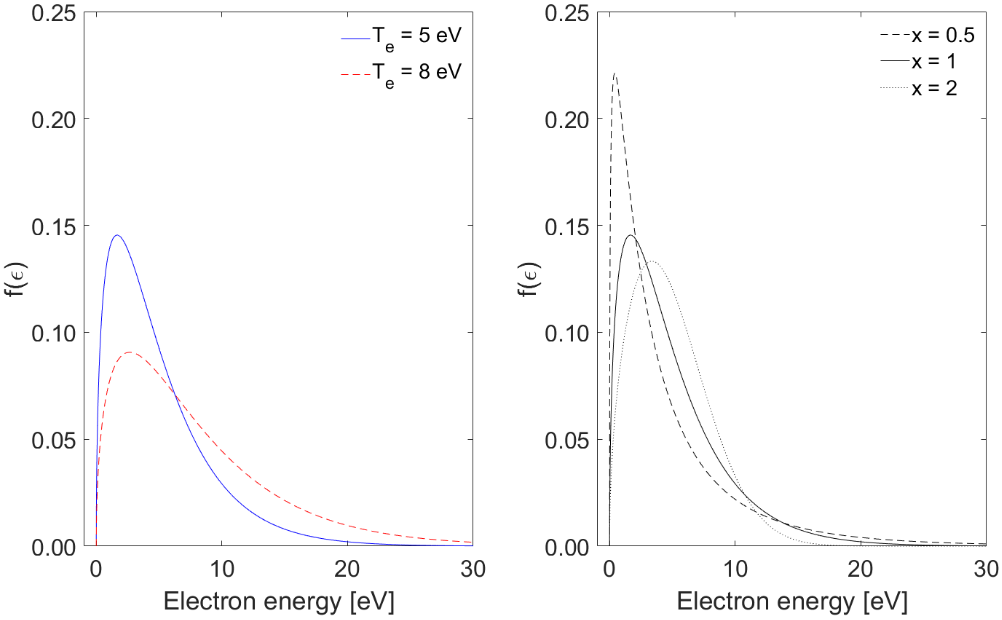

Figure 2.7: Comparison of the electron energy distribution with different electron temperatures and collisionality parameter values. The high population in the tail is controlled by both the mean electron energy and the type of distribution parameter, x. On the left, higher electron temperatures flattens the distribution, and populates the tail population with more energetic electrons. Meanwhile, the right plot shows that for the same mean electron energies, the distribution can dramatically vary, with Druyvesteyn distributions seen to have depletion of the tail these due to inelastic collisions.

Since this work focuses on an ICP plasma that contains molecular oxygen, it is appropriate to find x as such, although exact determination is complex. Firstly, it was found in an inductive oxygen glow discharge that the collisionality parameter varied with pressure from Bi-Maxwellian to Druyvesteyn [122]. Moreover, the shape of the EEDF is subject to many parameters, including whether there is electrostatic shielding and spatially dependency [123].

Non-Maxwellian distribution were found in rare gas mixtures and O_2 and therefore could cause error in modelling [124]. A modelling program, BOLSIG+ could be employed where it is able to self-determine the EEDF based on the gas composition, which could be integrated in future work.

Nonetheless, it may be considered nearly Maxwellian in the centre of the discharge for high densities ($> 10^{11}$ cm^{-3}) and low pressures (< 10 mTorr) [123]. Although the operating pressure is rather different, the analysis of ERA takes place in the region of strongest excitation [61, 62] - the discharge centre is assumed to be synonymous with this. Moreover, EEDFs in H-mode O_2-Ar plasma i.e. similar gas mixtures of interest, were also found to also be nearly Maxwellian [125]. Furthermore, higher pressure cases ($3 - 100$ mTorr) in a pure oxygen ICP indicate towards this distribution [117]. Finally, results can be compared with other works that have also assumed the case [101, 126]. Consequently, a Maxwellian distribution is assumed.

2.2.3 Excitation cross-sections

The chance that an electron producing excitation upon collision with a target is dependent on its energy. To extend the ERA technique, the cross-sections that have been used in its previous applications are employed here for consistency. The direct electron impact excitation cross-sections of Chilton et al. are used for $Ar(2p_1)$ from the ground state [127]. No metastable cross-sections are considered for this since it is expected that i) $Ar(2p_1)$ is primarily contributed from the ground state and ii) molecular oxygen sufficiently quenches these species so there is minimal contribution. For the direct electron impact excitation cross-sections of the two oxygen lines, these were taken from Laher and Gilmore [50]. Finally, the dissociative excitation cross-sections were taken from Schulman et al. [39]. These cross-sections are also desirable as they have been measured experimentally. Moreover, the data were assumed to have zero cross-section at the threshold energy and interpolated over the energy range of interest to enable better resolution of possible excitation rates.

2.2.4 Calculation of excitation rates

The excitation rates are a convolution of the EEDF and the energy dependent cross-section and is calculated using equation (2.28) [128, 129]. The shape of the EEDF was assumed to be a Maxwellian as studies have shown this to be the case in H-mode [120, 130, 131]. So, the excitation reaction rate k is calculated using a range of these EEDFs with varying mean electron energy.

$$k = \sqrt{\frac{2e}{m_e}} \int \sigma(\epsilon)\epsilon^{1/2} f(\epsilon) d\epsilon \tag{2.28}$$

2.2.5 Theoretical excitation ratios

Once the excitation rates have been calculated, equations (2.29a) and (2.29b) are used to determine the theoretical excitation ratios. f_{Ar} and f_{O2} are the fraction of argon and molecular oxygen in the experiments. An added advantage of taking excitation ratios is that some unknown parameters needed for calculations cancel out, such as the electron density. Consequently, these excitation ratios are plotted as a function of the plasma parameters in figure 2.8, which is also specific to the gas fraction. From here, the experimental excitation ratios are needed to know which specific contour lines to take in order to resolve the plasma parameters.

$$\frac{E_{750}}{E_{844}} = \frac{f_{Ar}}{f_{O2}} \frac{k_{750}(\langle\epsilon\rangle)}{r_O k_{844,d}(\langle\epsilon\rangle) + k_{844,de}(\langle\epsilon\rangle)} \tag{2.29a}$$

$$\frac{E_{777}}{E_{844}} = \frac{r_O k_{777,d}(\langle\epsilon\rangle) + k_{777,de}(\langle\epsilon\rangle)}{r_O k_{844,d}(\langle\epsilon\rangle) + k_{844,de}(\langle\epsilon\rangle)} \tag{2.29b}$$

2.2.6 Experimental excitation ratios

The experimental excitation ratios are obtained via using PROES. The use of a camera with high repetition rate can be triggered to record emission at a particular phase in the rf cycle. Using a variable delay, the entire rf cycle emission can be recorded. This technique works when the natural lifetime of the excited state is less than the rf cycle as the modulation of the emission can be easily resolved [132].

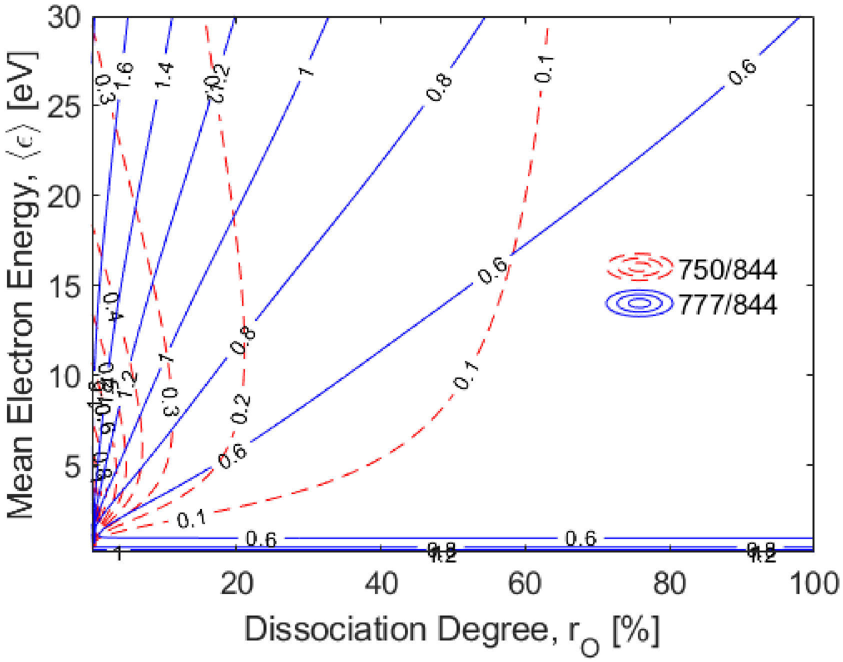

Figure 2.8: Contour plot of the theoretical excitation ratios as a function of dissociation degree and mean electron energy. The contour lines are also influenced the fraction of argon and molecular oxygen in the system. These contours assume a mixture of O_2-10%Ar. The experimental excitation ratios narrows down which specific contour line is applicable for the operating condition and the plasma parameters are determined where these intersect.

The origins of emission is detailed by equation (2.30) which shows that there can be several contributions. Firstly, a ground state species, n_0 can be directly excited. This also includes dissociative excitation and were calculated from the EEDF and excitation cross-sections earlier. Secondly, there can be step-wise excitation from long-lived metastable species, n_m. Thirdly, even higher excited states may radiate down (cascades) with a probability $A_{c\to i}$ i.e. the Einstein coefficient, with an escape factor from this level g_{ci}. These first three terms all contribute into the excited state, n_i. The latter two terms are loss processes through spontaneous emission into all allowable, lower lying levels, n_k and also from quenching with other species, n_q with a quenching coefficient, k_q.

$$\frac{\mathrm{d}n_i}{\mathrm{d}t} = n_0 E_{0\to i} + n_m E_{m\to i} + \sum_k n_c g_{ci} A_{c\to i} - \sum_i^k n_i g_{ik} A_{i\to k} - \Sigma n_i n_q k_q \tag{2.30}$$

However, with PROES, the contribution from cascades can be minimised [97]. Moreover, metastable contributions are expected to be small as quenching with molecular oxygen is particularly potent for Ar* [115]. Although metastable population has been seen to increase with small additions of oxygen [133], the conditions here have argon as a much smaller fraction than the other gases. Of note, small amounts of argon do not impact an oxygen plasma significantly, and in fact excitation has to rely on direct excitation from the ground state due to quenching of these metastables [112]. Oxygen metastables have been found to be orders of magnitude lower than the ground states as well so are also not considered [53, 114]. The excitation rate can then be rearranged as equation (2.31).

$$E_{0\to i} = \frac{1}{n_0}\left(\frac{\mathrm{d}n_i}{\mathrm{d}t} + n_i \Sigma (n_q k_q + g_{ik} A_{i\to k})\right) \tag{2.31}$$

Where the excited state density n_i is related to the measured emission, I_i and the Einstein coefficient for that particular transition:

$$n_i = \frac{I_i}{A_{ij}} \tag{2.32}$$

There is also both a time and space dependent aspect with the recorded measurements for PROES - the electron energy can change with time across the rf cycle, whereas the atomic oxygen density is much slower to respond [61]. Thus, the relative amounts of excitation contribution will also depend where the emission originates from in the plasma. As such, the region of maximum excitation is taken to be where only direct excitation dominates, making these assumptions more applicable.

Once these experimental excitation ratios have been obtained, these can be compared with the theoretical calculated values. These excitation ratios will define a particular contour that is a function of the plasma parameters, and where these intersect are taken as the measured values. Yet, to improve the robustness of this method, in particular application in the H-mode, Bayesian inference is employed and will be covered next.

2.2.6.1 Possible radiation trapping effects

Radiation trapping is the phenomenon where a photon emitted from an excited state are re-absorbed by the same lower-lying, de-excited level of a different particle. This photon may undergo several absorption-emission cycles before being able to escape the plasma. This also assumes that none of the intermediate excited states are quenched, thereby losing the photon. Subsequently, the perceived intensity from this emission line by the detecting optics may appear weaker in comparison to those that do not have this process. Although the ERA method takes into account radiation trapping when calculating the effective decay rate, A_i through the escape factor g_{ik}, these have to be reconsidered in cases where the plasma is optically thick. Thus, corrections can be made to the model to improve on the quantitatively obtained values.

It is often assumed negligible from the argon $2p_1$ state [134]. Although, radiation trapping effects are more prevalent if cascades are from a resonant level - indirect contribution to the 750 nm emission would increase with pressure. Nonetheless, the optical cross sections and Einstein coefficients for these are much smaller than the Ar(750) line, so it may be assumed negligible in comparison. Moreover, argon consists of a small fraction in the studied gas mixtures of $\sim 2\%$, so it is unlikely that there would be a significant population of lower state densities to enable radiation trapping.

On the other hand, it is expected that the density of atomic oxygen will be higher in the H-mode, and consequently there is the possibility that the observed oxygen emission lines will be prone to this phenomenon too. Despite the O(777) suffering from more self-absorption effects, it became negligible in high oxygen mixtures, and the O(844) was not observed to have any radiation trapping effects [114].

2.3 Bayesian Inference

Bayesian inference involves the use of Bayes' Theorem where an observation of a phenomenon can be attributed to a cause with a certain degree of probability. Applications of this technique have been applied towards fusion studies [135] and diagnostics development [136, 137] where there are a number of underlying physics that are possibly unknown, and thus makes it challenging to fully and accurately model. Consequently, rather than perfectly recreate the system, Bayesian inference allows for uncertainties to be modelled as another parameter.

It must be noted that the parameter values determined through this technique are those that maximise the probability of matching these in the model to the observed data. As a consequence of this, there can be disparity in results derived from this technique compared to other reported literature. However, a powerful advantage of Bayesian inference is that the belief in a model and its parameter values can be updated when given more information about the system. It also enables the consideration of the uncertainty when taking measurements as well as other possible physics models. Thus, the approach is adaptive and allows for changes in the model and its parameters as more information about the physics is included.

Equation (2.33) is Bayes' Theorem and can be used to return the probability of our parameter value of interest, θ, given an observed result, D i.e. our measured data. θ may be a single parameter, or it can be multiple parameters, where it will be denoted as $\underline{\theta}$. In this case, the mean electron energy and dissociation degree: $\underline{\theta} = \left[\langle\epsilon\rangle, r_O\right]$. $P(\theta|D)$ is known as the *posterior distribution.*

$$P(\theta|D) = \frac{P(D|\theta)P(\theta)}{P(D)} \tag{2.33}$$

$P(D|\theta)$ is the *likelihood* and contains the physics model - it gives the probability of seeing data values when given input parameters. The likelihood is used to compare the physics model with actual observed measurements. Assuming that the error is Gaussian, the likelihood takes the form of equation (2.34).

$$P(D|\underline{\theta}) \propto \exp\left[-\frac{1}{2}\sum_i\left(\frac{y_i - f(x_i, \underline{\theta})}{\sigma_i}\right)^2\right] \tag{2.34}$$

Where y_i is a measured point and $f(x_i, \underline{\theta})$ is the forward model. In the case of ERA, it compares each experimental excitation ratio with its corresponding theoretical model in equations (2.35a) or (2.35b). σ_i is the uncertainty of the measurement and can include errors such as the accuracy of the experimental equipment.

$$\frac{E_{750}}{E_{844}} = \frac{f_{Ar}}{f_{O2}} \frac{k_{750}(\langle\epsilon\rangle)}{r_O k_{844,d}(\langle\epsilon\rangle) + k_{844,de}(\langle\epsilon\rangle)} \tag{2.35a}$$

$$\frac{E_{777}}{E_{844}} = \frac{r_O k_{777,d}(\langle\epsilon\rangle) + k_{777,de}(\langle\epsilon\rangle)}{r_O k_{844,d}(\langle\epsilon\rangle) + k_{844,de}(\langle\epsilon\rangle)} \tag{2.35b}$$

$P(\theta)$ is the *prior probability distribution* and represents previous knowledge of the system. Low temperature plasmas have been observed to possess electron temperatures between 2-8 eV in inductively coupled plasmas [56, 101, 138]. So, there is a high degree of confidence that values in this range will be measured. Conversely, electron temperatures of hundreds to thousands of electronvolts would be expected from nuclear fusion processes [2], and so is highly unlikely to be seen in the investigated experimental set-ups. Defining the prior distribution has to be done carefully as one can easily influence the output by only focusing on a strict range of values and completely neglecting others.

Figure 2.9 illustrates two possible prior distributions: a) a flat prior distribution in which a given range of mean electron energy values all have the same probability. On the other hand, b) a shaped distribution could be used where there are higher probabilities within a certain range than extremely high or low electron temperatures. A beta distribution was chosen as its shape can easily be manipulated to reflect the expected T_e, such as between 2-8 eV.

Despite the cited ranges of mean electron energy, these were often at much different operating pressures (< 100 mTorr) or different working gas than used here. Discrepancies between experimental set-ups, namely the plasma source, or or slight variances in the ICP modifications of the GEC reference cell may have unknown influence. Consequently, the prior knowledge in these cases may not be applicable. As such, a flat prior distribution was initially assumed.

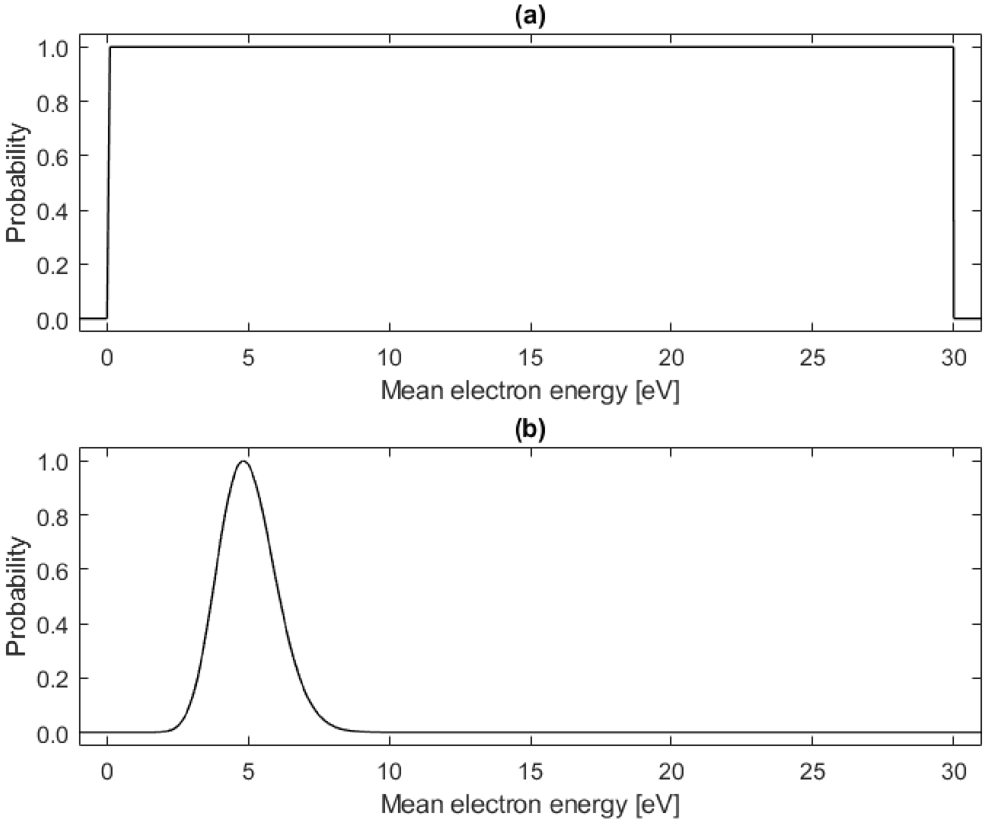

Figure 2.9: Different prior probability distributions for the mean electron energy. a) A flat prior distribution where all probabilities within a range are equally likely, or b) a beta distribution shaped around mean electron energies of 2-8 eV, becoming increasingly less likely outside of this range. These plots are scaled to unity for visualisation.

Lastly, $P(D)$ is often a normalising function that is used when there are different models to compare, called *model evidence*. In this case however, only one is used and so this denominator is taken as $P(D) = 1$.

For numerical practicality, it is advantageous to work with natural log-probabilities [135], and taking the log of equation (2.33) becomes equation (2.36). Since a flat prior is assumed and a single model is used, $\ln\big(P(\theta)\big)$ and $\ln\big(P(D)\big)$ are equal to 0. Thus, the posterior distribution is equal to the likelihood. One particular reason for working with log-probabilities is because when the value inside the exponent of equation (2.34) is very negative, the exponential value of this will return a very small probability that may also be beyond the computer's hardware limitations. So, before converting back into probability values, the log-probabilities, $\ln\big(P(D|\theta)\big)$ is scaled by the computing expression:

$$\ln\big(P(D|\theta)\big) = \ln\big(P(D|\theta)\big) - \max(\ln\big(P(D|\theta)\big))$$

As a result, the probability distribution function will then return more reasonable values and also clearly show where parameters best maximise the probability of the observed data.

$$\ln\big(P(\theta|D)\big) = \ln\big(P(D|\theta)\big) + \ln\big(P(\theta)\big) - \ln\big(P(D)\big) \tag{2.36}$$

The physics model can be a function of multiple parameters, with some of interest and others less so, but the latter still necessary to facilitate the model output. Nonetheless, the Bayesian approach is capable of calculating particular probabilities of interest through marginalisation of parameters. In this work, the excitation ratios are a function of two parameters i.e. the mean electron energy,$\langle\epsilon\rangle$ and dissociation degree, r_O. Each combination of $\langle\epsilon\rangle$ and r_O will produce a theoretical ratio value, and in turn a probability value that reflects its agreement with the observed data. Thus, once all possible combinations of investigated input variables have been evaluated, marginalisation of this posterior distribution will result in the individual probability distribution of a specific parameter component from which the measured value can be inferred.

Two fundamental rules are needed in order to carry out the marginalisation process. Firstly, equation (2.37) gives the sum rule for a continuous variable where the total probability of all outcomes must add up to 1 i.e. a normalisation condition. Secondly, equation (2.38) is the product rule and provides an identity for decomposing the joint probabilities of $\underline{\theta}$ in the posterior distribution to obtain individual probabilities. Therefore, the probability for combined events A and B for given condition I can be rewritten. Since $P(A,B|I) \equiv P(B,A|I)$, there are complementary forms, and rearrangement of these gives Bayes' rule defined in equation (2.33) earlier.

$$\int_{-\infty}^{+\infty} P(A|I)\,\mathrm{d}A = 1 \tag{2.37}$$

$$P(A,B|I) = P(A|B,I)P(B|I) = P(B|A,I)P(A|I) \tag{2.38}$$

If the probability distribution of event B is desired, then both sides are integrated with respect to all other parameters, in this case A, and seen in equation (2.39). Due to the sum rule, the integral on the right-hand side of this equation is equal to one, leaving the probability distribution of a parameter given an observation, $P(B|I)$. Similarly, integrating with respect to B can be done to obtain $P(A|I)$.

$$\int P(A,B|I)dA = P(B|I)\int P(A|B,I)\,\mathrm{d}A \tag{2.39}$$

Since the marginal probabilities can result in a value greater than 1, the probability distribution is scaled by the maximum, again done using a computing expression:

$$P(\theta|D) = \frac{P(\theta|D)}{\max(P(\theta|D)}$$

This makes it so that the most probable value corresponds to unity. In fact, the integrated area underneath the distribution should be unity due to the sum rule, and will be treated accordingly. Nonetheless, the output may be presented in this way for visualisation purposes.

A Gaussian fit is applied to this distribution and the modal value i.e. the peak of the marginal distribution can be taken as the parameter value. Otherwise, the mean, μ is calculated from equation (2.40) where x is the parameter value and $P(x)$ is its probability. The uncertainty can also be defined from the limits where the integrated area under the distribution is equal to a certain confidence level, such as 95% probability. In this latter case, the marginal distribution has to be re-scaled so that the total area underneath the curve sums to 1. The Highest Density Interval (HDI), where values are within a region that makes up 95% of the probability, are considered more credible. Similarly, an Equal Tail Interval (ETI) may be chosen instead where each tail region have 2.5% probability. The choice between HDI and ETI has a dependency on whether or not the marginal distribution is heavily skewed [139]. Regardless, the latter is used in this case as it is much easier to compute.

$$\mu = \int xP(x)dx \tag{2.40}$$

To illustrate this process, figure 2.10 shows the 2-dimensional probability distribution function (PDF) after comparing the theoretical excitation ratios with the experimental measurements. To get the individual probability distributions of the mean electron energy and dissociation degree, these need to undergo marginalisation. So, an example for obtaining the total probability of a mean electron energy of 2 eV would be to sum the probability across all the dissociation degree values that it shares joint probability with: $\int P(\langle\epsilon\rangle = 2, r_O|D)dr_O$. This is repeated for all the other mean electron energy values, and also the reverse case for the dissociation degree. After scaling the peak probability to be unity, this ultimately results in marginalised distributions of figures 2.11a and 2.11b. These can also be thought of flattening the 2D PDF to the axis of interest. There were more evaluation points for the mean electron energy (1000) than the dissociation degree (200), and so is reflected the number of data points in these figures. These could always be increased to have a better resolution of possible values. From the Gaussian curve fit of the marginalised distribution, the plasma parameters and uncertainties were inferred from the mean value and the 95% confidence interval of the ETI.

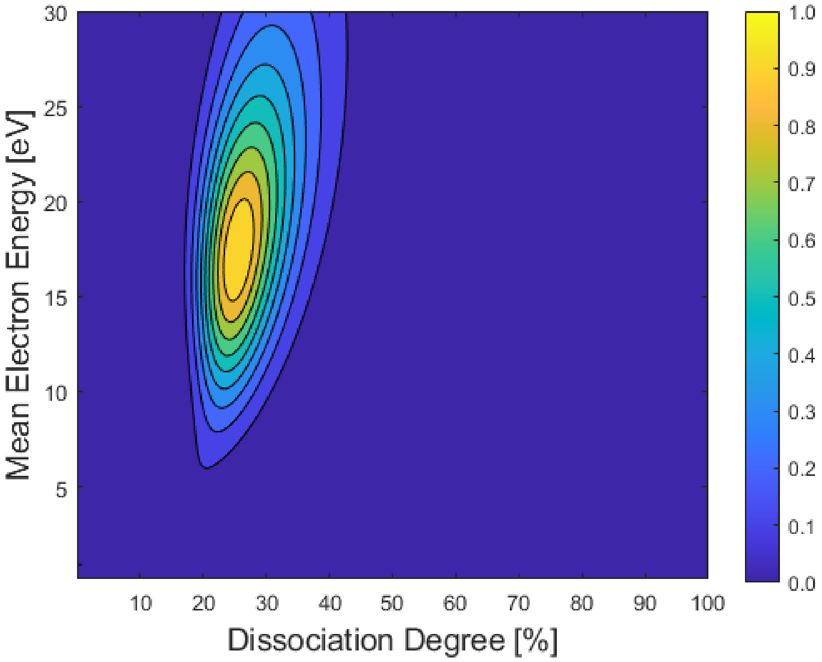

Figure 2.10: Probability distribution function after comparing the theoretical model with the experimental data for O_2-10%Ar, 10 Pa at 700 W.The colour bar shows the probabilities of the plasma parameters that best meet the measured data. Through marginalisation, the probabilities for the value of each individual parameter are obtained.

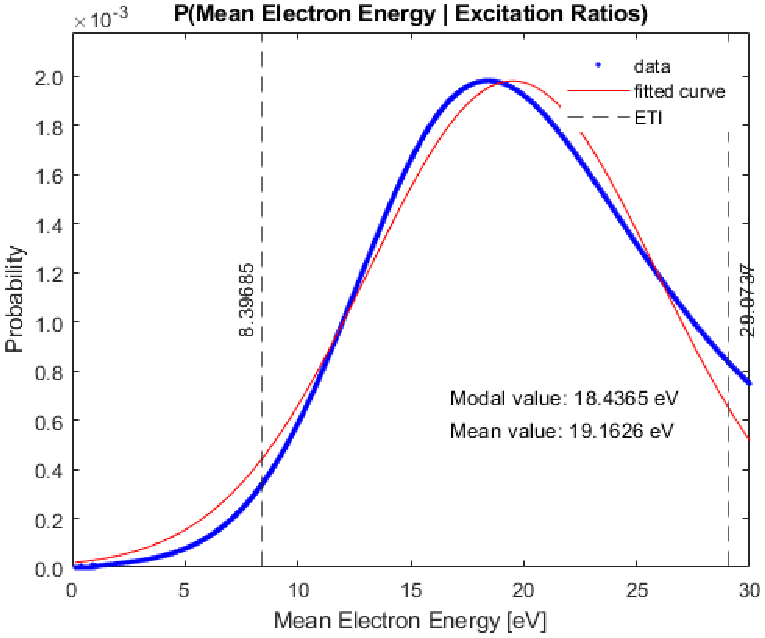

(a)

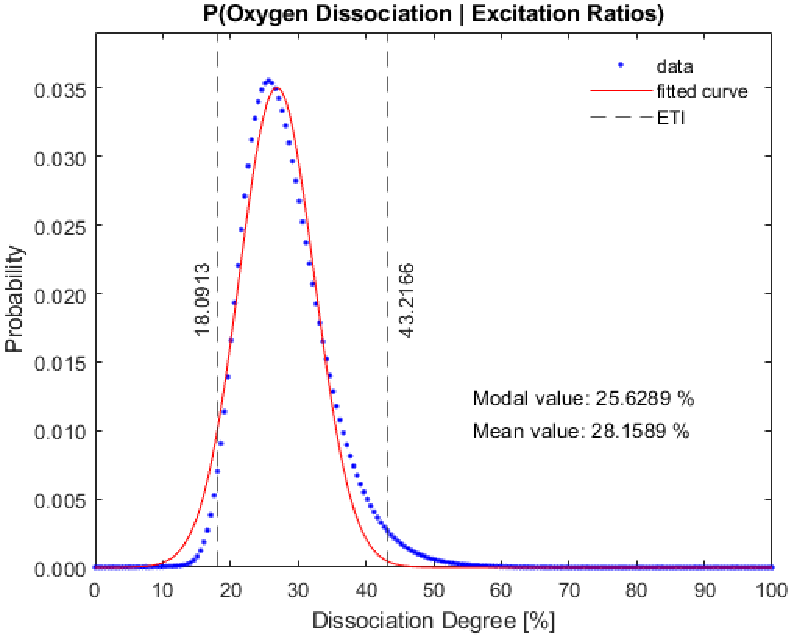

(b)

Figure 2.11: Marginalised probabilities of a) mean electron energy and b) dissociation degree from the PDF. The area under the curves have been normalised to equal 1. The mode or mean value can be used to infer the plasma parameters as well, with the latter utilising ETI to calculate the confidence interval and is synonymous with uncertainty.

Chapter 3

Experimental set-ups

For direct comparison of the techniques, both TALIF and ERA were carried out on the same modified Gaseous Electronics Conference reference cell. This source is of particular interest since it promotes better comparison of plasma parameters with other works. Moreover, ERA was also demonstrated on another GEC-like reactor to assess its effectiveness. Thus, this chapter details the set-ups and experimental methodology undertaken to perform the measurements.

3.1 Gaseous Electronics Conference reference cell

The experiments for both TALIF and ERA were conducted on a Gaseous Electronics Conference (GEC) reference cell. It was a modified variant to have inductive coupling via a planar five-turn copper coil at the top and a grounded stainless steel bottom electrode that were water-cooled.

Before all of the experiments, the chamber was evacuated using the vacuum system consisting of a rotary pump (Pfeiffer Duo 20 MC) and a turbomolecular pump (TurboVac Mag W 600 iP). When pumping the chamber down to very low pressures, an Oerlikon Leybold Vacuum PENNINGVAC PTR 90 gauge, which had a full range of 10^{-6} to 10^{5} Pa, was used to monitor continued pressure changes. The rotary pump was first used to pump the chamber down for at least 30 minutes, allowing the pressure gauges to warm-up and provide correct readings. The pressure in the chamber during these events was monitored and is shown in figure 3.1 to highlight that partial pressures of impurities remain if using just the rotary pump. Consequently, once this reached its capabilities of around 1-2 Pa, the turbomolecular pump was activated to continue lowering the pressure. The turbo-pump was switched off once it was pumped down to pressures below 2×10^{-3} Pa. Then, it was isolated by closing off the various valves leading to it in order to prevent further unnecessary work on it.

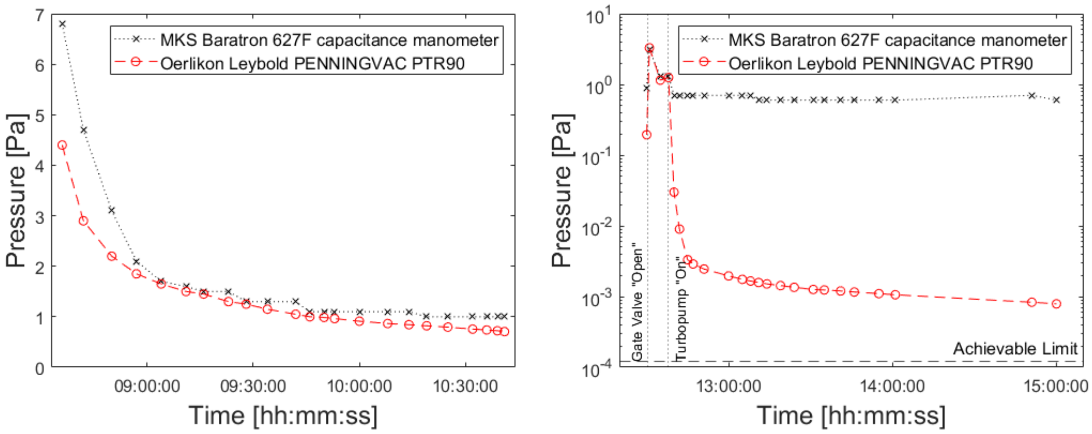

(a) (b)

Figure 3.1: Monitoring the pressure inside the chamber using a) the rotary pump followed by b) the turbomolecular pump. Once the pressure reached a 1-2 Pa as measured by the pressure gauges, the turbomolecular pump was turned on. Afterwards, the pressure continued to drop by a further several orders of magnitude. The experiments were carried out once the turbo-pump reached below 2×10^{-3} Pa. A spectra was taken before and after to check for removal of impurities.

Then, feed gases of helium, oxygen and argon were permitted. An MKS 4-channel controller was used to control the gas admixture ratios alongside with MKS Mass Flo® controllers. For all gas mixtures, trace amounts of argon (2%) were added despite its emission not being required for the TALIF measurements. This was deemed necessary to maintain consistency with the ERA measurements. Plus, other optical diagnostics, i.e. optical emission spectroscopy, may potentially be carried out with alternative advanced actinometric techniques in future studies. The gases were pumped out through the lower bellows of the GEC system to provide more symmetric pumping by the rotary pump.

An MKS Baratron Type 627F capacitance manometer was used to sense the pressure as it was independent of the gas mixture. This was connected to an MKS series pressure controller, which altered the pumping rate out of the chamber and therefore the pressure through the position of its butterfly valve.

To confirm the presence and removal of impurities, such as water and nitrogen, an Ocean

Optics MAYA 2000 Pro broadband spectrometer was used to take spectra before and after the use of the turbo-pump. A comparison of the spectra before and after using the turbo-pump is seen in figure 3.2. The emission associated with OH around 300 nm was present for both cases, but lower when using the turbo-pump. Conversely, all of the other emission lines were larger when the turbo-pump was used. It can be said that the removal of the water vapour reduces the amount of quenching for all excited species. Hence, resulting in higher emission intensities. However, the fact that there were some remaining impurities present suggest that there were leaks into the gas line or outgassing from the chamber walls. Thus, although a cleaner environment may be achieved with this, there was no guarantee that all impurities are removed by using the turbo-pump. The effects on the plasma parameters will be seen in later chapters.

RF power at 13.56 MHz was supplied by an Advanced Energy®, CESAR® 1310 rf generator at a rate of 10 Hz, 10% duty cycle. Although it was connected to an Advanced Energy®, Navio automatic matching unit, matching values were set manually on the generator. Consequently, the same optimal settings of the capacitors' tune and load values C_T and C_L, respectively, that gave minimum reflected power could be re-used for each case. As a result, more stable and reproducible pulsed plasmas allowed for better reliability of repeat measurements.

The plasma was run for a minimum of ten minutes to allow a steady-state to be achieved before taking measurements for each new condition. This was verified when the plasma condition was changed, and both the background and fluorescence signals before and after this duration were compared; there was little difference found, indicating no further change in the atomic oxygen density.

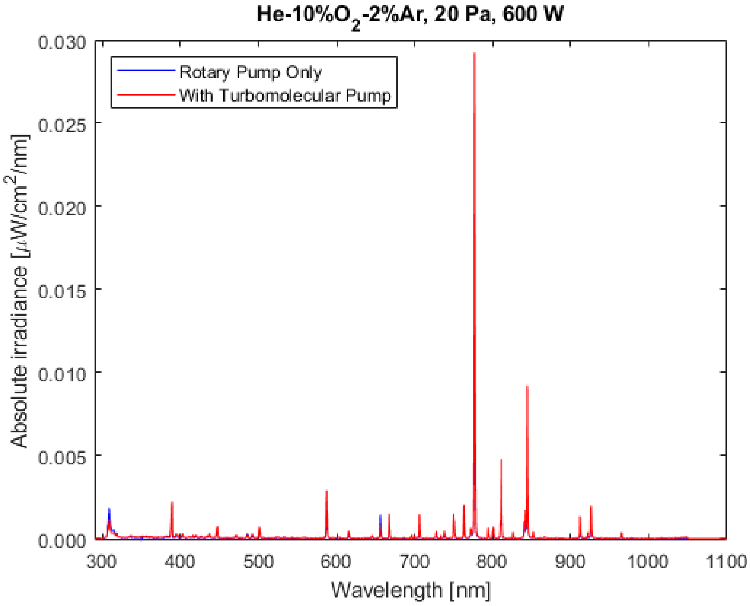

(a)

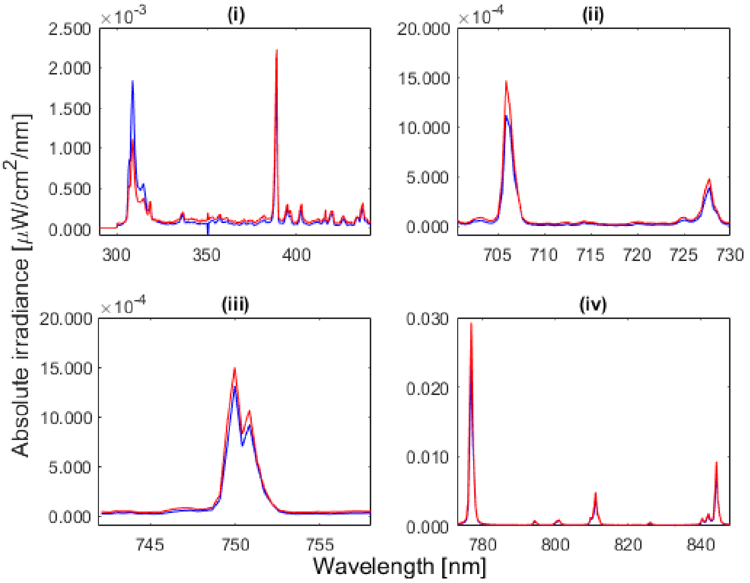

(b)

Figure 3.2: Emission spectra before and after using the turbomolecular pump taken using a MAYA 2000 Pro USB spectrometer. a) The entire broadband spectra and b) Zoom-in on the (i) OH and nitrogen, (ii) helium, (iii) argon, and (iv) oxygen emission lines.

3.1.1 GEC-like reactor

ERA was also applied to another GEC-like plasma source which can be seen in figure 3.3 and the details of this particular reactor is described in [92]. Nonetheless, the main differences include a water-cooled, three-turn double-bar spiral copper coil at the top, whereas the bottom electrode was a grounded aluminium plate (106 mm diameter) in a stainless steel holder. The coil configuration helps reduce the capacitive coupling effects and improve plasma homogeneity [31], and also achieve inductive coupling more easily.

While the recombination coefficient from the different surface material may have an effect on the atomic oxygen density, no difference in its production were found at the pressures investigated here [129]. Thus, similar n_O are expected to be found in this reactor as the GEC reference cell with varying input parameters.

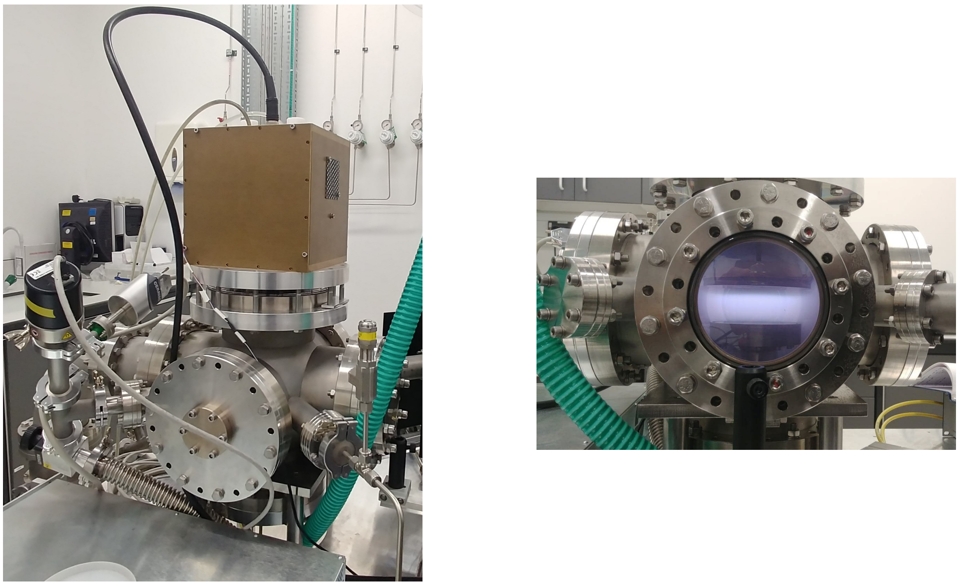
(a) (b)

Figure 3.3: The GEC-like experimental reactor used in ERA measurements. a) Overview b) Front view close-up. The in-house manufactured L-type matching unit (bronze-coloured) sat on top and matched using the white dials.

The reactor was pumped down to base pressures of less than 2 Pa using a scroll pump (Edwards nxDS 15i) before the gases were admitted. The turbomolecular pump on this system was not used here to assess the robustness of the ERA technique. The minimum attainable pressure was determined by the flow rates and admixture of the gases using the same mass flow controllers and MKS 4-channel controller, and also the valve positions that connected to the pump instead of an automated system. The pressure was sensed using another capacitive sensor (CERAVAC CTR 100 N).

Manual matching was carried out using an in-house manufactured L-type matching network. The tune and load positions were not readable given the lack of markings on these dials. So, producing a pulsed H-mode plasma was made more difficult. Moreover, reproduction at the same applied powers may not have been at the same C_T and C_L values. Nonetheless, these were set so that the reflected power was minimised to be less than 5% of the forward power.

3.2 Two-photon Absorption Laser Induced Fluorescence

3.2.1 TALIF experimental set-up

Figure 3.4 shows the experimental set-up of the TALIF measurements. A Continuum Surelite EX Nd:YAG laser was used to produce a pump wavelength of 355 nm (5-7 ns FWHM) into a Continuum Horizon Optical Parametric Oscillator (OPO), which then tuned to desired wavelengths within its available range of 192-2750 nm. This OPO unit was controlled via its Horizon software where the probe wavelength for the two-photon excitation schemes was selected. For the cases of atomic oxygen and xenon, two 225.65 nm and 224.31 nm photons are required, respectively. However, there was a wavelength offset of ~2.12 nm in the experimental case - setting the output wavelengths as 223.52 nm and 222.19 nm gave peak fluorescence signals. Subsequently, the integrated signal was scanned over this range with 0.01 nm resolution.

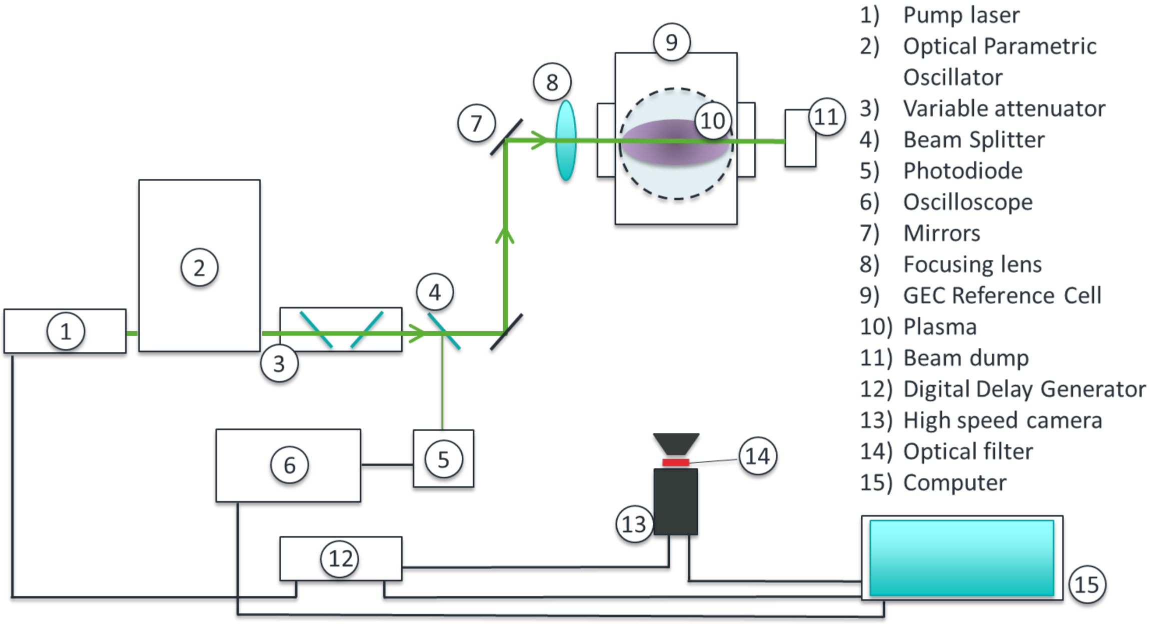

Figure 3.4: An overview of the TALIF experimental set-up. Not shown is the power-cooling unit connected to the laser head.

Once the desired UV output was generated, it passed through a variable attenuator that had a pair of coated CaF_2 optics (Layertec). One had just a single-coated side and the other with both sides coated. Both had central transmission wavelength at 226 nm. The second of these optics was the compensator where it redirected the laser beam back along its original path after passing through the first. These were mounted on a stage and simultaneously adjusted using a stepper motor (Zaber T-NM17A04). Angling them relative to the laser direction altered the amount of transmission and by extent the laser energy, which was required to keep it below saturation.

For the set of measurements using the turbo-pump, the optics of the variable attenuator were static; these were manually angled to allow a certain amount of energy for the atomic oxygen and xenon below the saturation level. The transmittance of these optical attenuators were taken to be constant according to their performance sheets, especially considering only a small wavelength range change should not drastically alter the permitted energy. On the other hand, the rest of the data were taken with an automated energy control mechanism that assisted with maintaining the target energy, especially when there was a drift in the laser energy, and will be described next.

After passing through the variable attenuator, a beam splitter reflected a small fraction of the laser beam to a photodiode (Thorlabs DET10A/M) and the generated voltage was measured by an oscilloscope (LeCroy Waverunner 204MXi-A 2GHz Oscilloscope 10GS/s). Consequently, the signal was sent to a computer running a Python script that set the PID values of the stepper motor controller and also the maximum allowable laser energy settings. As a result, this feedback loop enabled the variable attenuator to adequately adjust the laser energy to meet the target energy while also avoiding saturation effects.

The rest of the laser pulse was directed to the GEC reactor via reflective mirrors. Prior to entering the plasma chamber, an iris and a lens were used to trim the outer edges and focus the beam respectively to improve the beam quality. The beam passed through the GEC reactor, 14 mm above the bottom electrode, before ending at the beam dump. The GEC reactor had a quartz window ($\sim$20 cm diameter) that allowed for optical access to the system. Thus, the fluorescence was captured perpendicularly to the laser direction by an Intensified Charge-Coupled Device (ICCD) camera (Andor iStar DH334T-18U-73, 500 kHz maximum repetition rate). Bandpass filters (LOT Oriel) 844.6±1 nm and (Laser Components UK Ltd.) 835 ±10 nm were used for the oxygen and xenon emissions, respectively. A lens (SIGMA DC Optical Stabilizer) was mounted in front of the camera to assist with imaging the fluorescence onto the Charge-Coupled Device (CCD). The Andor SOLIS software was used to record the images for subsequent processing. Lastly, to remove possible background noise originating from either the plasma or the camera, a background camera measurement was taken in the absence of the laser fluorescence.

$$I(Laser) = I(Laser + Background) - I(Background) \tag{3.1}$$

3.2.2 Pulse-timing synchronisation of components

The Stanford Research Systems DG645 digital delay generator was used as the master trigger for the plasma, laser and camera acquisition. The BNC cables used to attach the DDG to these components were of varying length, and so the timings shown correspond to the sent electrical signals in order to synchronise the capture of the fluorescence signal. The general timing scheme is shown in figure 3.5. The DDG externally pulsed the plasma power for 10 ms on, 90 ms off to create a 10% duty cycle, at a rate of 10 Hz and coincided with the laser pulse rate. The laser flashlamp signal, $T_{Flashlamp}$ could be variably triggered from the beginning of the plasma pulse, T_0, with the Q-switch triggered 225 µs later to maximise the output energy of the laser's power-cooling unit. Incidentally, the laser pulse itself always arrived 225 µs afterwards as measured by a photodiode and oscilloscope i.e. firing the flashlamps at T_0 + 10 ms resulted in the laser pulse arriving at T_0 + 10.225 ms. Lastly, the camera was triggered shortly afterwards, around 300 ns. As a result, the camera was able to capture the moment just prior to when fluorescence was started to be detected. Thus, the camera trigger was essentially fixed relative to the laser flashlamp timing so that the temporal study of atomic oxygen densities in the afterglow could also be probed by varying $T_{Flashlamp}$ relative from T_0.

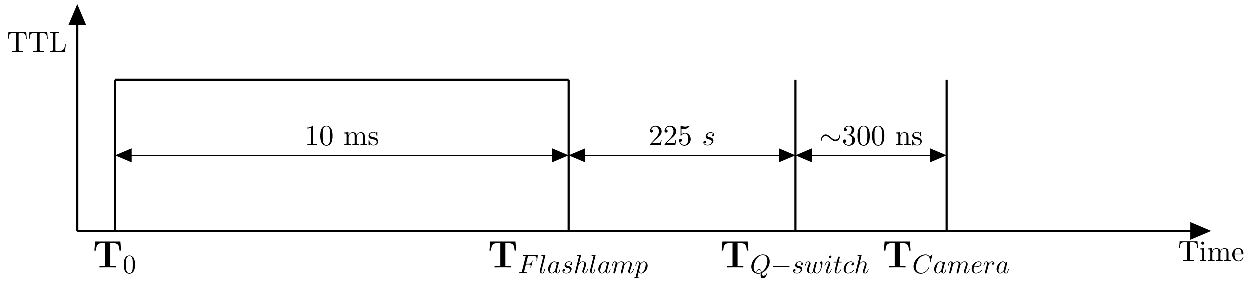

Figure 3.5: The timing scheme, synchronising the plasma pulse, laser and camera shot timing from time reference T_0, not to scale for improved visualisation. These timings correspond to the electrical signals sent from the DDG to the various components.

This scheme was tested for possible jitter through repeated measurements at various times after the plasma pulse. Figure 3.6 shows the mean and standard deviation of 20 separate measurements of the laser fluorescence at various times in the afterglow. The variability in counts was less than 1% after the end of the pulse. Consequently, this gave confidence that the same point in the afterglow was being probed with good precision by using the DDG as the master trigger.

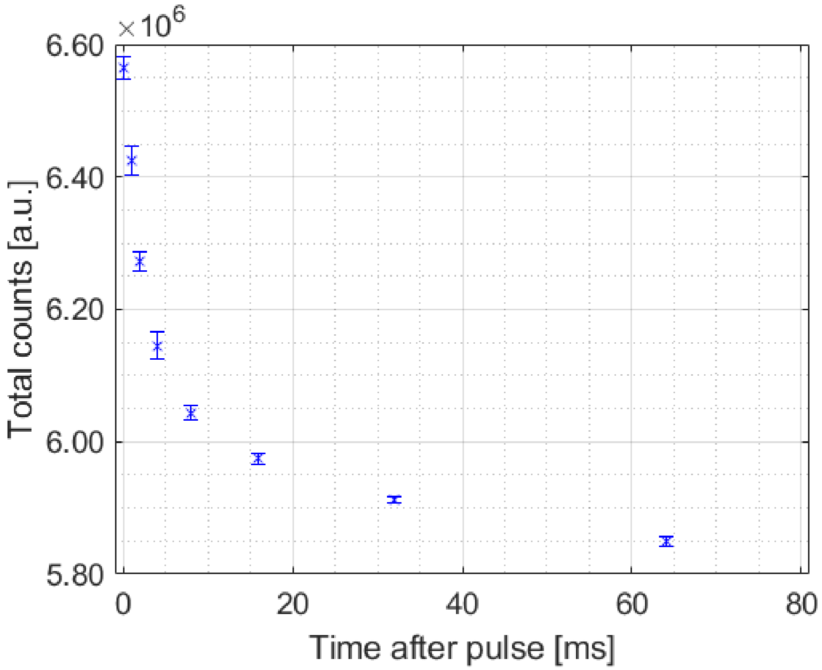

Figure 3.6: The intensity of the fluorescence in the afterglow averaged over 20 shots. The small standard deviation of each point illustrates the reliability of the laser triggering scheme.

3.2.3 Selecting the Region of Interest for analysis of fluorescence

The ICCD detector has an array of 1024×1024 pixels, but were binned 2×2 in the x and y axes to produce better signal-to-noise. For the analysis of the data, the fluorescence signal was summed from the counts of all pixels within a defined Region of Interest (ROI). This is shown in figure 3.7 and was manually chosen where the laser fluorescence was observed in the images read from the data; only counts that are a direct result of two-photon absorption were to be summated, whereas anything outside of this region was background noise. Thus, focusing the analysis in a localised region also improves the signal-to-noise ratio of the total fluorescence signal for both the lifetime and spectral measurements. As the beam focus was near the centre of the reactor, the ROI was also chosen to span around this spot as opposed to the entire length of the beam.

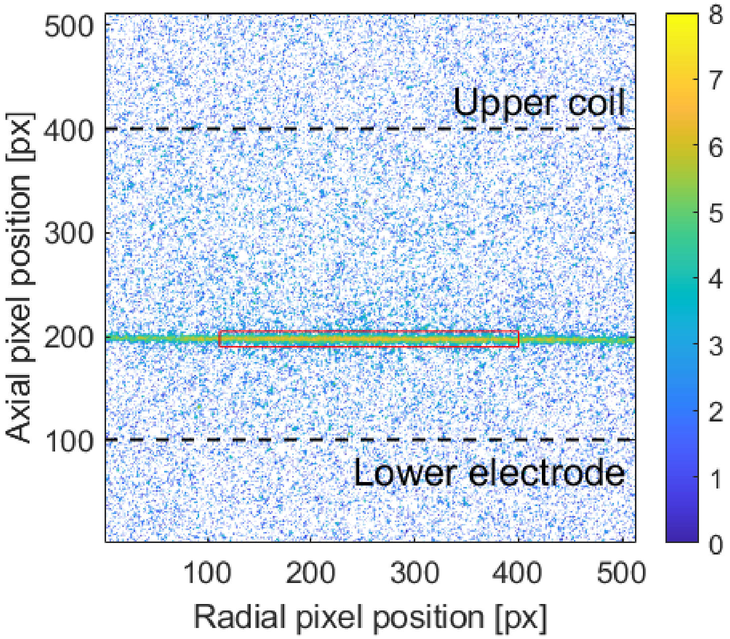

Figure 3.7: Region of interest used in analysing the fluorescence signal. This was manually chosen to encompass the fluorescence signal. The axes values refer to the CCD pixel value. The contour plot here is on a logarithmic scale of the signal for easier visualisation and identification of the beam location. Coil and electrode positions are approximate.

3.2.4 Determining length of camera gatewidth time

The camera TTL setting controlled the length of the ICCD photocathode gate per trigger and needed to be separately chosen for the spectral and lifetime measurements. In both cases, if the gate is too long, then more of the captured signal will be background noise, and will reduce the signal-to-noise ratio. Figure 3.8 shows how increasing the camera gate time allows for more of the fluorescence signal to be captured. However, the total counts gradually reached a finite value. In contrast, the background value increased, although very slightly. Nevertheless, a gate time of 100 ns was chosen so as to capture more than 95% of the fluorescence signal.

While the choice of gatewidth does not have an impact on the calculated lifetime as demonstrated by [108], ideally the gatewidth time should be comparable to the timestep between measurements to only sample that particular window. The drawback is that the lifetime scans have nanosecond timesteps, and this restricts the amount of light that is detected. A balance between maximised signal and signal-to-noise ratio was desirable. Thus, a shorter TTL of 5 ns was used for the lifetime measurement sampling 25 points in 2 ns steps to ensure good fitting of the lifetime signal.

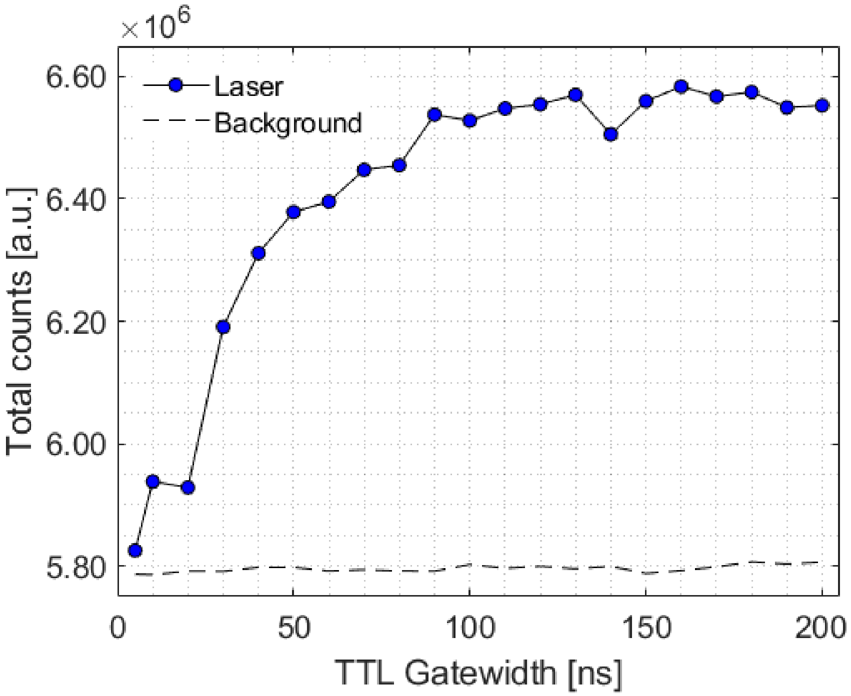

Figure 3.8: Effect of camera gatewidth on measured signal. Increasing the camera gatewidth allows for more signal to be captured. However, the signal will reach a saturation point, from which additional counts are a result of background counts.

3.2.5 Calibration to obtain absolute atomic densities

There are several methods that can calibrate the relative intensities of the TALIF fluorescence signal into absolute number densities, such as titration methods. However, these add further experimental complexity. Instead, the calibration method by [60] was adopted where the atomic oxygen fluorescence intensities were compared with xenon's as it has a similar two-photon excitation scheme. For excitation out of the ground state of oxygen $O(^3P_2)$ to the upper states $O(3p^3P)$, two photons at 225.65 nm are needed. On the other hand, xenon requires two photons at 224.31 nm to reach the $6p'[3/2]_2$ level. It should be noted that oxygen has a fine structure at both the ground and upper level, with subscripts to distinguish between each. Figure 2.1 shows this in order of lowest to highest energies. It was assumed that the $O(^3P_2)$ ground state is the most populated, and so the atomic oxygen densities obtained will reflect this level. Assumption or reliable measurement of the gas temperature can be used in the Boltzmann fraction equation to calculate the total ground state density in all three sub-levels. Specific excitation to the upper level was not possible as the laser system used was not able to resolve the small energy difference between the lowest and highest energy level 0.7 cm^{-1}. The noble gas calibration measurements were taken at 20 Pa; since it is already an atomic species, no rf power was applied. Thus, the gas temperature of xenon was assumed to be at room temperature - $T_g = 293$ K and using the ideal gas law, $n_R = p/k_B T_g$ the total number density of atomic oxygen n_X can be found using equation (2.1).

3.2.6 Determination of laser saturation energy

Higher signal-to-noise can be achieved by increasing the laser energy. When the resulting fluorescence response is directly proportional to the square of the input, the assumptions of TALIF are valid in this regime. However, supplying too much energy can cause non-linearity due to saturation effects. Moreover, it can result in a loss of signal through photoionization and Amplified Spontaneous Emission (ASE). There would be a loss in the fluorescence signal and would plateau, or even decrease. This will ultimately result in an underestimation of the ground state densities. Conversely, high energies may cause photodissociation effects. An initial laser pulse may cause the O_2 molecule to dissociate, and a subsequent pulse would then detect the resulting atoms. This would lead to an increase in the fluorescence signal and would display a cubic relationship.

To determine the maximum laser energy, single shot TALIF signals at the central resonance wavelength were captured, and the resulting intensity was compared with the square of the laser input energy. This was done for both atomic oxygen and xenon and shown in figure 3.9. The linear portion of the line of best fit is the non-saturated region.

No saturation effects were seen for the laser energies applied for 20 Pa, 20% oxygen at 500 W given that there was no deviation from a linear relationship between the measured signal and the square of the laser energy. Thus, no photodissociation, ASE or photoioinization effects were present. Nonetheless, an intermediate value of around 630 µJ was chosen as a precaution in the case that laser saturation may occur under different applied conditions. Similarly, xenon showed linear relationship for all the range of energies tested - all noble gas calibrations were taken at 20 Pa and 160 µJ.

It may be noted that oxygen at the lowest laser energies strays from the best fit line through the origin. No fluorescence should be observed with zero laser energy. The cause of this was due to the background subtraction of the raw data was only done for when the plasma was off i.e. only the camera background noise was subtracted. In hindsight, there may be some residual background from the plasma in the afterglow, hence causing this offset in count at low energies. The figure inset is another scan for the pure oxygen case with the appropriate background removed, and proves this to be the case. Moreover, this is further reinforced by the fact that this phenomenon does not occur for the xenon case since the plasma is not needed for these measurements. Consequently, using a higher laser energy aids with improving the signal-to-noise of the data.

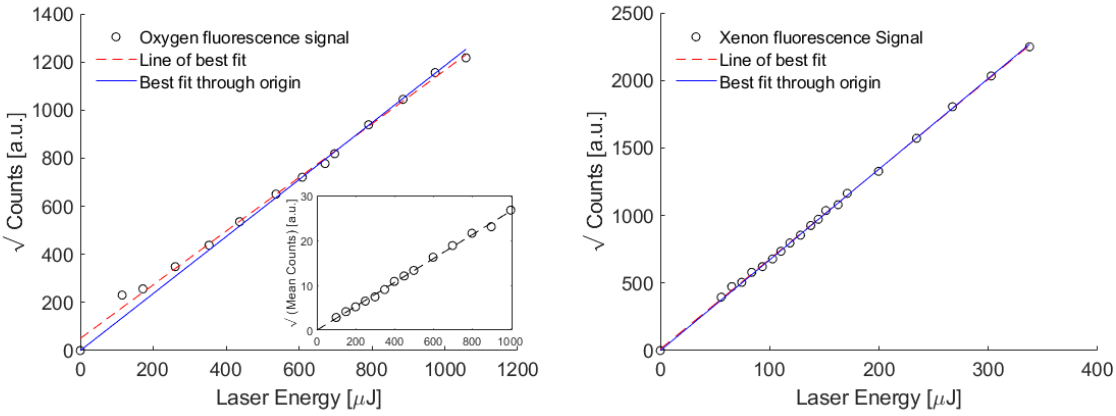

(a) (b)

Figure 3.9: Laser input energy versus the square root of fluorescence for a) He-20%O_2 and inset is a pure O_2 case both at 20 Pa, 500 W, and b) Xenon, 20 Pa. The inset figure was to verify that the response was linear at lower energies with the appropriate background subtracted, which was not the case for He-20%O_2 as it did not remove lingering plasma emission. These plots identify saturation when non-linear response occurs for atomic oxygen and xenon, which is not present here.

3.2.7 Error estimation

The absolute densities are derived using equation (2.1), and each component has an associated uncertainty that affects the absolute density values. These can be split into stochastic and systematic errors; the former including variability during the experiment, and the latter ultimately affecting the magnitude of the calculated values.

Where possible, repeat measurements were made to verify results were reproducible, and the error was calculated from the mean and standard deviation. Nonetheless, the theoretical and experimental sources of uncertainty are detailed here for cases where only a single set of measurements were made.

3.2.7.1 Stochastic uncertainties

Firstly, the stochastic errors are discussed beginning with the laser energy. Prior to measurements, the laser energy and stability was determined over 1000 shots using a Gentec energy meter (QE23-LP-S-MB-INT-D0). The typical stability for the oxygen shots were less than 4% whereas for xenon was less than 6%. Moreover, prolonged use of the laser can reduce its efficacy for the duration of the experiments. Consequently, the laser energy was measured at the start and end of the day using the energy probe, and was observed to decrease up to 5% between the first and last measured points over an 8-hour period.

The effective lifetime uncertainty stemmed from the exponential curve's goodness of fit to the data. Since the noble gas calibration measurement was carried out under the exact same conditions, the uncertainty was calculated from the average effective lifetime across several experiments. On the other hand, the 95% confidence intervals from the fit result for the atomic oxygen was used to estimate the lower and upper effective lifetimes. As such, the uncertainty was determined from the maximum percentage difference between these and the fitted effective lifetime value. For each measured data point, the uncertainty from each individual fit was applied.

The fluorescence signal was fitted using a Gaussian equation as it was assumed that the laser line profile was dominant compared to other broadening mechanisms. The 95% confidence interval from the fit via MATLAB resulted in uncertainties of the integrated signal of around 2.5%.

3.2.7.2 Systematic uncertainties

The rest of the uncertainties were fixed and so will only influence the magnitude of the atomic oxygen density. A chief example of this would be in the uncertainty in the two-photon excitation cross-section ratio between xenon and oxygen, $\sigma^{(2)}(Xe)/\Sigma_{J'}, \sigma^{(2)}_{J \rightarrow J'} = 1.9$ and has an uncertainty of 20% [60]. However, this is likely to be higher and the determined n_O could effectively be halved [88].

The branching ratio uncertainty is affected by both the pure branching ratio and the natural lifetime. In the case of $O(3p^3P)$, the only allowed transition is to $O(3s^3S)$ and so the pure branching ratio is unity. On the other hand, xenon has other pathways - the $6p'[3/2]_2 \rightarrow 6s'[3/2]_1$ transition has a probability of 0.733 [140]. The natural lifetimes used were 34.7 ± 1.7 ns (4.90%) and 40.8 ± 2.0 ns (6.49%) for O and Xe, respectively [60].

The optical filters used are sensitive and transmission can be affected by the angle that light is incident on it. This effect was explored by [141]. The transmission coefficients for the optical filters were carried out by [142] using a Shimadzu UV spectrophotometer UV-1800 with the following values: $T_O = 83.580\%$, $T_{Xe} = 62.917$, who noted negligible error using these optics.

The quantum efficiency for the detected photons were obtained from the Andor iStar manufacturer's brochure [143]. Specifically, the QE was taken from the Gen 3 18x-73 curve. The emitting photons of the oxygen (844 nm) and xenon (835 nm) had QE values of 18.45% and 20.08%, respectively. Yet, no uncertainty values in these could be found. As a crude estimate, the sensor quantum efficiency was assumed to be less than 5% for both.

Parameter	O	Xe
Filter Transmission Efficiency [%]	83.580	62.917
Sensor Quantum Efficiency [%]	18.45	20.08
Pure Optical Branching Ratio	1.000	0.733
Natural Lifetime [ns]	34.7	40.8
Laser energy [uJ]	630	160

Table 3.1: Tabulated values of the constants used.

Parameter	O	Xe
Filter Transmission Efficiency	-	-
Sensor Quantum Efficiency	5	5
Pure Optical Branching Ratio	-	-
Natural Lifetime	4.90	6.49
Two-photon cross-section	20	
Total Systematic	22.7	
Laser energy	4	6
Signal	2.5	2.5
Effective lifetime	8.66	5.43
Total Stochastic	13.6	

Table 3.2: Tabulated percentage uncertainties of the associated constants.

3.3 Energy Resolved Actinometry

3.3.1 ERA experimental set-up

The set-up and components of the plasma reactor were largely the same for the ERA measurements as TALIF, namely the vacuum system, gas admixture delivery, rf power, and the camera and its optics. Figure 3.10 illustrates the experimental set-up for ERA on the GEC plasma source.

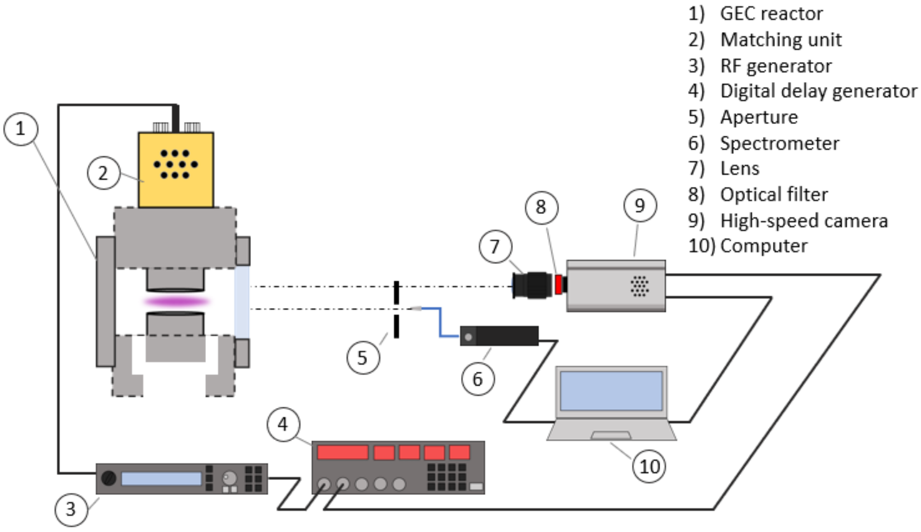

Figure 3.10: The set-up of the PROES measurements used to carry out ERA.

However, there were a few minor differences in the case where this was applied to the GEC-like reactor. Firstly, the camera (DH334T-18U-C3) had slightly different performance compared to the TALIF camera, so settings such as the gatewidth was accordingly set from its specification booklet - in this case, ~3.3 ns TTL corresponded to the 2 ns fully open gate.

Secondly, in lieu of a laser fluorescence signal to focus on, figure 3.11 shows that imaging the centre of the discharge was assisted by inserting a sample substrate holder into the reactor. Thus, the lens was adjusted to properly image the plasma onto the CCD. The optical components were affixed to a rail to ensure alignment if re-positioning was required.

Lastly, instead of using an aperture, the spectrometer was placed as far as possible from the plasma, roughly a metre away from the centre of the reactor, with the camera and lens sat behind it. Moreover, the optical fibre head was able to be positioned just below the lens of the camera to prevent obstruction to its line-of-sight. This way, the plasma emission could be recorded concurrently by both of these diagnostic tools.

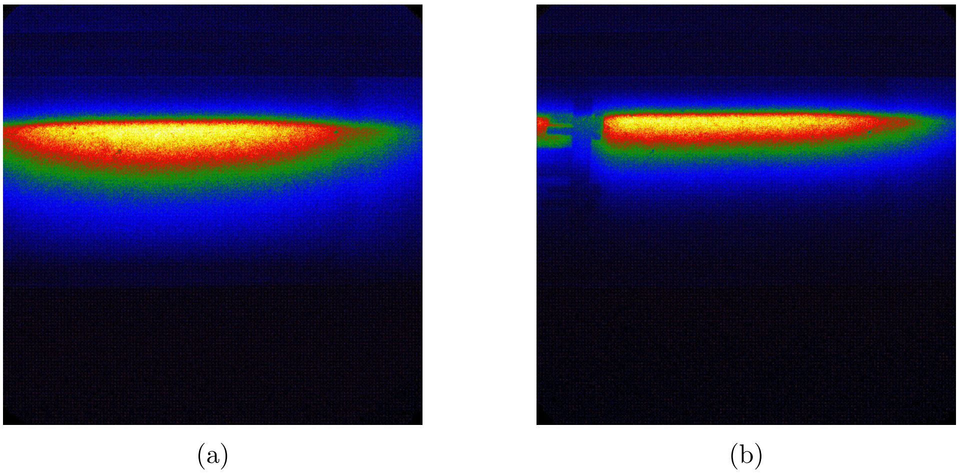
(a) (b)

Figure 3.11: Imaging of a plasma discharge on the GEC-like reactor. a) Image of a plasma discharge. b) Image of the plasma discharge with a sample substrate holder seen on the left side. In order to image the centre of the discharge onto the CCD, an object was inserted into the GEC-like reactor so that the lens can be adjusted to it.

3.3.2 PROES acquisition

Instead of using the DDG, the plasma pulse was internally triggered by the rf generator at 10 Hz, 10% duty cycle. Consequently, the output rf signal from the generator was connected to the external trigger of the DDG. It then prescaled the 13.56 MHz signal to trigger the camera 1 in every 30 rf cycles. This was because the (Andor iStar ICCD DH334T-18U-C3) camera had a maximum repetition frequency of 500 kHz.

For each plasma condition, three sets of PROES images were taken for each emission line, with the optical filter substituted as needed. These were LOT-Oriel QuantumDesign bandpass filters: 844.6 ± 1.0 nm, 777.4 ± 2.0 nm and 750.4 ± 0.5 nm. The camera exposure time was adjusted to allow for emission from multiple rf cycles to be integrated, increasing the signal-to-noise of the image. Moreover, the gain of the microchannel plate was also set to maximise the counts on the CCD, which could safely read up to (3×10^4) counts. As the O(777) line typically had the highest counts, the camera settings were optimised for this emission so as to avoid saturating or even over-exposing the CCD. So, the exposure time and gain were the same for all three lines. These settings were entered into a script that also controlled the variable delay of the triggering in order to automate the acquisition of the emission over the rf cycle.

3.3.3 Image calibration

A custom Ocean Optics HR4C4860 VIS spectrometer with an optical fibre (Ocean Optics QR600-2-SR; 600µm) was used to record a calibration spectrum for each condition in lieu of accounting for each specific optical component's particular response to each wavelength [141]. The spectrometer uses a diffraction grating to disperse the light onto a (Toshiba TCD1304AP) linear CCD array of 3648 pixels over a wavelength range of 680-870 nm (0.05 nm/pixel). The raw counts were calibrated from a file that had the recorded spectral response of the CCD array against a well-defined light source. As the plasma was pulsed, multiple spectra were taken and averaged. A similar procedure was carried out for a background spectra to subtract from the raw data. These were saved using the SpectraSuite software. Finally, the integrated area from absolute irradiance for each peak was used to calibrate each set of PROES images.

The optical fibre head was placed in front of the camera's optical stabilizer. However, due to the intensity of emission from the plasma posing saturation issues to the spectra, an aperture was placed immediately in front of it so that light could only enter a pinhole-sized gap and limit the collection area. Since this caused an obstruction to the camera, both the aperture and optical fibre head were connected to the same base on the same aligning rail of the camera and lens. As such, it was appropriately placed back in the same position when the calibration spectra was needed to be taken. The integration and boxcar width were also tuned to increase the detected signal as much as possible.

3.3.4 Discussion on the difference in detection volume

As seen in this section, ERA captures the emission from the entire plasma discharge region and the subsequent analysis takes place in the temporal and spatial region of maximum excitation. This is opposed to TALIF which probes the region just above the grounded electrode. As a consequence of this, the measured atomic oxygen densities should not be directly equal; atoms emanating from the main plasma region may be lost to the walls or by recombination as it travels from the main plasma discharge towards the grounded electrode. Consequently, it is expected that the atomic oxygen densities measured by ERA will not give exactly the same values. Nonetheless, the core objective of the application of this diagnostic is to test the effectiveness of the passive, optical-based method. Firstly, by checking whether the same trends with input parameters are identified with both diagnostics, and secondly, if number densities on similar orders of magnitude are obtained. Then, further work can be undertaken to improve the ERA model to account for other factors such as these.

Chapter 4

Atomic oxygen densities using TALIF in the pulsed ICP afterglow

As mentioned in chapter 1, determination of the absolute number densities of oxygen helps to improve our understanding of plasma physics through comparison between experiments and theoretical models. These have been measured in continuous wave inductively coupled plasmas using the well-established technique, TALIF [56,85]. Here, it was applied in the early afterglow of the H-mode plasma pulse since modulating the plasma has additional benefits, such as time-averaged heat loads at the substrate [31]. Moreover, the temporal evolution of the atomic state densities in the ground state sub-levels were monitored and used to determine the neutral gas temperature under various conditions. This chapter focuses on the results of the two-photon absorption laser induced fluorescence measurements taken in the early afterglow of the pulse to determine the absolute number densities of atomic oxygen and will provide validation of the extended ERA approach in the HERA chapter. The determined gas temperatures that can provide input in the generation of excitation profiles will be presented following this chapter.

4.1 Atomic oxygen densities and lifetime measurements

4.1.1 Laser fluorescence signal in the afterglow

Firstly, to obtain the best signal-to-noise ratio of the laser fluorescence, the 844 nm emission in the afterglow was studied to identify the optimal time to take the atomic density measurements. On one hand, taking the laser measurements as close to the end of the pulse would limit the loss of atomic oxygen to processes such as recombination, and by extent the signal strength. However, taking it too early may have led to the fluorescence signal overlapping with residual plasma emission. Thus, distinguishing between the two would have proven difficult. Consequently, determining when plasma emission was considered to have abated while maximising the signal from atomic oxygen before loss processes became significant was carried out.

After the desired on-time of the plasma was reached, the rf power was turned off at T_0 +10 ms. However, energetic electrons do not immediately disappear and linger in the afterglow. Nonetheless, it was expected that these are quickly expended shortly after the pulse through inelastic processes. Consequently, plasma emission was expected to show a rapid decay on a very fast timescale owing to the lack of production of energetic electrons that cause direct impact and dissociative excitation processes. Furthermore, the maximum atomic oxygen density values are expected to be at the end of the pulse as no more atomic oxygen is produce from electron-impact dissociation. This is observed in figure 4.1.

Figure 4.1a shows the emission signal, with the origin from time T_0 +10 ms when the plasma power is turned off. Independent of applied power, the emission profile at the end of the pulse is similar. For each case, at time $0 < t < 10$ µs the same amount of emission continues to be observed and corresponds to remaining energetic electrons in the afterglow. Yet, as there is no longer production of these, there is a steep loss of emission and is observed from $10 < t < 15$ µs. From 15 µs onwards, the observed counts plateaus off, but not to a background level corresponding to a no-plasma case i.e. camera background signal. The background value was noted to increase for increasing applied power and persisted at this level from 50 µs onwards even up to the next pulse. Efforts were made to mitigate this effect. Nonetheless, to avoid as much noise as possible from plasma emission, the timing of the observed fluorescence signal was adjusted to arrive after 50 µs where it was considered that the background was sufficiently diminished.

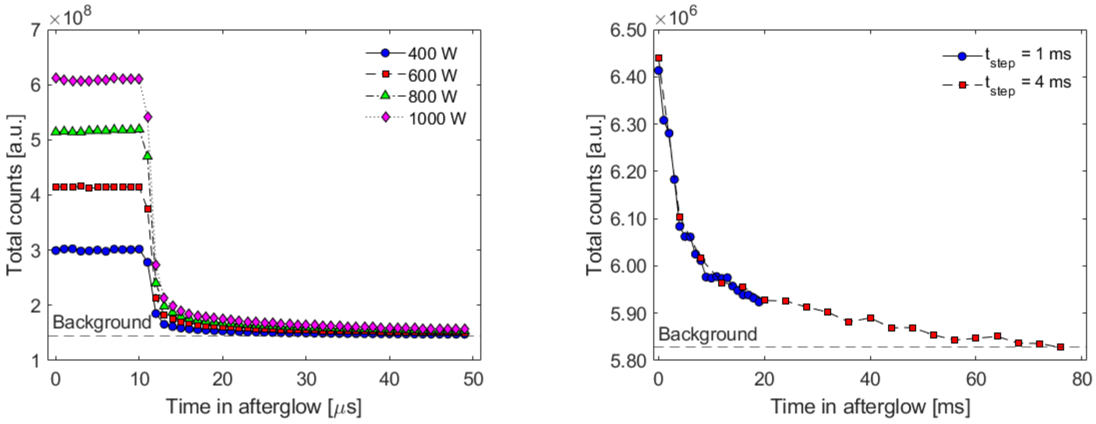

(a) (b)

Figure 4.1: Timescale comparison of captured 844 nm originating from a) plasma emission and b) laser fluorescence after the end of the plasma pulse. The plasma emission profile was taken in the absence of the laser being operated, and exhibits the same decaying microsecond timescale independent of applied power, whereas the fluorescence signal decays on a millisecond timescale after the end of the plasma pulse. Both figures were taken at He-10%O_2-2%Ar, 20 Pa at 500 W, but with different camera gain settings.

In contrast, figure 4.1b shows that the fluorescence intensity, and by extent the atomic oxygen density, decreases on a millisecond timescale after the end of the plasma pulse. Timesteps of 1 ms and 4 ms were taken to obtain temporal resolution immediately after the pulse and the majority of the off-time duration. Both show that there is a sharp decrease in the first 10 ms before slowly levelling off to the background value. Similar decay times were observed by [144] in a pure oxygen parallel plate reactor; the effect of duty cycle on the decay rate of n_O was also studied by [79] and these also tended to decay on a millisecond timescale. From this, the fluorescence measurements were taken as early as possible to maximise signal-to-noise from the atomic ground state. As such, the fluorescence signal was further investigated within the first millisecond after the end of the pulse.

Figure 4.2 compares the 844 nm emission strength with and without the use of the laser, the latter corresponding to background noise from residual plasma emission. The x-axis refers to the time in the afterglow when the measurements were taken. It can be seen that the raw fluorescence signal decreases in tandem with the background in the same period of a few hundred microseconds. Then, the signal peaked slightly at 0.2 ms whereas the background continued to level off. Finally, the raw signal fell again at 0.6 ms from which it was expected to follow the continued decay displayed on the millisecond timescale earlier. This trend was observed over several operating conditions and is explored further in chapter 5.

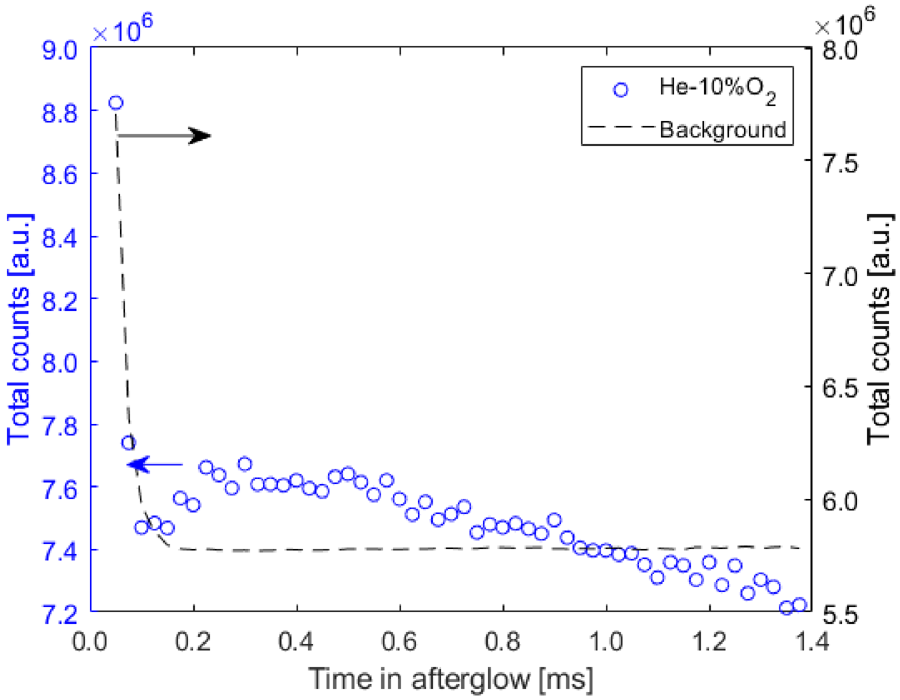

Figure 4.2: Observation of raw versus background signal in the afterglow for He-10%O_2 at 20 Pa, 600 W. To optimise the fluorescence strength while minimising the background noise, the signal was more closely observed in the first millisecond after the pulse. The x-axis refers to the time in the afterglow when the measurements were taken. The slight rise in emission between 0.2-0.6 ms was considered to have the highest signal-to-noise for the absolute density measurements.

Ultimately, the best signal-to-noise ratio was deemed to be at this peak that occurred consistently at the same time point and also when the background noise had already levelled off. Thus, TALIF measurements were taken at this time; the laser flashlamps were triggered at T_0 + 10.2 ms followed by the Q-switch. In effect, the laser pulse arrived roughly 425 µs after the end of the plasma pulse for the TALIF measurements.

4.1.2 Effect of impurities on measured atomic oxygen densities

As the ERA technique was to be tested on the GEC-like reactor without fully pumping down to extremely low pressures, the effect of possible impurities on the atomic oxygen densities were compared using TALIF on the GEC.

As seen in figure 4.3 these were largely within the calculated experimental errors for both cases where the turbo-pump was and was not used for He-10%O_2. The second 500 W measurement taken after the highest power was plotted with a +5 W shift to distinguish from the first 500 W point. It shows that the atomic oxygen density has a weak dependence with applied power.

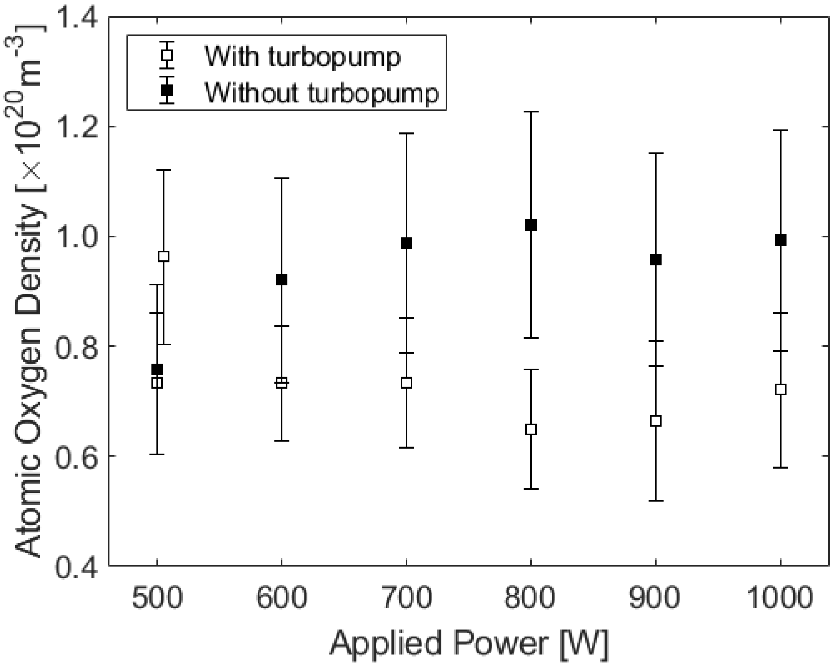

Figure 4.3: TALIF atomic oxygen densities with and without turbo-pump. The atomic oxygen densities measured were largely the same even after using the turbo-pump for He-10%O_2, 20 Pa. Therefore, impurities such as nitrogen are presumed to have negligible effects.

The effective lifetimes in figure 4.4 show that there was little change with applied power and is mostly within uncertainties of previously reported natural lifetime, 34.7 ± 1.7 ns [60] displayed as the dashed and dotted lines. The high helium content and reduced molecular oxygen both reduce the quenching rate of the excited oxygen state, and so the $O(3p^3P)$ state lives at its natural lifetime. In addition, as seen later in figure 4.8b at the same power (600 W) and pressure (20 Pa), the effective lifetime values were within the calculated uncertainties of this point (40 ± 2 ns).

Nevertheless, the first 500 W and 800 W data points have uncertainties that fall outside of this cited literature value. Although higher values have been reported of 40 ± 3 ns [145], table 4.1 summarises previously measured natural lifetimes of $O(3p^3P)$, with more recent measurements tending towards 35 ns. Consequently, the measured lifetimes here are noticeably higher, and it will be seen in this chapter that these are prevalent particularly for the helium-oxygen admixtures.

Paper	Natural lifetime [ns]	Reference
Niemi et al. 2005	34.7(1.7)	[60]
Niemi et al. 2001	35.1(3.0)	[105]
Bittner et al. 1988	36.2(0.69)	[146]
Kröll et al. 1985	36(4)	[147]
Bischel et al. 1982	39.1(1.4)	[148]
Bromander et al. 1978	40.3(3)	[145]

Table 4.1: Reported $O(3p^3P)$ natural lifetime values tend towards 35 ns. The uncertainties are in parentheses.

Re-analysis of the lifetime plots was carried out to assess the accuracy of these values. This was done by applying the exponential fit to the data from when the laser pulse intensity had fully diminished. Thus, its influence on the lifetime is inferred from comparing the different cases and will be seen later.

That aside, this particular set of lifetime measurements was rather noisy and the fitting suffered from fluctuations as a result. However, it was not the case for the rest of the data. Nonetheless, setting the gatewidth to be small reduces the quality of the signal. Therefore, increasing the gatewidth and number of points would likely improve on these uncertainties.

The rest of the atomic oxygen density results from hereon were taken without the use of the turbo-pump as it made little difference.

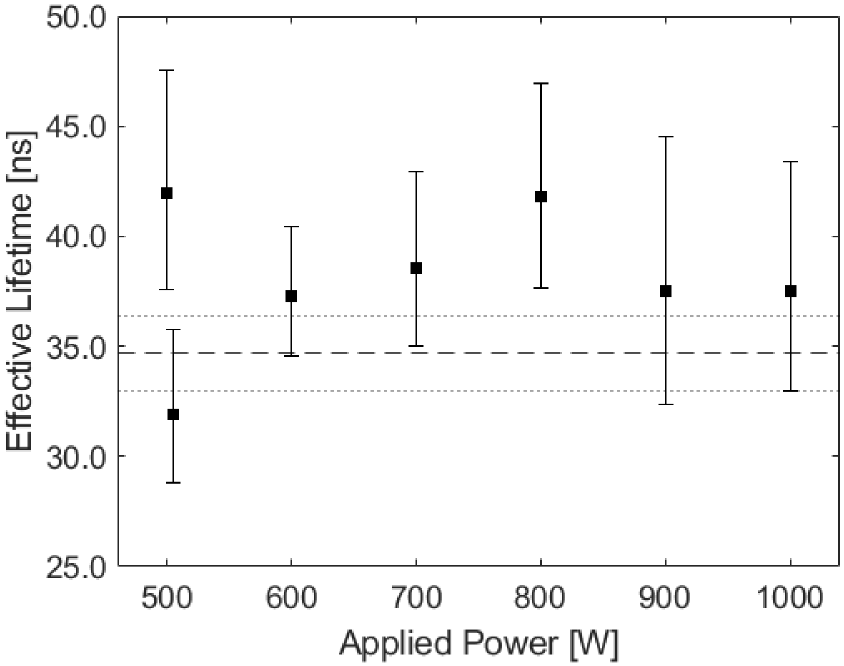

Figure 4.4: Effective lifetimes in He-10%O_2, 20 Pa. The effective lifetimes showed little variation with increasing applied power and are similar to the natural lifetimes for He-10%O_2, 20 Pa reported later in figure 4.8b where the turbo-pump was not used. Hence, impurities have little effect on τ_{eff}.

4.1.3 Effect of varying applied power

4.1.3.1 Pure O_2

Increasing applied power produced a weakly increasing amount of atomic oxygen as seen in figure 4.5a. The atomic oxygen density increased from 1.20×10^{20} m^{-3} at 500 W to 1.32×10^{20} m^{-3} at 1000 W for 11 Pa; an increase of roughly 10% overall. This is a much smaller increase than other works such as Zeng et al. [85] who have around a factor of 2.55 increase. Nonetheless, at 500 W, 11 Pa the atomic oxygen density value here is close to their experimental results at the same power and pressure. It is also similar to theoretical values predicted by Gudmundsson et al. [52], at the same power at 13 Pa.

At 20 Pa, it increases from 1.95×10^{20} m^{-3} at 500 W to a peak of 2.19×10^{20} m^{-3} at 900 W. The increase of 12.3% is similar to that of the 11 Pa case. Overall, the positive correlation found here is also consistent with Corr et al. [56] and Fuller et al. [101]. This is expected due to the increased energy supplied to the plasma in each pulse, causing more dissociative processes to occur.

As a consequence of the increasing atomic oxygen density with higher applied power, the effective lifetime of the $O(3p^3P)$ state also weakly increased. Since more molecular oxygen particles are dissociated, there is a reduction in this quenching partner density; excited atomic oxygen has a quenching coefficient of $k_q^O = 8.2 \pm 8.2 \times 10^{-17}$ m^3 s^{-1} [80]. It is an order of magnitude lower compared to molecular oxygen, $k_q^{O2} = 9.4 \pm 0.5 \times 10^{-16}$ m^3 s^{-1} [60]. This combination results in the slight increase in effective lifetime. This is observed in both pressure cases of pure oxygen in figure 4.5b.

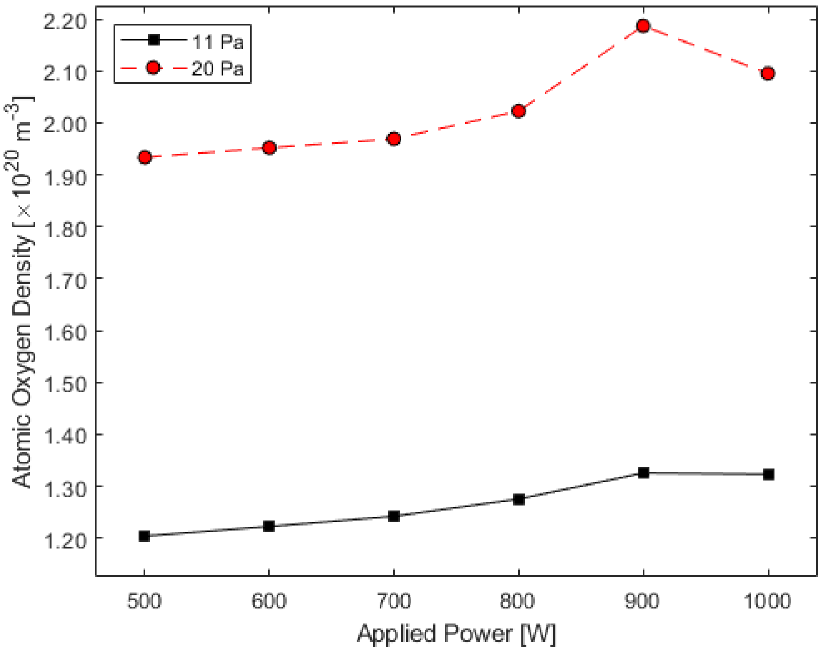

(a)

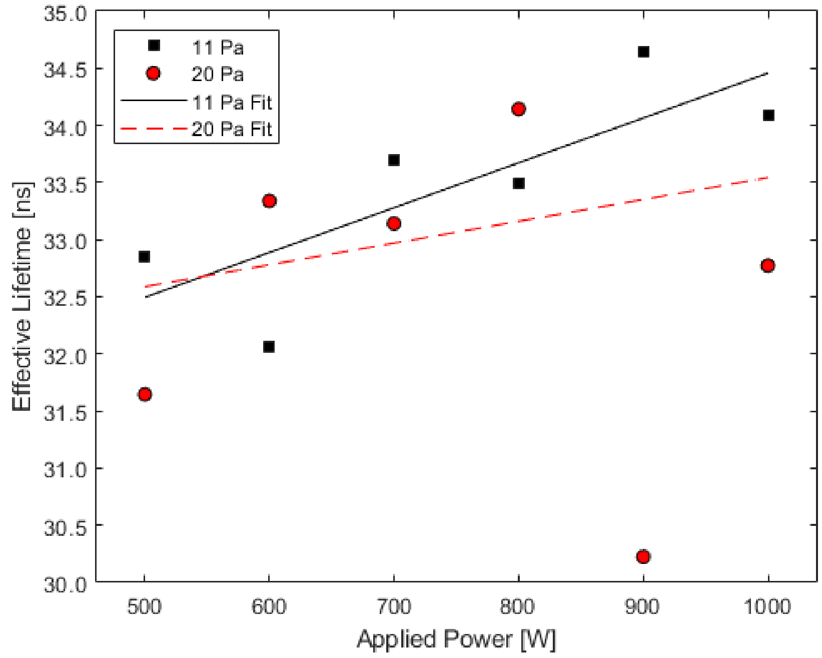

(b)

Figure 4.5: Measured parameters of a) atomic oxygen densities and b) effective lifetimes in pure O_2, 20 Pa with varying power. Higher applied powers gently increases the atomic oxygen density, whereas pressure does so significantly. The effective lifetimes weakly increase with applied power - as more atomic oxygen is produced, there is a reduction in molecular oxygen and in turn reduces quenching rate. The fit line for 20 Pa omits the 900 W point as an assumed outlier.

4.1.3.2 He-20%O_2

The helium-oxygen admixture with power variation is seen in figure 4.6a and also exhibits a trend of gently increasing atomic oxygen density with applied power. n_O increases from 1.10×10^{20} m^{-3} to 1.36×10^{20} m^{-3} from 500 W to 900 W at 20 Pa. Taylor and Tynan [93] studied controlled oxygen dissociation in noble gas mixtures, including varying helium content, and used actinometry and atomic mass spectrometry to measure atomic oxygen density. Their results showed similar weak increase with power: at 10 mTorr and the same admixture ratio, their atomic oxygen density ranged from 1.3×10^{18} to 2.0×10^{18} m^{-3} between 500 to 2000 W. Despite the power increasing four-fold, the overall magnitude remained the same. Consequently, the linear production of n_O through increasing applied power offers fine adjustments in atomic density.

Unlike the pure oxygen case, the effective lifetimes does not show any particular relationship with applied power, averaging 37.4 ± 2.6 ns across all applied powers and shown in figure 4.6b. This is slightly higher than the natural lifetime of the $O(3p^3P)$ state 34.7 ± 1.7 ns reported by [60]. Nonetheless, it is still within the range from their previous work of 35.1 ± 3.0 ns [105]. Furthermore, given that the dominant species, He, has a small quenching coefficient $k_q^{He} = 0.0017 \pm 0.002$ m^{3}s^{-1}, and the fraction of molecular O_2 is comparatively low, the plasma can be considered to have little quenching. This is further evident when compared to the pure oxygen case at 20 Pa, the effective lifetime values are higher at each corresponding power for the helium-oxygen mixture.

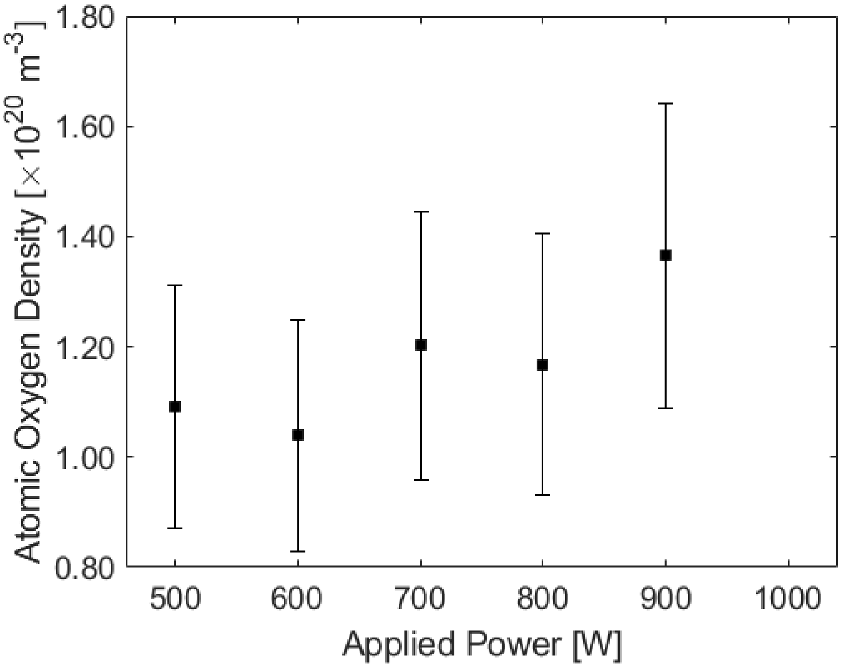

(a)

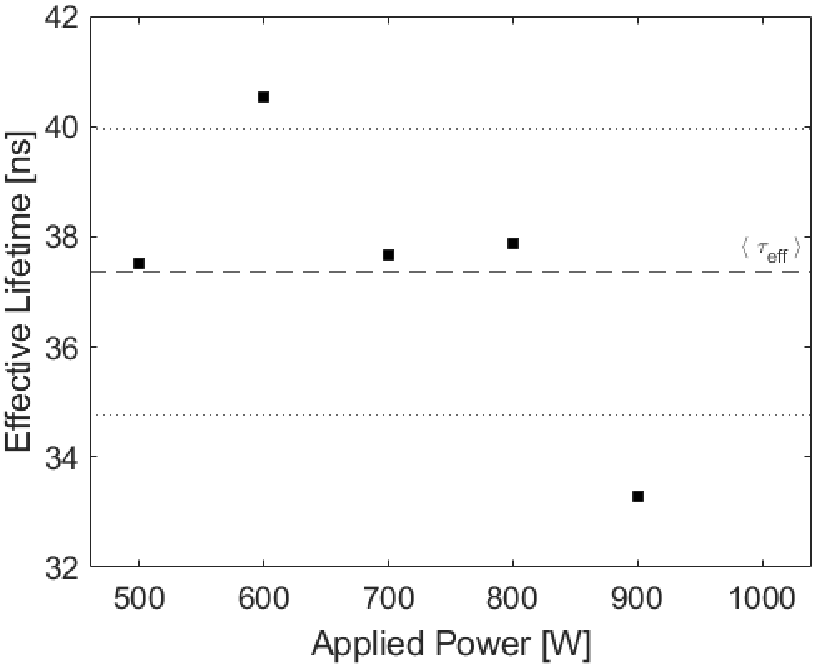

(b)

Figure 4.6: Measured parameters of a) atomic oxygen densities and b) effective lifetimes in He-20%O_2, 20 Pa with varying power. Similarly to pure oxygen, higher applied powers increase the atomic oxygen density. The effective lifetimes remain constant with applied power. The dashed line is the mean lifetime across the power variation, whereas the dotted lines illustrate the standard deviation. The effective lifetimes are higher than the pure O_2 case and are approximately equal to reported natural lifetimes. Thus, molecular quenching is almost negligible under these conditions.

4.1.4 Effect of varying pressure

4.1.4.1 Pure O_2

The immediate effect of increasing the pressure is a near proportional increase in absolute atomic oxygen density as seen in figure 4.7a. From 10 to 50 Pa, n_O increased from 1.33×10^{20} m^{-3} to 4.89×10^{20} m^{-3}. This is attributed to a greater amount of available molecular oxygen to dissociate giving an overall increase in product. Hsu et al. [149] also see the same response of 2.5×10^{18} to 1.75×10^{19} m^{-3} for 5 and 40 mTorr, respectively. Taylor and Tynan [93] observe similar increases with pressure in the 5-25 mTorr range, 1×10^{18} m^{-3} to 6×10^{18} m^{-3}. Although, with the exception of their 5 mTorr measurement, they had a much steeper increase at lower pressures. Finally, others that also note this positive correlation, include Corr et al. [56], and Gudmundsson et al. [52]. Although, the aforementioned literature are at pressures below 100 mTorr.

In contrast, Zeng et al. [85] studied a pressure range from 10-80 Pa and are more similar to this work. They instead observed decreasing n_O with pressure at constant power and attribute this decreased dissociation with $O(^3P)$ produced through an alternate process at these pressures compared to the previous cases. $O(^3P)$ was purported to be generated by energy transfer between $O(^1D)$ and ground state molecular oxygen given by equation (4.1) [129].

$$O(^1D) + O_2(X^3\Sigma_g^-) \rightarrow O(^3P) + O_2(b^1\Sigma_g^+) \tag{4.1}$$

On the other hand, the population of $O(^1D)$ has been shown to be much smaller than the $O(^3P)$ state [101, 150]. Plus, the global models of Gudmundsson et al. [52] show that the $O(^1D)$ population is negligible above 10 mTorr compared to the other neutral species. Thus, given the contrasting trends between this work and Zeng et al., it is unlikely that there is a change in dominant production process of atomic oxygen through this energy transfer reaction occurring here. Consequently, electron-impact dissociation is still considered to be the main production process at these pressures.

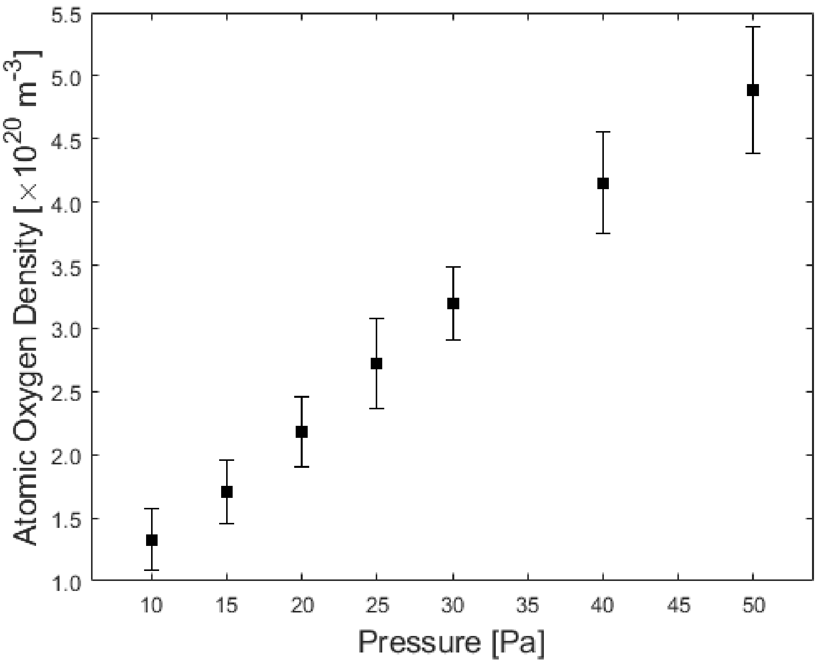

(a)

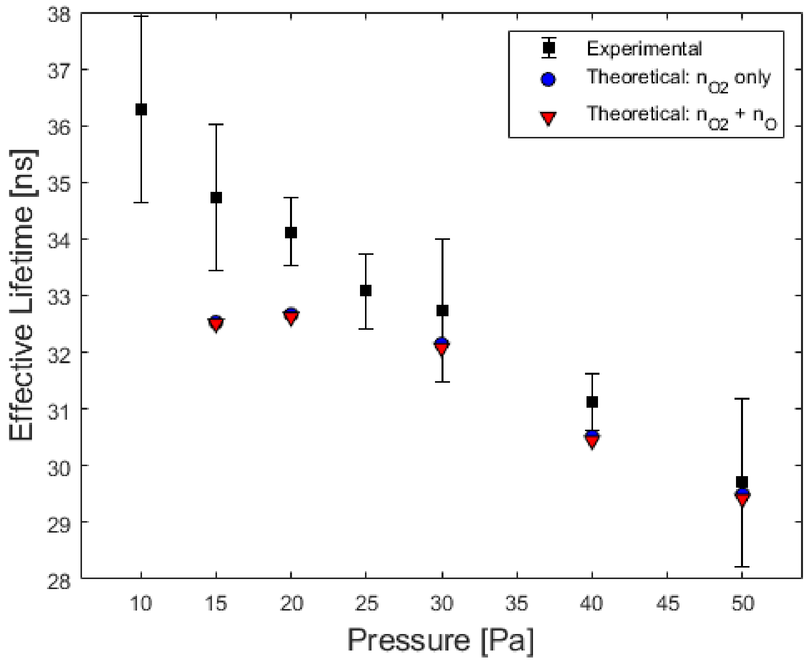

(b)

Figure 4.7: Measured parameters of a) atomic oxygen densities and b) effective lifetimes in pure O_2, 600 W with varying pressure. n_O proportionally increases with pressure due to greater amount of O_2 to dissociate. This also decreases τ_{eff} from the increased amount of quenching. Calculation of the theoretical lifetimes were shown in figure 2.3. Thus, the same process was applied here after determining the dissociation degree and gas temperature to compare with the experimental values.

The dissociation degree, calculated as the quotient of the measured atomic oxygen density and the total feed molecular oxygen density, $r_O = n_O/n_{O2}$, are displayed in table 4.2. Inductively couple plasmas can have significant gas heating, and since $n_{O2} = p/k_BT_g$, the dissociation degree will be influenced by the gas temperature. On one hand, a constant temperature may be assumed for comparison purposes. Far into the afterglow, the T_g was observed to return to 400 K, and so will be used in the calculations. The determination of these results are covered in chapter 5.

Pressure [Pa]	n_O [10^{20} m^{-3}]	r_O [%]
15	1.71	6.28 %
20	2.18	6.02 %
30	3.20	5.88 %
40	4.15	5.73 %
50	4.89	5.40 %

Table 4.2: Dissociation degree of pure oxygen using $T_g = 400\ K$ in the afterglow with varying pressure.

Table 4.2 gives the pressures and measured atomic oxygen densities used to calculate the corresponding dissociation degree, r_O assuming a constant gas temperature of 400 K. The dissociation degree shows a decreasing trend for higher pressures from 6.28% to 5.40% over 15-50 Pa. The determined dissociation degree values align with [129] who predict the atomic oxygen yield falls below 20% at 100 mTorr. While the definition of dissociation degree can vary, such as in [87] who use $r_O = [O(^3P_T)]/2[O_2]$, they similarly calculate the total molecular oxygen density with just a gas temperature and no dissociation i.e. compare the feed molecular oxygen density with the atomic oxygen density present in the afterglow. Aside from the use of the total atomic oxygen used instead of just the lowest ground state sub-level, there is a difference of factor 2 in the denominator. There is a general consensus with this work that dissociation degree decreases with pressure.

The effective lifetimes were observed to decrease linearly with pressure seen in figure 4.7b. It has the highest lifetime of 36.2 ns at 10 Pa and drops to 29.8 ns at 50 Pa. The reduced dissociation degree combined with the increased amounts of molecular oxygen with higher pressure contribute to greater quenching. The theoretical effective lifetime values are also plotted considering quenching partners in the cases of only O_2, and both O_2 and O. There is good agreement between the experimental and theoretical values. Furthermore, quenching by atomic oxygen has negligible effect on the calculation of effective lifetime.

4.1.4.2 He-10%O_2

Similarly to the pure oxygen case, the atomic oxygen density increased proportionally for a fixed amount of O_2 with pressure. Figure 4.8a shows that n_O increased from 0.59×10^{20} m^{-3} to 2.07×10^{20} m^{-3} for pressures of 15 Pa and 50 Pa, respectively. For diluted oxygen discharges in argon, theoretical models of Gudmundsson et al. [53] matched results of Hsu et al. [149], with both also seeing increased n_O with pressure.

Pressure [Pa]	n_O $[10^{20}\ m^{-3}]$	r_O [%]
15	0.59	21.7 %
20	0.73	20.1 %
30	1.19	21.9 %
40	1.58	21.9 %
50	2.07	22.8 %

Table 4.3: Dissociation degree of He-10%O_2 using $T_g = 400\ K$ in the afterglow with varying pressure.

The dissociation degree is much higher in the helium-oxygen admixture compared to the pure oxygen case, yet stays constant with increasing pressure at around 22% between 15 and 50 Pa. The sheer difference in dissociation degree is likely as a result of the low proportion of molecular oxygen in the admixture; they receive more energy from the pulse as there is less O_2 to distribute electron energy between. Additionally, helium can only be excited or ionized, but since these processes require higher energies than the dissociative threshold of molecular oxygen, electrons are more likely to be used up in interactions with oxygen than helium.

Figure 4.8b shows particularly high effective lifetimes. It is lowest at 15 Pa, rising to a peak at 25-30 Pa and then started to decline. The experimental fitting value returns 41.01 ± 3.23 ns at 30 Pa and is still comparable with the reported natural lifetime by [105]. This suggests that quenching is negligible for high content helium admixtures, including containing oxygen with as much as 10%. It may be lowest at 15 Pa as the determined temperature was the coldest, resulting in a relatively denser and therefore more collisional plasma. Nevertheless, judging from the errorbars, it may simply be the case that the effective lifetime is more or less constant. The theoretical calculations do not show any appreciable change in effective lifetime value, though there is a slightly negative correlation with pressure due to the presence of more quenching partners of molecular oxygen. Overall, the $O(3p^3P)$

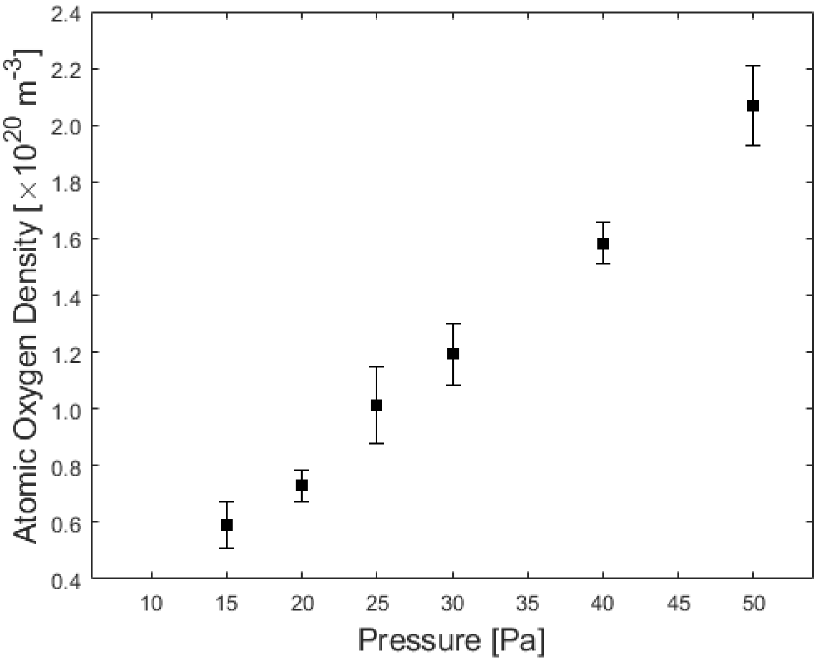

(a)

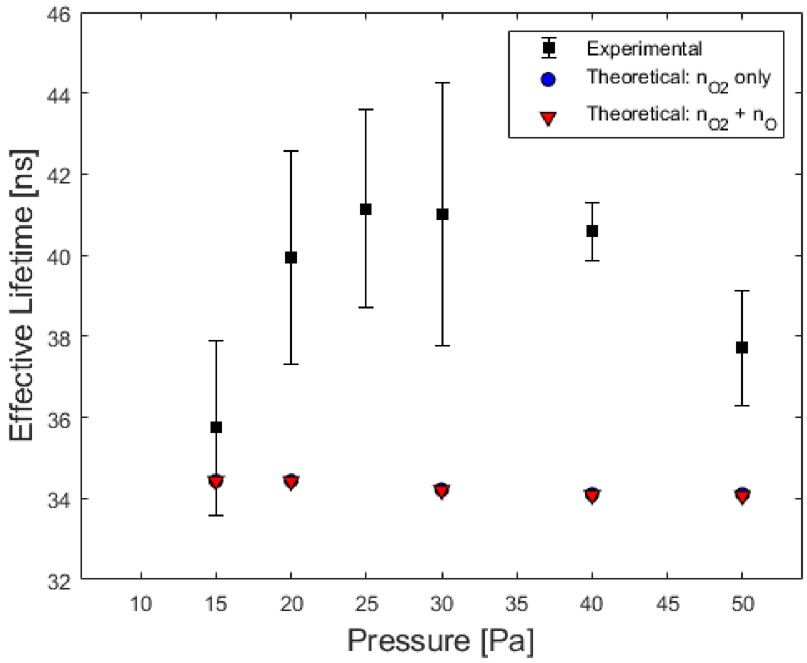

(b)

Figure 4.8: Measured parameters of a) atomic oxygen densities and b) effective lifetimes He-10%O_2, 600 W with varying pressure. Similarly to the pure oxygen case, n_O increases proportionally with pressure. However, τ_{eff} appears to be constant and close to reported natural lifetimes. This implies that quenching is minimal for these helium-oxygen admixtures.

state has a near natural lifetime value for all pressures in He-10%O_2.

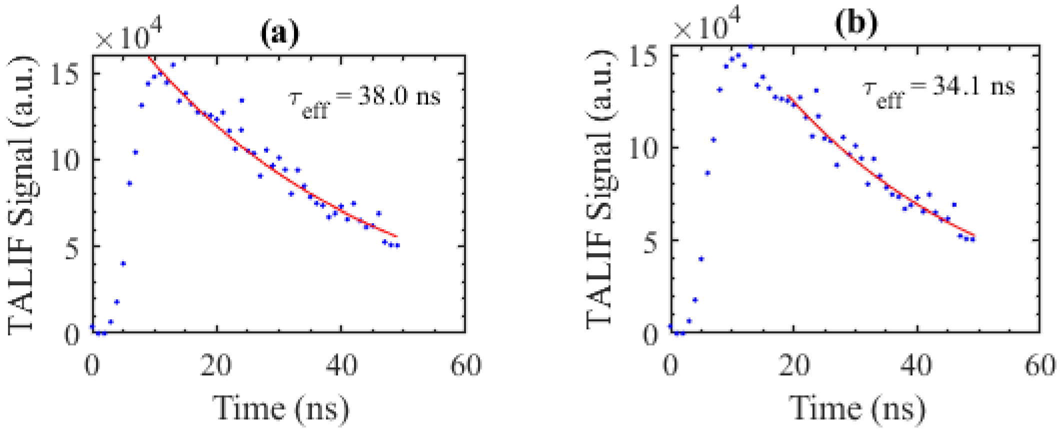

Figure 4.9: The fitted lifetime values from two exponential fits starting either at a) the peak fluorescence or b) where the laser pulse was estimated to have subsided. The maximum difference in lifetime value was 10.2% at He-10%O_2, 600 W, 30 Pa.

Figure 4.9 shows the effect of adjusting the start of the exponential fit to account for the laser pulse width for one of the sets of data at He-10%O_2. The maximum difference in the measured lifetime was 10.2% at 30 Pa. Applying this same analysis to the previous measurements mostly showed discrepancies of less than 10%, with the exception of one case that had a 20% difference in effective lifetime. Consequently, the laser pulse width can be considered to have a small effect on the measured lifetime. Instead, the goodness of the fit was more dependent on the recorded data. Taking more points would be prudent when the signal is weak to improve the fitting from possible outliers. Regardless, notably higher lifetimes than [60] were still measured in the helium-oxygen cases.

As a result, it is believed that the higher lifetimes stem from metastable helium interacting with atomic oxygen ground states since these have energy greater than 19 eV. While Reuter et al. found that He* are quickly lost in collisions with ground state He for a pure helium atmospheric plasmas discharge [151], the low-pressures here provide lower collisionality. Thus, metastable helium may survive long enough in the afterglow to interact with ground state atomic oxygen and provide an alternate source of $O(3p^3P)$ excited state.

4.1.5 Effect of varying O_2 content

Figure 4.10a shows the atomic oxygen density increases with higher oxygen contents. Firstly, the biggest increase comes from doubling the oxygen content from 10% to 20% giving 0.72×10^{20} m^{-3} to 1.31×10^{20} m^{-3}, respectively - almost twice the O density. However, as the mixture tends towards pure oxygen the benefits become less pronounced and plateaus to around 2.0×10^{20}m^{-3}. The rf power for each pulse has to be distributed over more molecular species for higher oxygen contents. Thus, it is similar to the varying pressure case where more n_O is produced as there is more O_2 to dissociate. On the other hand, Taylor and Tynan [93] observed a monotonic increase in atomic oxygen density with partial pressure at 10 mTorr.

A possible reason for this slight discrepancy is that, as the gas mixture moves from nearly pure helium to pure oxygen, there is a reduction in electron temperature and so reduces the dissociation rate. Ma and Pu [116] saw that the electron temperature was greater in higher helium contents in He-N_2 plasma. The higher ionization threshold energy of helium necessitates T_e to increase in order to sustain the plasma. Thus, there is a trade-off between reduced T_e versus having a greater availability of molecular oxygen to dissociate. The net effect under the conditions studied here is that there is an overall gain with more oxygen but decreasing amounts. Moreover, the higher pressures compared to Taylor and Tynan would also reduce the electron temperature as inelastic collisions are more prevalent.

With the exception at the 10% datapoint, the effective lifetime showed a gradual decrease with higher oxygen content seen in figure 4.10b. It is highest at 20% oxygen content at 38.2 ns and lowest at 100% at 30.9 ns. Since molecular oxygen has a significant quenching coefficient, this causes the quenching rate to go up when it constitutes more of the mixture. The theoretical values also show the same trend, but more linear decrease.

The gas temperatures for the 10%, 20% and pure O_2 cases were taken from the gas temperature analysis in chapter 5. The gas temperatures used for 10% and 20% oxygen content was 850 K determined from the 20% O_2, 20 Pa, 600 W condition. On the other hand, the pure oxygen gas temperature was 1400 K at the corresponding power and pressure. While the actual gas temperature values for these intermediate cases were not measured, it was presumed that it would be a value between 850-1400 K. The theoretical lifetimes shown in figure 4.10b for these cases use the pure oxygen gas temperature and could explain why there is only a gradual decrease since the effective lifetime is then only dependent on the molecular

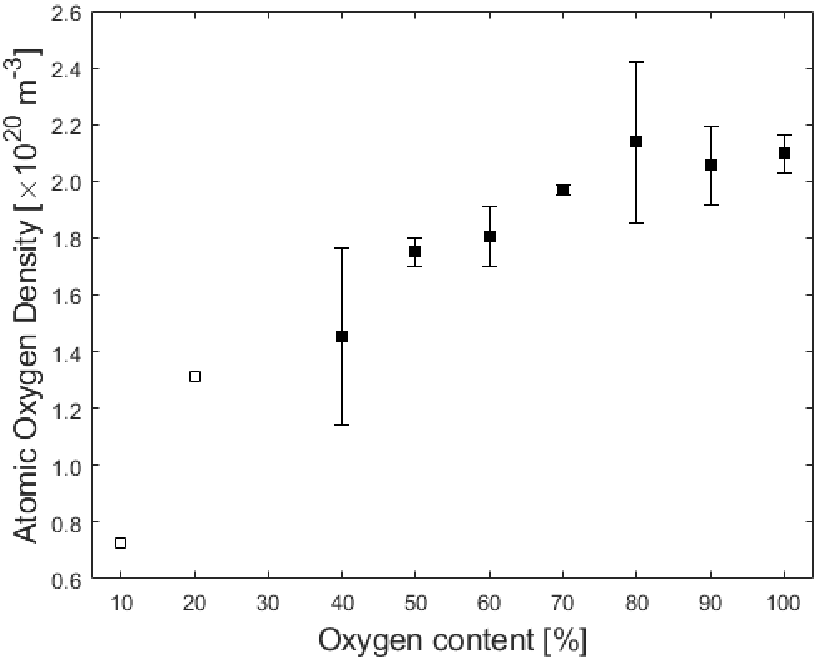

(a)

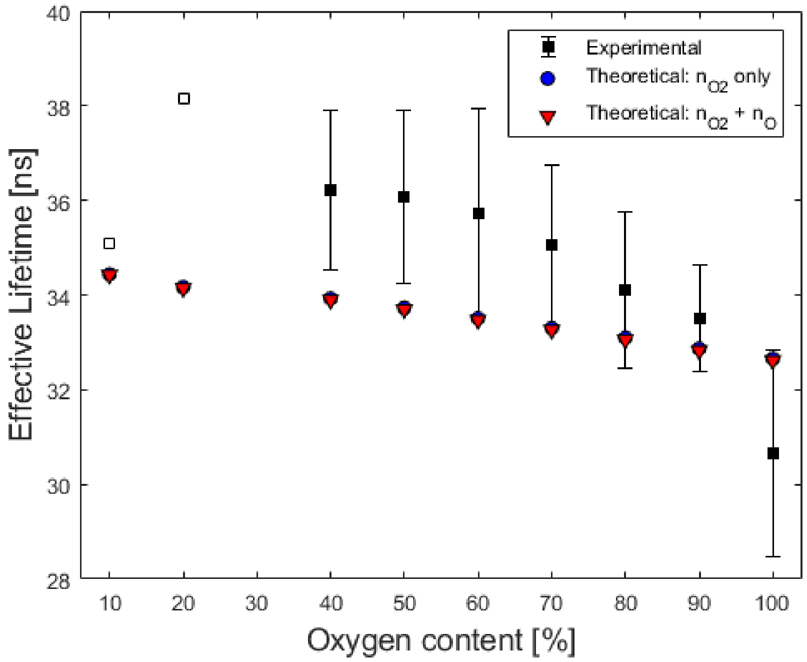

(b)

Figure 4.10: Measured parameters of a) atomic oxygen densities and b) effective lifetimes at 500 W, 20 Pa with varying O_2. Where available, repeated points are averaged, and filled points indicate that at least three separate measurements have been taken. Atomic oxygen density increases with oxygen content. However, it is not a proportional increase for oxygen contents as high as 40%. There is minimal difference in overall density at 80% compared with 100%. The effective lifetime values of $O(3p^3P)$ decrease with increasing oxygen content, which is likely due to higher quenching from increased amount of molecular O_2.

oxygen density. On the other hand, using the lower gas temperature value gave slightly smaller effective lifetimes, but less than 2% difference. Consequently, the effective lifetimes are weakly dependent on the gas temperature and are affected greatly by the quenching partner density. This is further reinforced by the fact that the quenching rate is directly proportional to $n_q(\mathrm{O_2})$ and $1/\sqrt{T_g}$, with the latter having a reduced contribution as T_g increases due to reduced collisionality.

4.2 Summary

TALIF has been carried out to study the production of atomic oxygen in the early afterglow of a pulsed, inductively coupled plasma in the high power regime. This well-established technique was used to investigate the effects of varying power, pressure and admixture on this parameter. The absolute atomic oxygen densities were obtained via noble gas calibration of the fluorescence signal strength with xenon. Consequently, these results aim to benchmark the alternative optical-based technique, ERA.

Control cases using pure oxygen were first studied to explore the effects of changing input parameters. It was found that an increase in both applied rf power, and pressure had a positive influence on the production of atomic oxygen. For each pressure case at 10 and 20 Pa, the number density gently rose by 11% and 13% from 500-1000 W, respectively. This was due to the greater amount of energy supplied per pulse and thus enabling more dissociation. On the other hand, higher pressures at 600 W generated a near proportional response due to more molecular oxygen available to dissociate. Since the measurements were taken as close to the end of the pulse, these trends were corroborated and agreed with cw plasma, pure oxygen cases reported in literature.

Then, the experiments were repeated for varying admixtures of helium and oxygen. The change in composition in tandem with inert properties of noble gases, in this case helium, can control the amount of reactive species while maintaining desired operating pressure and avoiding additional unwanted chemistry. The trends in atomic oxygen densities followed the pure oxygen cases with power and pressure. Moreover, transitioning from mostly helium to pure oxygen led to more atomic oxygen species, with marked increase going from 10% to 20% $\mathrm{O_2}$. Again, this was due to more molecular oxygen available to dissociate. Yet, increasing the proportion of oxygen until saturation yielded diminishing returns since the energy is distributed between more molecular species and thereby reducing the amount of dissociation. It was also affected by the trade-off of having more oxygen to dissociate versus lower electron temperatures and reducing the dissociation rate as it transitioned to pure oxygen.

The study of the effective lifetimes were also discussed as these were necessary in determining the atomic oxygen densities. The effective lifetimes were greatly affected by the amount of molecular oxygen in the system as it has a high quenching coefficient - there are more energy loss processes with this species. The study of how it was affected by changing input parameters gave a qualitative insight into the amount of quenching there may be. This can be used to further improve the analysis of optical emission based measurements where quenching can reduce the perceived amount of light from a particular species, in this case, atomic oxygen.

Ultimately, the purpose of these measurements was to obtain both qualitative and quantitative data of atomic oxygen densities in a high-power, pulsed inductively coupled plasma containing oxygen. On one hand, similar measurements have been carried out in literature and results from these could be extrapolated instead for benchmarking. On the other, slight variations, such as the plasma source configuration or higher pressures, make it difficult to know for certain whether trends continue to be valid. As such, by performing the measurements over the same range of conditions and on the same GEC reactor, more direct comparison can be made on the accuracy of ERA. Consequently, the TALIF measurements themselves have been compared with reported literature to verify correlation and expected orders of magnitude.

Chapter 5

Gas temperature measurements in the afterglow through analysis of atomic oxygen sub-level populations

In the previous chapter, TALIF was used to determine the atomic oxygen densities and effective lifetimes in the afterglow of the plasma pulse. However, these measurements only probed atoms in the $O(^3P_2)$ *energy level which is typically the most populous of the three ground state sub-levels. The total number density of the ground state can be determined if the population of the other two sub-levels are known. Alternatively, if these population densities are in thermal equilibrium, the Boltzmann relationship can be used to calculate total* n_O *through assumption of a gas temperature. However, this value may not be the same for all plasma conditions, and can change with power [92] and pressure [27, 29, 30, 90].*

This chapter investigates the determination of gas temperatures in the afterglow of the high-powered pulse of an ICP through the comparison of the relative fluorescence intensities from each ground state sub-level. Each of the $O(^3P_J)$ *states were excited by the laser and the emission behaviour in the afterglow was studied in detail. This was carried out under similar experimental conditions as the previous chapter where gas temperatures were needed for calculation of parameters such as theoretical lifetime and dissociation degree. Moreover, the phenomenon where the signal rose slightly shortly after the end of the pulse is investigated.*

5.1 Temporal profile of atomic oxygen ^3P_J states

The evolution of the fine-structure distribution is studied with the aim of inferring a gas temperature. In the afterglow, production of atomic oxygen will have ceased. Thus, the relative proportions in each sub-level will re-distribute if there are enough collisions between themselves and the background gas. These sub-levels have a defined energy difference that is normally expressed as a wavenumber, but can be converted to an equivalent thermal energy. Therefore, if a neutral particle in the plasma has sufficient kinetic energy during a collision, then the upper levels of ground state atomic oxygen can be populated through energy transfer. As a result, the relative population distribution will reflect the mean kinetic energy of the neutral particles. Consequently, this will be referred to as the overall gas temperature, T_g.

Earlier, the atomic oxygen density was seen to decay quickly on a millisecond timescale. Yet, a few hundred microseconds after the end of the plasma pulse, the $O(^3P_2)$ sub-level showed a peak increase in counts. This occurred consistently for all plasma conditions studied and at more or less the same time in the afterglow. Thus, by varying the laser trigger time from a reference point, T_0, the fluorescence response in the afterglow was monitored and is discussed here.

Tuning the laser excitation wavelength allowed for the resulting fluorescence to originate from one of the specific level of the $O(^3P_J)$ states. Figure 5.1 show that after pumping down to very low pressures, the $O(^3P_2)$ sub-level in the left-hand figure does have a peak in normalised intensity. Although, it is not definite since it is within the standard deviations of its neighbouring time values. Nonetheless, all three sub-levels show decay with time. The right-hand figure shows the relative branching ratios between the sub-levels, with $O(^3P_2)$ having the most. Furthermore, the ratio is roughly 5:3:1 at the start, and the $O(^3P_2)$ tending towards higher values in the afterglow.

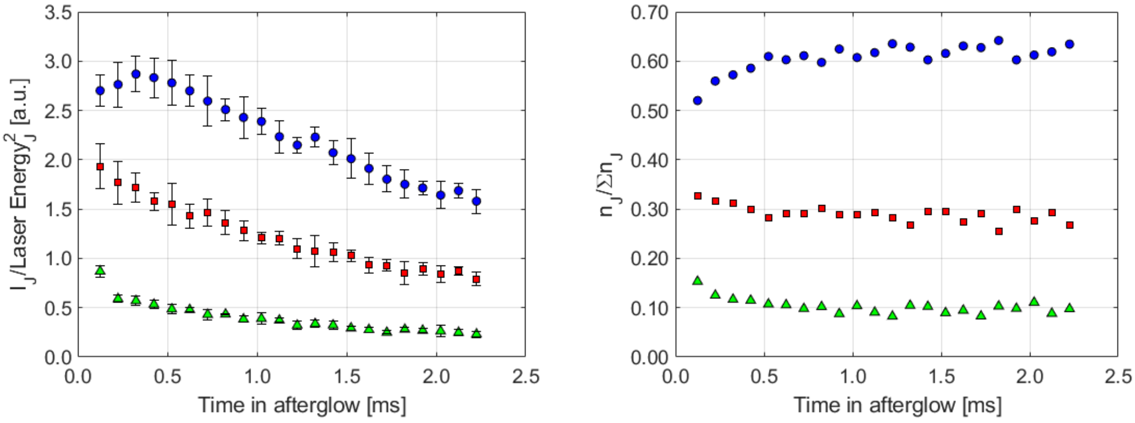

(a) (b)

Figure 5.1: Temporal evolution of a) the ground state atomic oxygen sub-levels and b) ground state fractions in He-10%O_2-2%Ar, 20 Pa at 600 W. J = 2,1,0 represented by ●, ■ and ▲, respectively. A peak in the $O(^3P_2)$ level is seen. Moreover, the Boltzmann fractions are close to the statistical values of 5:3:1.

Similarly for the case with just using the rotary pump, figure 5.2 shows that the background subtracted signal for all three sub-levels decreased in the afterglow in pure oxygen at 20 Pa, 600 W. This was expected as atomic oxygen density is lost to processes such as recombination. However, especially for the case of $O(^3P_2)$ population, there was a brief observed increase in fluorescence. Consequently, this temporal profile influenced the specific laser trigger time used in the TALIF measurements covered in the previous sections. Since the technique probes the $O(^3P_2)$ level, increasing the signal-to-noise as much as possible was highly desirable.

The cause for this is unlikely to be due to additional atomic oxygen production through electron processes. Earlier, plasma emission decayed within a few tens of microseconds after the plasma power was turned off, and in turn the loss of high-energy electrons that could provide dissociative excitation. Furthermore, these laser measurements were a hundred microseconds onwards from the end of plasma pulse which is well after any surviving energetic electrons. It is also unlikely to be due to a delayed response from the rf generator since any delay in power would also contribute to the other levels as well.

Currently, the behaviour of these other sub-levels was unable to be verified against other works. Similar investigation of atomic oxygen densities in the afterglow have been carried out: Veis and Cernogora used a double-pulse in a DC discharge [44] whereas Peverall et al. [87] used cavity ringdown spectroscopy (CRDS) in an ICP. Both approaches saw a decrease in n_O in the afterglow on a millisecond timescale. Nonetheless, both lacked microsecond resolution to corroborate the slight increase noted here, especially the CRDS approach as it can also distinguish between $O(^3P_2)$ and $O(^3P_1)$.

The bottom-right sub-figure in figures 5.2 and 5.3 show each $O(^3P_J)$ intensity normalised to the maximum value of its own respective level for that plasma condition. It shows that the highest energy sub-level $O(^3P_0)$ decayed the most rapidly, followed by $O(^3P_1)$ and lastly $O(^3P_2)$ with a relative slow decay rate. The reason for this particular order is due to redistribution of the population in each sub-level. As the gas cools, the highest sub-level relaxes to a lower state and can do so to either the $O(^3P_1)$ or $O(^3P_2)$. Likewise, $O(^3P_1)$ can relax to $O(^3P_2)$. As a result, the overall effect is the peak intensity of the lowest energy state and also explains the delay in decay compared to the other states by a couple of hundred microseconds. Afterwards, it stops seeing a net increase and loses its population as normal.

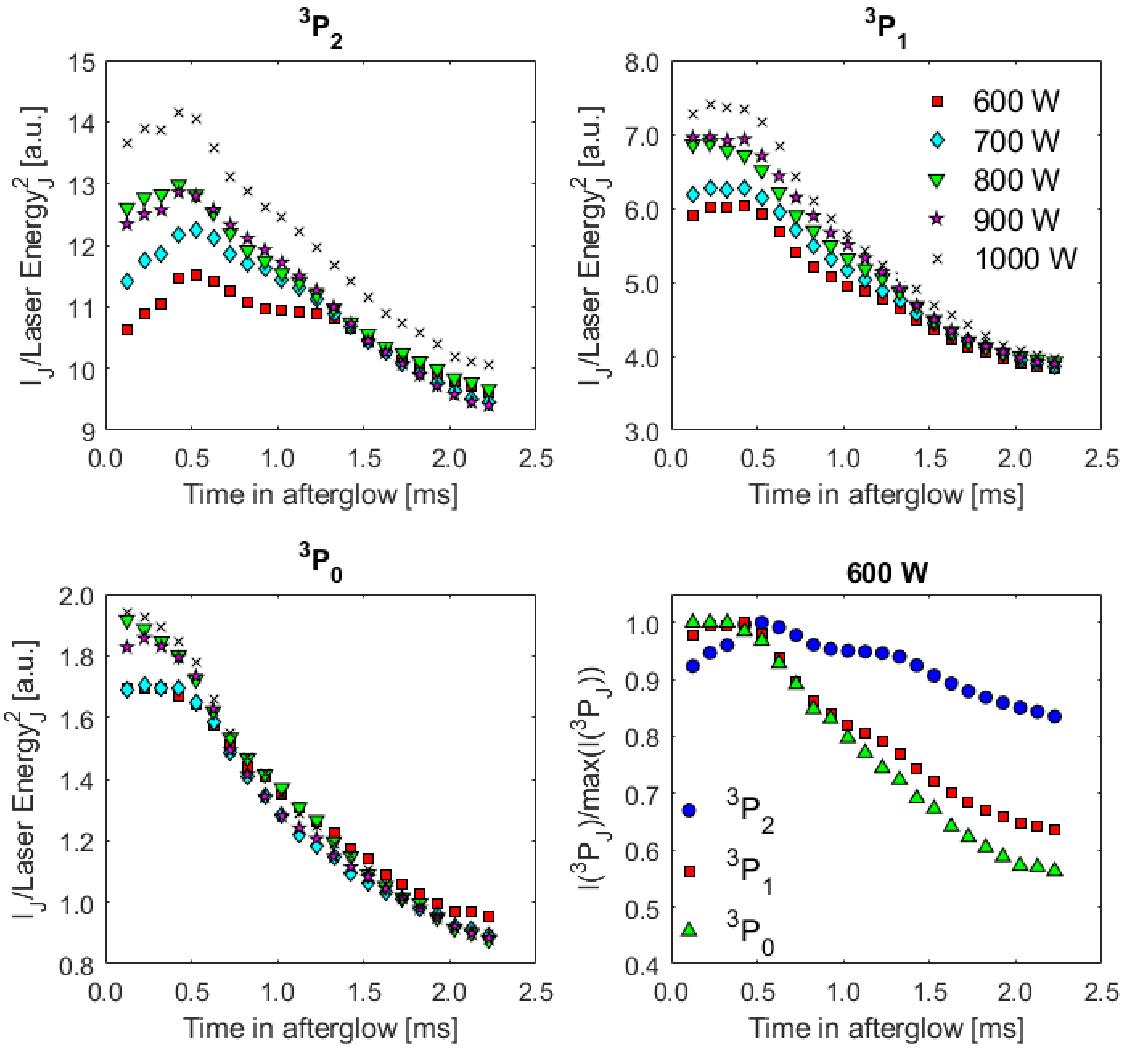

Figure 5.2: The time profile of $O(^3P_J)$ levels in pure oxygen with varying power. The relaxation into lower levels is inferred through the different loss rate of the fluorescence signal. In the bottom-right subfigure, each level is normalised to its maximum value for the 600 W case.

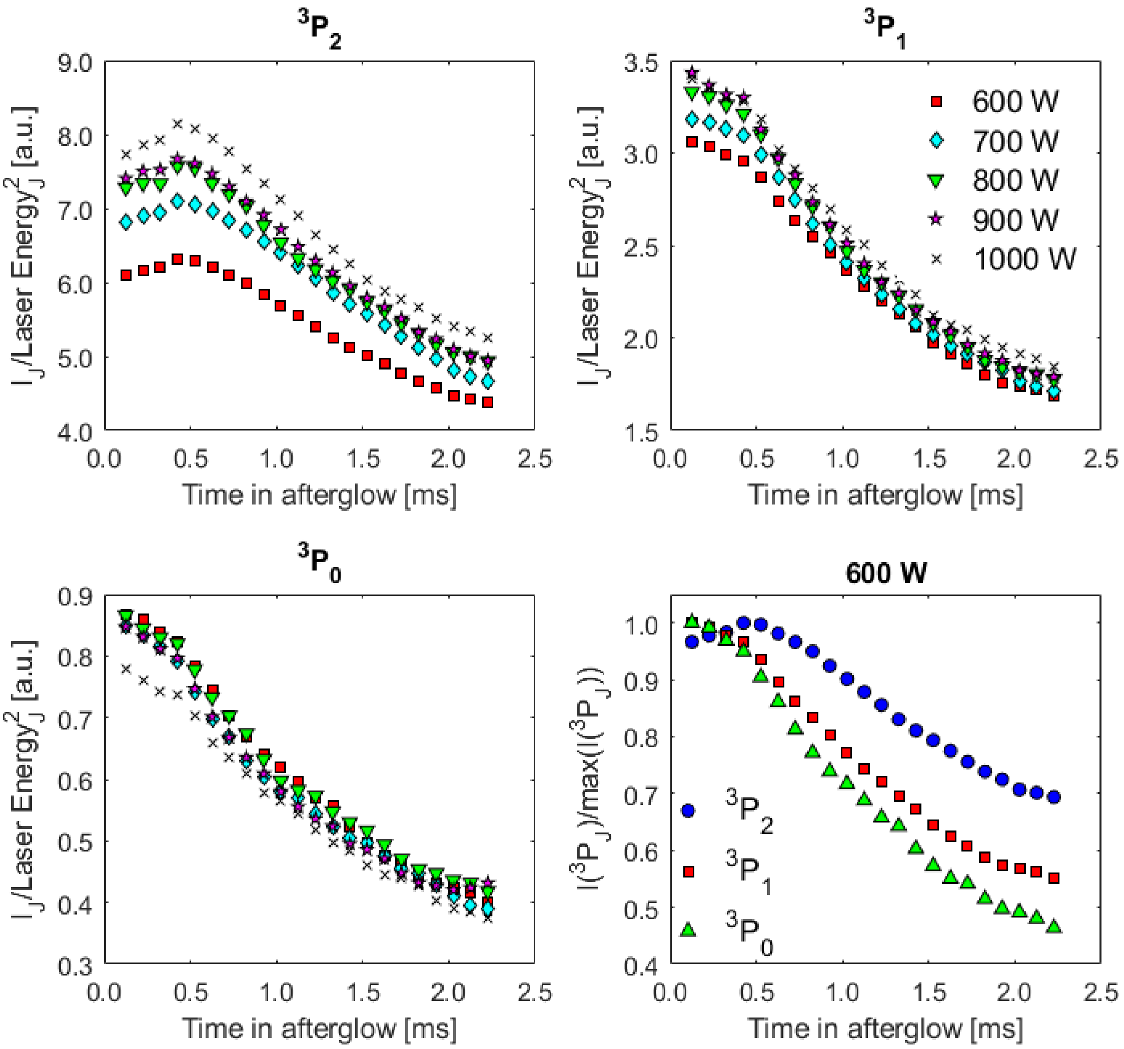

Figure 5.3: The time profile of $O(^3P_J)$ levels in He-20%O_2 with varying power. Similar trends were found in the helium-oxygen admixture as the pure oxygen case. In the bottom-right subfigure, each level is normalised to its maximum value for the 600 W case which highlights this phenomenon.

Alternatively, the ground state sub-levels could also be populated by the $O(3s^3S)$ state. As the $O(3s^3S)$ state relaxes, this transition emits photons at 130 nm wavelength which can only be observed under vacuum. The corresponding wavelengths to each sub-level are listed in table 5.1. The transition from the $O(3s^3S)$ to $O(^3P_2)$ has the highest Einstein coefficient. This can also be a source of contribution and also explains why there is a more pronounced peak of $O(^3P_2)$ than the others. However, the densities of these upper states are much smaller than even the $O(^1D)$ state and therefore unlikely to provide significant contribution [114].

λ [nm]	A_{ik} [s^{-1}]	Lower level, k	Upper level, i
130.2168	3.41e+08	$O(^3P_2)$	$O(3s^3S)$
130.4858	2.03e+08	$O(^3P_1)$	$O(3s^3S)$
130.6029	6.76e+07	$O(^3P_0)$	$O(3s^3S)$

Table 5.1: Transition strengths from the $O(3s^3S)$ level to the ground state.

Figures 5.4 - 5.6 show the mean counts of each sub-level for pure oxygen, He-20%O_2 and Ar-20%O_2, respectively for various pressures. Comparing pure oxygen with He-20%O_2, it is clear to see that all of the sub-levels are lower for the latter case. However, this is not completely the case for Ar-20%O_2. While at 15 and 20 Pa there are fewer counts in the argon mixture compared to pure oxygen, this is reversed at higher pressures from 25 Pa onwards. It is likely that argon has an impact on the number of ground state species. Consequently, high argon contents can affect the diagnostic measurements as seen when determining gas temperatures. In contrast to the other gas mixture cases, figure 5.6 shows a constant decrease of all levels in the afterglow i.e. there was no peaked value of $O(^3P_2)$ in the same observed timeframe.

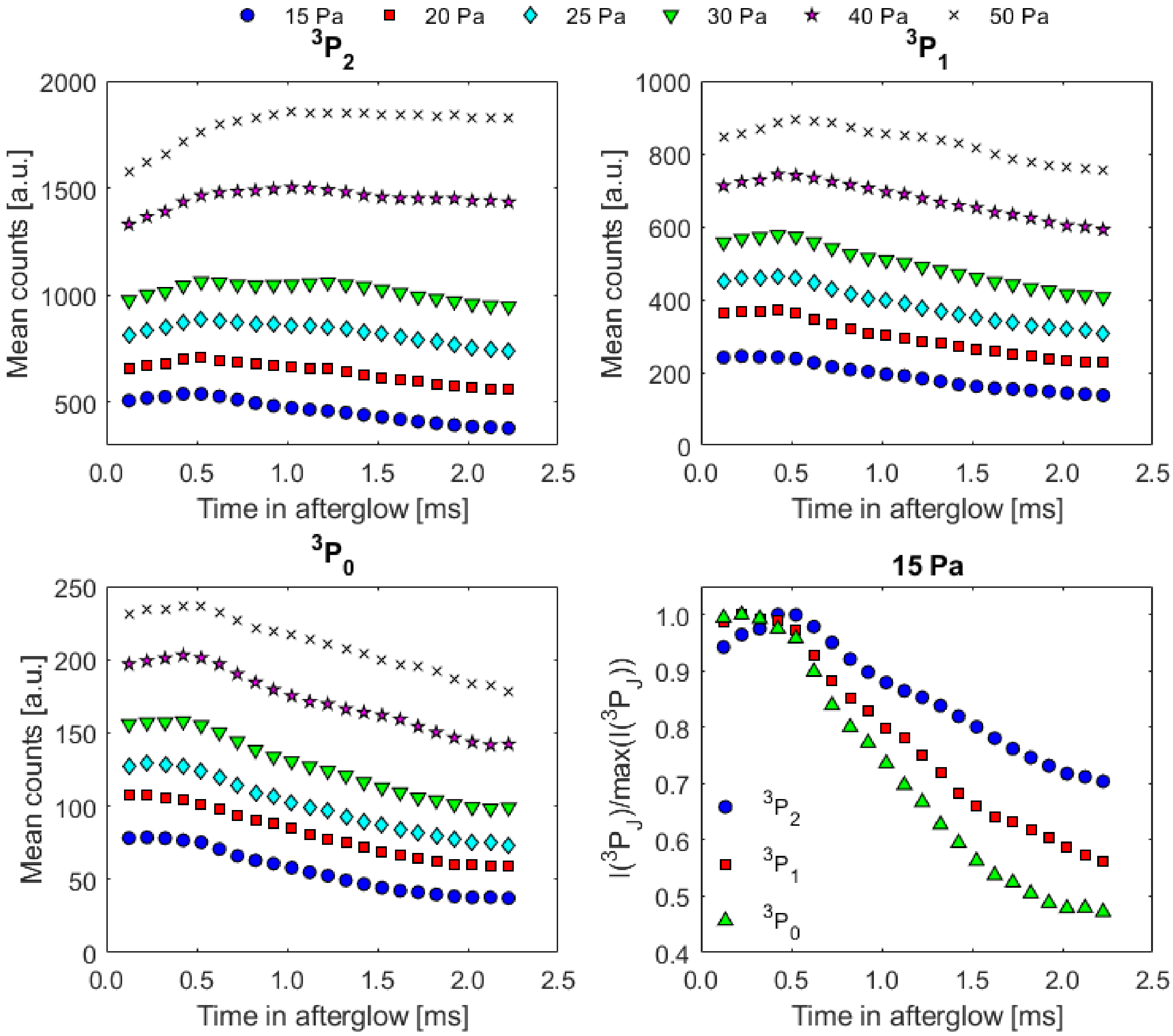

Figure 5.4: The time profile of $O(^3P_J)$ levels in pure O_2, 600 W with varying pressure.

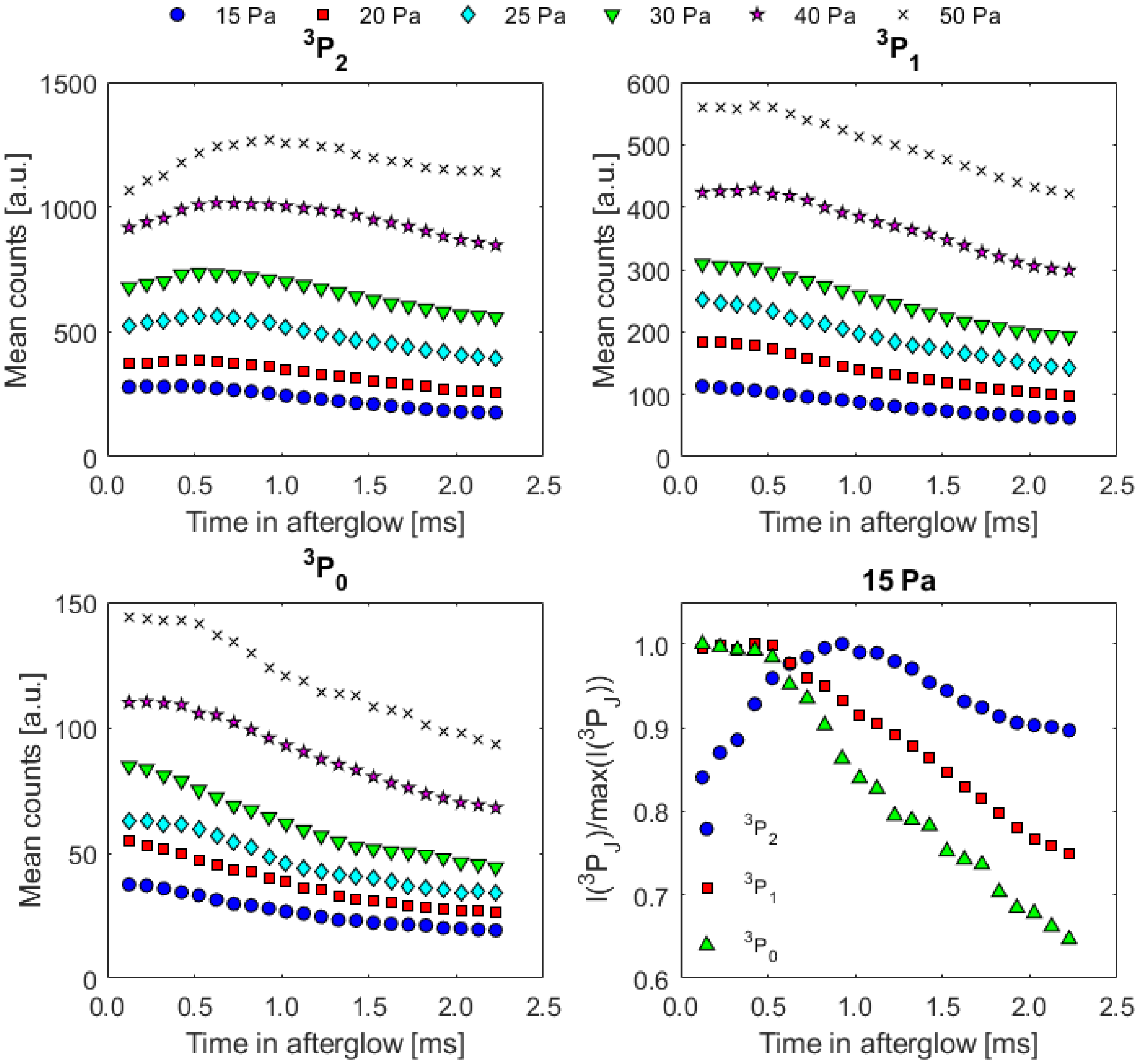

Figure 5.5: The time profile of $O(^3P_J)$ levels in He-20%O$_2$, 600 W with varying pressure.

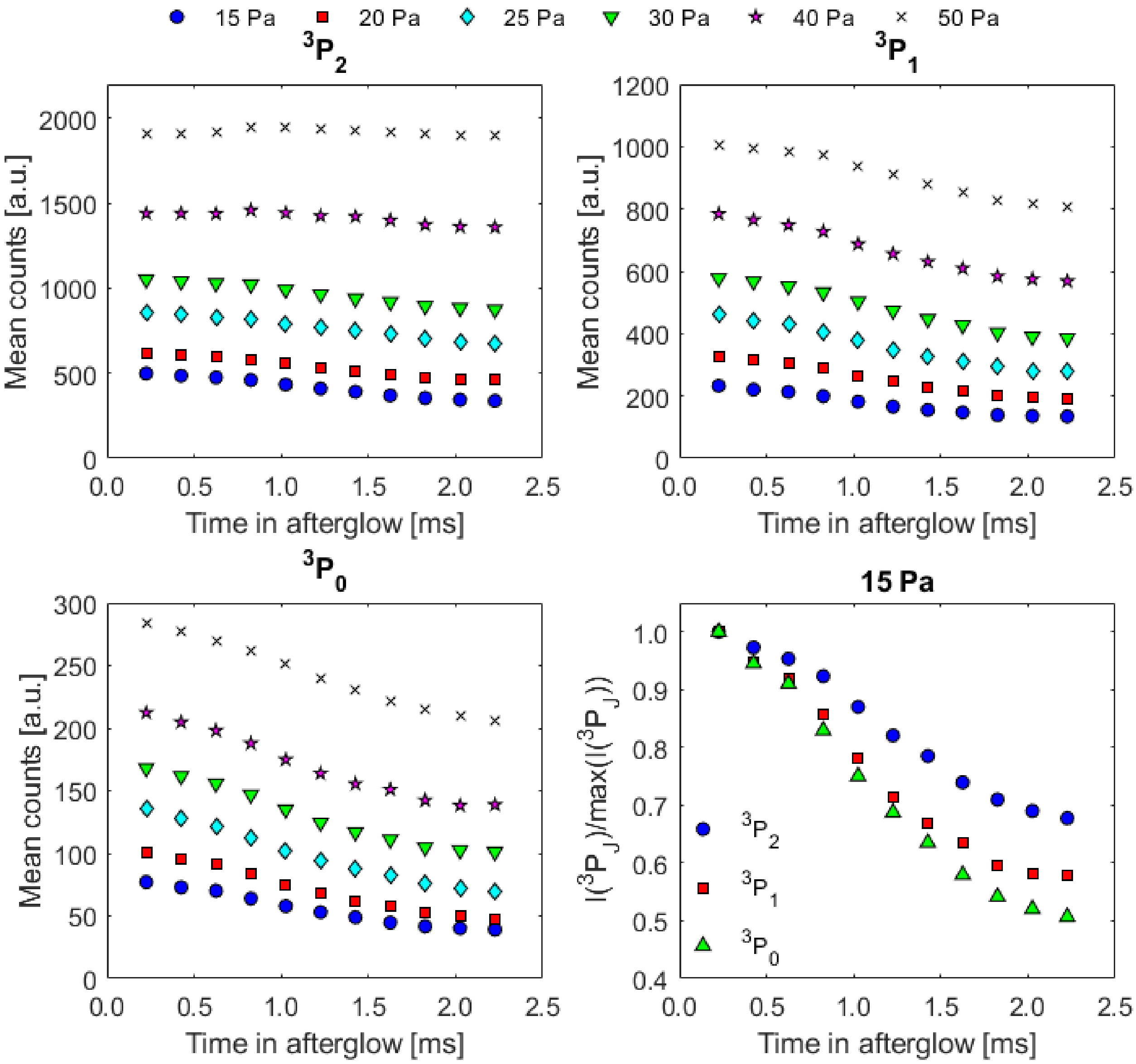

Figure 5.6: The time profile of $O(^3P_J)$ levels in Ar-20%O_2, 600 W with varying pressure. At higher pressures, the perceived counts was as much as the pure O_2 case and thus can have an influence on the gas temperature measurements.

Figure 5.7 compares the effect of this peak signal position of $O(^3P_2)$ with power and pressure. The signal was normalised against its own maximum value for each input parameter. The position does not move with power, but does so with pressure. The signal decay rate can be explained by the diffusion coefficient, equation (5.1) of atomic oxygen in molecular oxygen from [62].

$$D = \frac{3}{8n_{O2}\sigma_{12}^2}\sqrt{\frac{k_B T_g}{2\pi}\left(\frac{1}{m_O}+\frac{1}{m_{O2}}\right)} \tag{5.1}$$

Where n_{O2} is the density of molecular oxygen; $\sigma_{12} = (\sigma_1 + \sigma_2)/2$ where σ_1 and σ_2 are the Lennard Jones collision cross-sections for atomic and molecular oxygen, and m_O and m_{O2} are the masses of atomic oxygen and molecular oxygen, respectively. The signal decreases faster at higher powers; if it is expected that gas temperatures increase with applied power, it will cause higher D to the walls, which is what is observed. Conversely, atomic oxygen loss is seen to be slowed with increased pressure. Again, higher amounts of molecular oxygen is present and reduces D due to n_{O2} being in the denominator of the equation. The exact same trends are observed in the He-20%O_2 mixture as well as the other sub-levels.

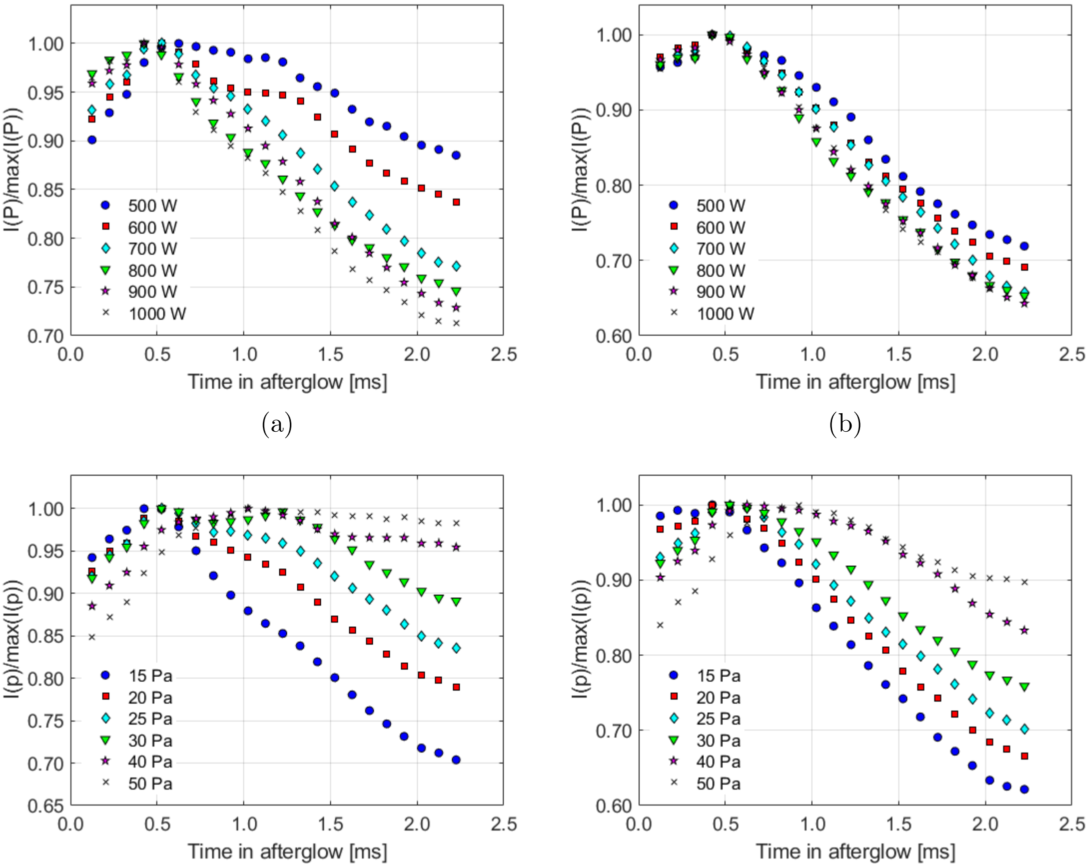

(a) (b)

(c) (d)

Figure 5.7: The time profile of $O(^3P_2)$ for a) pure O_2, varying power, b) He-20%O_2, varying power, c) pure O_2, varying pressure, and d) He-20%O_2, varying pressure. At each power or pressure, the fluorescence signal was normalised against its maximum value. The peak signal position does not change with power, but progresses with pressure and is likely due to diffusion of bulk atomic oxygen from the plasma core to the walls. The varying power cases were at 20 Pa whereas the varying pressures were at 600 W.

One other process that can contribute to generation of atomic oxygen species in the afterglow could be due to mutual neutralisation of atomic oxygen ions. Ishikawa et al. [71] saw that there was a relationship between the emission of both oxygen emission at 777 and 844 nm due to equation (5.2) where two oppositely charged atomic oxygen ions produce an excited and ground state species, with the process likely to produce an excited state due to the potential energies before the reaction.

$$O^{+} + O^{-} \rightarrow O^{*} + O \tag{5.2}$$

However, high density plasma sources have typical plasma densities of $10^{17} - 10^{18}\mathrm{m}^{-3}$ [1], which is a couple of orders of magnitude less than the neutral densities in the inductive mode. Therefore, it is unlikely that contribution through mutual neutralization is significant enough.

Photolysis studies of oxygen containing molecules have had a particular emphasis on the relative branching of $O(^3P_J)$. Huang and Gordon also suggested that the relative splitting depended on the rapidity of dissociation, as well as specific dissociation path. The latter can result in preferential population, but was not seen here [152].

Figure 5.8 replots the 20 Pa, 600 W measurements for the different gas mixtures for better comparison with Abe et al. [153]. The evolution of these ratios followed the same trends; not only does the J = 2 ratio increase with time while the J = 1,0 levels decrease, both see saddle points shortly after the dissociation process. Moreover, the relative values of these ratios are comparable. One key difference is that their measurements thermalise to a Boltzmann by 10 µs whereas those presented here have not yet reached it. They ascribed the near-statistical ratio values was due to high effective translational temperatures from the generation of hot $O(^3P_J)$ atoms and fast intramultiplet relaxation [153]. If measurements taken earlier in the afterglow were to match their results, then this can be corroborated.

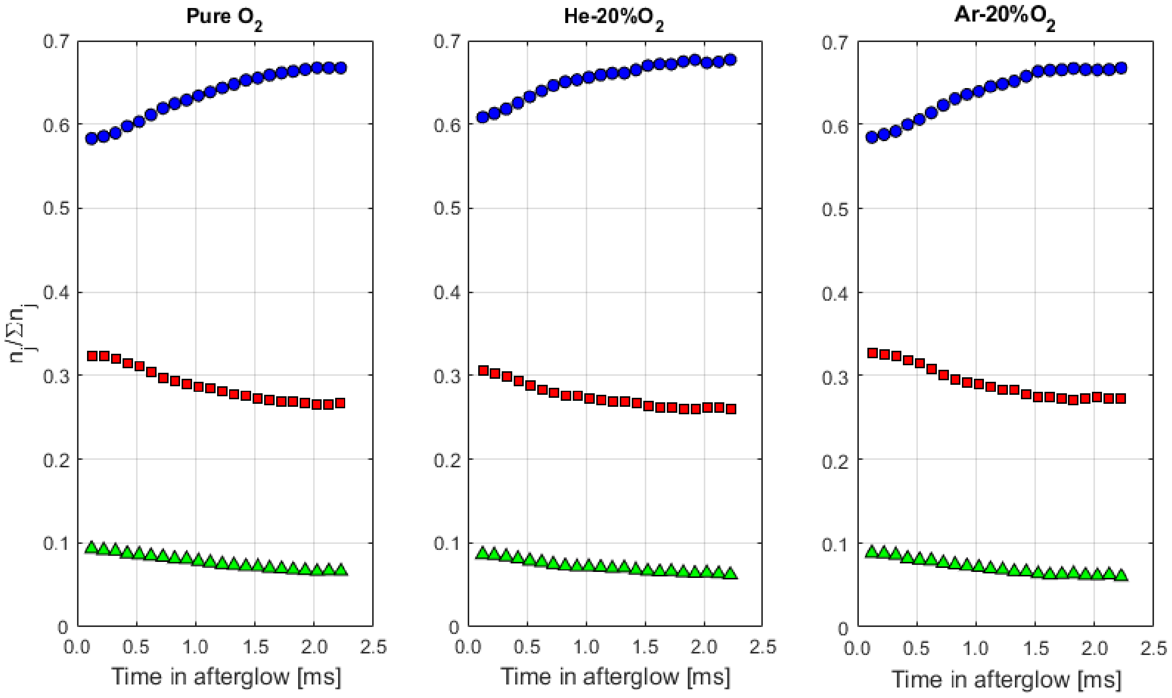

Figure 5.8: The population ratios as function of time in the afterglow in the style of [153] for comparison at 20 Pa, 600 W. The ratios are close to the statistical degeneracy values early on for all mixtures, 5:3:1. While it does not reach it within the observed timescale here, these tend towards Boltzmann distribution values similarly to [153]. J = 2,1,0 represented by ●, ■ and ▲, respectively.

Figure 5.9 is another reinterpretation of the branching between levels to directly compare with Matsumi et al. The increase in $O(^3P_2)$ was due to de-excitation of $O(^1D)$, and this contribution was also mentioned earlier by [53]. Matsumi et al. also saw the population reach a Boltzmann distribution, again on a short timescale of a few tens of microseconds [154]. This difference could be related to the quantity of atomic oxygen in the system as both [153] and [154] produce $O(^3P_J)$ through photodissociation of a few mTorr of SO_2 and NO_2, respectively. As there is much more hot atomic oxygen produced in this work, it takes longer to thermalise. Consequently, the Boltzmann fraction is not valid, but instead the total number density of $O(^3P)$ can be calculated from the probed $O(^3P_2)$ density and the statistical proportions if taken at the same time in the afterglow when this occurs.

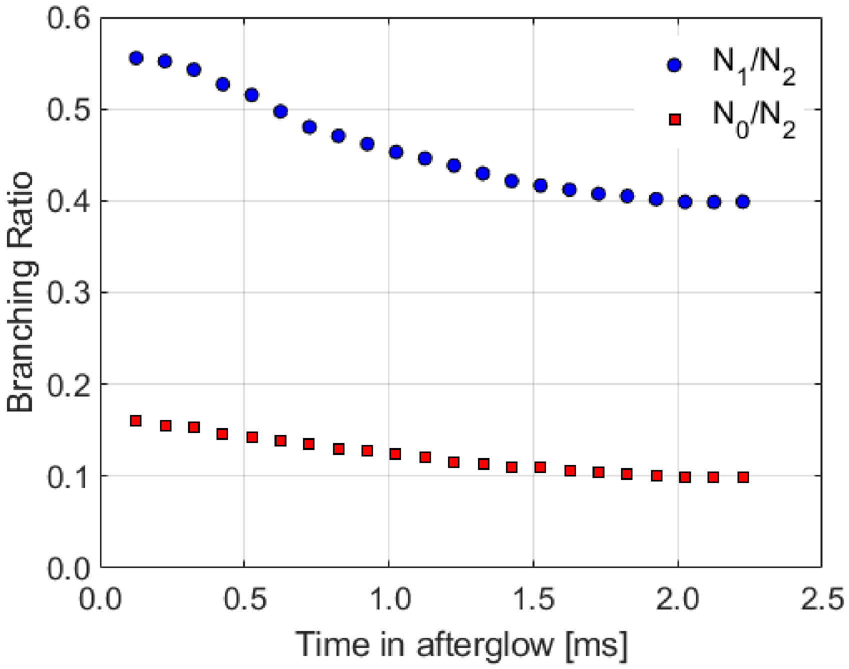

Figure 5.9: The population branching ratios in the style of [154] for comparison for pure O_2, 20 Pa, 600 W. The relative values and temporal evolution were consistent with the cited work.

5.2 Gas temperatures using Boltzmann plots

The gas temperature can be determined from the slope of a Boltzmann plot of the normalised fluorescence intensities at peak excitation wavelength against the energy level of each sub-level. This was done for select times in the afterglow, including the earliest, peak $O(^3P_2)$, and latest measurement as seen in figure 5.10. The lowest two states peak at 425 µs; all three decrease in value from this point onwards at different rates, signifying cooling and atomic oxygen loss.

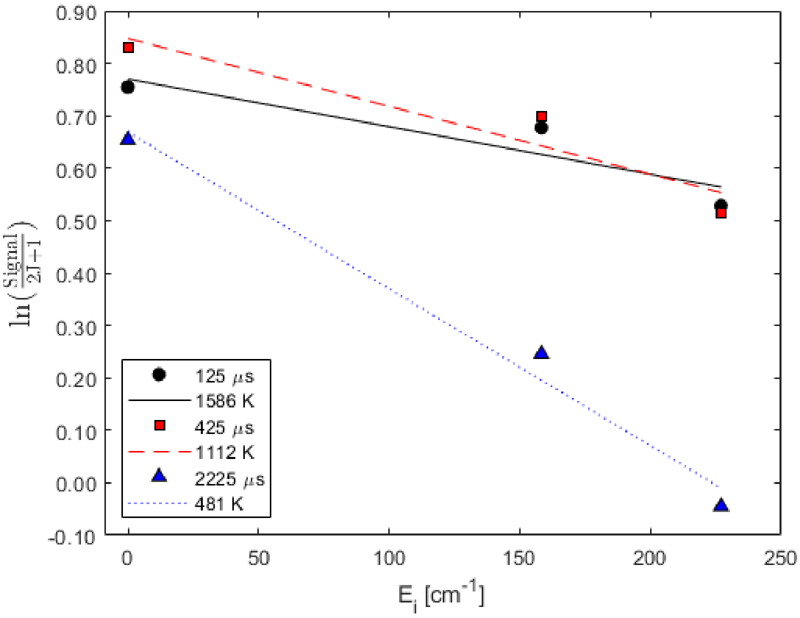

Figure 5.10: The gas temperatures of pure oxygen at 20 Pa, 600 W determined using the slope of a Boltzmann plot. The time refers to how far in the afterglow that T_g was measured, which is observed to cool quickly.

The $O(^3P_1)$ sub-level tended to lie above the best fit lines and was the same as [91], whereas it was below for [60]. The former probed the pulsed plasma jet in situ, in contrast to the latter probing the atomic species after it was transported from the site of generation, allowing for thermalisation. Thus, it is surmised that the gas is not in thermal equilibrium in the short timescales investigated when oxygen is freshly dissociated. Yet, both papers determined temperatures of 300 K in the atmospheric plasma jets with similar He-O_2 admixtures - this may be due to sufficient cooling by the helium gas.

The measured temperature shows dependence if the fitted slope uses all three states, or just the two most populated as seen in figure 5.11. The gas temperature was 1590 K if all three points were used in the fitting whereas it was nearly twice this at 2950 K using only the two. In similar plasma conditions i.e. low-pressure, high-oxygen content oxygen, pulsed ICP, translational gas temperatures of around 1300 K were obtained by [92].

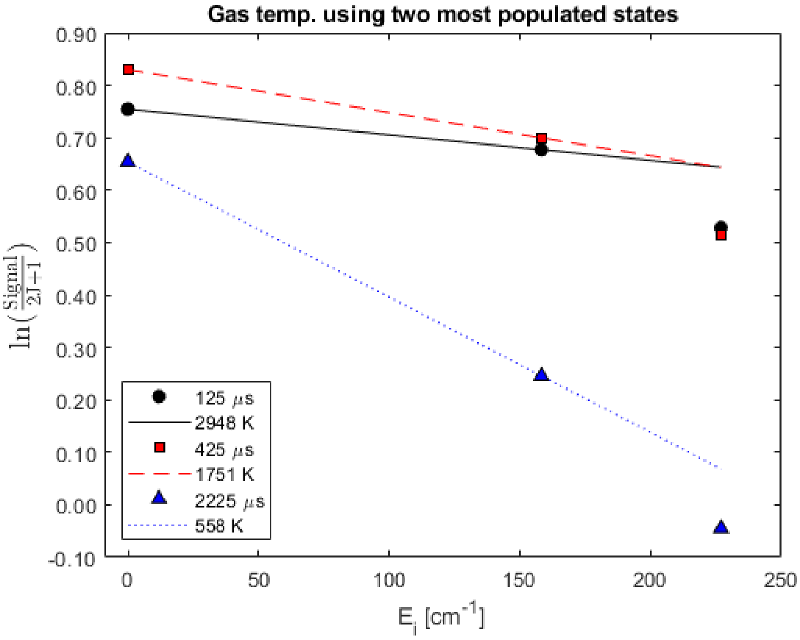

Figure 5.11: The gas temperatures of pure oxygen at 20 Pa, 600 W determined via the slope of a Boltzmann plot fitted to the two most populated states. This gives higher gas temperatures than using all three data points as the fitting is no longer affected by the weak fluorescence signal from the $O(^3P_0)$ which has low signal-to-noise.

Due to the drastically different values from fitting either all three or only two points, another set of repeated measurements were taken in pure oxygen at 20 Pa, 600 W. This was to ensure that there was no dependence on the laser performance or possible increased background noise over the course of the experiment. As such, several sets were taken in varying order. For example, one set would have the laser tuned to excite $O(^3P_2)$, $O(^3P_1)$ and $O(^3P_0)$, then another set $O(^3P_1)$, $O(^3P_0)$ and $O(^3P_2)$ etc. This was done for all possible arrangements. However, there was no energy feedback control available for these, so the variable attenuator was set at a fixed position for all three and the energies recorded in every run. The background was also temporally recorded to check whether there was any rise in noise between each set. The mean background value was subtracted from the raw fluorescence of each measurement at each corresponding time point.

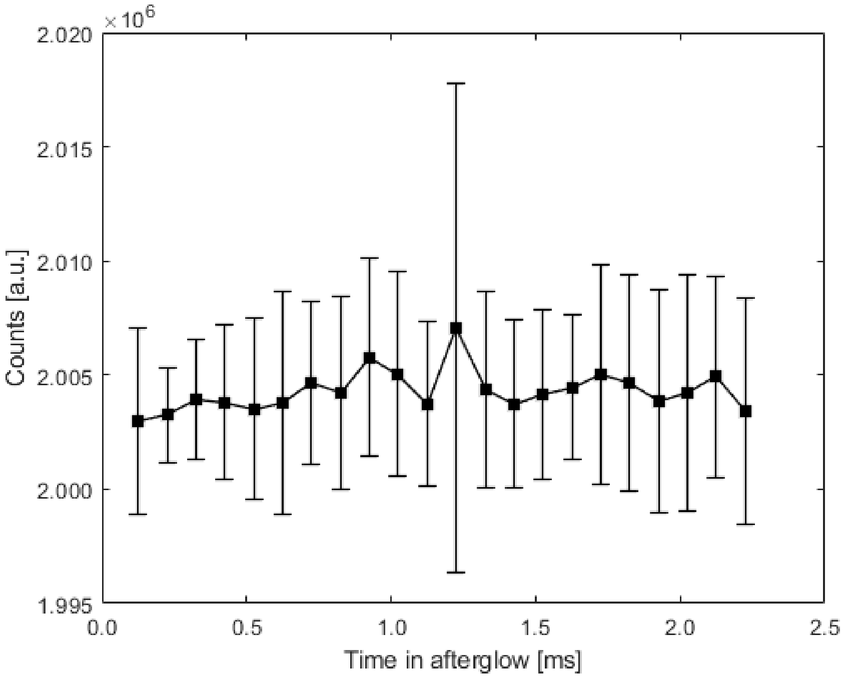

Figure 5.12: Observed background counts in afterglow. Over the course of the experiment, the background value remained largely the same.

Figure 5.12 shows that during the course of the experiment, the background signal did not change drastically. It was important to check this because the highest energy state returns the lowest signal, and so would be most susceptible to background subtraction. Hence the reason that the order was changed each time in each set of measurements. Nonetheless, there was minimal variation.

Again, similar trends as before were observed regarding the population state sub-levels when plotted on a Boltzmann plot. However, as the laser input energies were also recorded for each set, it was found that there was a strong correlation whether the $O(^3P_1)$ level sat above or below the best fit line for these measurements: if it was less than the input energy of the $O(^3P_0)$ then it sat below and vice-versa. Regardless, there was little correlation between placements that gave high or low T_g.

Figure 5.13 shows the average gas temperatures determined from the Boltzmann plots at this repeated condition. One set of measurements returned values that were an order of magnitude higher than the rest of the results, with the earliest point giving temperatures over 20,000 K. These were considered outliers and subsequently omitted from the averaging process. Aside from this, the gas temperatures show a constant decrease. The earliest temperature assumed to be synonymous with that during the on-time of the plasma pulse is comparable to [92] albeit a lot more variable 960 ± 320 K. It cools rapidly within a couple of milliseconds in the afterglow, and the uncertainty also shrinks to 387 ± 56 K which indicates it is reaching room temperature values.

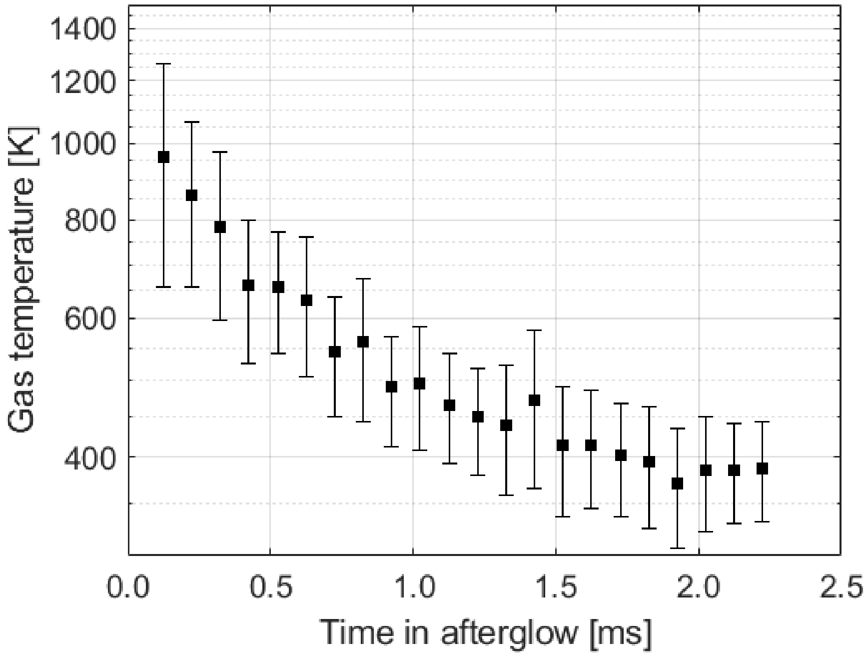

Figure 5.13: Averaged gas temperature: pure oxygen, 20 Pa, 600 W. The excitation of each sub-level was taken in alternating order to check that T_g determined via Boltzmann plot was independent of laser performance when changing excitation wavelength. The gas temperature decreases from approximately 1000 K to 400 K. This is cooler than previously observed, highlighting the sensitivity of the measurements.

Again, impurities had little impact on the measurements: in figure 5.14, the gas temperature profile showed rapid decay, being hotter closer to the end of the plasma pulse and cooling towards a stable temperature of around 400 K for He-10%O_2 at 20 Pa, 600 W. Three sets of measurements were made at this condition, with the order of the excitation wavelength varied to ensure independence of input. Thus, the errorbars are from the mean and standard deviation from temperature derived from the fitted slopes of these Boltzmann plots. The errorbar at at 125 µs is smaller due an omitted data-point that had a negative value of T_g. Otherwise, the uncertainty decreased with time, and the temperature was also similar that determined when comparing the peak intensities before.

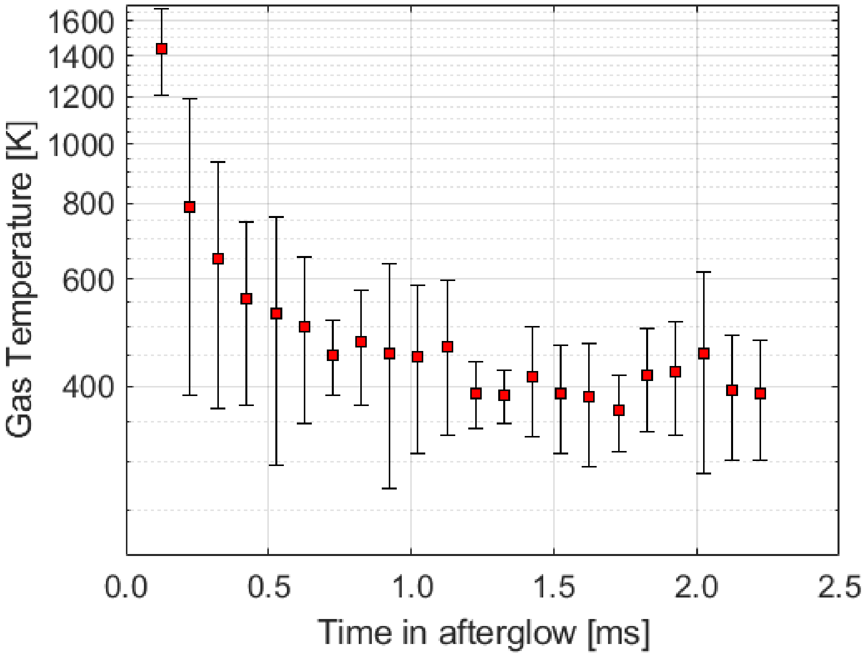

Figure 5.14: Gas temperatures at He-10%O_2-2%Ar, 20 Pa, 600 W after using the turbo-pump to evacuate the GEC. T_g shows the same decreasing trend and supports earlier determined values where it was not used.

5.3 Gas temperatures determined through comparison of intensity ratios to a Boltzmann fraction

The alternative method that was proposed to obtain the gas temperature was by comparing the ratio of an $O(^3P_J)$ level against the total $O(^3P)$ with an equivalent value deduced from the Boltzmann fraction. The motivation for this is whether a faster but still accurate determination of temperature is possible; if knowing both the measured intensity and laser energy can provide a look-up table for an equivalent gas temperature, then the need for plotting and fitting of a Boltzmann plot can be removed. Since the measured peak intensity may not be the true peak value given the limited resolution of the laser system, and also assumption that the line broadening is the same, the intensity ratios were compared between the full excitation profile against just the peak value.

These were taken at the same time as the TALIF measurements i.e. the laser was triggered at $T_0 + 10.2$ ms i.e. 425 µs in the afterglow. A Gaussian fit was then applied to each of these as it was assumed that the broadening profile by the laser was the most dominant.

Table 5.2 summarises the four different test cases, including pure oxygen at 20 Pa, 600 W as the control to compare with that determined using the Boltzmann plot previously. The other three changed a single parameter of either power, pressure or oxygen content. These were 1000 W, 50 Pa, and He-20%O_2 respectively. Due to better detected signal, the gas temperature values using the two most populated states i.e. $O(^3P_2)$ and $O(^3P_1)$ for comparison and also checking the self-consistency of results.

Condition	O_2 [%]	Pressure [Pa]	Power [W]	T_g $O(^3P_2)$ [K]	T_g $O(^3P_1)$ [K]
A	100	20	600	2760	2370
B	100	20	1000	4990	4140
C	100	50	600	5000	5000
D	20	20	600	803	714

Table 5.2: Gas temperatures calculated using the full integrated fluorescence over the central wavelengths and comparing the results using the $O(^3P_2)$ and $O(^3P_1)$ states against a theoretical Boltzmann fraction value.

Figure 5.15 shows the full excitation line profiles of pure oxygen at 20 Pa, 600 W for each of the ground state sub-levels. The experimental excitation wavelengths are plotted against the resulting fluorescence intensity. Then, a Gaussian fit was applied to each of these and the integrated area was normalised against the square of each respective laser energy. Thus, the gas temperature was determined using the Boltzmann fraction method.

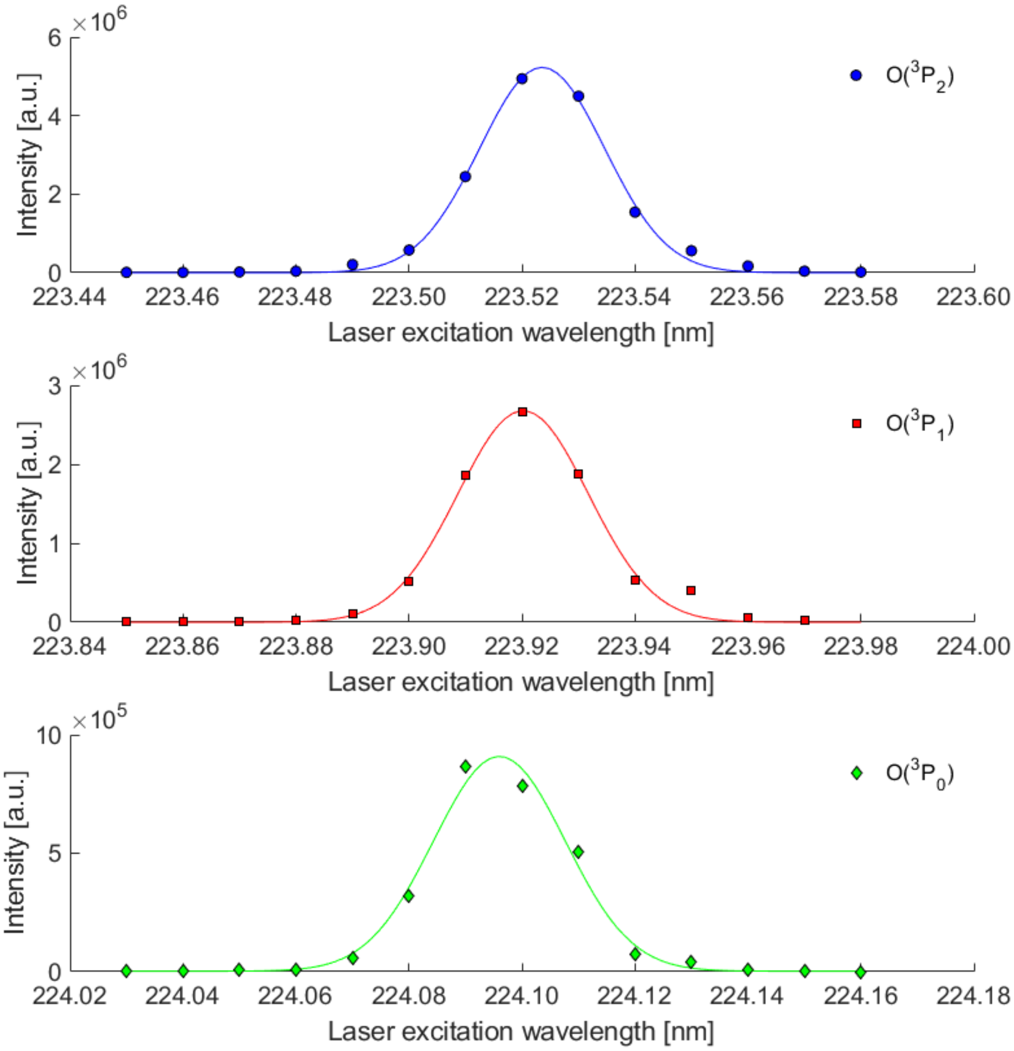

Figure 5.15: The full line profiles of the ground state sub-levels in pure oxygen at 20 Pa, 600 W.

Firstly, the experimental values that gave the most fluorescence did not always align with the fitted peak for the $O(^3P_2)$ state and has much more noticeable difference in maximum value, whereas the case of $O(^3P_1)$ has the least discrepancy. The Gaussian fit of the $O(^3P_0)$ state was the poorest for all cases, and especially evident in figure 5.16. This results in larger uncertainty in the integrated area of this highest energy level, which in turn affects the calculated gas temperature. Nevertheless, given it has the smallest population, it is unlikely to significantly alter the gas temperature. Moreover, the agreement between T_g from $O(^3P_2)$ and $O(^3P_1)$ suggests it is more sensitive to these populations.

The poor Gaussian fitting issue stemmed from the laser system not being capable of finely resolving the individual transitions to the upper state where the difference between the lowest and highest state is less than 1 cm^{-1}. In contrast, others were capable of achieving specific excitation between sub-levels [60, 91] and multiple Gaussian fits were used. These authors then determined the gas temperature using Boltzmann plots. This is much more refined and may give a clearer relationship between gas temperature and input parameters. Indeed, Booth et al. [90] was able to establish these through the width of the fine-structure excitation profiles in DC oxygen discharges, but again using a high-resolution laser.

As mentioned, table 5.2 shows the various conditions and resulting gas temperatures using the $O(^3P_2)$ and $O(^3P_1)$ states. Similar gas temperatures were found when using either of these states. Increasing applied power to 1000 W resulted in an increase in gas temperature of the control case from 2760 K up to 4990 K. However, in the case of 50 Pa, the analysis was not able to determine a gas temperature exactly since the stated value of 5000 K corresponded to the upper limit of the input gas temperatures. Lastly, there is a reduced gas temperature with helium addition down to 803 K. In comparison, the fits from Boltzmann plot of this same data returned 1400 and 850 K for conditions A and D, respectively. The control case was similar to the gas temperature value determined previously, but is half that of the Boltzmann fraction approach. Both methods returned similar, cooler values for the He-O_2 mixtures. In contrast, the B and C had gas temperatures excessively high (>10 000 K) or negative, which are highly unlikely.

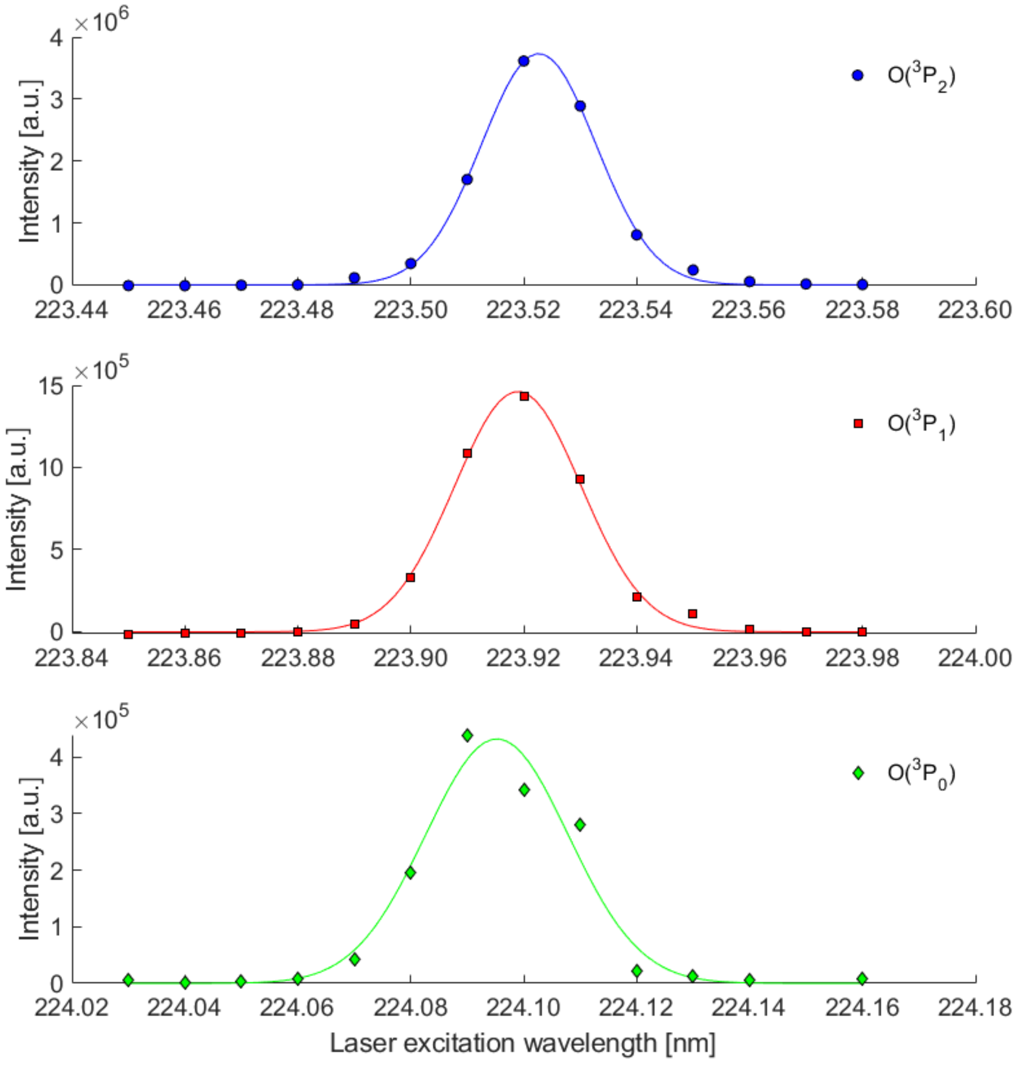

Figure 5.16: The full line profiles of the ground state sub-levels in He-20%O_2 at 20 Pa, 600 W. The Gaussian fit appears poorer for the $O(^3P_0)$ state.

Lastly, the gas temperatures determined using the full excitation line profile or if simply using the peak excitation is sufficient are compared in tables 5.3 and 5.4. Firstly, the ratios of $O(^3P_2)$ and $O(^3P_1)$ between the full excitation profiles via using the peak excitation values and the integrated area of the fitted Gaussian curves are close to the statistical degeneracies, 5:3:1, for the $O(^3P_J)$ multiplet. The ratios determined from the simple and full case differ by at most 5%, with the highest in both sets at condition D, the He-20%O_2. Consequently, taking ratios using the peak excitation gives practically the same values as using the full excitation profile.

On the other hand, the resulting gas temperature values have a much larger discrepancy. Comparing the full ratio of conditions A and B, going from 0.578 to 0.568 results in T_g of 2760 K and 4990 K. This is practically twice the temperature for nearly twice the applied power. On the other hand, the corresponding simple ratio of 0.580 and 0.583 instead resulted in a decrease in temperature from 2530 K to 2250 K with only a 300 K difference. Consequently, the derived gas temperature using this technique is highly sensitive to the ratio value and can introduce uncertainty. The worse condition appears to be condition B where using the $O(^3P_2)$ has a gas temperature difference of +122% between the full integrated profile and the simple case. Condition C was considered to not be applicable as the analysis was limited to gas temperature of 5000 K. The smallest differences was the control condition, A of less than 10% between the full and peak ratios.

Nevertheless, there is better agreement for two of the test conditions: A and D. At condition A, the simple case returned T_g as 2530 K whereas it was 2760 K using the full excitation profile. Likewise, for condition D, it was 601 K compared to 803 K. Both conditions only had a difference of 200 K. However, in the other two tests, B and C predicted much higher gas temperatures than the simple case. In fact, it reached the 5000 K asymptotal value i.e. the ratio of the intensity of the $O(^3P_J)$ against all of the sub-levels eventually corresponded to a finite T_g. Thus, it shows that the method loses sensitivity at these fluorescence ratios.

One argument for the high T_g is that in these cases there is a lot of atomic oxygen production owing to the higher applied power or pressure for B and C, respectively. This may be in part due to the thermal energy from the dissociation process causing oxygen atoms to be excited towards the higher levels. This can be inferred through the increase in the $O(^3P_1)$ ratio. Consequently, $O(^3P_2)$ ground state population is lowered, pushing the ratio to the asymptotal gas temperature values. As a result, this has a much more adverse effect

	$O(^3P_2)/\Sigma O(^3P_J)$			T_g [K]		
Condition	Simple	Full	Difference [%]	Simple	Full	Difference [%]
A	0.580	0.578	-0.247	2530	2760	+9.11
B	0.583	0.568	-2.538	2250	4990	+122
C	0.567	0.552	-2.698	5000	5000	n/a
D	0.655	0.631	-3.718	601	803	+33.7

Table 5.3: Ratio and gas temperature comparisons between simple and integration over full excitation profile for $O(^3P_2)$. Ratios and T_g written here to 3 significant figures, but percentage differences are from full values, and are relative to the simple case.

	$O(^3P_1)/\Sigma O(^3P_J)$			T_g [K]		
Condition	Simple	Full	Difference [%]	Simple	Full	Difference [%]
A	0.320	0.317	-0.997	2900	2370	-18.3
B	0.316	0.324	+2.565	2230	4140	+85.3
C	0.327	0.335	+2.434	5000	5000	n/a
D	0.266	0.279	+5.001	573	714	+24.6

Table 5.4: Ratio and gas temperature comparisons between simple and integration over full excitation profile for $O(^3P_1)$. Ratios and T_g written here to 3 significant figures, but percentage differences are from full values, and are relative to the simple case.

on the determined gas temperature. Further testing in pure O_2 with varying power and pressure appears to corroborate this theory - there was no clear relationship between T_g and these parameters.

Finally, using either the $O(^3P_2)$ or $O(^3P_1)$ ratio gives similar gas temperatures for each test condition. Conditions A and D have the most consistent temperatures when also considering the values determined from both the simple and full ratios. Thus, it appears that more accurate gas temperatures are obtainable when there is less n_O or fewer dissociation processes. Furthermore for condition D, the agreement can be attributed to helium playing an active role in cooling the gas. The heat from dissociation contributes to the $O(^3P_1)$ and $O(^3P_0)$ populations and affects accurate gas temperature determination as seen in conditions C and D. However, it is mitigated by the presence of helium. As it was shown that the helium-oxygen mixtures were rather consistent, especially as the Boltzmann plot method returned similar values, these cases can be considered more reliable.

5.4 Summary

This chapter investigated the fluorescence signal in the early afterglow of the plasma pulse from excitation of all three atomic oxygen ground state sub-levels. From this, the changing gas temperature was inferred from the population distribution over time.

As the evolution of gas temperature relied on the fluorescence response from the $O(^3P_J)$ states, these temporal profiles were first looked at closely to identify possible causes for the peaking phenomenon observed in $O(^3P_2)$. It was achieved by appropriately tuning the laser output excitation wavelength to the upper level, $O(3p^3P)$. Moreover, the time at which it was fired from the end of the plasma pulse was adjusted to gain insight in the population densities at a specific point from the corresponding fluorescence strength.

Firstly, the most populated was the lowest energy state, $O(^3P_2)$, followed by $O(^3P_1)$ and then the highest, $O(^3P_0)$. While the gas cools in the afterglow, the higher states relax and feed into the $O(^3P_2)$ level, and causes the slight increase in fluorescence response. It was also reflected in the rate at which these sub-levels decay in the afterglow. The sub-level populations increase with power, pressure, and even with sufficient amounts of argon. The latter supports the fact that there was interaction between argon and oxygen species that affected the gas temperature. Replotting these to see the changing ratio values over time saw very similar profiles as works that utilised photolysis to produce atomic oxygen, and the growing proportion of $O(^3P_2)$ was due to thermalisation through collisions.

Next, the normalised intensities at select times in the afterglow were plotted on a Boltzmann plot, and the gas temperatures were determined from the linear fit for pure oxygen, 20 Pa, 600 W. Depending on whether all three points were used for fitting, or the two most populated levels had an effect on the determined gas temperature. In both cases, the temperature decreased with time. The former started at 1590 K at 125 µs falling to 480 K at 2225 µs in the afterglow, and the latter returning higher values of 2950 K down to 560 K at the same corresponding time points. Repeated measurements to remove any dependence on the laser performance gave average gas temperature at 125 µs of 960 ± 320 K. Irrespective of gas mixture, there was cooling to a rest temperature of 400 K in the afterglow. This can be used to determine the density of O_2 prior to pulsing the plasma using the ideal gas law and therefore the dissociation degree.

An alternative approach was also tried where the gas temperature was obtained by directly comparing the ratio of normalised fluorescence intensities for all three ground state sub-levels with an equivalent Boltzmann fraction value, which is theoretically only a function of gas temperature, potentially allowing for more easier monitoring of this parameter in the afterglow. The obtained gas temperature was also compared with the Boltzmann plot method applied to the same set of data.

More consistent agreement between calculation of this ratio was found in pure oxygen and He-20%O_2, both at 20 Pa and 600 W using either ratio value. Although, T_g determined from this method (2760 K) was twice that of the Boltzmann plot method (1590 K) for pure oxygen. Moreover, there was a large discrepancy for the 1000 W case, and neither was able to determine a fixed gas temperature at 50 Pa. The reason for this was linked to the amount of dissociation occurring, and the energy from this process exciting the ground state atoms into higher sub-levels. Consequently, the ratios tended towards statistical values which in turn returned finite $T_g = 5000$ K.

While using only the peak excitation values gave comparable ratios as the full excitation profile, it did not necessarily mean similar gas temperatures. Under certain conditions, extremely small deviations in the ratio value led to exponentially different T_g. Thus, the Boltzmann fraction approach is unsuitable for precise measurements. More investigation is needed to verify and determine the threshold when this diagnostic becomes less effective.

Ultimately, the gas temperature long into the afterglow may be safely assumed to be around 400 K. In contrast, T_g values for high oxygen-containing discharges are ambiguous, and would be better obtained using other sources' values where the plasma conditions are similar, such as 1300 K from [92]. Meanwhile, T_g for mixtures with high-helium content, the values here of 570-800 K agree well with [28].

Chapter 6

Application of Energy Resolved Actinometry in high-power, pulsed ICP

So far, the characteristics of the plasma has been investigated using TALIF. This information is invaluable in understanding how the plasma behaves in the high-power regime. More importantly, it provides benchmark values for other diagnostics, in this case the purely passive optical method: ERA. This technique has already been applied in atmospheric pressure plasmas [61], and oxygen plasmas operated in capacitively-coupled [62] and low-power, inductively coupled [86] sources. In this chapter, ERA is further applied to the high-powered, inductive mode where characteristics, such as the high plasma density, is of interest for industrial processing. The measurements are made during the on-time of the pulse where the two-line ratio method alongside with Bayesian inference are used to determine plasma parameters.

6.1 E- versus H-mode emission differences

The difference between operating modes of an inductively coupled plasma is very distinctive visually. The change in particular emission line intensities can be quantified using a spectrometer. The emission spectra is compared in figure 6.1 for O_2-10%Ar, 15 Pa at 100 and 600 W. The immediate difference is that in the high-power mode, the two oxygen lines jump significantly. In comparison, the argon lines see a relatively modest increase.

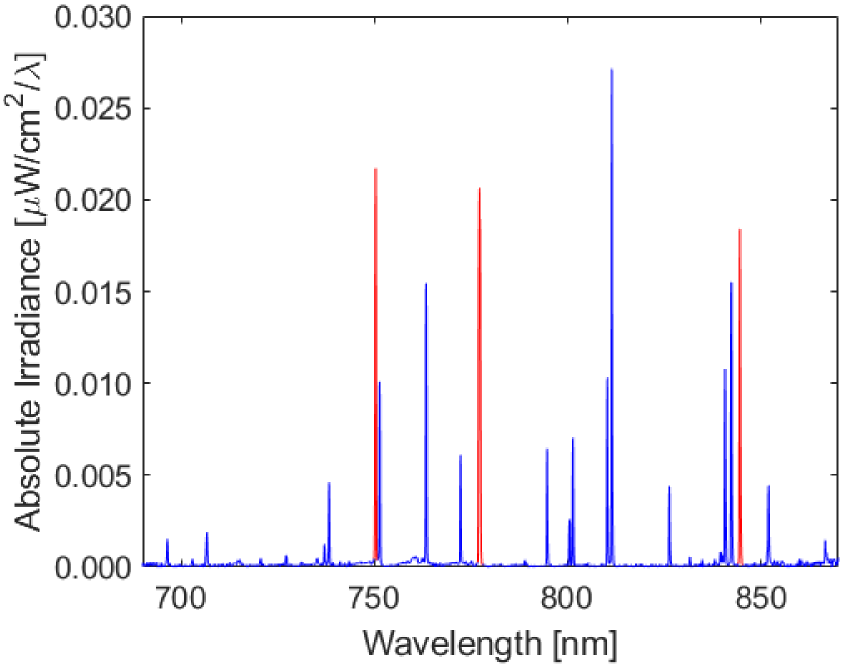

(a)

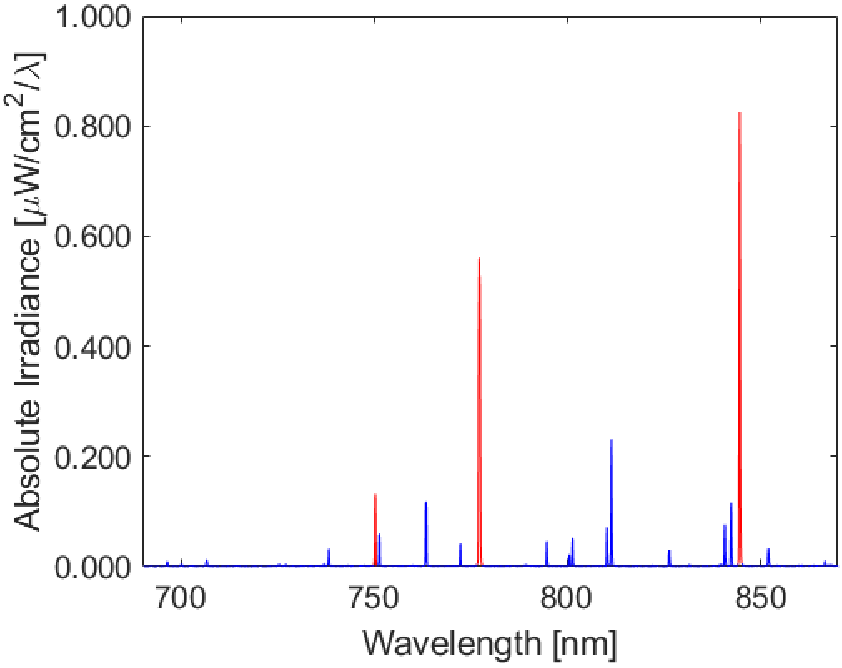

(b)

Figure 6.1: Comparison of emission spectra between a) E-mode (100 W) and b) H-mode (600 W). Both taken at O_2-10%Ar, 15 Pa. The peaks in red highlight the emission lines used in ERA i.e. Ar(750), O(777) and O(844). The oxygen lines see a significant increase in intensity, whereas it is less than an order of magnitude for all of the argon lines.

Table 6.1 quantifies the increase of select emission lines from the E- to H-mode by comparing the integrated peaks against themselves. The two oxygen lines at 777 and 844 nm increase by 26.6 and 42.7 times their value, respectively, and is caused by high amount of atomic oxygen present as well as numerous dissociative excitation processes. On the other hand, the argon transition Ar(706) has the smallest increase of 3.1, whereas Ar(811) has the most at 8.4. The latter is particularly susceptible to stepwise excitation. As mentioned previously, the electron density in H-mode is significantly higher than in E-mode and generally will have lower electron temperatures. This will produce a much higher population of metastables versus ground state and hence increase the Ar(811) emission much more than the Ar(750) emission. Subsequently, the high number of dissociation processes reduce the population of molecular oxygen and in turn the amount of quenching of metastables. Thus, these long-lived argon species may have a greater contribution. Both transitions dominated by direct-electron impact i.e. Ar(750) and Ar(751) change by the same amount. Nevertheless, all of the argon lines do not see an order of magnitude increase unlike oxygen. The overall increase is caused by the higher electron density upon transition to the H-mode [155]. As a result, the number of electron-impact excitation processes affects all of the line transitions somewhat equally.

Wavelength	I(H-mode)/I(E-mode)	Transition
O(777)	26.6	$O(3p^5P) \rightarrow O(3s^5S)$
O(844)	42.7	$O(3p^3P) \rightarrow O(3s^3S)$
Ar(750)	5.9	$Ar(2p_1) \rightarrow Ar(1s_2)$
Ar(751)	5.9	$Ar(2p_5) \rightarrow Ar(1s_4)$
Ar(811)	8.4	$Ar(2p_9) \rightarrow Ar(1s_5)$
Ar(706)	3.1	$Ar(2p_3) \rightarrow Ar(1s_5)$
Ar(738)	6.7	$Ar(2p_3) \rightarrow Ar(1s_4)$
Ar(764)	7.4	$Ar(2p_6) \rightarrow Ar(1s_5)$
Ar(794)	7.2	$Ar(2p_4) \rightarrow Ar(1s_3)$

Table 6.1: Quantifying the increase of emission intensities from E- to H- mode. The intensity of each line was compared against itself between the operating modes. The oxygen lines see a significant increase compared to the argon lines.

Overall, the study of emission using conventional spectroscopy is a powerful technique, and allows straightforward identification of species and underlying processes present within the plasma. Actinometry of a single line ratio between oxygen and argon is able to give the atomic oxygen density, but requires knowledge of the electron temperature. In principle, a second line ratio could provide complementary information about this. However, time-integrated emission is made complicated where contributions are not only from direct and dissociative excitation, but also stemming from cascade and metastable contributions. These were deemed to have a notable effect, particularly for the 777 nm emission [156]. For accurate models, information about the population densities and relevant excitation cross section from these would also have to be measured or known. Hence, PROES was selected to simplify the analysis because during strong electron heating in an rf cycle, direct electron impact excitation processes dominate, and so it is much easier to model.

To carry out PROES, the light is captured onto the CCD of a fast camera. However, it uses optical filters to control the specific wavelengths of light that falls onto the CCD. As such, the transmission and quantum efficiencies of both of these components, respectively, also need to be known. Otherwise, the actual measured intensity may be skewed since the quantum efficiency of detectors tend to decrease towards the infrared region of light. Nonetheless, this can be circumvented by calibrating the perceived amount of light using the spectrum recorded by a spectrometer under the same discharge conditions [141].

Another aspect to this method is that the inclusion of argon can be problematic given its many transitions may cause overlap of emission lines of interest. Hence, employing narrowband optical filters of ±0.5 nm was vital, especially since argon line at 750.46 nm has a close emission line at 751.49 nm, and the broadened emission profile from the latter could contribute to the observed emission by the CCD. Consequently, use of a spectrometer with high enough resolution to resolve these two peaks reduces potential error from this. Moreover, when calibration of the CCD was done by integrating over the wavelength range around the 750.46 nm line as done in [141], there was no overlap with the neighbouring 751.49 nm peak. Consequently, the optical filter was able to discriminate between the two argon lines. In the case of the two oxygen lines, these were far enough from any other argon transition.

Lastly, the background signal from sources such as the spectrometer itself was subtracted from the raw spectra before integrating the peaks. Although, this process still left some spectra with a non-zero baseline, and would have an unintentional contribution to the integrated emission. On one hand, the argon and oxygen emission lines had intensities at least a couple of orders of magnitude greater than this. Thus, the overall effect it had on the total intensity was minimal. Conversely, this would be problematic if the residual background signal had a similar magnitude to weaker emission lines. As seen in the next chapter, helium emission was on par with the background. Regardless, the percentage difference of the integrated peak accounting for a non-zero baseline was used as an approximation of uncertainty in the line ratios, which is another strength in Bayesian methods; the uncertainty itself is a parameter that accounts for possible error in the measurements.

Next, the key difference in excitation between the two modes using PROES is exhibited in figure 6.2. The excitation profile in the E-mode was assumed to be at 400 K as in [62], while the H-mode was taken to be at a gas temperature of 2500 K based on results from the previous chapter. Regardless, the gas temperature had a negligible effect on the overall excitation profile in the high power regime. This was because higher T_g reduced the quenching value - the quenching rate is proportional to both $\sqrt{T_g/300}$ and $p/k_B T_g$, and the overall effect is an inversely proportional relationship, $k_q \propto 1/\sqrt{T_g}$.

Unlike the low-power mode where the plasma was operated in cw mode, pulsing the plasma at high powers to reduce the time-averaged heat load had potential issues. Since the output rf signal from the generator was constant, the camera would have also been triggered during the ignition, capacitive-inductive transition, and the plasma-off periods. Ideally, the camera only captures emission during the stable H-mode to improve the signal-to-noise. Nonetheless, figure 6.2b shows two periods of excitation per rf cycle which is characteristic of inductive coupling from the heating of two half-cycles [113, 157]. This confirms that not only is the plasma in the inductive mode, but also that the experimental set-up is able to capture this without explicit need for gating the captured emission. This was because the rf generator supplied power in phase with its in-built rf signal. Thus, as the camera is also triggered by the same signal, it would be already synchronised. Still, further work could be done to only capture the stable H-mode for comparison.

In the E-mode, the location of strong sheath heating was located between 10-20 ns. The effects of capacitive coupling from pulsing the plasma may be indicated by the excitation at the same time point in the H-mode being slightly stronger than the second half i.e. 47-57 ns. One location of maximum excitation in the H-mode was between 25-40 ns and the other at the very end/beginning of the recorded rf cycle. The relative shift of these maxima locations between the two modes is consistent with that observed by O'Connell et al. [157]. Consequently, while there may be capacitive effects, the heating observed in the H-mode is more likely to be from the inductive coupling than sheath expansion, especially as the former appears to have weakened considerably by then. Moreover, the time for which it is in the E-mode has been shown to be relatively very short compared to the overall plasma-on time [42]. Thus, emission recorded from the E-mode contributes minimally compared to the many cycles taken during H-mode.

Since excitation primarily stems from the ground state for Ar(750), the plasma parameters were inferred from the excitation ratios taken at the location of maximum excitation of this emission line. Yet, this may not be the same for the oxygen lines. Consequently, ratios were also calculated at the maximum location for each of these lines as well, and the standard deviation between these was used as the input for uncertainty in the Bayesian analysis.

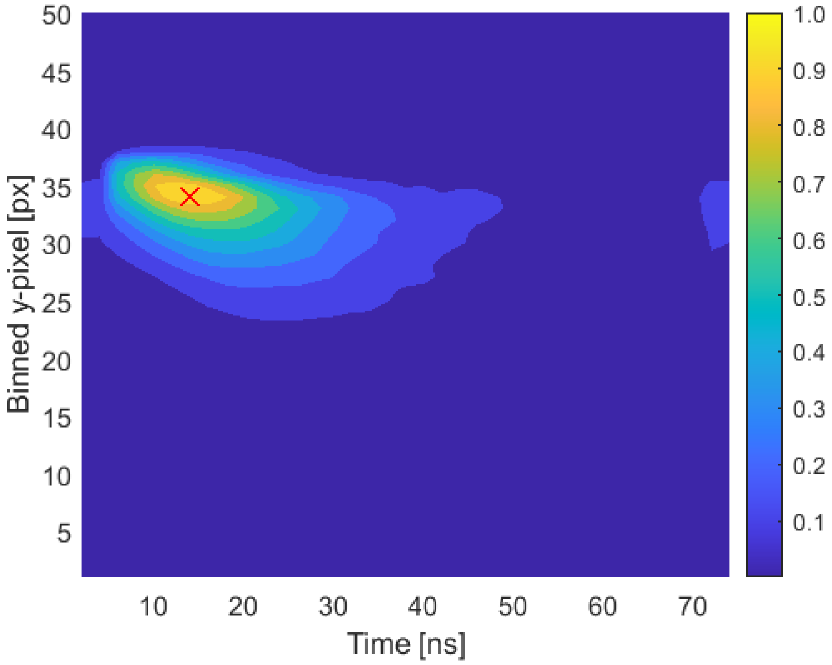

(a)

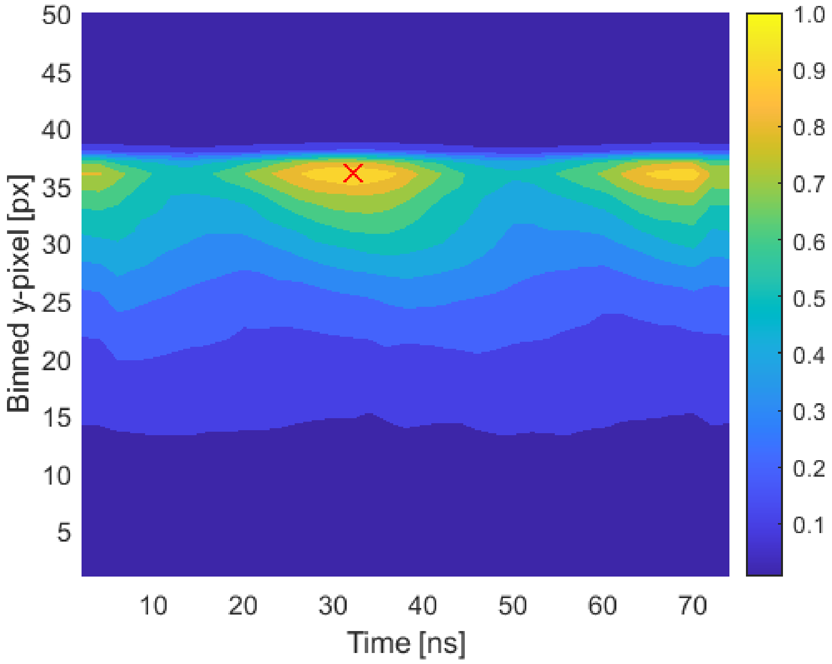

(b)

Figure 6.2: Comparison of normalised excitation profiles of Ar(750) between a) E-mode (100 W) and b) H-mode (500 W). Both taken at O_2-10%Ar, 15 Pa. The excitation profile for E-mode shows strong heating due to sheath expansion taking place once per cycle. Conversely, two periods of heating can be seen per cycle for the H-mode, which has been noted in literature [113, 157]. The red crosses mark the locations where ERA analysis takes place as excitation from direct-electron impact are most prominent here and where the assumptions of the model are more valid.

6.2 Application of ERA in the H-mode

In this section, the plasma parameters in the high power regime derived using ERA is discussed. [86] did investigate applying this technique to the H-mode, but was unable to find match between theoretical models and experiments. Hence, in this work, Bayesian inference was employed to improve the analysis. After comparing the experimental excitation ratios with the theoretical model, and assuming that the uncertainty was Gaussian, the marginalised probabilities of the plasma parameters were normalised to the most probable value. A Gaussian fit was then applied to these curves from which the fitting coefficients gave the mean electron energies and dissociation degrees. This is seen in figures 6.3a and 6.3b for O_2-10%Ar at 15 Pa and 500 W. Although traditional actinometric methods use around 2-5% argon as trace gas [59, 99, 125]in order to minimise the influence it has on the plasma parameters [98], 10% was used to obtain better signal for the Ar(750). Still, this proportion of argon does not significantly alter the amount of atomic oxygen and could even be as much as 50% before it starts to affect these quantities [53].

Firstly, unlike the low power case where dissociation is expected to be small, the theoretical excitation ratios were generated over a much larger range of dissociation degrees. Although it is not shown here, when the analysis was carried out over a parameter space with less than 15% dissociation, the two-line ratio method returned ambiguous results. Multiple solutions were found to best fit the experimental ratios, with extreme values of low mean electron energy and the dissociation degree tended towards the upper bounds of the analysis. Thus, by increasing the parameter space to include up to 100% dissociation, more defined results were able to be found for both.

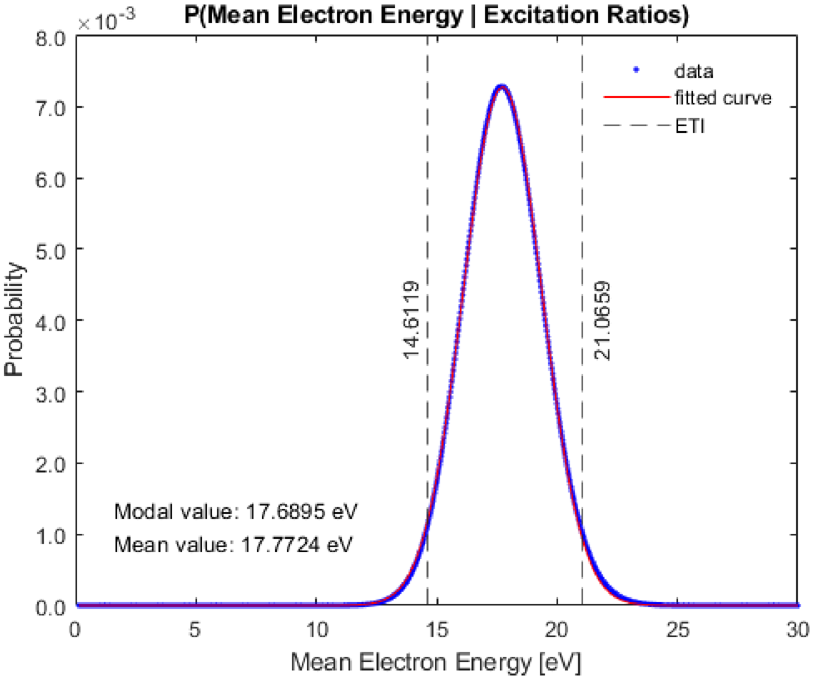

(a)

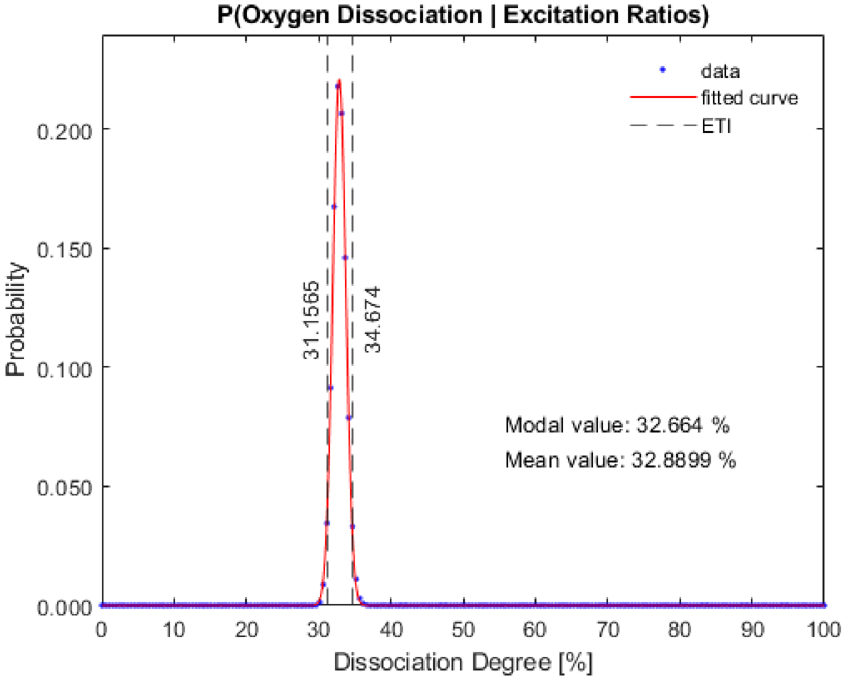

(b)

Figure 6.3: Marginalised probabilities of a) mean electron energy, $\langle \epsilon \rangle$ and b) dissociation degree, r_O. Plasma parameter values determined using ERA at O_2-10%Ar, 15 Pa, 500 W.

Figure 6.4 shows the plasma parameter values of the investigated conditions. Firstly, the atomic oxygen densities are about twice the amount at 15 Pa than at 10 Pa which is not proportional. Secondly, it is unclear whether there is positive correlation with power due to the size of the uncertainties. However, the overall magnitude and relative values of these atomic oxygen densities are rather close to those taken with TALIF in pure O_2 in the TALIF chapter. The dissociation degree of the plasma varied in the range of 23-27% at 10 Pa, while it was 31-38% at 15 Pa. [53, 125] saw an increase with applied power, but [53] noted a decrease with pressure. Moreover, these are an order of magnitude higher than the capacitively-coupled case of a few percent [62] and similarly the E-mode [86]. Contrastingly low dissociation degree was also found in [101] of a few percent in transformer coupled plasma even at the highest powers. Nonetheless, Peverall et al. had dissociation fractions of around 15% for pressures between 10-100 mTorr in inductive plasma [87]; they determined this with an extra factor of 2 in the denominator compared to this work's definition, $r_O = n_O/n_{O2}$. Thus, high dissociation degrees were obtained as expected in these high density plasma sources.

On the other hand, the mean electron values are in excess of 15 eV for all conditions which is a higher value than seen in the capacitive case of [62]. Then again, it is lower than E-mode of [86]. Typically, the inductive mode sees lower electron temperatures [56,101,120], but compared to these works it is excessively high. Moreover, at higher pressures the mean electron temperature should decrease due to the higher collisionality. However, it appears to be the opposite case. Then again, the large uncertainties of this parameter make it difficult to confirm this relationship.

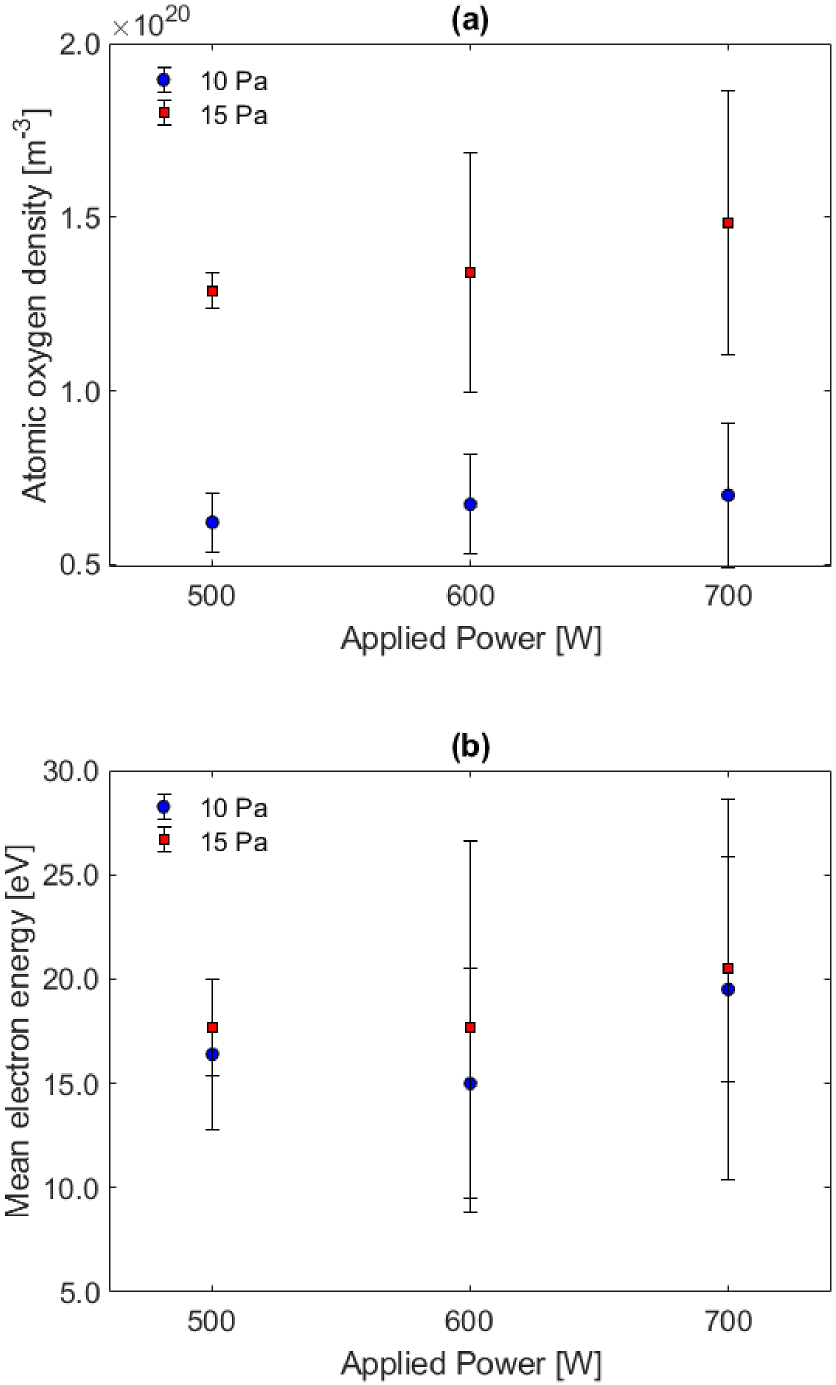

Figure 6.4: a) atomic oxygen densities and b) mean electron energies of O_2-10%Ar at various powers and pressures. The latter parameter gives large values in excess of 15 eV and is disproportionately high compared to other works.

For easier comparison between the two diagnostic techniques, the pure oxygen measurements with varying power that were taken with TALIF are replotted against the O_2-10%Ar results using ERA in figure 6.5. Although the latter had slightly lower oxygen content, the difference in n_O between 90% and 100% oxygen content was marginal. It is worth noting that the TALIF number densities are only of the $O(^3P_2)$ sub-level, whereas the ERA number densities are for atom in of $O(^3P)$. Nonetheless, these diagnostic results are within an order of magnitude of each other and qualitatively resemble each other - n_O increases with pressure and weakly with applied power.

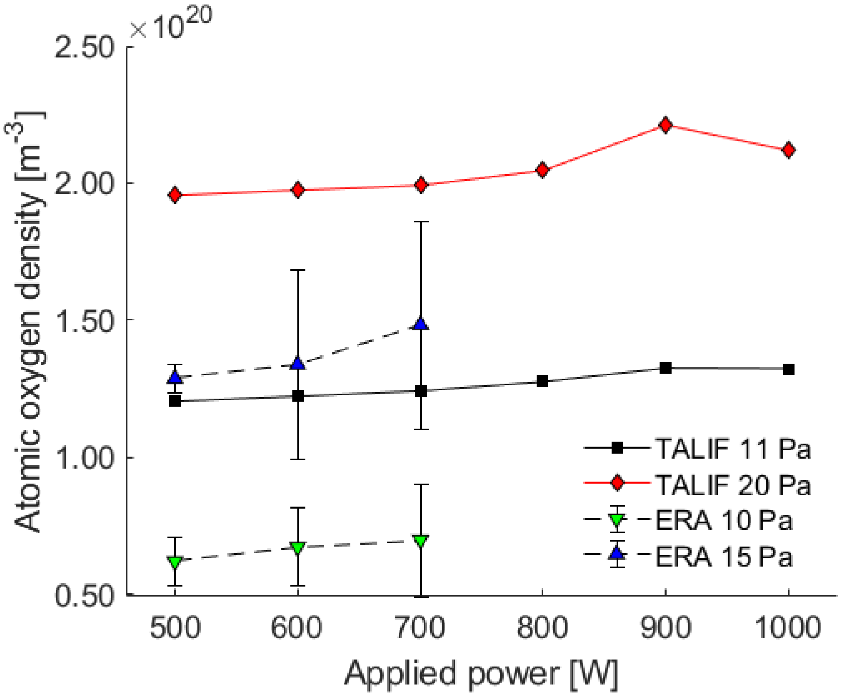

Figure 6.5: Comparison between the atomic oxygen densities between TALIF taken in pure oxygen versus ERA in O_2-10%Ar. Similar orders of magnitude were found using ERA, and it also predicts increase in n_O with pressure and weakly with applied power.

To identify the cause behind these results, the process in which the results are determined is examined. Figure 6.6 shows that for the experimentally calculated excitation ratios, there are fewer distinct crossing point as dissociation degree increases, and they intersect at increasingly high mean electron energy values. Moreover, the 777/844 contours show multiple solutions of either high or low mean electron energies towards high dissociation degrees. Using the 750/844 to find an intersecting point, this can happen at either very low mean electron energies and dissociation degrees. However, it is highly unlikely that the inductive mode produces small amounts of dissociation. Conversely, towards the other end the contours run parallel to one another. Earlier it was mentioned that if the analysis only looked at r_O of less than 15%, there was no well-defined solution. Expanding the analysis to include up to 100% dissociation overcame this, and crossing points were able to be found. Although, this tended $\langle\epsilon\rangle$ to be large. The Bayesian method was adjusted to shape the prior distribution further, such that it reduced the probability of these extreme values. That is, instead of assuming that all mean electron energies between 0 and 30 eV having the same probability, more probable values lay within a defined region between 2 and 15 eV. Consequently, $\langle\epsilon\rangle$ outside this range had drastically decreasing likelihood. Yet, by effectively ignoring the solutions as those found above 15 eV, better agreement between using the two-line ratios were found towards low dissociation degrees with increasing applied power. Hence, this ended up giving negative correlation between them which is contrary to trends identified previously.

Applied power [W]	E_{750}/E_{844}	E_{777}/E_{844}
10 Pa		
500	$0.1853 \pm 6.19\%$	$0.8675 \pm 6.67\%$
600	$0.1793 \pm 9.25\%$	$0.7965 \pm 10.64\%$
700	$0.1757 \pm 12.79\%$	$0.8698 \pm 14.67\%$
15 Pa		
500	$0.1502 \pm 1.75\%$	$0.7883 \pm 4.20\%$
600	$0.1504 \pm 11.18\%$	$0.7517 \pm 14.51\%$
700	$0.1437 \pm 11.03\%$	$0.7935 \pm 3.57\%$

Table 6.2: The corresponding excitation ratios and uncertainties used to determine the plasma parameters.

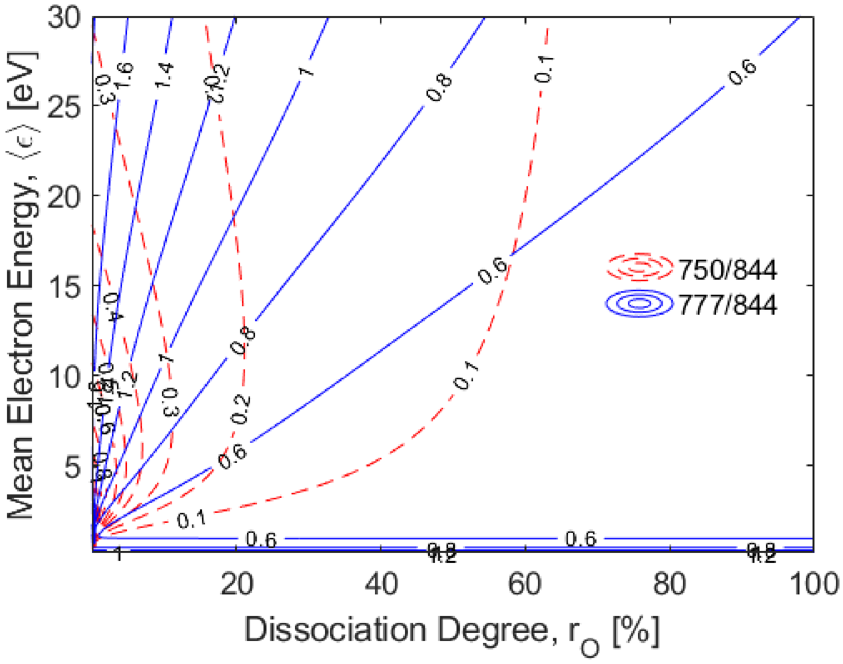

Figure 6.6: Contour plot of the theoretical excitation ratios for O_2-10%Ar at 15 Pa. It shows that for the given experimental ratios, there are few crossing points in the range of high dissociation.

6.3 Possible improvements on the model

The theoretical calculations for both E_{750}/E_{844} and E_{777}/E_{844} were evaluated to see if any improvements could be made to the model. Difficulty was also encountered by [86], who remarked that there could be additional excitation and de-excitation processes that are not accounted for. In the same way that the inclusion of dissociative excitation has improved the accuracy of actinometry measurements [59], consideration of additional processes may prove to have a similar effect.

More detailed modelling could include excitation between atomic oxygen levels. Theoretical excitation cross-sections to $O(3p^nP)$ are available [158] and could be incorporated if these state densities are known. In particular, the magnitude of the cross-sections from the $O(3s^nS)$ states are much higher in comparison to the ground state, and so excitation from these levels can have a significant contribution if these populations are high. This was also mentioned by [156] where $O(3s^5S)$ can build up at low pressures due to slow collisional relaxation.

Metastable oxygen molecules were also suggested to be the cause for discrepancies surrounding the O(777) giving dissimilar results in actinometry compared to O(844) [59]. Expanding on this, similarly to the earlier comment on how Ar(811) emission increases due to increased metastable contributions, the same would be true for both oxygen 777 and 844 nm with the former more sensitive to metastable contributions. While it has little bearing on ERA in the E-mode likely due to insignificant population, these may become prominent in the H-mode. The additional observed excitation from these is artificially compensated by unreasonable mean electron energy as the 777 nm line will have stronger contribution from dissociative excitation with higher threshold energy.

Finally, the ratio between the O(777)/O(844) was shown to be also dependent on both the operating pressure and electron density, and not just the mean electron energy and dissociation degree [156]. Accounting for all of these in the model would require many more input variables. However, this also further increases the amount of measured parameters and computation needed, and it was preferable to seek solutions that minimise the complexity of the analysis.

There are other phenomena that can occur, one is that the $O(3p^3P)$ can be quenched into the $O(3p^5P)$ state by as much as 8% [159]. Thus, the branching ratio and observed emission would have to be corrected to account for this. Another is that the emission at 777 nm can be recaptured by high densities of $O(3s^3S)$ [114]. As a result, an escape factor can be added to account for any photons that may be reabsorbed by this lower state. As this was nearly a pure oxygen case, an escape factor of 0.9 was used to correct the theoretical excitation calculation. However, this did not improve the results, and in fact tended to push the resulting mean electron energies higher.

The last aspect that was considered was the calculation of the excitation rates require accurate cross-section data, and these are difficult to measure close to the threshold energy. Consequently, the direct impact cross-sections from [50] were generated to create a more accurate dataset for modelling. However, they based these on earlier work by [160] which had very limited experimental results. Of these, the cross-sections near the threshold had uncertainty of 50%. From this, the $O(3p^5P)$ cross-sections for <20 eV is likely to have the biggest uncertainty as there was no experimental verification, and was smaller than theoretical values of [161] by up to a factor of 2 at the lowest energy. Thus, this has a potential knock-on effect on the calculated excitation rates from high-energy electrons in the tail population of the EEDF that meet the threshold energy. In contrast, the dissociative cross-sections have estimated uncertainty of only 15% [39]. Overall, evidence suggests that there is much uncertainty using the 777 nm emission line in the analysis.

6.4 Summary

ERA was applied to the high-power regime of a pulsed inductively coupled plasma in pure oxygen. Moreover, Bayesian analysis was also implemented in the analysis to determine the mean electron energy and dissociation degree in O_2-10%Ar at 10 and 15 Pa, and over 500-700 W. This aimed to extend the applicability of this technique where it has seen good agreement in other types of plasma. In particular, to a high density plasma which is of interest for industrial purposes.

The emission was first compared between E- and H-mode to highlight the differences between the two operating regimes of an inductively coupled plasma. The oxygen emission intensities at 777 nm and 844 nm rose markedly, whereas the argon lines by less than an order of magnitude. The PROES measurements showed two periods of strong excitation in the inductive mode compared to one in capacitive. This also confirmed that the experimental set-up was capable of capturing the spatial and temporal profile in pulsed mode. Subsequently, the analysis was carried out at the location where the excitation was strongest.

Then, the excitation ratios from each of these PROES measurements for Ar(750), O(777) and O(844) were compared against theoretical calculations. These resulted in quantitatively similar atomic oxygen densities as the TALIF measurements in pure oxygen plasma. Moreover, it rose with pressure as observed before, but the relationship was less clear for applied power. Regardless, the complementary mean electron energy values were over 15 eV for all cases - these are much higher than seen in literature. Consequently, it gives doubt on the accuracy of the measured atomic oxygen densities.

The cause for these high mean electron energy values were examined. Firstly, the contour plots of the excitation ratios saw a lack of clear crossing points towards high dissociation degrees; these eventually intersected at higher mean electron energies. Moreover, the 777/844 ratio had multiple solutions which added more ambiguity. Therefore, additional excitation mechanisms that could affect the theoretical model were looked into. Nonetheless, incorporating these into the calculations would also require knowledge of the densities of these states. Ultimately, this would add greater complexity to the analysis, and detract from the motivation to have simpler diagnostics.

The conclusion was that ERA using the two oxygen emission lines and one argon line gave tentative results. Given that it is most susceptible to dissociative excitation in this operating regime as well as other evidence gathered, it was deemed that the 777 nm line in particular had the highest amount of uncertainty. Thus, the use of an alternative emission line can clarify whether the mean electron energy value is valid or not. In contrast, the ratio between Ar(750) and O(844) has traditionally returned good agreement of the atomic oxygen densities and so will still be an excitation ratio used in future analysis.

Chapter 7

Extension of Energy Resolved Actinometry using helium emission to determine plasma parameters in high-power, pulsed ICP

In the previous chapter, the use of the 750, 777 and 844 nm excitation ratios were employed in the ERA technique in a pulsed ICP at high powers. However, the model failed to provide distinct crossing points in regions of high dissociation degrees and low mean electron energies. With the introduction of Bayesian inference, the model did give clearer output values. While increasing applied power did return greater dissociation degree, the mean electron energies were unusually high for an ICP and were contrary to established literature. It was suspected that the sensitivity of the model in this regime is not given.

This chapter covers how the ERA approach was modified to overcome weakness of the original technique in the H-mode. The idea proposes using an alternate line ratio that had no dependence on the atomic oxygen density. Helium emission was investigated whether it can substitute the 777 nm line to provide more reliable results. Thus, by first locking-in the mean electron energy, subsequent dissociation degrees could be determined through commonly used actinometry ratios, but still accounting for other processes i.e. dissociative excitation which also requires the electron energy. As such, the 750 and 844 nm emission lines were kept due to their established history of more accurately tracking atomic oxygen density.

7.1 Helium

7.1.1 Helium emission

Helium was a candidate considered to help tackle the problems encountered with ERA. It has many favourable characteristics that makes it attractive for experimental applications. Firstly, it is a readily available gas already set-up in laboratory experiments. Moreover, it is an inert gas so there will be no loss of atomic oxygen species through chemical reactions upon mixing. Finally, as it is one of the simplest atoms, it has already been studied in-depth. As such, there is a wealth of literature and data about it which facilitates development of theoretical models. Helium has two prominent emission lines at 706.5 nm and 728.1 nm - selecting one of these to replace the oxygen 777 nm emission was believed to help overcome the issues that arose from the latter. The excitation scheme for the 706.5 nm transition is depicted in figure 7.1 and requires 22.7 eV. For comparison, Ar(750) only needs 13.48 eV, almost half of the energy.

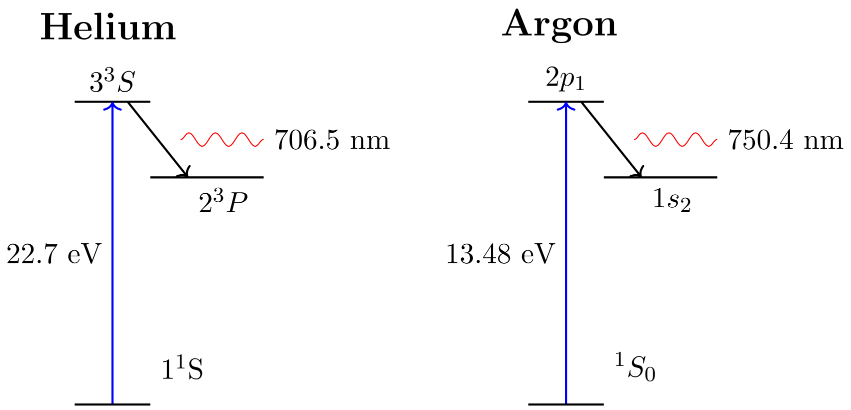

Figure 7.1: Helium versus argon excitation energy schemes. The electron energy needed to excite helium requires almost 10 eV more than argon from the ground state to the upper level. Subsequent de-excitation to an intermediate lower level produces emission at 706.5 nm and 750.4 nm for helium and argon, respectively.

Neon was also considered as an alternative gas for emission lines. Although, it is not commonly used and is relatively expensive compared to the other gases. Nonetheless, it is able to provide very intense emission at 585.3 nm and so only a small amount is required. Future work could explore using this as well, either in conjunction with helium emission to help verify the accuracy of the results. Or, it could be used as a trace gas in investigation of purer oxygen admixtures and replace using the 777 nm altogether.

7.1.2 Helium excitation cross-sections

The ERA technique relies on comparing excitation rates that are calculated using a mathematical description of an EEDF with energy-dependent cross-section values. In the case of helium, the direct electron impact excitation cross-sections from the ground state, 1^1S, were taken from Ralchenko et al. [162]. The two transitions of interest are $3^3S \rightarrow 2^3P$ and $3^1S \rightarrow 2^1P$ which result in photons of 706.5 and 728.1 nm, respectively. The threshold excitation energy for these two helium upper levels are 22.7 and 22.9 eV [103, 134]. This is significantly higher than argon at 13.48 eV and even the dissociative excitation threshold energy of oxygen of ∼16 eV. Consequently, the intensity of the emission will be very sensitive to changes in the tail portion of the EEDF.

The input values of the helium excitation cross-section can be calculated through equations provided by Ralchenko et al. [162], and is rewritten here for clarity.

$$\sigma(E, \Delta E) = \pi a_0^2 \frac{R_y}{g_l E} \Omega \left(\frac{E}{\Delta E} \right) \tag{7.1}$$

a_0^2 is the radius of a hydrogen atom, R_y the Rydberg energy, 13.6057 eV, g_l the statistical weight of the initial state, E the incident electron energy and ΔE the threshold energy of the transition. $\Omega(x)$ is the collision strength where $x = E/\Delta E$. This last parameter depends on whether the transition is dipole or spin forbidden, in which case equations (7.2) and (7.3) are used in each respective case. The $1^1S \rightarrow 3^1S$ is dipole forbidden while $1^1S \rightarrow 3^3S$ is spin-forbidden. Using the fitting parameters listed in table 7.1, the cross-sections can be recreated for the $1^1S \rightarrow 3^3S$, but not the $1^1S \rightarrow 3^1S$ transition. It is likely that there is a misprint in the fitting parameters in the paper, but it is not known which value needs to be corrected. As the cross-sections diverge near the threshold, the fitting parameter that affects this most is A_4. Indeed, changing it by a factor of ten does alter the shape and magnitude of the cross-section value accordingly. Yet, the fitting was still poor in the energy range $10^1 - 10^2$ eV of interest. Currently there have been no corrections published by the original author in regards to this transition.

$$\Omega(x) = \left(A_1 + \frac{A_2}{x} + \frac{A_3}{x^2} + \frac{A_4}{x^3}\right)\left(\frac{x^2}{x^2 + A_5}\right) \tag{7.2}$$

$$\Omega(x) = \left(A_1 + \frac{A_2}{x} + \frac{A_3}{x^2} + \frac{A_4}{x^3}\right)\left(\frac{1}{x^2 + A_5}\right) \tag{7.3}$$

i	f	A_1	A_2	A_3	A_4	A_5
1^1S	3^1S	4.033[–02]	–1.872[–02]	2.368[+00]	–1.379[+00]	1.258[+02]
1^1S	3^3S	9.392[–02]	–1.641[–01]	7.605[–02]	–4.536[–03]	–9.246[–01]

Table 7.1: Oscillator strength fitting parameters from initial (i) to final (f) states taken from Ralchenko et al. [162] - these generate the helium excitation cross-sections of interest.

Alternatively, the cross-sections could be extracted using third-party software, in this case WebPlotDigitizer [163]. The user converts the figure into an image file and then calibrates the axes so that each pixel can be interpolated to reproduce the results. Thus, data from a figure can be exported as a tabulated file for modelling. A comparison of the two methods for both transitions is shown in figure 7.2. The solid blue line is that from the fitting function whereas the black dots were data points extracted from the original figures using WebPlotDigitizer. The numerical data agreed with both methods for the transition to 3^3S. Conversely, the 3^1S cross-section values using WebPlotDigitizer disagreed with the fitting from the Ralchenko et al. publication, but recreated the original figure. Thus, the fitting functions work for the 706 nm cross-sections. Nonetheless, for consistency, the WebPlotDigitizer approach was used instead of using the fitting parameters to obtain the excitation cross-sections of both transitions for the theoretical calculations.

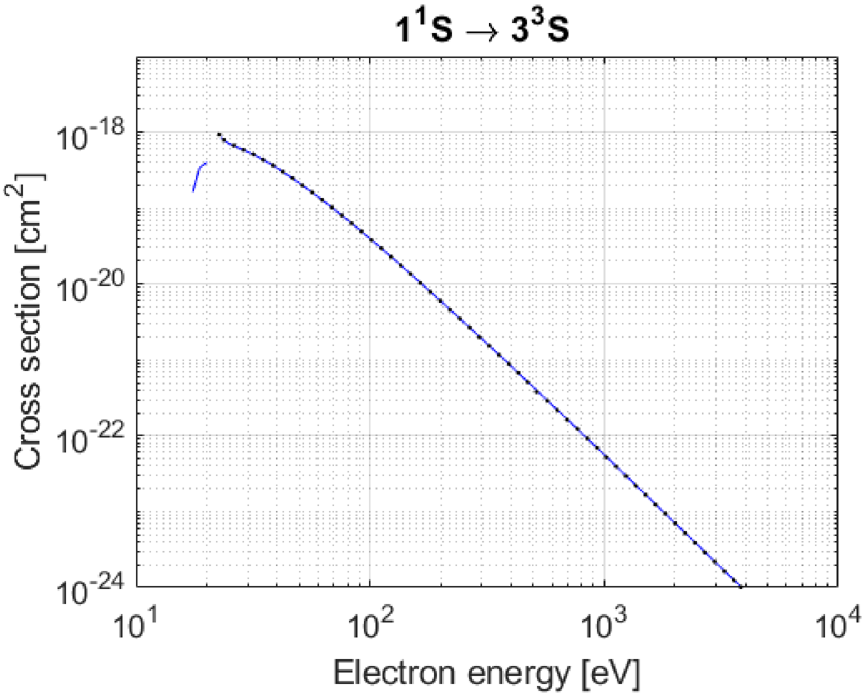

(a)

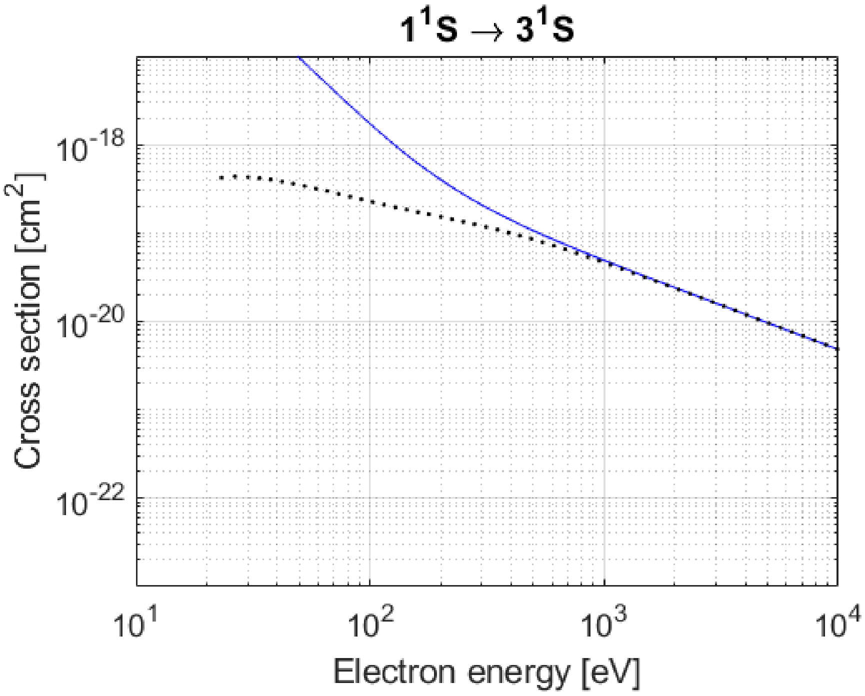

(b)

Figure 7.2: Excitation cross-section data from Ralchenko et al. [162] showing the transitions of a) $3^3S \rightarrow 2^3P$ and b) $3^1S \rightarrow 2^1P$. Upon de-excitation, these will generate photons of wavelength 706.5 and 728.1 nm, respectively. The black circles are from extraction of the data from their figures using third-party software, WebPlotDigitizer [163] whereas the blue curves are from fitting parameters and equations cited in the paper. However, the fitting parameters for the $1^1S \rightarrow 3^1S$ transition do not reproduce the same curve - a misprint of one of the values is suspected.

These cross sections are then used to calculate the excitation ratios in the same manner as before. Figure 7.3 show that the ratio between He(706) and Ar(750) are independent of the dissociation degree and also provide more crossing points. Consequently, the mean electron energy may first be determined and then used to pinpoint the dissociation degree from the according excitation ratio between O(844) and Ar(750).

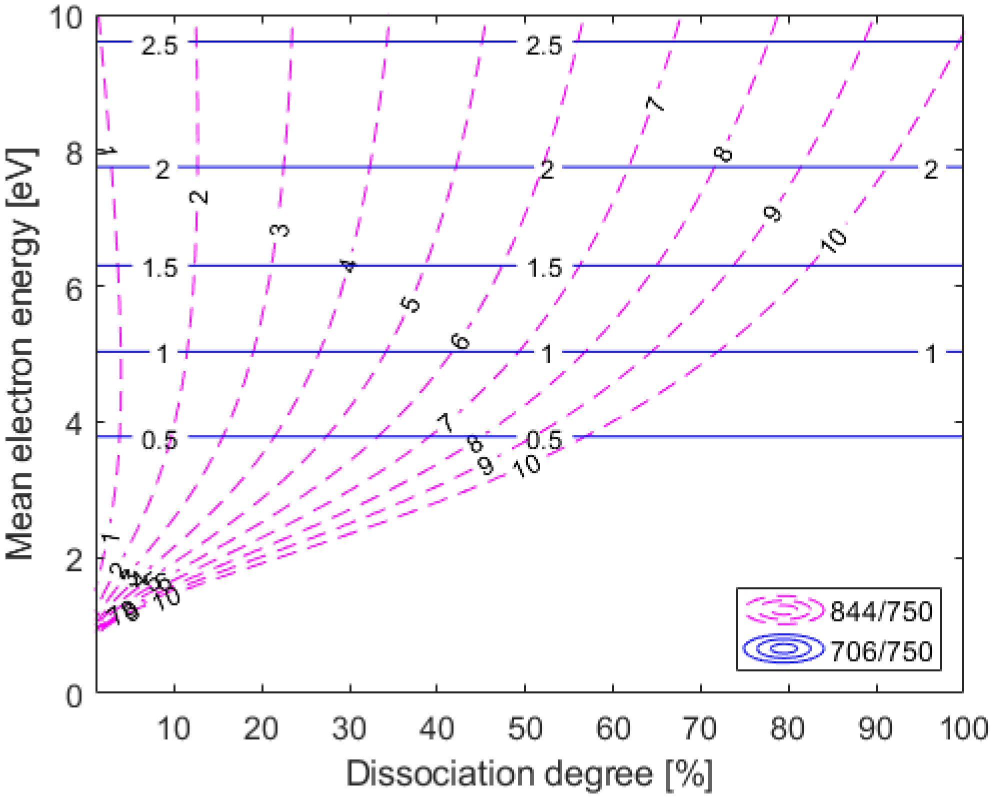

Figure 7.3: The contour plot for helium energy resolved actinometry. Excitation ratios between He(706) and Ar(750) are used to improve the likelihood of crossing points at higher dissociation degrees.

7.2 Feasibility study using helium emission lines

A feasibility study was carried out to assess the viability of using helium emission in the ERA approach, where the response of its intensity was investigated with varying plasma conditions. These included varying the applied power, pressure, and admixture ratio.

7.2.1 Study of helium emission lines in pure He

Firstly, the location of the helium emission lines on the spectra was determined in a pure helium plasma. Figure 7.4 shows the spectra of a pure helium plasma at 50 Pa, 100 W. Although only helium gas was admitted into the GEC reactor, there was some impurity as seen by the presence of oxygen emission lines. Nonetheless, these do not interfere with the identification of the helium peaks.

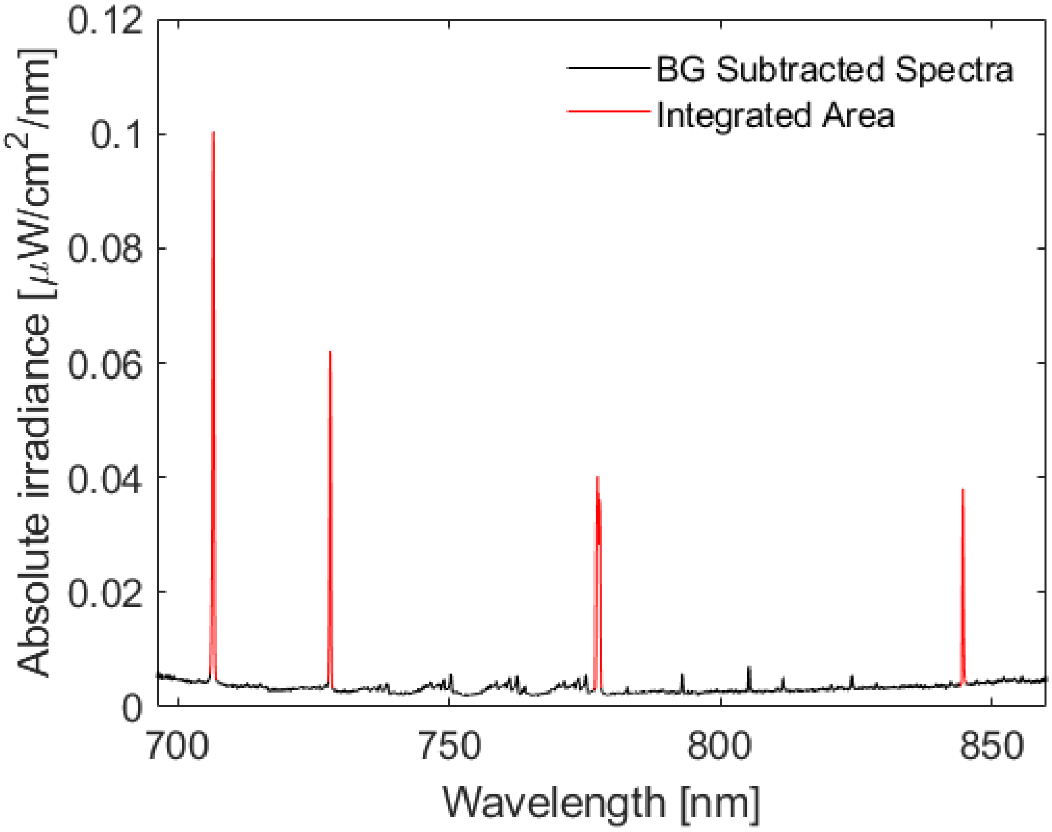

Figure 7.4: The spectra of pure helium at 50 Pa, 100 W. Oxygen emission lines can be seen as well, likely due to the inability to achieve perfect vacuum. Taking pure helium spectrum allows for easier identification of emission peak locations and its subsequent study with varying operating conditions.

After integration of these peaks, figure 7.5 shows the ratios between the 706 and 728 nm emission with varying pressure. The I_{706}/I_{728} ratio increases with pressure. It is known that the mean electron energy reduces with higher pressures due to increased collisions. So, since the direct electron impact excitation threshold energy is lower for the 3^3S level than the 3^1S, there will be fewer electrons with sufficient energy to excite the latter state and result in fewer photons of 728 nm. Despite the small difference in excitation energy, the helium emission is sensitive enough to reflect the change in mean electron energy. On the other hand, the presence of helium metastables allows an alternative excitation route, and is more prominent for 706 nm at lower T_e.

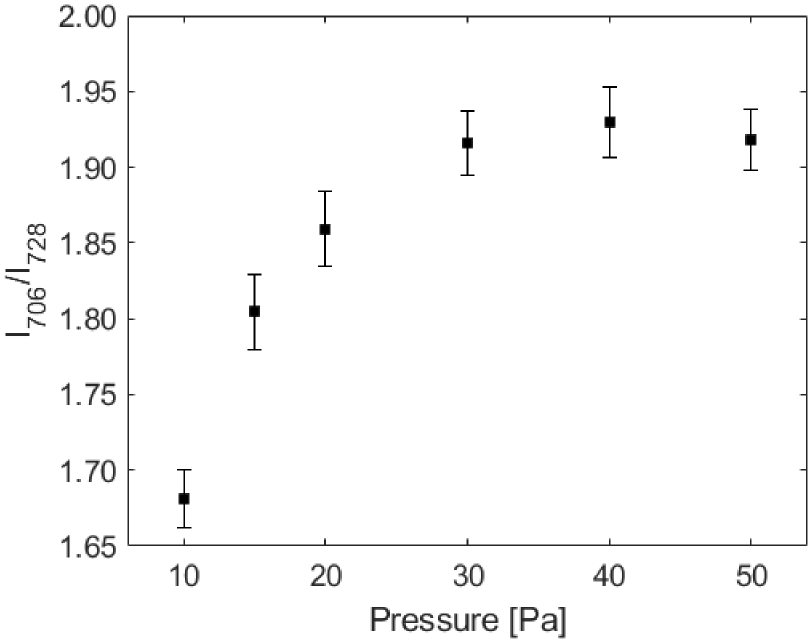

Figure 7.5: The ratio of the two helium emission lines at constant applied power of 100 W - the plasma was in E-mode. As pressure increases, the ratio increases, which corresponds to decreasing mean electron energy since the 3^3S level (706 nm) has a slightly lower excitation threshold energy from the ground state than the 3^1S (728 nm). Alternatively, greater amount via metastable excitation favours the I_{706} line.

7.2.2 Effect of oxygen addition on helium emission

Next, the effect of oxygen addition on the helium emission lines was investigated. As seen in figure 7.6, the helium emission lines are very weak in a 50-50 mixture of helium and oxygen. They were no longer observable with lower helium content. Although there is less helium available to contribute to the emission, the primary cause of the reduction is due to the oxygen molecules. Since the helium emission lines have much higher threshold energies than oxygen, it is much more sensitive to changes in the tail population of the EEDF. Thus, the intensity of the helium emission lines greatly decreases with oxygen addition. Consequently, the first limitation of the proposed technique is restricted to gas mixtures that give enough helium signal, chiefly by keeping the oxygen content as a small fraction.

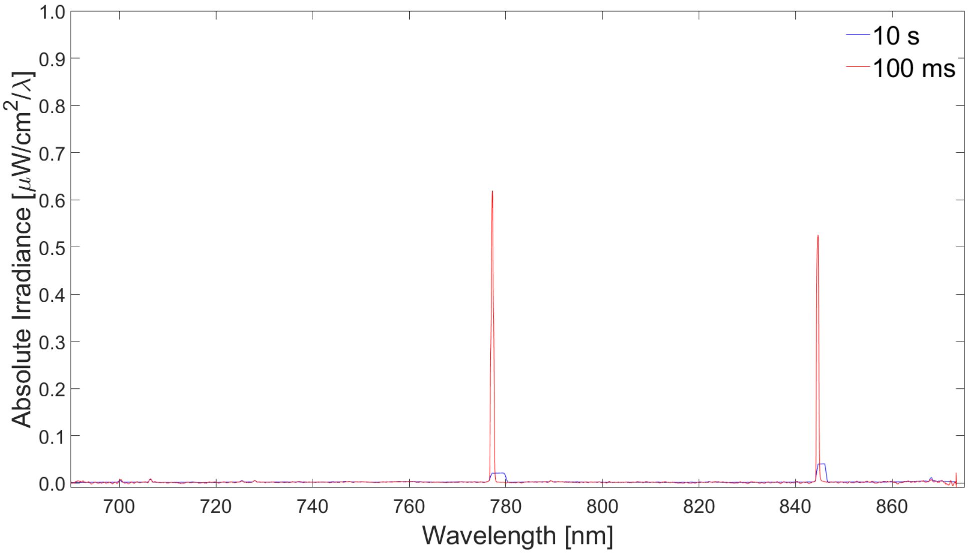

(a)

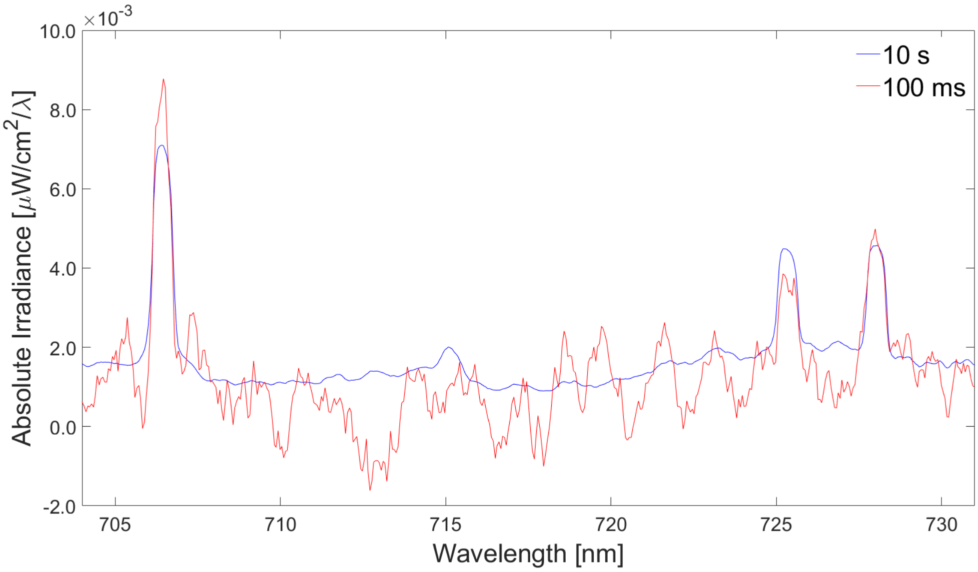

(b)

Figure 7.6: The effect of integration time on recorded spectrum signal: a) Full spectrum of the plasma captured using the HR4C4860 VIS spectrometer with equal amounts of helium and oxygen at 15 Pa, 600 W and b) Close-up on the helium emission lines of the same spectrum. The oxygen lines are much more identifiable than helium's and only need short exposure time to obtain good signal. It becomes well saturated at 10 s. Conversely, adjusting this allowed for easier identification and integration of the helium peaks from the background.

As with the pure helium case, the effect of pressure was investigated in a He-20%O_2 mixture. Figure 7.7 shows that the I_{706}/I_{728} steadily increases with pressure. Thus, the addition of oxygen does not have an immediate negative impact on the qualitative description of the mean electron energy using the helium emission lines. Although, the uncertainty is much greater - since the energy threshold difference between the helium lines is small, deriving the mean electron energy from this ratio can result in large uncertainty. Hence why comparison with an argon line is needed since it has a much lower threshold energy and so would be less sensitive to fluctuations. Compared with the pure helium case, the I_{706}/I_{728} ratio is lower in the He-20%O_2 mixture, corresponding to higher mean electron energies. Anjum et al. [164] also observes this effect upon slight addition of oxygen, and noted that there was a reduction in the electron density. Conversely, the analysis of ratios employed here should mean that the dependencies on n_e cancel out. Instead, metastable helium that is likely to be present in pure helium are quenched by the addition of oxygen. Looking at the excitation cross-sections from these metastable and lower-lying states in [162], the 2^3S is larger at lower energies than the 2^1S. As a result, elimination of step-wise excitation affects the 706 nm line more.

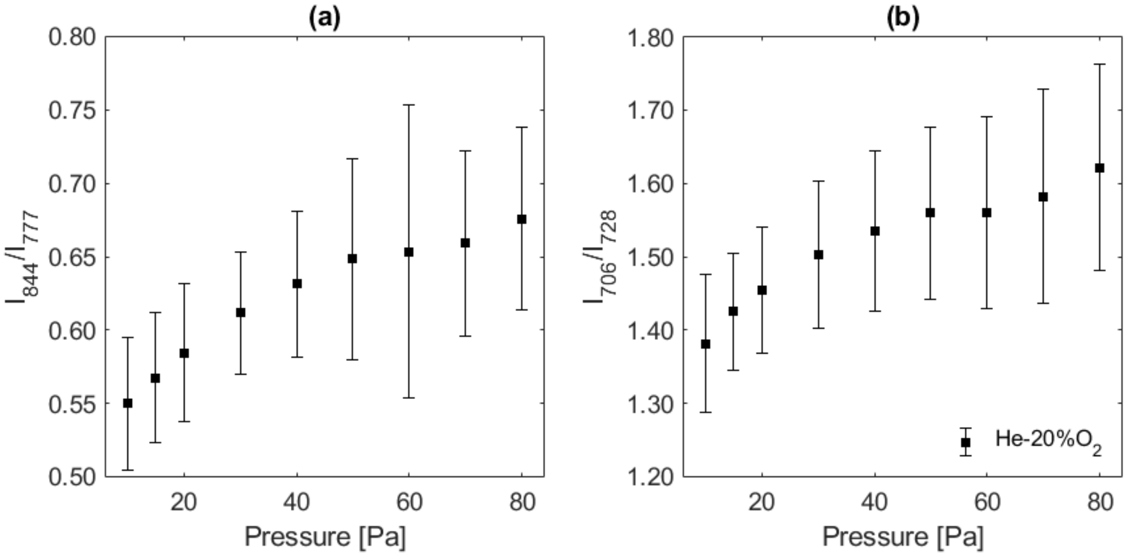

Figure 7.7: Effect of varying pressure on a) oxygen I_{844}/I_{777} and b) helium I_{706}/I_{728} emission intensity ratios for He-20%O_2 at 100 W. Increase in the I_{706}/I_{728} with pressure is still observed with oxygen addition for the same reasons as seen in the pure helium case.

On the other hand, figure 7.8 shows that increasing the applied power reduces the I_{706}/I_{728} ratio, which translates to an increase in mean electron energy. The rate at which the ratio decreases also seems to be affected by the pressure as the change is more pronounced at the highest pressure at 80 Pa. This overall trend with applied power is contrary to the capacitively coupled case of Anjum et al. [164]. Nonetheless, this work utilises inductive heating and the effect of increasing power can have a combination of two effects. Firstly, there will be reduced capacitive coupling and in turn the high energy tail EEDF will be less, though this would instead show I_{706}/I_{728} to increase. Secondly, gas heating can cause the plasma to become less dense and therefore reduce the amount of collisions. This would allow electrons to gain energy and so this explanation would match the trend observed.

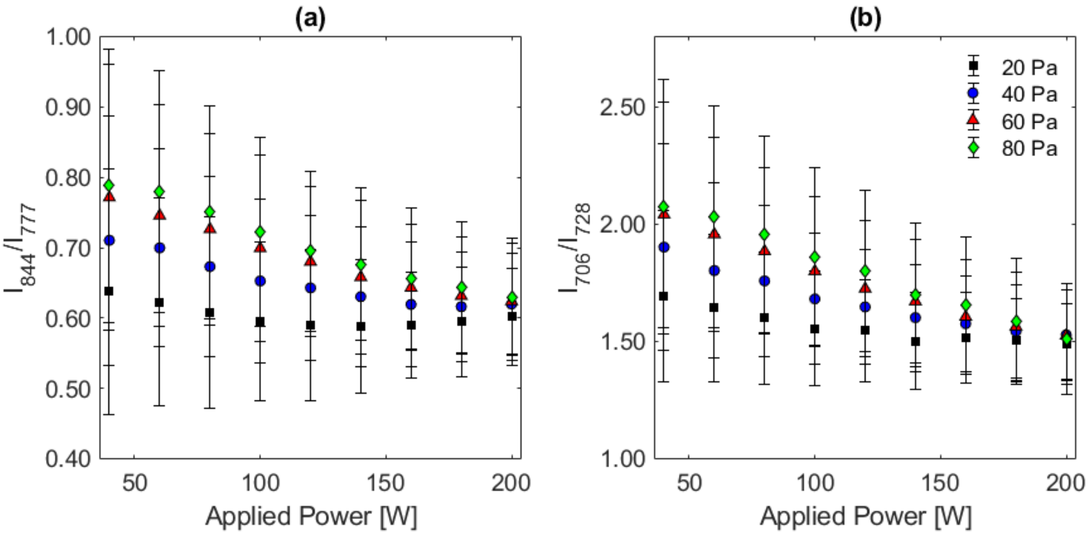

Figure 7.8: Effect of varying power on a) oxygen I_{844}/I_{777} and b) helium I_{706}/I_{728} emission intensity ratios for He-20%O_2 at 20 Pa.

7.2.3 Effect of argon addition on helium emission

Finally, argon is required for actinometry of atomic oxygen through the 750 nm emission. Also, this line will provide better contrast of the tail population since the excitation threshold is 13.48 eV compared to helium at ∼23 eV, as opposed to comparing both helium lines with each other where the slight energy difference between the excitation threshold energies of only ∼0.2 eV may make it more sensitive to uncertainty. However, argon has many other transitions that populate the spectra. Figure 7.9 shows many more spectral lines with the slightest addition of argon. Unfortunately, a few of these transitions overlap with the helium emission lines as well. At 706 nm, an argon transition overlaps directly with the helium. Similarly, the 728 nm emission line has two weaker argon transitions in close proximity to it.

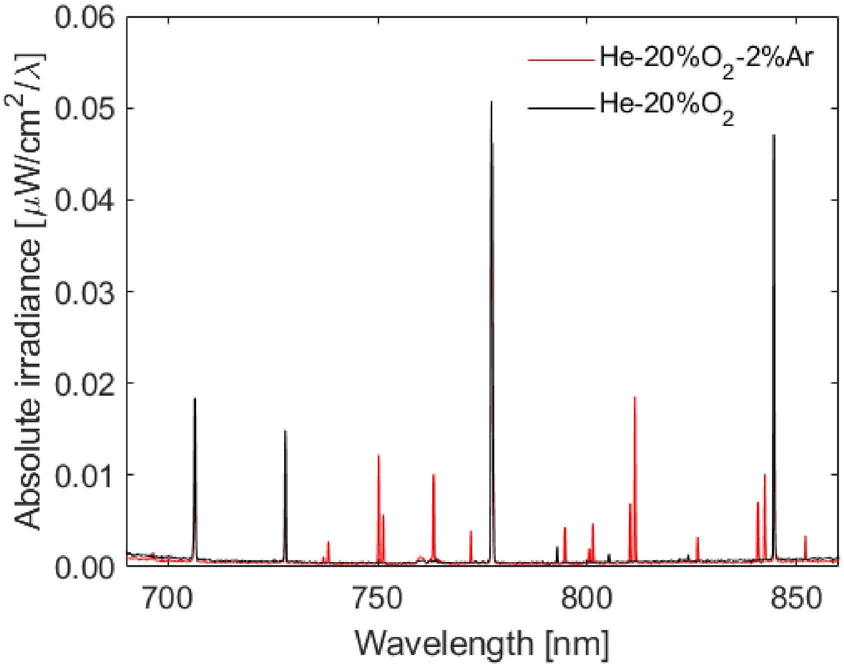

Figure 7.9: The addition of argon introduces many emission lines that can overlap with the helium emission lines of interest.

Figure 7.10 is a close-up of the previous figure - the helium and argon cannot be easily resolved using the USB spectrometer, and the relative contributions from each species can change with input parameters. This can add unwanted noise in the determination of mean electron energy. Nonetheless, the addition of argon reduces the emission intensities at these helium wavelengths; it subtly reduces the mean electron energies, and in turn the helium emission. Others have also used minute quantities of argon so as not to perturb the plasma [100, 101]. In contrast, this is where the use of neon may be advantageous; since it has a distinct emission line, there is unlikely to be much overlap with other transitions and therefore its application could be investigated in future work.

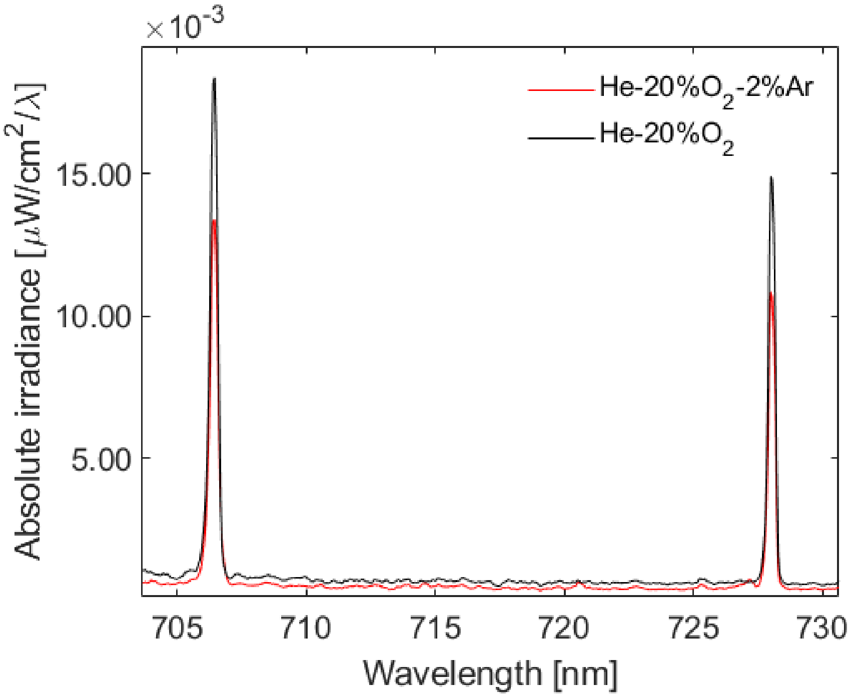

Figure 7.10: A close-up of the helium emission peaks. Addition of 2% argon does not increase the 706 nm emission line where there is a possible overlap.

7.2.3.1 Study of varying Ar on emission intensity ratios

Figure 7.11 shows the effect of increasing argon addition has on the emission intensity ratios. In particular, the 706/728 emission intensity ratio greatly increases as the proportion of argon increases. Compared to the zero argon case, the 706/728 emission intensity ratios are similar with argon contents of 2-5%. Any more than this results in a much significant change.

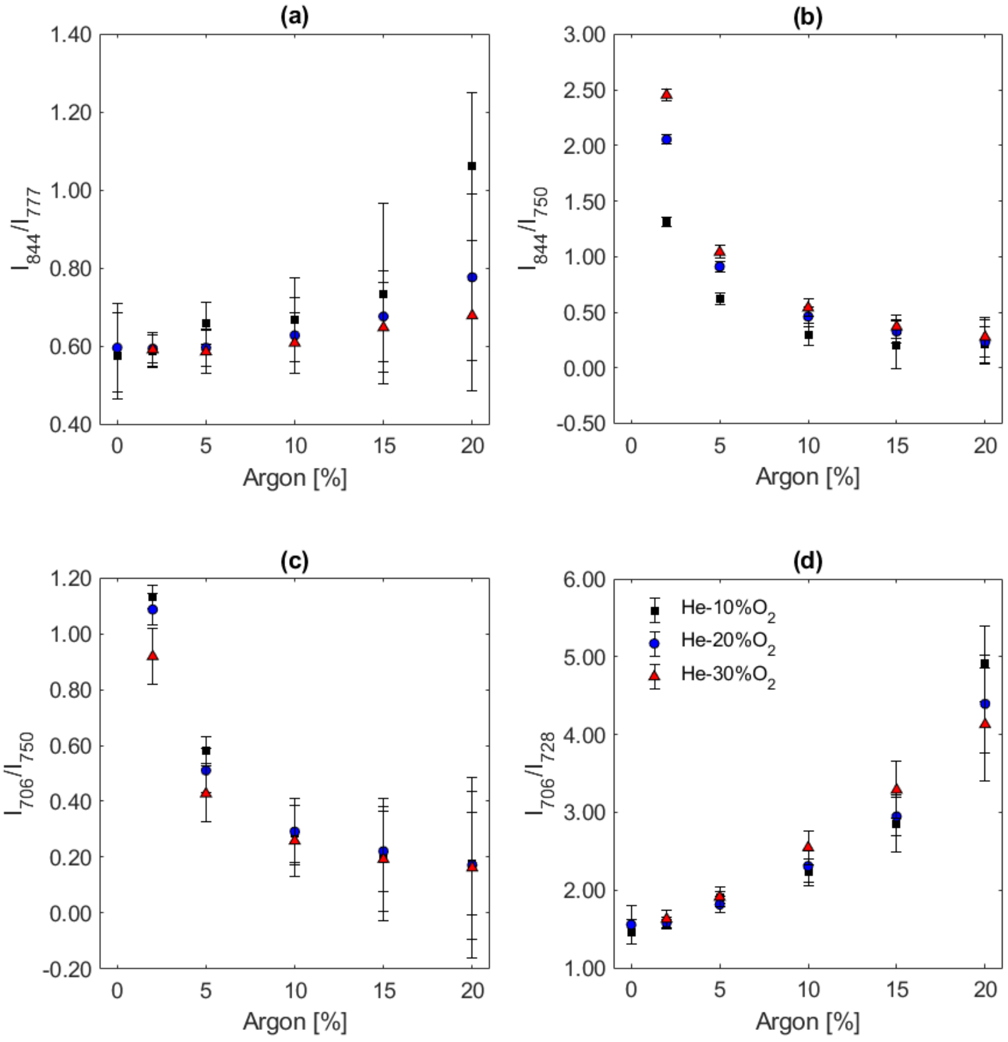

,

Figure 7.11: Effect of argon on various emission ratios of interest: a) oxygen ratio, I_{844}/I_{777}, b) actinometric ratio, I_{844}/I_{750}, c) helium-argon ratio, I_{706}/I_{750} and helium ratio, I_{706}/I_{728}. Increasing the proportion of argon in the admixture strongly promotes its contribution to the 706 nm emission intensity. All taken at 20 Pa, 100 W.

To mitigate this issue, varying amounts of argon were admitted as a proportion of the gas mixture in order to find out when the determination of mean electron energy becomes less reliable. Since the 706 and 728 nm have roughly the same excitation threshold energy, taking emission intensity ratios with argon 750 nm should roughly give the same mean electron energy. The point at which these results start to give unreliable values, or when they disagree with each other will be considered to be when the argon emission has become dominant.

As an estimate, the mean electron energy was determined by comparing the emission intensity values of both I_{706}/I_{750} and I_{728}/I_{750} with their corresponding theoretical effective excitation ratios e.g. $I_{706}/I_{750} \approx E^*_{706}/E^*_{750}$. The intensities from the spectrometer were also adjusted to account for the photon energy and also the natural lifetimes of the excited state such that $I_\lambda \propto n_i E_\lambda / A_{ik}$, where A_{ik} were 4.5e7, 1.55e7 and 1.83e7 s^{-1} for the 750, 706 and 728 nm, respectively.

Figure 7.12 shows that both ratios report similar T_e for 2% argon content, notwithstanding the He-20%O_2-2%Ar measurement. Afterwards, they return different values and trends. The 706/750 ratio predicts almost no change in electron temperature of 22.5 eV after 5%. This is due to the overlap between the helium and argon lines at this wavelength and so the contribution is likely to be dominated by argon at this point. Table 7.2 shows the Einstein coefficients of argon at the 706 nm wavelength are much greater than the 728 nm line, so more argon would have increasing contribution. Thus, the calculated temperature is not valid for these argon contents. As a side note, the intensities between argon states may reach an equilibrium with itself, hence showing no apparent change in temperature.

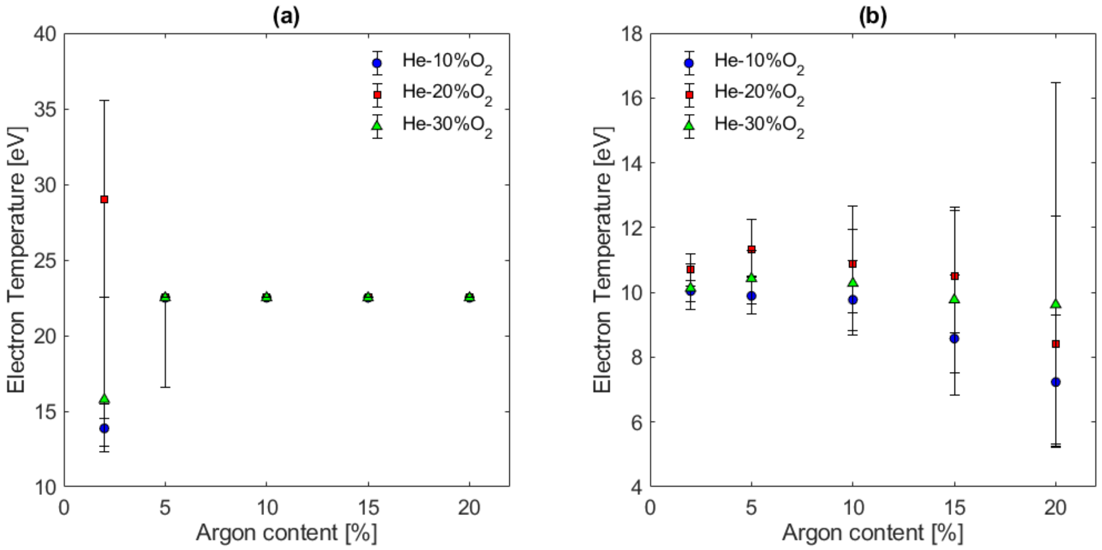

Figure 7.12: Approximated electron temperatures determined from emission intensity ratios between helium and argon using (a) I_{706}/I_{750} and b) I_{728}/I_{750} with varying argon and oxygen contents at 20 Pa, 100 W. The electron temperatures determined from this show that there is greater uncertainty as more than argon is added.

On the other hand, T_e obtained by the 728/750 ratio returns much more reasonable values, though with increasing uncertainty. It somewhat peaks at 5% and decreases with additional argon content which is consistent with cooler T_e observed by [116]; argon has a lower ionization threshold so a lower T_e is needed to sustain the plasma.

The relative increase in the 706/728 emission intensity ratio between the two cases is presumed to correspond to that caused by argon. Figure 7.13a shows the relative increase in the 844/777 and 706/728 emission intensity ratios, between the He-O_2-2%Ar and the control case of He-O_2. For the oxygen ratios, there is little effect that 2% argon addition has, with the ratio being near unity. On the other hand, it has an average of a 15% increase for all He-O_2 admixtures. Figure 7.13b has smaller changes with varying power - on average of 10% increase. Although, the uncertainties in these are rather large. The fact that the ratios between the helium lines are slightly higher is due to the slight lowering of the electron temperature upon argon addition as mentioned earlier. Since the 706 nm threshold energy is lower than the 728 nm, it would be less affected by the reduction of high energy of electrons.

The reason for the large uncertainties in figure 7.13b was related to the integration time of the spectrometer. The power variation of the He-O_2 measurements were all taken at fixed 1 second integration time to expedite the process. In contrast, the He-O_2-2%Ar mixture had integration times adjusted to maximise the signal-to-noise, from 10 seconds at 40 W to

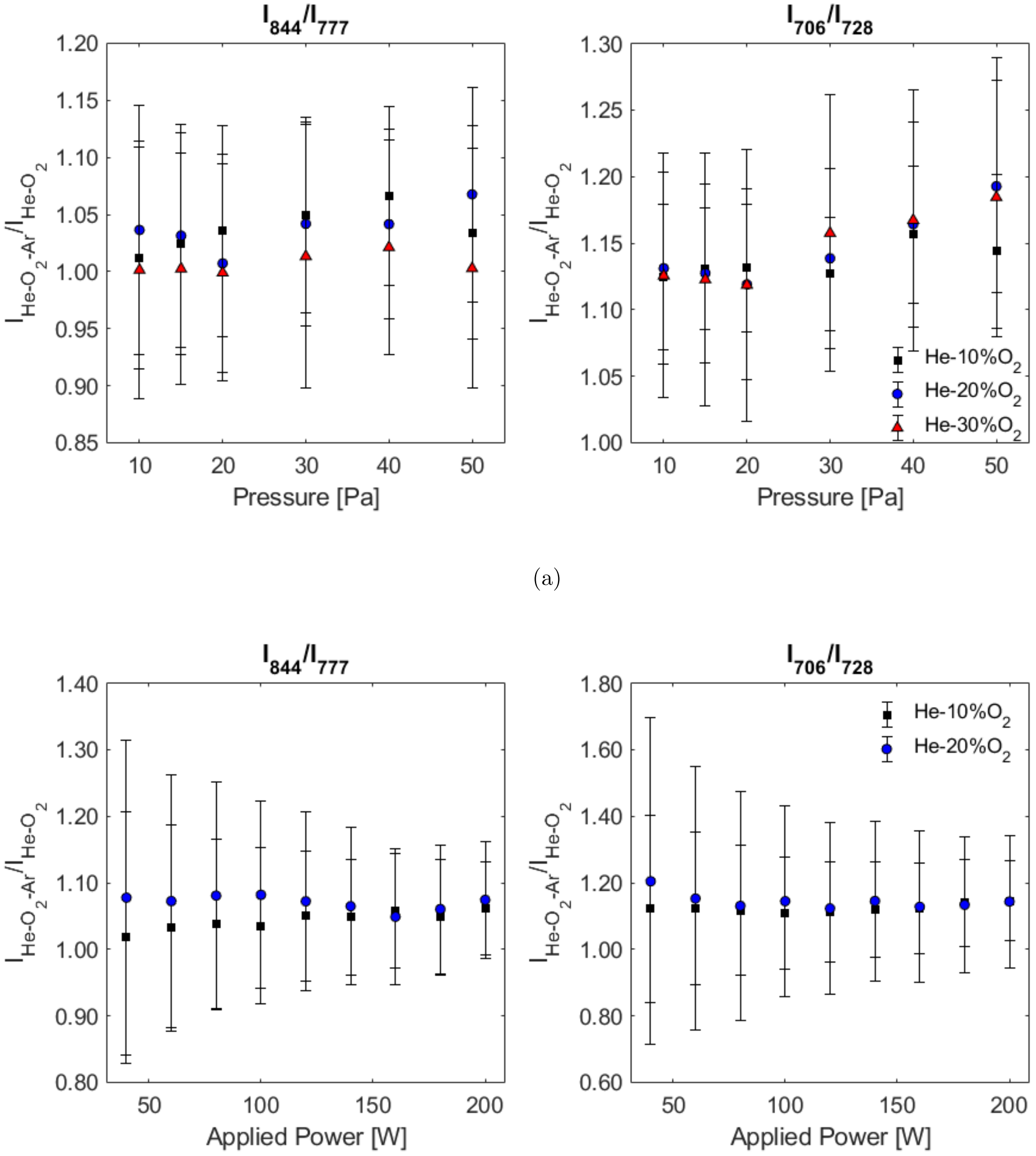

(a)

(b)

Figure 7.13: Quantifying the effect of 2% argon addition on the helium lines with variation of a) pressure and b) applied power. The effect of 2% argon on the 706 nm emission line was approximated by observing the relative change of the 706/728 emission intensity ratio in admixtures with and without under the same operating conditions. It was more prominent with increasing pressure whereas it remained constant with applied power.

3 seconds at 200 W. As a result, the latter set had much smaller error, as seen in figure 7.14. It is believed that retaking the He-O2 measurements with longer times would reduce the uncertainty.

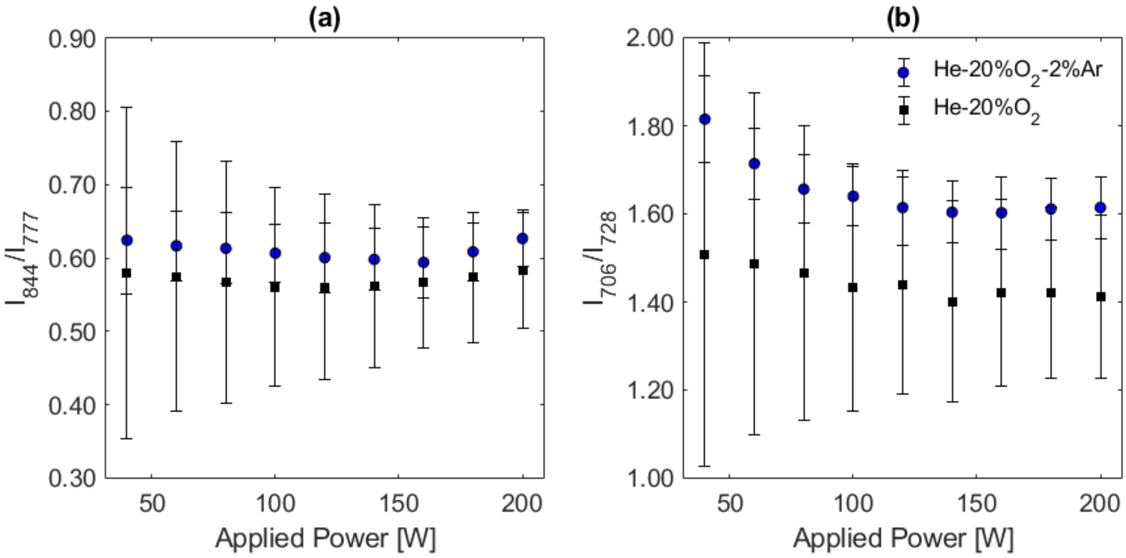

Figure 7.14: The emission intensity ratios of a) I_{844}/I_{777} and b) I_{706}/I_{728} for varying power at He-20%O$_2$, with and without 2% Ar. Longer integration times at each power were taken for the sets with argon, resulting in much smaller uncertainty. Hence, the large errorbars observed can be mitigated by optimising the spectra exposure time and reduce its impact on the calibration of the subsequent PROES images.

Figure 7.15 shows the uncertainties for the varying pressure case with the same admixtures. Again, the uncertainties in these ratios were lower when more signal was captured through longer integration times (a few seconds). The ratios were consistently larger with the argon addition, but within the limits of errorbars of the no argon case too, reinforcing the notion that this has a small impact on the measured ratios.

In conclusion, the amount of argon in the system should be as minimal as possible, with no more than 2% of the total mixture if using 706 nm emission, or 5% even 10% if using 728 nm. Moreover, to get as much signal from the helium emission lines as possible, the maximum amount of oxygen investigated will be 20% and have as much integration time on the spectrometer for the calibration.

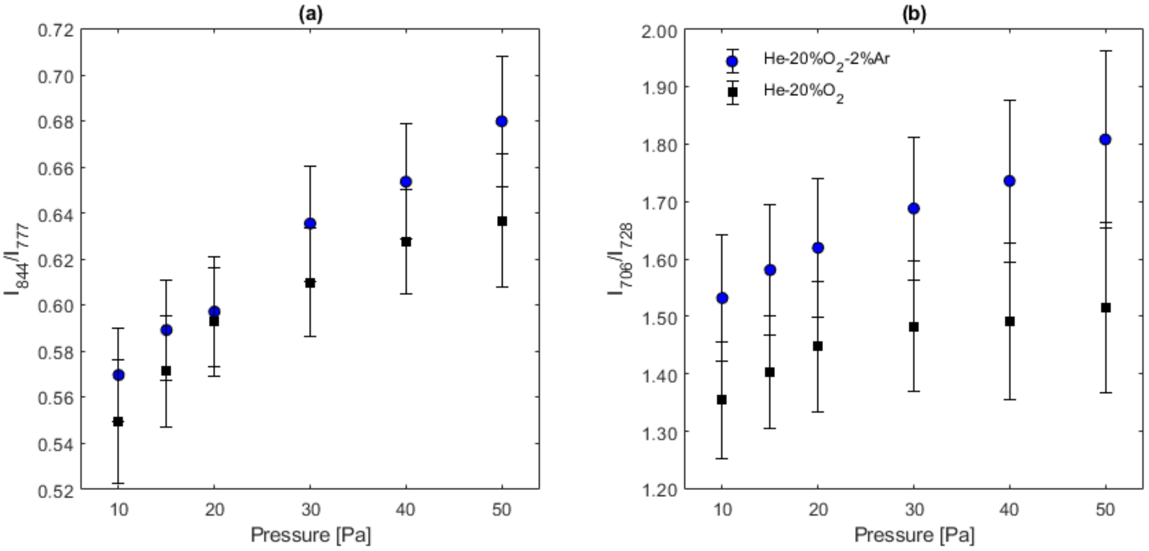

Figure 7.15: The emission intensity ratios for a) I_{844}/I_{777} and b) I_{706}/I_{728} for varying pressure at He-20%O_2, with and without 2% Ar. The ratios are within the calculated uncertainties - addition of small amounts of argon do not affect these values greatly and therefore will have minimal impact on derived parameters.

λ	Lower - Upper	E_{th} [eV]	A_{ij} [$10^6 s^{-1}$]
706.72	$1s_5 - 2p_3$	13.30	3.80
706.87	$2p_8 - 3s_5$	14.85	2.0
720.70	$2p_3 - 3s_2$	15.02	2.48
726.52	$2p_7 - 4d_2$	14.86	0.17
727.29	$1s_4 - 2p_2$	13.33	1.83
731.17	$2p_7 - 3s_4$	14.85	1.7
731.60	$2p_2 - 3s_2$	15.02	0.96
735.3	$2p_8 - 4d_4$	14.78	0.96
735.3	$2p_7 - 3s_5$	14.84	0.20
737.21	$2p_9 - 4d'_4$	14.76	1.9
738.40	$1s_4 - 2p_3$	13.30	8.47
739.30	$2p_6 - 3s_4$	14.85	0.72
725.1		13.4^a	

Table 7.2: Argon transitions taken from Boffard et al. [165]. It was prudent to account for possible interference with the helium emission intensities as this would influence the determination of plasma parameters in the excitation model. The final wavelength listed is an atomic oxygen line, which potentially adds further ambiguity.

7.2.4 Experimental modifications to enable HERA

The experimental procedure in taking the PROES images were largely the same as the ERA case. However, another optical filter was needed to filter out the helium emission line studied. The 728 nm helium line could be used, but given the available optical filter (Thorlabs) to study this line, 730 ± 10 nm, this would also pick up neighbouring emission, especially the more prominent $Ar(2p_3) \rightarrow Ar(1s_4)$ transition. These have different Einstein coefficients and therefore can affect the temporal emission profile.

On the other hand, the 706 nm was the favoured candidate as it had the strongest observed emission between the two helium lines. The optical filter used was an LOT Quantum Design narrow bandpass filter 706.5 ± 0.5 nm. Despite this, there is possible overlapping emission at 706 nm from argon. This can affect the calibration of the PROES images as not all of the intensity will be from helium, but the $Ar(2p_3) \rightarrow Ar(1s_5)$ and $Ar(3s_4) \rightarrow Ar(2p_8)$ transitions as well, though the latter is likely to be quite weak. Due to the potential issue with argon, various admixture ratios were tested to determine the allowable amount that did not impact the emission severely.

To produce the excitation profiles, additional information is needed regarding the quenching coefficients of the helium excited states. Unfortunately, no data exists of these with molecular oxygen. Instead, the quenching coefficient between molecular hydrogen and excited helium are used as an approximation.

Helium	$k_q^{H_2}$ [m^3s^{-1}]
$He(3^3S)$	9.6e-16
$He(3^1S)$	10.7e-16

Table 7.3: Quenching coefficients of the excited helium states using H_2. No data exists for the quenching coefficient of helium with molecular oxygen. Instead, that with hydrogen is used instead as a substitute from Gans et al. [97].

7.2.4.1 Calibration spectra

For each plasma operating condition, a series of spectra were taken, and similarly the same number of background measurements with the plasma off. Then, the average background value was subtracted from the average spectra measurements. This background-removed data was then used as in the ERA calibration where the area underneath the emission peaks was used to adjust the total counts of the recorded PROES images.

7.3 Helium Energy Resolved Actinometry results

7.3.1 Comparison of plasma parameters between ERA and HERA

To initially gauge the accuracy of the modified technique, both it and conventional ERA were applied to the same plasma conditions in the E-mode. ERA has been shown to agree well with TALIF, so by extension good agreement between HERA and ERA can give confidence to this alternative approach. Moreover, it is much more straightforward to change filters than carrying out TALIF. Thus, the results using the 750, 777 and 844 excitation ratios were compared with the 750, 706 and 844 (HERA-706), and also 750, 728 and 844 (HERA-728) excitation ratios.

Figure 7.16 shows good agreement between the original ERA ratios and HERA-706 except at 20 Pa. In contrast, HERA-728 predicts much lower mean electron energies - it is roughly half that of the ERA ratios. Although, it does show a drop in mean electron energy with pressure more noticeably than HERA-706. Moreover, in figure 7.17 the dissociation degree is the highest using the HERA-728 in lieu of lower mean electron energies. The fact that this is the case may be the reason why lower electron energies are found from the higher energy threshold line - it is due to the Bayesian analysis where better agreement was found for these values. Similar dissociation degree values are found between ERA and HERA-706.

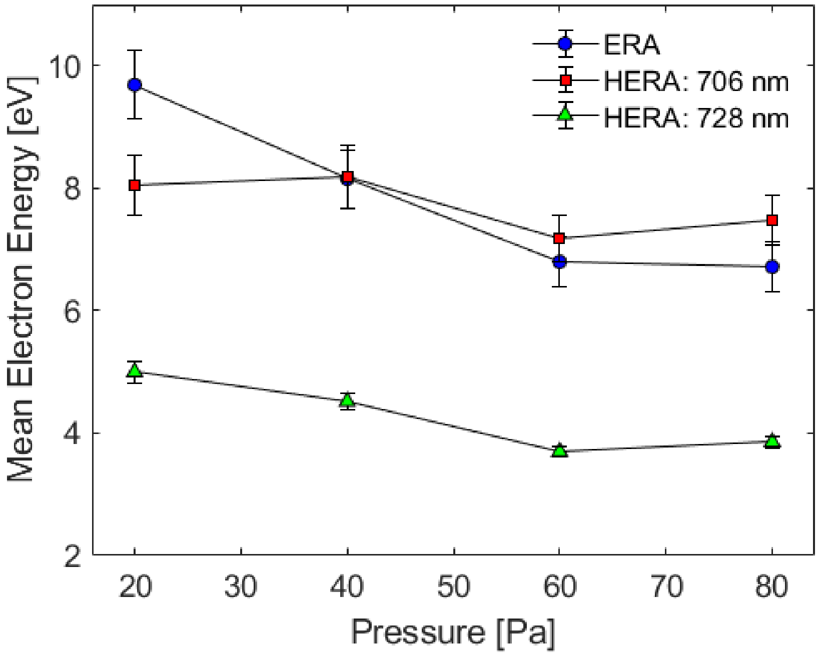

Figure 7.16: A comparison between using the original excitation ratios of ERA and an alternative helium line to obtain the mean electron energy in E-mode (100 W), He-20%O_2. Using the 706 nm emission gave similar mean electron energies as the conventional ERA lines. Conversely, the 728 nm line returned nearly half of these values.

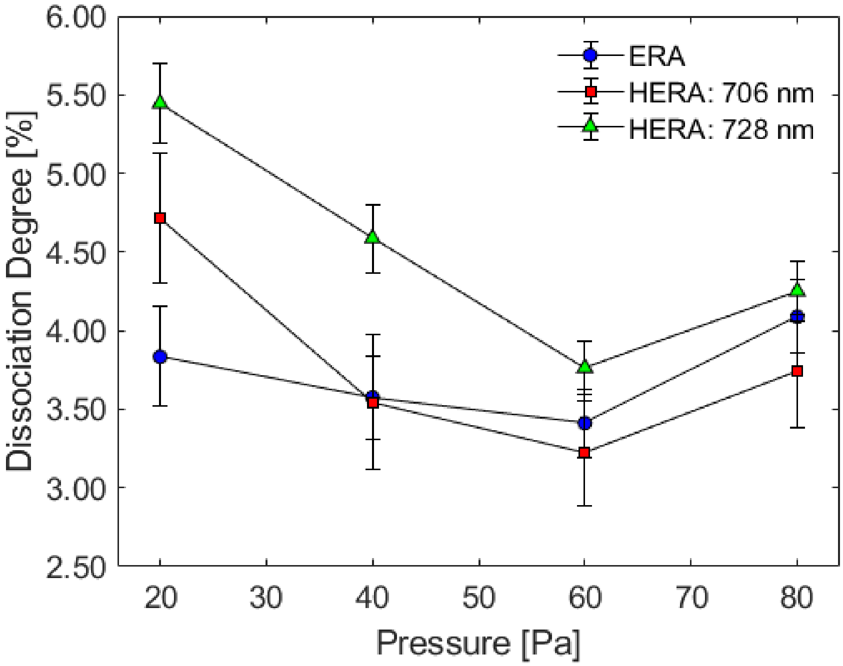

Figure 7.17: A comparison between using the original excitation ratios of ERA and an alternative helium line to obtain the dissociation degree in E-mode (100 W), He-20%O_2. Similar values were found using both helium lines.

Overall, figure 7.18 shows that using either HERA ratios give comparable atomic oxygen densities that increase with pressure. The atomic oxygen densities were all calculated assuming a gas temperature of 400 K.

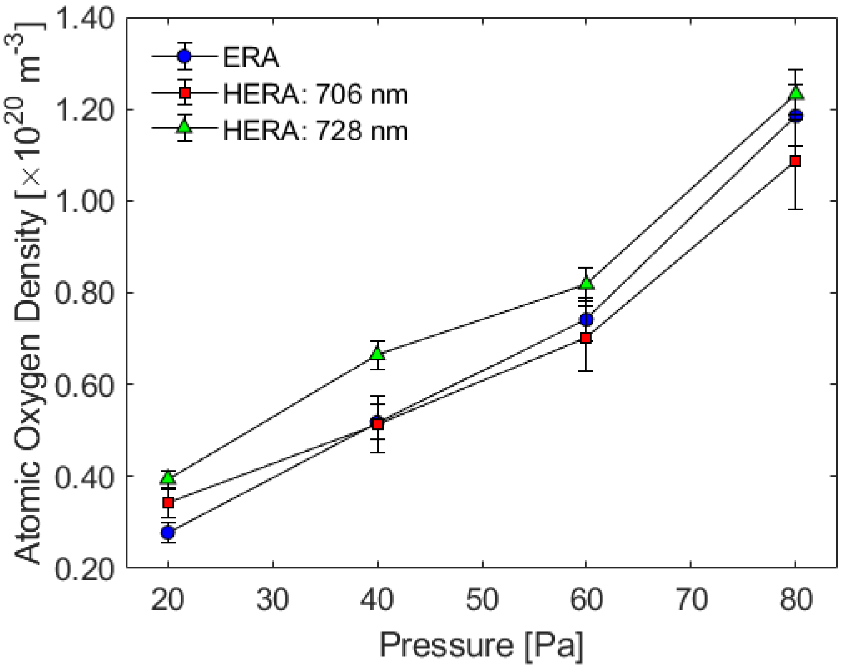

Figure 7.18: A comparison between using the original excitation ratios of ERA and an alternative helium line to obtain the atomic oxygen density in E-mode (100 W), He-20%O_2. Overall, similar n_O values were found over the pressures explored.

To recap, the use of a helium emission line has been proposed to substitute the less reliable oxygen 777 nm emission in ERA. Thus, admixtures comprising of helium, oxygen and argon were investigated; the subsequent proportions of oxygen and argon on the helium emission intensity were optimised so that plasma parameters could be obtained without too much adverse affects from quenching and overlapping emission. Also, the effects of applied power and pressure on the spectra helped to assess the feasibility. Of the two helium lines, HERA-706 gives the most agreement with the original excitation ratios of ERA. Consequently, HERA will refer to ERA using the helium 706 nm emission line from hereon, and will be applied to H-mode plasmas.

7.3.2 Direct comparison of measured n_O between TALIF and HERA on the GEC in H-mode.

The absolute atomic oxygen densities from the TALIF chapter are directly compared with HERA for 10% oxygen case under varying power at 20 Pa in a system that was pumped down using the turbo-pump. An immediate issue with using the same excitation equation as before was that it yielded dissociation degrees in excess of 100%, which is physically impossible. As a result, an alternative case where dissociative depletion was considered, where the excitation contribution from molecules reduces after having been dissociated into atoms. The excitation ratio E_{844}/E_{750} was updated as in equation (7.4) to reflect this. Thus, the definition of dissociation degree was the same as [87], with the total number of atomic oxygen and remaining molecular oxygen species accounted for each r_O.

$$\frac{E_{844}}{E_{750}} = \frac{f_{O2}}{f_{Ar}} \frac{2r_O k_{844,d}(\langle\epsilon\rangle) + (1 - r_O)k_{844,de}(\langle\epsilon\rangle)}{k_{750}(\langle\epsilon\rangle)} \tag{7.4}$$

With this, more reasonable values of dissociation degree were obtained, ranging from $20.9 \pm 8.5\%$ at 500 W to $32.2 \pm 10.7\%$ at 1000 W in figure 7.19. From this, the calculation of $n_O = 2r_O \cdot p/k_B T_g$ where $T_g = 400$ K yielded similar order of magnitude of atomic oxygen densities as TALIF, as seen in figure 7.20. This gas temperature was used because the atomic oxygen species was shown to cool to around this value previously. Thus, the background molecular oxygen was deemed to be at this gas temperature prior to dissociation of each pulse. The increase with applied power was slightly more apparent than TALIF under the same conditions and is likely associated from the intensity of light passively observed having a more consistent relationship with applied power. Aside from the 500 W point, the HERA measurements were roughly 3 times larger than TALIF.

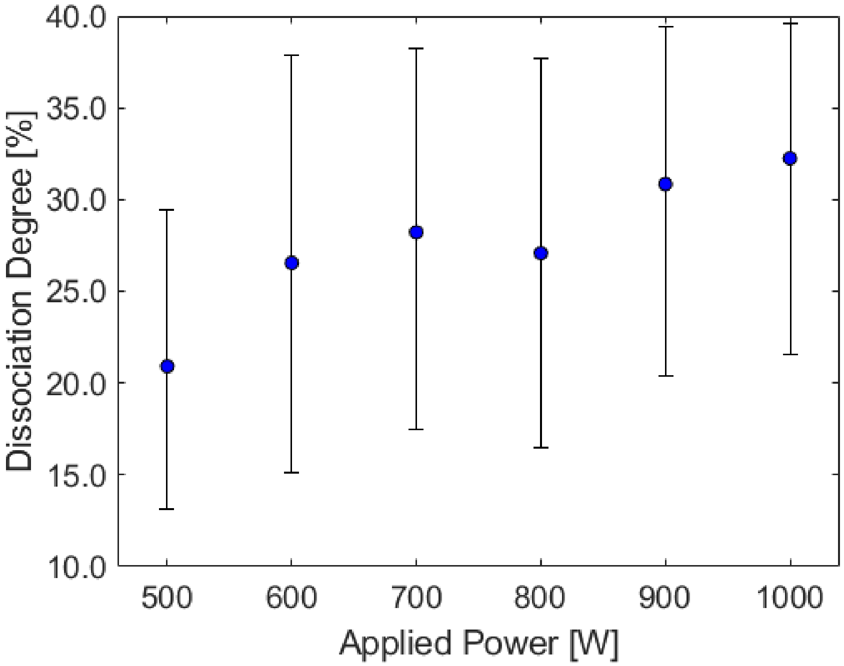

Figure 7.19: Dissociation degree with applied power in the H-mode using HERA. The model for the E_{844}/E_{750} excitation ratio was updated to better account for the relative contributions of 844 nm. After accounting for dissociative depletion, the dissociation degree increases with applied power. He-10%O$_2$, 20 Pa.

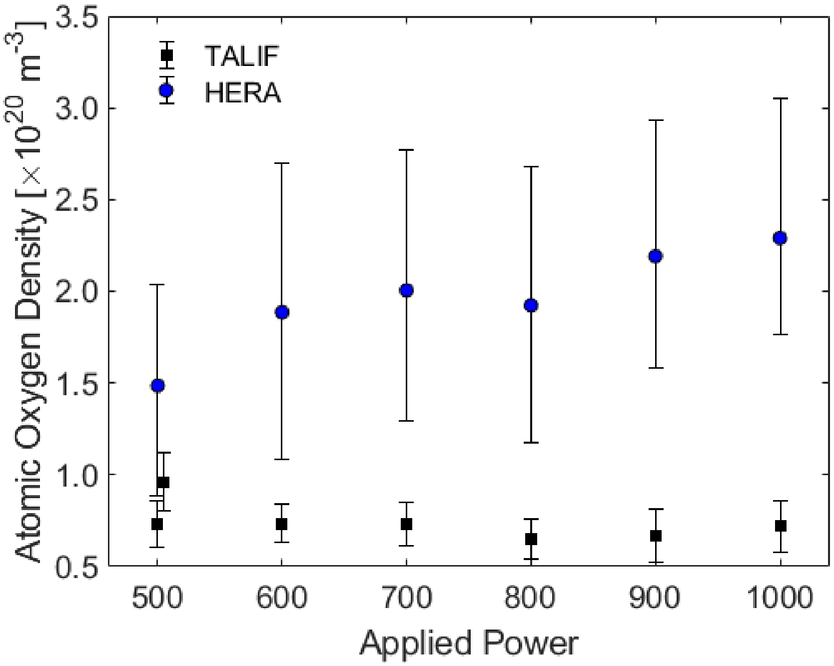

Figure 7.20: TALIF versus HERA measured n_O with increasing applied power on same GEC reactor. Atomic oxygen densities were around 3× higher than TALIF for He-10%O$_2$ at 20 Pa.

As mentioned in previous chapters, the technique also determines the mean electron energy. The analyses assumed a Maxwellian electron energy distribution, so electron temperature can be interchangeably used in this case to describe the mean energy. Figure 7.21 shows that the mean electron energies ranged between 6.6 ± 1.8 and 8.2 ± 3.1 eV. While similar electron temperatures were found in this range [101], the pressure in this work was much higher. Nonetheless, this may be offset given that the admixture here is high in helium content rather than pure oxygen, and so higher mean electron energies are needed to sustain the plasma given the former's high ionization energy threshold (24.6 eV).

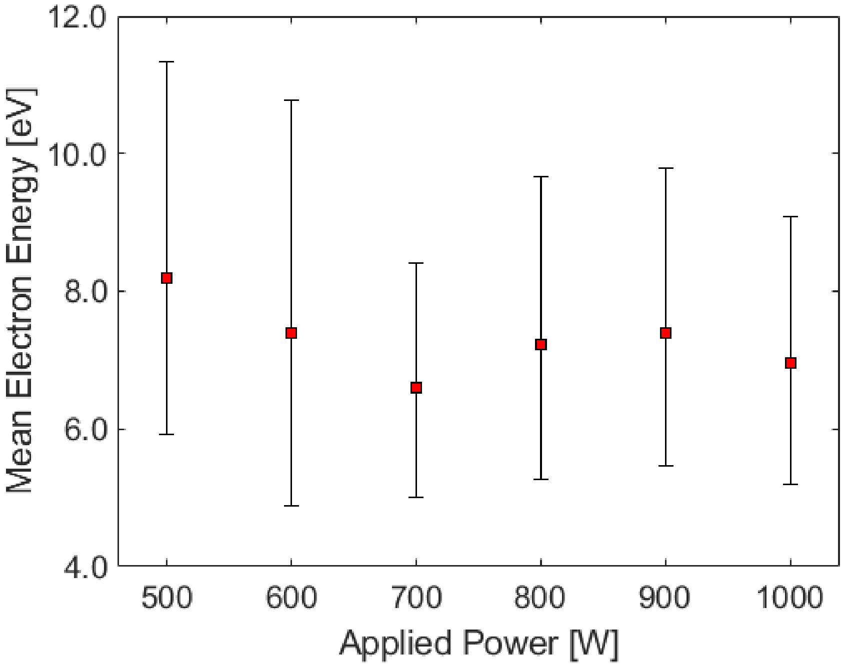

Figure 7.21: Effect of applied power on the mean electron energy. The mean electron energy remains somewhat constant with applied power. He-10%O_2, 20 Pa.

7.3.3 Application of HERA on the GEC-like reactor

Having seen that the HERA technique gives similar values of atomic oxygen density as TALIF, it was implemented onto a different plasma source. The purpose of this was to firstly reinforce the expected measured atomic oxygen densities with varying input parameters using this method over broader conditions of the helium-oxygen admixtures. Moreover, since the technique simultaneously determines the mean electron energy through passive means, it is worth verifying whether this parameter also behaves as in reported literature i.e. compared to Langmuir probes or OES methods. The mean electron energy is responsible for the determination of the plasma chemistry. Thus, studying it offers a valuable insight into how desired proportions of neutral radical species can be manipulated. Finally, it serves as a potential tool to compare the effectiveness of atomic oxygen generation between two different plasma sources.

7.3.3.1 Atomic oxygen densities

Figure 7.22 shows the effects of varying applied power and pressure in a He-10%O_2 gas mixture. Firstly, the atomic oxygen density increases linearly with applied power. At 15 Pa, the atomic oxygen density ranges from 0.73×10^{20} m^{-3} to 1.20×10^{20} m^{-3} as the applied power changes from 400 to 1000 W. This is due to an increase in power density enabling more dissociation processes. Similarly, increasing the operating pressure promotes the amount of atomic oxygen produced. At 500 W, 15 to 25 Pa sees n_O increase from 0.83×10^{20} m^{-3} to 1.63×10^{20} m^{-3}. The greater amount of oxygen available in the system to dissociate led to this increase.

The order of magnitude between the E- and H-modes can be compared in the case of He-20%O_2 at 20 Pa. From figure 7.18, n_O goes from 0.34×10^{20} m^{-3} at 100 W to 1.31×10^{20} m^{-3} at 500 W (figure 7.23). It is not an entire order of magnitude increase between modes as seen in Fuller et al. [101] and Corr et al. [56] since it is a slightly different plasma composition. Nonetheless, there was still a jump in density of 3.85 times from E- to H-mode.

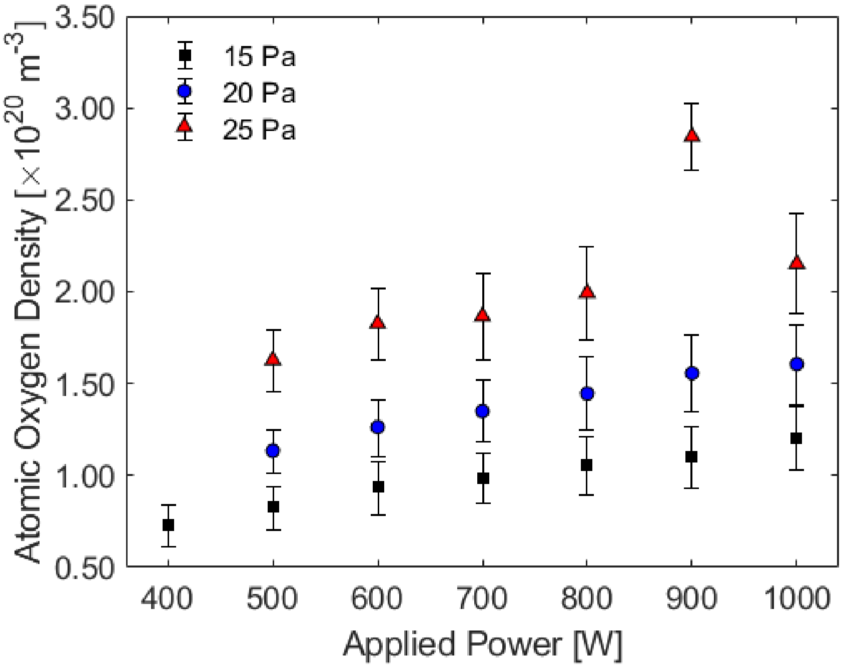

Figure 7.22: Effect of applied power and pressure on the atomic oxygen densities for He-10%O_2 on the GEC-like reactor. HERA predicts increasing atomic oxygen densities with both of these input parameters.

Figure 7.23 compares the effect of increased oxygen content. It is clear that having a higher proportion of this in the gas mixture will result in more atomic species. However, it is important to also note that while the proportion of oxygen has doubled from 10% to 20%, the overall atomic oxygen density does not give twice the amount. It is also interesting to see that the rate of increase in n_O with varying power is steeper for the higher oxygen case. Again, the higher power density in combination with more molecular oxygen present can produce more dissociation. The point for He-20%O_2 at 1000 W was omitted since the spectrometer experienced saturation from the plasma emission - the value could not accurately be determined.

7.3.3.2 Mean electron energies

Figure 7.24 shows the complementary mean electron energy values for He-10%O_2 obtained as a result of the technique simultaneously resolving two plasma parameters. Firstly, the mean electron energies were lower than the GEC reactor's results by over 1 eV at 20 Pa. This likely stemmed from increased quenching by remnants of water vapour that had not been completely evacuated, resulting in an decrease in observed emission than in the earlier case.

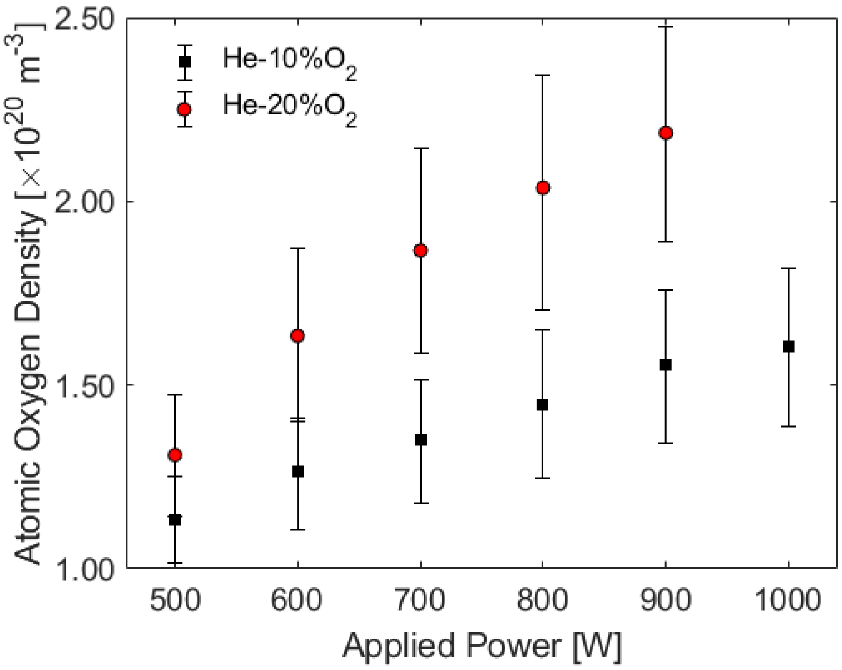

Figure 7.23: Effect of varying oxygen content on the atomic oxygen densities at 20 Pa. Greater oxygen content gives more atomic oxygen, but doubling it in the admixture does not give twice the value.

Consequently, the helium excited states suffered more from the presence of this impurity than argon's. So, less emission from the higher energy threshold was reflected by a decrease in mean electron energy. Secondly, it can be seen that the electron temperature goes down with pressure for a given applied power which agrees with [56, 120, 129]. This is due to more collisions taking place between the electrons and heavy particles limiting the amount of energy gained by the former.

Conversely, the electron temperature can be seen to increase with applied power and has been noted by others [149, 155, 166] who attribute this to neutral gas heating. Due to the ideal gas law, as the gas temperature increases while keeping the gas pressure constant, the neutral density decreases.

However, Siepa et al. [167] investigated using an argon line ratio that was sensitive to changes in the electron density: I_{706}/I_{750} and it was shown that this ratio increased with power. Although efforts were made to minimise the contribution of the argon from helium's 706 nm transition, it may be possible that the apparent increase in electron temperature is a result of the increase in electron density which has been seen to (linearly) increase with applied power [93].

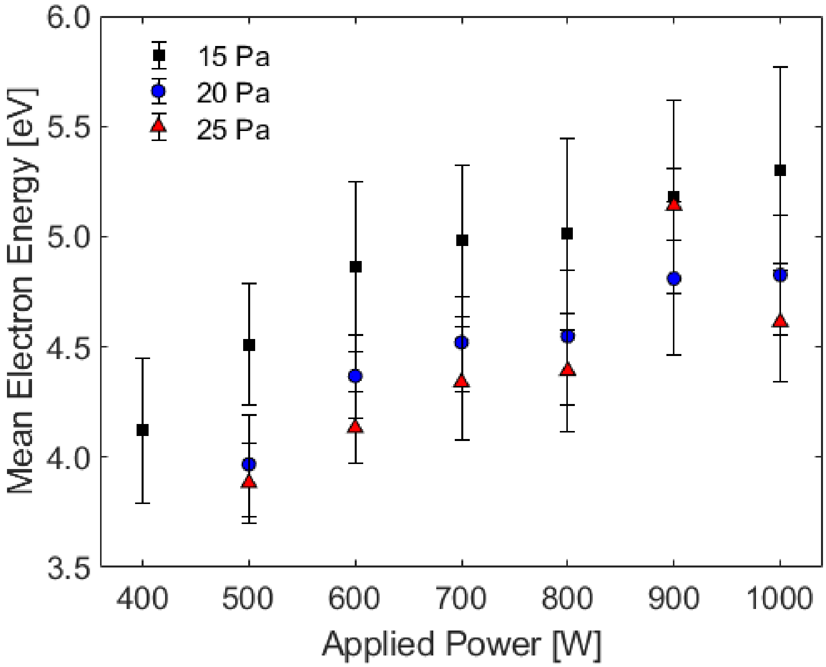

Figure 7.24: Effect of applied power and pressure on the mean electron energy in He-10%O_2. The mean electron energy increases with applied power, and decreases with pressure.

The electron temperatures determined in the E-mode were much higher than the H-mode. At 20 Pa, 20%O_2, the electron temperature was 8.05 eV at 100 W, dropping down to 2.73 eV at 500 W. Wegner et al. [120] also saw that the electron temperature dropped by at least half upon transition to the high power regime. Generally, the inductive mode has lower electron temperatures than capacitively coupled plasmas and this is seen here.

Figure 7.25 shows the effect of higher oxygen content on the mean electron energy at 15 Pa. It is lower with higher oxygen content for a given applied power. 10%O_2 ranged from 4.13 eV to 5.30 eV, whereas 20%O_2 ranged from 3.11 eV to 4.31 eV. Similar observations were made by Ma and Pu [116] in which the electron temperatures were the highest in pure helium, and the addition of nitrogen greatly reduced this value. The presence of molecular species allows for more energy loss pathways - inelastic collisions can remove energy that the electrons gain during the heating cycles. On the other hand, helium has a very high ionization threshold (24.6 eV) compared to molecular oxygen (12.6 eV). In order to sustain the plasma, the ionization rate must equal that to electrons lost, such as to the walls. Changing the plasma from pure helium towards oxygen mixtures reduce the need for high energy electrons to facilitate electron production. This is also the same argument made by

Tynan and Taylor [93] who conducted experiments using noble gas mixtures with oxygen - helium had the highest electron temperatures, compared to argon or xenon.

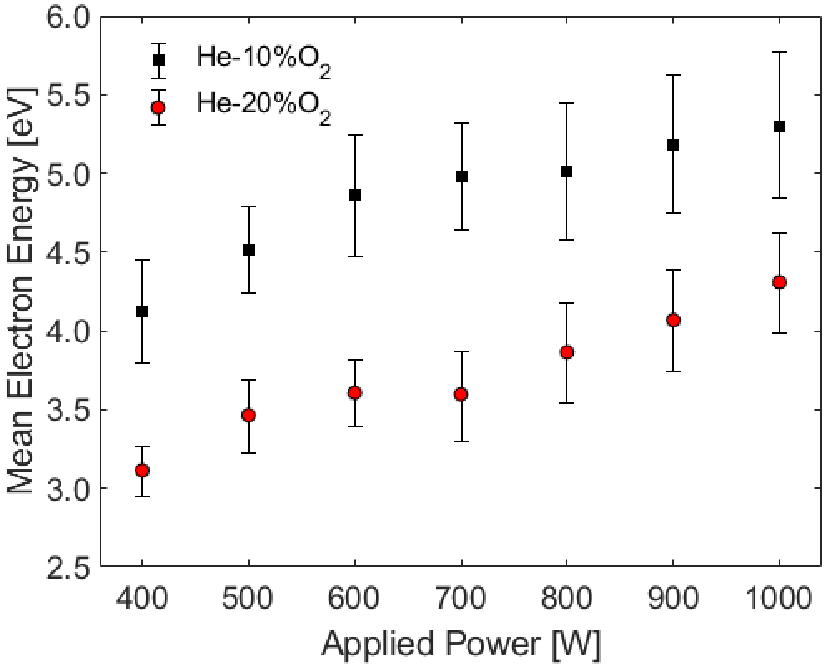

Figure 7.25: Effect of oxygen content and varying power on the mean electron energies. The mean electron energy drastically decreases with more molecular oxygen, and it is likely due to inelastic collisions. These results were at 15 Pa.

7.3.4 Comparison of trends between TALIF and HERA

Lastly, the results between the extended actinometry approach using helium emission on the GEC-like reactor are compared against TALIF measurements on the GEC under the same conditions for validation of these trends. As a reminder, the HERA measurements taken in a GEC-like reactor had a three-turn double spiral planar coil, whereas the TALIF set-up used a five-turn planar coil. The advantages of the former configuration are the reduced effects of capacitive effects [31] and also provides greater plasma homogeneity [21]. Moreover, other subtle differences such as the bottom electrode material may also have an effect on the production of atomic oxygen. Despite these, the effects of applied power in both reactors were shown to be the same as seen in figure 7.26.

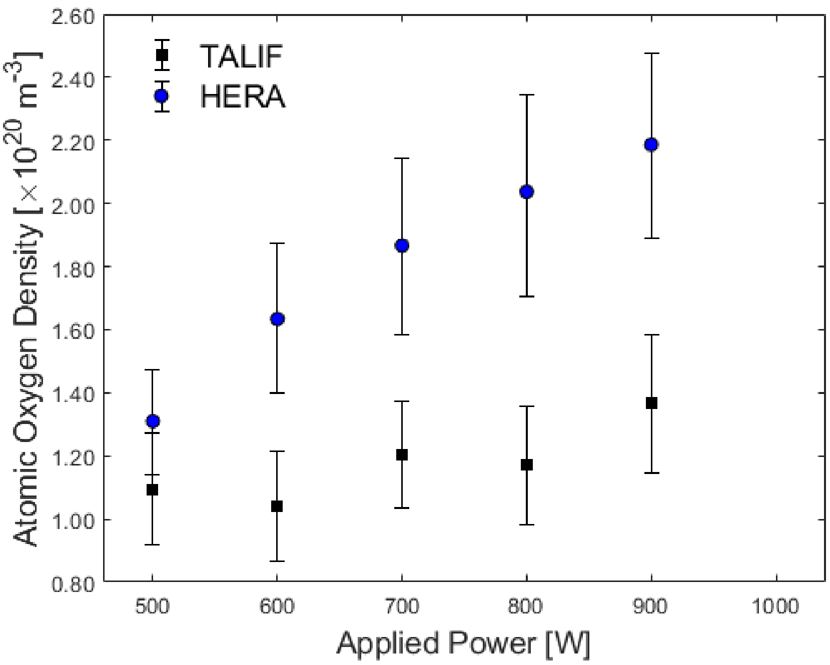

Figure 7.26: Comparing the atomic oxygen production with varying applied power of the GEC with the GEC-like reactor, with TALIF used on the former and HERA on the latter to measure the atomic oxygen densities at He-20%O_2, 20 Pa with varying applied power. A positive trend is more observable with HERA and also predicts greater n_O.

Finally, figure 7.27 compares the two diagnostics for He-10%O_2 at 600 W for several pressures. As with the power variation, both were able to measure an increase due to the greater availability of molecular oxygen to dissociate.

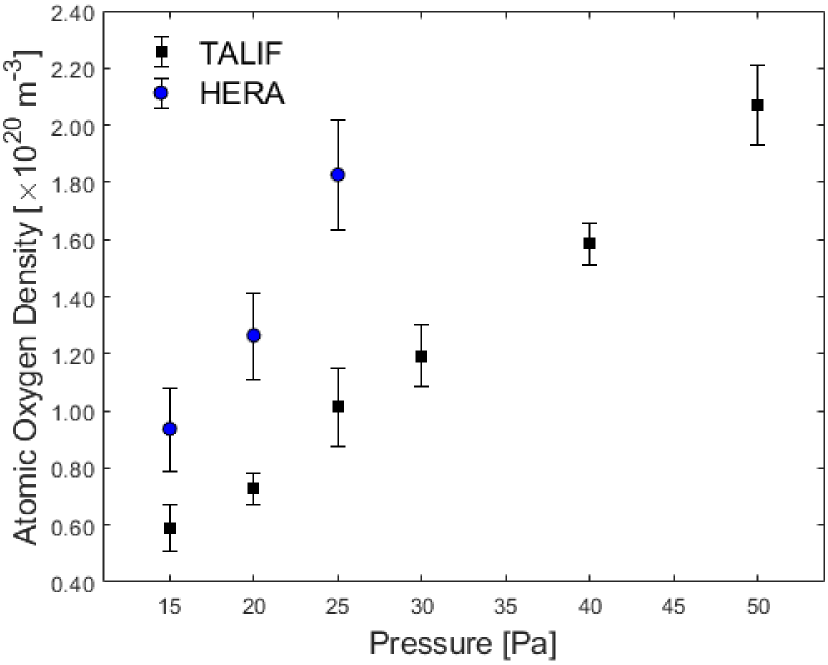

Figure 7.27: TALIF versus HERA of atomic oxygen densities for He-10%O_2, 600 W with varying pressure. Both diagnostics show good agreement, although the HERA method again measures higher values.

The dissociation degree calculated from the HERA measurements returned minor increase with pressure at constant assumed temperature of $T_g = 388 \pm 188$ K, from 17.6% at 15 Pa to 20.6% at 25 Pa, whereas those through TALIF were approximately constant all the way up to 50 Pa - the mean value was 10.9 ± 0.5%. This is shown in figure 7.28a. As a result, there is confidence in r_O measured by HERA. In contrast, the pure oxygen case in figure 7.28b shows a decrease in dissociation degree with pressure (assuming constant $T_g = 387 \pm 56$ K from similar gas temperature measurements in pure O_2). This was also observed by [56, 87] and it also approached low dissociation degree values similar to [101].

The reason for this contrasting behaviour is thought to be related to the electron density. Higher pressures typically result in lower mean electron energies, so the reaction rate for dissociative excitation should be lower. On the other hand, plasmas with high helium contents tend to exhibit higher electron densities [164, 168]. Furthermore, [131, 164, 168] all saw the electron density increase and electron temperature decrease with increasing pressure in a CCP, magnetic pole enhanced ICP, and planar ICP, respectively. Although [169] only reported the increase with n_e, it was in the same pressure range studied here for a non-planar inductive discharge. So, evidence suggests that in the case of helium, more dissociation is still

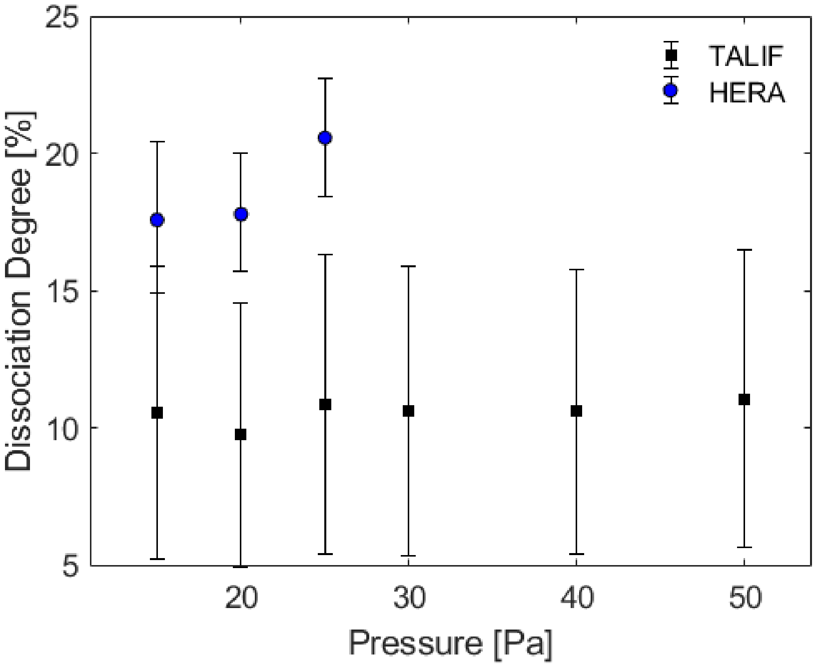

(a)

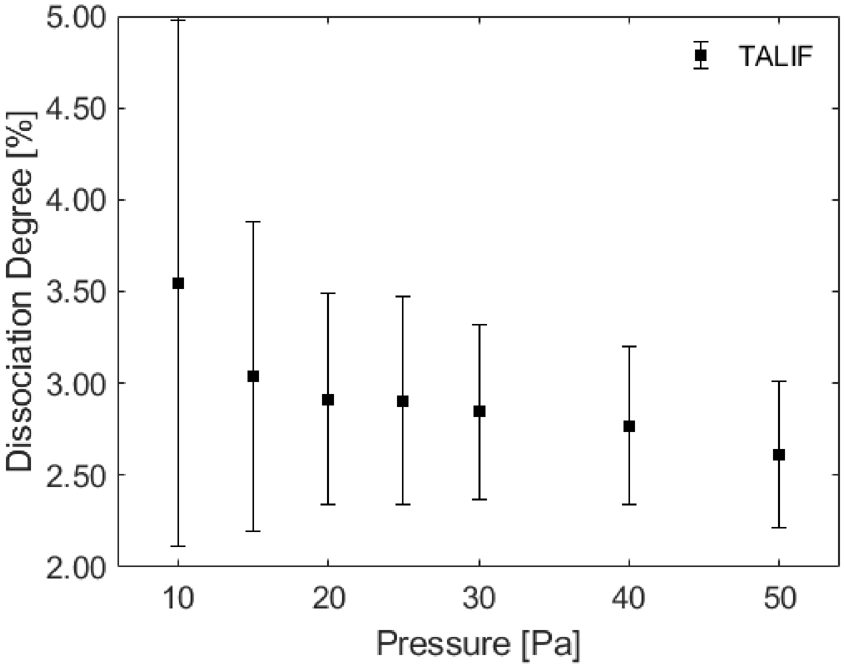

(b)

Figure 7.28: The dissociation degree of TALIF measurements between a) He-10%O_2 and b) pure oxygen with varying pressure. Contrasting trends are seen where the mixture containing helium shows constant r_O whereas the pure oxygen case decreases with increase pressure.

possible as there is a greater chance of electron collisions despite lower electron temperatures with pressure.

Thus, these qualitative effects observed by the HERA technique show the commonality of increasing input parameters across different plasma sources. Moreover, high density plasma can be generated through other means, such as electron cyclotron resonance (ECR) or microwave discharges [1]. As HERA is much less complex than laser methods, it has the potential to compare the performance of different plasma sources more easily.

Finally, it is worth mentioning that TALIF itself has been scrutinised. Peverall et al. [87] has highlighted flaws with the technique, including when using the noble gas calibration scheme which depends on two-photon cross-section ratios with high uncertainties. The xenon cross-sections were also explored by Drag et al. who found that there was a discrepancy as much as a factor of 2 [88]. Consequently, the absolute number densities measured through the TALIF measurement may be half of what is measured. Nevertheless, a key focus of developing diagnostics is to find passive techniques that are able to show qualitative agreement. Here, ease of use was also sought after. Moreover, both techniques showed similar orders of magnitude values and similar scaling with input parameters. These give confidence in the results and can be used to further refine models.

7.4 Summary

ERA was previously applied in the high-power, inductively coupled pulsed regime at pressures of 10 and 15 Pa, from 500 to 700 W. Here, the 844/750 and 844/777 excitation ratios were used to simultaneously resolve the mean electron energies and dissociation degrees. However, although there were positive trends of increased atomic oxygen density with power, the complementing mean electron energy was unusually higher than that of capacitively coupled case. Nonetheless, it was believed that the premise of using two excitation ratios to solve two unknown parameters was still viable if an alternative excitation ratio was used. Helium was selected and the 706 nm emission line was chosen to replace the less reliable oxygen 777 nm. Thus, the excitation ratio between helium (706) and argon (750) was used instead of the oxygen ratio.

Argon is a key component in determining the oxygen density. Yet, its many transition lines included overlap with the helium lines investigated. Thus, efforts were made to minimise these contributions and its effect on the resulting plasma parameters. The use of the alternative excitation ratio was tested against the ones used in conventional ERA under the same plasma operating conditions in E-mode, with both showing good agreement.

Consequently, HERA was applied to a pulsed, H-mode plasma under various applied powers, pressures and oxygen content. The model equation had to be adjusted in order to account for dissociative depletion. Otherwise, dissociation values greater than 100% were found. Good agreement was found when directly comparing both HERA and TALIF on the GEC reactor. It was then applied to the GEC-like reactor to establish its robustness on another plasma sources where similar trends were found.

Atomic oxygen densities showed a positive response when any of these parameters were increased. The decrease in dissociation degree with pressure for pure oxygen was consistent with previously observed results. However, it was found to slightly increase with pressure in He-10%O_2 and was backed up by the TALIF results. It was thought to be due to higher electron densities and so increases the number of dissociation reactions, despite a decrease in electron temperature.

The complementary mean electron energy values from these were also discussed. The electron temperature increased with applied power as a result of neutral gas heating. On the other hand, it decreased with pressure and higher oxygen contents owing to collisional effects and reduced ionization thresholds to sustain the plasma. Moreover, the E-mode T_e values were higher than the H-mode. Consequently, the technique continued to have qualitative agreement with reported literature.

Chapter 8

Conclusions and Further work

8.1 Conclusions

The thesis was motivated by the need to develop compatible diagnostics for practical use within the semiconductor manufacturing industry. As such, a low pressure, inductively coupled plasma was operated in pulsed high-power mode to recreate plasma processing conditions of interest. Moreover, molecular oxygen was the species of interest given its likeness to etch gases, simplicity of modelling and practical uses in surface modification of wafers. Consequently, since atomic oxygen influences the surface modification process, these number densities were obtained using Energy Resolved Actinometry and benchmarked using Two-photon Absorption Laser Induced Fluorescence.

The TALIF measurements were taken in the early afterglow and assumed to be the same as the on-time of the plasma pulse. This was so that the laser-induced fluorescence could be distinguished from plasma emission. The atomic oxygen densities were shown to only have a slightly positive relationship with applied power. For pure oxygen, the atomic oxygen density rose from 1.20×10^{20} m^{-3} at 500 W to 1.32×10^{20} m^{-3} at 1000 W at 11 Pa; a slight increase of roughly 10% overall. Similarly, for He-20%O$_2$, it rose from 1.10×10^{20} m^{-3} at 500 W to 1.36×10^{20} m^{-3} at 900 W at 20 Pa. While the relationship was weak compared to other works in the pure oxygen case, n_O was similar at 500 W, 11 Pa to these. Moreover, the weak dependency on applied power for He-O$_2$ mixtures was also seen by others. In contrast, it was much clearer with increasing pressure and oxygen content. For pure oxygen, it scaled almost linearly from 1.33×10^{20} m^{-3} to 4.89×10^{20} m^{-3} over 10 to 50 Pa. Similarly, He-10%O$_2$ rose from 5.91×10^{19} m^{-3} to 2.07×10^{20} m^{-3} from 15 to 50 Pa. For varying oxygen content, the benefits of increasing the ratio of oxygen is greater at small proportions i.e. 10 to 20%, but plateaus to a finite value quickly from 50% onwards.

The effective lifetimes were found to be notably higher in plasma conditions consisting of high amounts of helium; the highest determined value was 42 ns in He-10%O_2 at 25-30 Pa whereas the most recent literature value was found to be 34.7 ns. Consequently, the existence of helium metastables may interact and prolong the population of the excited atomic oxygen state. As a result, it will impact the amount of n_O. Conversely, due to the relatively low amount of atomic oxygen present, the signal-to-noise of the fluorescence curve may have attributed to poor fitting. Thus, enhancing this may eliminate this uncertainty.

Overall, the general trends of atomic oxygen density with changing input conditions was also observed in comparable work, and so the values here provided the benchmarking results for the range of conditions desired for ERA for more consistent comparison.

TALIF was also used to probe the populations of the atomic oxygen ground state sub-levels. This was done by changing the excitation wavelength of the laser to excite each of the $O(^3P)$ states. In doing so, the resulting intensities were compared to obtain gas temperatures. Furthermore, by varying the laser trigger time, the temporal evolution of these were able to be monitored.

Early in the afterglow, the atomic oxygen $O(^3P)$ sub-levels have a population distribution proportional to their degeneracies, 5:3:1, with the most in the lowest energy level, the $O(^3P_2)$ state. Afterwards, these states redistributed themselves; the lower levels were initially fed from higher energy states, and so exhibited slower loss rates. Then, all of the sub-levels started to decrease as other loss mechanisms became dominant, such as recombination, leading to weaker detected signals observed on a millisecond timescale. The time of the peak value of $O(^3P_2)$ was independent of applied power - it was at 425 µs at 20 Pa in both pure O_2 and He-20%O_2, whereas it was further delayed with increasing pressure up to 1 ms into the afterglow in pure O_2 at 50 Pa. This means that pulsed TALIF measurements depends on the time that it was taken in the afterglow because the $O(^3P_2)$ was observed to peak briefly.

The gas temperature was also determined from this population distribution via both Boltzmann plot and a whether the ratio of normalised intensities from each $O(^3P)$ state could be compared with an equivalent Boltzmann fraction value since it is only a function of an input gas temperature. The Boltzmann plot method was applied to three time points for pure oxygen at 20 Pa, 600 W: immediately in the early afterglow at 125 µs, peak signal value at 425 µs, and the last in the temporal study at 2225 µs. The slope of the linear fit using all three points gave T_g of 1590, 1110 and 480 K, respectively. Fits using the two most populated levels differed by almost twice the value at the earliest time (2950 K), before tending towards similar values at the latest (558 K). In the far afterglow, the gas temperature returned to 400 K, regardless of gas mixture, reinforcing the benefits of pulsed plasma to reduce the time-averaged heat load.

The alternative method was tried using the integrated intensity of the entire excitation profile versus simply using the peak excitation value for at a specific time of 425 µs in the afterglow using four test conditions. The ratios using either case gave similar T_g in pure oxygen (∼2600 K) and He-20%O_2 (∼700 K), both at 20 Pa, 600 W. The equivalent values using Boltzmann plot from the integrated signal of the entire excitation for these were 1400 and 850 K. On the other hand, in the other two test conditions of pure oxygen at 20 Pa and 1000 W, and 50 Pa and 600 W, the amount of dissociation was deemed considerable, and this led to gas temperatures equivalent to an asymptotal value of 5000 K using the Boltzmann fraction. Moreover, the Boltzmann plot values for these cases were inconclusive. Consequently, consistent gas temperature measurements using this approach is challenging in pure oxygen environments, particularly in the early afterglow, and the accuracy is limited to certain conditions, which needs to be explored further.

The second part of the thesis was focused on using ERA, a passive, optical-based diagnostic, in order to obtain atomic oxygen densities through a passive means. It does so by matching experimentally determined excitation ratios using PROES with theoretically calculated ones. As a result, the input values that best match enables simultaneous determination of the mean electron energy and dissociation degree. It was applied to the aforementioned plasma regime after having seen successful implementation in other sources. While its previous application in the H-mode of an ICP was inconclusive, the introduction of Bayesian inference was sought to improve the determined results. Nevertheless, despite obtaining atomic oxygen densities that showed a similar weak trend with applied power of 6.21×10^{19} m^{-3} at 500 W to 6.99×10^{19} m^{-3} at 700 W at 10 Pa in O_2-10%Ar, the mean electron energies were unreasonably high, in excess of 15 eV. Even after adjusting the prior knowledge of the parameters to reduce the probability of these high values instead led to negative correlation of dissociation degree with applied power. Upon closer analysis of the method, it was deemed that the oxygen emission line at 777 nm was susceptible to other sources of excitation, including from its immediate lower-lying level. Given that in the H-mode there are also many dissociative processes occurring, the 777 nm was also more susceptible to dissociative excitation than the other oxygen line at 844 nm. In the end, the theoretical model was not able to give reasonable plasma parameter values because of this uncertainty.

Consequently, this technique was adapted to use helium emission to improve upon the original method, and benchmarked using two-photon absorption measurements taken in the early afterglow. A qualitative analysis of the behaviour of the two helium emission lines, 706.5 and 728.1 nm was conducted to assess the feasibility of its implementation as a diagnostic line. This was approximated through monitoring the ratio of their emission intensities with varying power and pressure and comparing with theoretical excitation ratios. A decrease in mean electron energy with higher pressures was inferred from the initial response. This trend gave confidence that use of an alternative line could be viable and also overcome the ambiguity encountered using the usual ERA lines. Subsequently, this was repeated alongside with applied power variation for mixtures of helium-oxygen and helium-oxygen-argon. The gas proportions were also carefully managed to optimise the helium emission signal and also minimise the impact of overlapping argon emission. As such, helium emission was still observable with up to 50% oxygen content, although for appreciable signal-to-noise, 20% is recommended. On the other hand, argon should not exceed 5% of the total admixture as it had significant influence on the determined mean electron energy with amounts greater than this.

As a result, substituting oxygen's 777 nm emission with either of the two helium lines gave similar atomic oxygen densities as the conventional lines in the low-power mode. From 20 to 80 Pa, the n_O using the 706 nm was 3.42×10^{19} m^{-3} to 1.08×10^{20} m^{-3} at 100 W, and the corresponding mean electron energies fell from 8.0 to 7.5 eV. However, despite the 728 nm givng similar atomic oxygen densities, the mean electron energy values were about half that of 706 nm. Since it was also returning the highest dissociation degree values of 5.44% to 4.25% over this pressure range, the discrepancy was attributed to an artefact of the Bayesian method when finding the best agreement with the forward model. Thus, the proof of concept of alternative excitation ratios was shown to be viable - the 706 nm was chosen since it was stronger than the 728 nm line and also less likely to be influenced by neighbouring emission from argon. Therefore, analyses using the new line ratios were carried out in the high power mode on both the modified GEC reactor and the GEC-like plasma source. Both HERA and TALIF returned similar trends and same order of magnitude for the number densities with varying applied power (500-1000 W), pressure (15-25 Pa) and oxygen content (10-20%O_2). Although, the atomic oxygen densities obtained by HERA were typically higher than measured by TALIF, showing a stronger correlation with the input parameters than exhibited through TALIF, and in some cases n_O differed by nearly a factor of 2. This may be a result from the abnormally high effective lifetimes from TALIF in high helium plasmas.

Since this method also returns the mean electron energy, this parameter increased with applied power from 4.1 to 5.3 eV between 400 to 1000 W in He-10%O_2 at 15 Pa, consistent with more energy deposited into heating the electrons. Between 15-25 Pa, it decreased with pressure from 5.3 to 4.6 eV, and reflects the higher collisionality present within the plasma hindering the electrons' ability to gain energy during the heating cycle. Lastly, changing the mixture from 10 to 20% lowered the mean electron energy from 4.13 to 3.11 eV at 15 Pa, 400 W and was due to the high ionization potential of helium needed to sustain quasineutrality of the plasma. The dissociation degree measured by both HERA and TALIF showed no correlation with pressure in He-10%O_2 with pressure. Nonetheless, in pure oxygen, TALIF showed a decrease with pressure similar to observations by other works.

As a whole, this adapted technique has demonstrated good agreement over a range of operating conditions while being much less experimentally complex than laser-based methods, which was the key aim of this thesis.

8.2 Further work

While the application of helium in ERA has proved promising, it is rather limited to cases where its emission is prominent enough, typically with large amounts of helium. Nonetheless, the principles of ERA has been shown to be extended using alternative excitation ratios. Consequently, other noble gases could be used, such as neon that has lower excitation threshold energy (19 eV), which would then only need smaller quantities to produce the emission of interest. Thus, admixtures tending towards pure oxygen can be studied and compared against the TALIF measurements made here. Moreover, this technique may be used to determine atomic hydrogen densities, which are also of interest to technological applications.

Future work could also explore using TALIF to obtain n_O and T_g in the axial direction to study how much atomic oxygen produced reaches the substrate and whether there are any temperature gradients that may affect the surface chemistry. Gas temperature determined from comparing the fluorescence between each of the ground state sub-levels has yielded qualitative temporal trends. Nonetheless, further clarification is needed to obtain consistent values for a range of conditions. It seems to be greatly affected by thermal energy from dissociation processes, particularly at high powers and pressures.

Appendix A

RF generator matching values - 10 Hz pulse frequency, 10% duty cycle.

	15 Pa		20 Pa	
Power [W]	C_T [%]	[C_L [%]	C_T [%]	[C_L [%]
400	23.0	82.6	23.1*	82.0*
500	23.3	81.3	23.5	80.6
600	23.9	79.9	24.0	79.1
700	24.1	79.6	24.3	78.6
800	24.6	78.2	24.5	78.5
900	24.6	78.2	24.9	77.6
1000	24.8	77.9	24.9	77.6

Table A.1: Match settings: He-20%O$_2$.
* 450 W

	15 Pa		20 Pa	
Power [W]	C_T [%]	$[C_L$ [%]	C_T [%]	$[C_L$ [%]
400	23.1	81.9	23.1	82.0
500	23.8	79.4	23.8	79.4
600	23.8	78.9	24.1	78.7
700	24.2	78.7	24.5	77.8
800	24.6	78.0	24.6	77.8
900	24.6	78.0	24.9	77.3
1000	24.8	77.9	25.0	76.7

Table A.2: Match settings: He-10%O_2.

	500 W		600 W	
Pressure [Pa]	C_T [%]	$[C_L$ [%]	C_T [%]	$[C_L$ [%]
15	23.3	81.3	24.0	78.7
20	23.5	80.3	24.0	78.7
25	23.6	80.0	24.0	78.7
30	23.6	80.0	24.0	78.7
40	22.5	85.5	23.8	78.7
50	22.7	83.3	23.3*	81.3*

Table A.3: Match settings: He-20%O_2, varying pressure.

*After initially setting to these values, slowly change to 23.6 and 79.3, respectively. Should obtain around 2 $W_r \pm 2\%$ W_T.

He-O_2 [%]	C_T [%]	$[C_L$ [%]
10	23.7	79.3
20	23.5	80.6
40	23.6	80.5
50	23.6	80.3
60	23.5	80.9
80	23.2	82.0
100	23.0	82.7

Table A.4: Match settings: He-Varying%O_2, 20 Pa, 500 W.

Power [W]	C_T [%]	$[C_L$ [%]
500	23.1	82.7
600	23.3	81.6
700	23.7	80.7
800	24.0	80.3
900	24.4	79.5
1000	24.5	79.5

Table A.5: Match settings: pure O_2, 20 Pa, varying power.

Pressure [Pa]	C_T [%]	[C_L [%]	C_T [%]	[C_L [%]
10	23.5	81.0	-	-
15	23.5	81.0	-	-
20	23.5	81.3	-	-
25	23.5	81.5	-	-
30	23.3	81.5	23.2	81.4
40	22.8	83.1	23.0	82.4
50	22.6	84.3	22.9	83.3

Table A.6: Match settings: pure O_2, 600 W varying pressure. Second set of C_T and C_L values are used once initial plasma has gotten close to desired applied power to minimise reflected power.

Pressure [Pa]	C_T [%]	[C_L [%]
15.5*	24.2	77.3
20	24.2	77.3
25	24.2	77.3
30	24.2	77.3
40	24.0	77.3
50	24.0	77.3
60	23.2	81.7

Table A.7: Match settings: He-10%O_2, 600 W, varying pressure.
* Minimum achievable pressure with 9 sccm He, 1 sccm O_2.

Pressure [Pa]	C_T [%]	[C_L [%]
15	25.6	78.1
20	25.8	78.2
25	25.6	78.2
30	26.0	75.7
40	25.9	75.7
50	25.7	75.7

Table A.8: Match settings: Ar-20%O_2, 600 W, varying pressure.
Help to start at 400 W from ignition using 25.0 and 78.0.

Power [W]	C_T [%]	[C_L [%]
500	23.3	80.5
600	23.9	79.5
700	24.0	79.5
800	24.3	79.0
900	24.7	78.4
1000	24.7	78.4

Table A.9: Match settings: He-40%O_2, 20 Pa, varying power.

List of References

[1] M. A. Lieberman and A. J. Lichtenberg. *Principles of Plasma Discharges and Materials Processing: Second Edition*. Wiley-Interscience, 2nd edition, 2005.

[2] A. von Keudell and V. Schulz-von der Gathen. Foundations of low-temperature plasma physics - an introduction. *Plasma Sources Science and Technology*, 26(11):113001, 2017. doi:10.1088/1361-6595/aa8d4c.

[3] I. Adamovich, et al. The 2017 Plasma Roadmap: Low temperature plasma science and technology. *Journal of Physics D: Applied Physics*, 50(32):323001, 2017. doi:10.1088/1361-6463/aa76f5.

[4] E. A. J. Bartis, C. Barrett, T.-Y. Chung, N. Ning, J.-W. Chu, D. B. Graves, J. Seog, and G. S. Oehrlein. Deactivation of lipopolysaccharide by Ar and H_2 inductively coupled low-pressure plasma. *Journal of Physics D: Applied Physics*, 47(4):045202, 2014. doi:10.1088/0022-3727/47/4/045202.

[5] M. Laroussi. Cold Plasma in Medicine and Healthcare: The New Frontier in Low Temperature Plasma Applications. *Frontiers in Physics*, 8, 2020. doi:10.3389/fphy.2020.00074.

[6] S. J. Doyle, A. R. Gibson, J. Flatt, T. S. Ho, R. W. Boswell, C. Charles, P. Tian, M. J. Kushner, and J. Dedrick. Spatio-temporal plasma heating mechanisms in a radio frequency electrothermal microthruster. *Plasma Sources Science and Technology*, 27(8):085011, 2018. doi:10.1088/1361-6595/aad79a.

[7] S. J. Doyle, A. R. Gibson, R. W. Boswell, C. Charles, and J. P. Dedrick. Control of electron, ion and neutral heating in a radio-frequency electrothermal mi-

crothruster via dual-frequency voltage waveforms. *Plasma Sources Science and Technology*, 28(3):035019, 2019. doi:10.1088/1361-6595/ab0984.

[8] J. W. Coburn and H. F. Winters. Plasma etching - a discussion of mechanisms. *Critical Reviews in Solid State and Material Sciences*, 10(2):119, 1981. doi:10.1080/10408438108243630.

[9] G. S. Oehrlein and S. Hamaguchi. Foundations of low-temperature plasma enhanced materials synthesis and etching. *Plasma Sources Science and Technology*, 27(2):023001, 2018. doi:10.1088/1361-6595/aaa86c.

[10] J. W. Coburn and H. F. Winters. Ion- and electron-assisted gas-surface chemistry - An important effect in plasma etching. *Journal of Applied Physics*, 50(5):3189, 1979. doi:10.1063/1.326355.

[11] K. Ishikawa, K. Karahashi, T. Ichiki, J. P. Chang, S. M. George, W. M. M. Kessels, H. J. Lee, S. Tinck, J. H. Um, and K. Kinoshita. Progress and prospects in nanoscale dry processes: How can we control atomic layer reactions? *Japanese Journal of Applied Physics*, 56(6S2):06HA02, 2017. doi:10.7567/JJAP.56.06HA02.

[12] Intel. Intel Trigate Presentation, 2011. (Accessed: 2018-07-31), <`https://www.intel.co.uk/content/www/uk/en/silicon-innovations/standards-22nm-3d-tri-gate-transistors-presentation.html`>.

[13] P. Kang, H.-j. Lee, S. Cho, D. Kim, J. Park, C.-K. Park, and S. Doh. A virtual metrology system for semiconductor manufacturing. *Expert Systems with Applications*, 36(10):12554, 2009. doi:10.1016/J.ESWA.2009.05.053.

[14] N. Agrawal, Y. Kimura, R. Arghavani, and S. Datta. Impact of Transistor Architecture (Bulk Planar, Trigate on Bulk, Ultrathin-Body Planar SOI) and Material (Silicon or III-V Semiconductor) on Variation for Logic and SRAM Applications. *IEEE Transactions on Electron Devices*, 60(10):3298 , 2013. doi:10.1109/TED.2013.2277872.

[15] C. G. N. Lee, K. J. Kanarik, and R. A. Gottscho. The grand challenges of plasma etching: a manufacturing perspective. *Journal of Physics D: Applied Physics*, 47(27):273001, 2014. doi:10.1088/0022-3727/47/27/273001.

[16] F. F. Chen. Industrial applications of low-temperature plasma physics. *Physics of Plasmas*, 2(6):2164, 1995. doi:10.1063/1.871477.

[17] M. Tuda, K. Nishikawa, and K. Ono. Numerical study of the etch anisotropy in low-pressure, high-density plasma etching. *Journal of Applied Physics*, 81(2):960, 1997. doi:10.1063/1.364189.

[18] P. Chabert and N. Braithwaite. *Physics of radio-frequency plasmas*. Cambridge University Press, 2011.

[19] H. Jansen, H. Gardeniers, M. De Boer, M. Elwenspoek, and J. Fluitman. A survey on the reactive ion etching of silicon in microtechnology. *Journal of Micromechanics and Microengineering*, 6(1):14, 1996. doi:10.1088/0960-1317/6/1/002.

[20] V. M. Donnelly and A. Kornblit. Plasma etching: Yesterday, today, and tomorrow. *Journal of Vacuum Science & Technology A: Vacuum, Surfaces, and Films*, 31(5):050825, 2013. doi:10.1116/1.4819316.

[21] T. Wegner, C. Kullig, and J. Meichsner. Electron heating during E-H transition in inductively coupled RF plasmas. *Plasma Sources Science and Technology*, 24(4):044001, 2015. doi:10.1088/0963-0252/24/4/044001.

[22] M. D. Logue, H. Shin, W. Zhu, L. Xu, V. M. Donnelly, D. J. Economou, and M. J. Kushner. Ion energy distributions in inductively coupled plasmas having a biased boundary electrode. *Plasma Sources Science and Technology*, 21(6):065009, 2012. doi:10.1088/0963-0252/21/6/065009.

[23] J. Ellis, J. Branson, K. Niemi, E. Wagenaars, and T. Gans. Influence of surface materials on the volume production of negative ions in a radio-frequency driven hydrogen plasma. *Journal of Physics D: Applied Physics*, 53:9, 2020. doi:10.1088/1361-6463/abae93.

[24] J. Hopwood. Review of inductively coupled plasmas for plasma processing. *Plasma Sources Science and Technology*, 1(2):109, 1992. doi:10.1088/0963-0252/1/2/006.

[25] H. C. Lee. Review of inductively coupled plasmas: Nano-applications and bistable hysteresis physics. *Applied Physics Reviews*, 5(1):011108, 2018. doi:10.1063/1.5012001.

[26] U. Kortshagen, N. D. Gibson, and J. E. Lawler. On the E -H mode transition in RF inductive discharges. *Journal of Physics D: Applied Physics*, 29(5):1224, 1996. doi:10.1088/0022-3727/29/5/017.

[27] V. M. Donnelly and M. V. Malyshev. Diagnostics of inductively coupled chlorine plasmas: Measurements of the neutral gas temperature. *Applied Physics Letters*, 77(16):2467, 2000. doi:10.1063/1.1318727.

[28] E. J. Tonnis and D. B. Graves. Neutral gas temperatures measured within a high-density, inductively coupled plasma abatement device. *Journal of Vacuum Science & Technology A: Vacuum, Surfaces, and Films*, 20(5):1787, 2002. doi:10.1116/1.1503901.

[29] H. Abada, P. Chabert, J.-P. Booth, J. Robiche, and G. Cartry. Gas temperature gradients in a CF_4 inductive discharge. *Journal of Applied Physics*, 92(8):4223, 2002. doi:10.1063/1.1505683.

[30] M. Shimada, G. R. Tynan, and R. Cattolica. Neutral gas density depletion due to neutral gas heating and pressure balance in an inductively coupled plasma. *Plasma Sources Science and Technology*, 16(1):193, 2006. doi:10.1088/0963-0252/16/1/024.

[31] T. Gans, M. Osiac, D. O'Connell, V. A. Kadetov, U. Czarnetzki, T. Schwarz-Selinger, H. Halfmann, and P. Awakowicz. Characterization of stationary and pulsed inductively coupled RF discharges for plasma sterilization. *Plasma Physics and Controlled Fusion*, 47(5A):A353, 2005. doi:10.1088/0741-3335/47/5A/026.

[32] S. Samukawa. Highly Selective and Highly Anisotropic SiO_2 Etching in Pulse-Time Modulated Electron Cyclotron Resonance Plasma. *Japanese Journal of Applied Physics*, 33(4S):2133, 1994. doi:10.1143/jjap.33.2133.

[33] J. Seok Seo, K. Nam Kim, K. Seok Kim, T. Hyung Kim, and G. Young Yeom. Characteristics of pulsed dual frequency inductively coupled plasma. *Japanese Journal of Applied Physics*, 54(1S):01AA10, 2015. doi:10.7567/JJAP.54.01AA10.

[34] D. J. Economou. Pulsed plasma etching for semiconductor manufacturing. *Journal of Physics D: Applied Physics*, 47(30):303001, 2014. doi:10.1088/0022-3727/47/30/303001.

[35] G. S. Hwang and K. P. Giapis. Mechanism of charging reduction in pulsed plasma etching. *Japanese Journal of Applied Physics*, 37(4S):2291, 1998. doi:10.1143/JJAP.37.2291.

[36] S. Banna, A. Agarwal, G. Cunge, M. Darnon, E. Pargon, and O. Joubert. Pulsed high-density plasmas for advanced dry etching processes. *Journal of Vacuum Science & Technology A: Vacuum, Surfaces, and Films*, 30(4):040801, 2012. doi:10.1116/1.4716176.

[37] S. H. Seo, H. Y. Chang, W. C. Yang, J. H. Kwon, D. H. Kim, Y. Y. Kim, J. H. Nam, and S. J. Moon. Experimental investigations of pulse-power-modulated inductive discharges. *Journal of the Korean Physical Society*, 48(3):414, 2006.

[38] L. G. Christophorou and J. K. Olthoff. Electron interactions with SF6. *Journal of Physical and Chemical Reference Data*, 29(3):267, 2000. doi:10.1063/1.1372164.

[39] M. B. Schulman, F. A. Sharpton, S. Chung, C. C. Lin, and L. W. Anderson. Emission from oxygen atoms produced by electron-impact dissociative excitation of oxygen molecules. *Physical Review A*, 32(4):2100, 1985. doi:10.1103/physreva.32.2100.

[40] C. Xue, F. Gao, D. Q. Wen, and Y. N. Wang. Experimental investigation of the electron impact excitation behavior in pulse-modulated radio frequency Ar/O_2 inductively coupled plasma. *Journal of Applied Physics*, 125(2):023303, 2019. doi:10.1063/1.5079585.

[41] A. Agarwal, P. J. Stout, S. Banna, S. Rauf, K. Tokashiki, J. Y. Lee, and K. Collins. Effect of simultaneous source and bias pulsing in inductively coupled plasma etching. *Journal of Applied Physics*, 106(10):103305, 2009. doi:10.1063/1.3262616.

[42] M. Zaka-Ul-Islam. Dynamics of a pulsed inductively coupled oxygen plasma. *Physics of Plasmas*, 23(11):113505, 2016. doi:10.1063/1.4967769.

[43] R. W. Boswell and R. K. Porteous. Etching in a pulsed plasma. *Journal of Applied Physics*, 62(8):3123, 1987. doi:10.1063/1.339362.

[44] P. Veis and G. Cernogora. Study of oxygen recombination with a double pulse discharge. *Czechoslovak Journal of Physics*, 48:75–87, 1998. doi:10.1023/A:1021292330657.

[45] P. Macko, P. Veis, and G. Cernogora. Study of oxygen atom recombination on a Pyrex surface at different wall temperatures by means of time-resolved actinometry in a double pulse discharge technique. *Plasma Sources Science and Technology*, 13(2):251, 2004. doi:10.1088/0963-0252/13/2/009.

[46] L. Magne, H. Coitout, G. Cernogora, and G. Gousset. Atomic oxygen recombination at the wall in a time afterglow. *Journal de Physique III*, 3(9):1871, 1993. doi:10.1051/JP3:1993247.

[47] J. P. Booth, O. Joubert, J. Pelletier, and N. Sadeghi. Oxygen atom actinometry reinvestigated: Comparison with absolute measurements by resonance absorption at 130 nm. *Journal of Applied Physics*, 69(2):618, 1991. doi:10.1063/1.347395.

[48] C. J. Mogab, A. C. Adams, and D. L. Flamm. Plasma etching of Si and SiO_2 — The effect of oxygen additions to CF_4 plasmas. *Journal of Applied Physics*, 49(7):3796, 1978. doi:10.1063/1.325382.

[49] W. Gordy and W. J. Orville Thomas. Electronegativities of the Elements. *The Journal of Chemical Physics*, 24(2):439, 1956. doi:10.1063/1.1742493.

[50] R. R. Laher and F. R. Gilmore. Updated excitation and ionization cross sections for electron impact on atomic oxygen. *Journal of Physical and Chemical Reference Data*, 19(1):277, 1990. doi:10.1063/1.555872.

[51] A. R. Gibson, M. Foucher, D. Marinov, P. Chabert, T. Gans, M. J. Kushner, and J.-P. Booth. The role of thermal energy accommodation and atomic recombination probabilities in low pressure oxygen plasmas. *Plasma Physics and Controlled Fusion*, 59(2):024004, 2017. doi:10.1088/1361-6587/59/2/024004.

[52] J. T. Gudmundsson, I. G. Kouznetsov, K. K. Patel, and M. A. Lieberman. Electronegativity of low-pressure high-density oxygen discharges. *Journal of Physics D: Applied Physics*, 34(7):1100, 2001. doi:10.1088/0022-3727/34/7/312.

[53] J. T. Gudmundsson and E. G. Thorsteinsson. Oxygen discharges diluted with argon: dissociation processes. *Plasma Sources Science and Technology*, 16(2):399, 2007. doi:10.1088/0963-0252/16/2/025.

[54] A. A. Ionin, I. V. Kochetov, A. P. Napartovich, and N. N. Yuryshev. Physics and engineering of singlet delta oxygen production in low-temperature plasma. *Journal of Physics D: Applied Physics*, 40(2):R25, 2007. doi:10.1088/0022-3727/40/2/R01.

[55] A. Bogaerts. Effects of oxygen addition to argon glow discharges: A hybrid Monte Carlo-fluid modeling investigation. *Spectrochimica Acta - Part B*, 64(11):1266, 2009. doi:10.1016/j.sab.2009.10.003.

[56] C. S. Corr, S. Gomez, and W. G. Graham. Discharge kinetics of inductively coupled oxygen plasmas: experiment and model. *Plasma Sources Science and Technology*, 21(5):055024, 2012. doi:10.1088/0963-0252/21/5/055024.

[57] J. E. Caplinger, G. P. Perram, and S. F. Adams. A combined actinometry approach for medium pressure N_2-O_2 plasmas. *Plasma Sources Science and Technology*, 30(1):015008, 2021. doi:10.1088/1361-6595/abd0de.

[58] D. Pagnon, J. Amorim, J. Nahorny, M. Touzeau, and M. Vialle. On the use of actinometry to measure the dissociation in O_2 DC glow discharges : determination of the wall recombination probability. *Journal of Physics D: Applied Physics*, 28(9):1856, 1995. doi:10.1088/0022-3727/28/9/014.

[59] H. M. Katsch, A. Tewes, E. Quandt, A. Goehlich, T. Kawetzki, and H. F. Döbele. Detection of atomic oxygen: Improvement of actinometry and comparison with laser spectroscopy. *Journal of Applied Physics*, 88(11):6232, 2000. doi:10.1063/1.1315332.

[60] K. Niemi, V. Schulz-von der Gathen, and H. F. Döbele. Absolute atomic oxygen density measurements by two-photon absorption laser-induced fluorescence spectroscopy in an RF-excited atmospheric pressure plasma jet. *Plasma Sources Science and Technology*, 14(2):375, 2005. doi:10.1088/0963-0252/14/2/021.

[61] A. Greb, K. Niemi, D. O'Connell, and T. Gans. Energy resolved actinometry for simultaneous measurement of atomic oxygen densities and local mean electron energies in radio-frequency driven plasmas. *Applied Physics Letters*, 105(23):234105, 2014. doi:10.1063/1.4903931.

[62] T. Tsutsumi, A. Greb, A. R. Gibson, M. Hori, D. O'Connell, and T. Gans. Investigation of the radially resolved oxygen dissociation degree and local mean electron energy in

oxygen plasmas in contact with different surface materials. *Journal of Applied Physics*, 121(14):143301, 2017. doi:10.1063/1.4979855.

[63] P. J. Hargis, K. E. Greenberg, and P. A. Miller. The Gaseous Electronics Conference radio-frequency reference cell: A defined parallel-plate radio-frequency system for experimental and theoretical studies of plasma-processing discharges. *Review of Scientific Instruments*, 65(1):140, 1994. doi:10.1063/1.1144770.

[64] J. K. Olthoff and K. E. Greenberg. The Gaseous Electronics Conference RF Reference Cell - An Introduction. *Journal of Research of the National Institute of Standards and Technology*, 100(4):327, 1995. doi:10.6028/jres.100.025.

[65] M. L. Brake, J. Pender, and J. Fournier. The Gaseous Electronic Conference (GEC) reference cell as a benchmark for understanding microelectronics processing plasmas. *Physics of Plasmas*, 6(5):2307, 1999. doi:10.1063/1.873482.

[66] M. J. Goeckner, J. M. Marquis, and B. J. Markham. Modified gaseous electronics conference reference cell for the study of plasma-surface-gas interactions. *Review of Scientific Instruments*, 75(4):884, 2004. doi:10.1063/1.1688443.

[67] S. Wang, A. E. Wendt, J. B. Boffard, C. C. Lin, S. Radovanov, and H. Persing. Noninvasive, real-time measurements of plasma parameters via optical emission spectroscopy. *Journal of Vacuum Science & Technology A: Vacuum, Surfaces, and Films*, 31(2):021303, 2013. doi:10.1116/1.4792671.

[68] J. Koo, D. Ha, D. Park, H.-J. Roh, S. Ryu, G.-H. Kim, K. H. Baek, and C. Han. Design of optical emission spectroscopy based plasma parameter controller for real-time advanced equipment control. *Computers Chemical Engineering*, 100:38, 2017. doi:10.1016/j.compchemeng.2017.02.009.

[69] A. J. M. Mackus, S. B. S. Heil, E. Langereis, H. C. M. Knoops, M. C. M. van de Sanden, and W. M. M. Kessels. Optical emission spectroscopy as a tool for studying, optimizing, and monitoring plasma-assisted atomic layer deposition processes. *Journal of Vacuum Science & Technology A: Vacuum, Surfaces, and Films*, 28(1):77, 2010. doi:10.1116/1.3256227.

[70] I. J. Kim and I. Yun. Real-time plasma monitoring technique using incident-angle-dependent optical emission spectroscopy for computer-integrated manufacturing. *Robotics and Computer-Integrated Manufacturing*, 52:17, 2018. doi:10.1016/j.rcim.2018.02.003.

[71] T. Ishikawa, D. Hayashi, K. Sasaki, and K. Kadota. Determination of negative ion density with optical emission spectroscopy in oxygen afterglow plasmas. *Applied Physics Letters*, 72(19):2391, 1998. doi:10.1063/1.121394.

[72] H. Yue, S. Qin, R. Markle, C. Nauert, and M. Gatto. Fault detection of plasma etchers using optical emission spectra. *IEEE Transactions on Semiconductor Manufacturing*, 13(3):374, 2000. doi:10.1109/66.857948.

[73] R. Chen, H. Huang, C. J. Spanos, and M. Gatto. Plasma etch modeling using optical emission spectroscopy. *Journal of Vacuum Science & Technology A: Vacuum, Surfaces, and Films*, 14(3):1901, 1996. doi:10.1116/1.580357.

[74] N. Krstulović, I. Labazan, S. Milošević, U. Cvelbar, A. Vesel, and M. Mozetič. Optical emission spectroscopy characterization of oxygen plasma during treatment of a PET foil. *Journal of Physics D: Applied Physics*, 39(17):3799, 2006. doi:10.1088/0022-3727/39/17/014.

[75] Z. Kregar, N. Krstulovic, S. Milosevic, K. Kenda, U. Cvelbar, and M. Mozetic. Inductively coupled rf oxygen plasma studied by spatially resolved optical emission spectroscopy. *IEEE Transactions on Plasma Science*, 36(4):1368, 2008. doi:10.1109/TPS.2008.920896.

[76] H. F. Döbele, U. Czarnetzki, and A. Goehlich. Diagnostics of atoms by laser spectroscopic methods in plasmas and plasma-wall interaction studies (vacuum ultraviolet and two-photon techniques). *Plasma Sources Science and Technology*, 9(4):477, 2000. doi:10.1088/0963-0252/9/4/304.

[77] H. F. Döbele, T. Mosbach, K. Niemi, and V. Schulz-von der Gathen. Laser-induced fluorescence measurements of absolute atomic densities: concepts and limitations. *Plasma Sources Science and Technology*, 14(2):S31, 2005. doi:10.1088/0963-0252/14/2/S05.

[78] R. E. Walkup, K. L. Saenger, and G. S. Selwyn. Studies of atomic oxygen in $O_2 + CF_4$ rf discharges by two-photon laser-induced fluorescence and optical emission spectroscopy. *Journal of Chemical Physics*, 84(5):2668, 1986. doi:10.1063/1.450339.

[79] E. J. H. Collart, J. A. G. Baggerman, and R. J. Visser. On the role of atomic oxygen in the etching of organic polymers in a radio-frequency oxygen discharge. *Journal of Applied Physics*, 78(1):47, 1995. doi:10.1063/1.360630.

[80] G. Dilecce, M. Vigliotti, and S. De Benedictis. A TALIF calibration method for quantitative oxygen atom density measurement in plasma jets. *Journal of Physics D: Applied Physics*, 33(6):33, 2000. doi:10.1088/0022-3727/33/6/101.

[81] J. Conway, S. Kechkar, N. O' Connor, C. Gaman, M. M. Turner, and S. Daniels. Use of particle-in-cell simulations to improve the actinometry technique for determination of absolute atomic oxygen density. *Plasma Sources Science and Technology*, 22(4):045004, 2013. doi:10.1088/0963-0252/22/4/045004.

[82] A. F. van Gessel, S. C. van Grootel, and P. J. Bruggeman. Atomic oxygen TALIF measurements in an atmospheric-pressure microwave plasma jet with in situ xenon calibration. *Plasma Science and Technology*, 22(5):055010, 2013. doi:10.1088/0963-0252/22/5/055010.

[83] J. B. Schmidt, B. Sands, J. Scofield, J. R. Gord, and S. Roy. Comparison of femtosecond- and nanosecond-two-photon-absorption laser-induced fluorescence (TALIF) of atomic oxygen in atmospheric-pressure plasmas. *Plasma Sources Science and Technology*, 26(5):055004, 2017. doi:10.1088/1361-6595/aa61be.

[84] S. Schröter, J. Bredin, A. R. Gibson, A. West, J. P. Dedrick, E. Wagenaars, K. Niemi, T. Gans, and D. O'Connell. The formation of atomic oxygen and hydrogen in atmospheric pressure plasmas containing humidity: Picosecond two-photon absorption laser induced fluorescence and numerical simulations. *Plasma Sources Science and Technology*, 29(10):105001, 2020. doi:10.1088/1361-6595/abab55.

[85] Q. Zeng, H. Jin, S. Meng, W. Liang, and H. Shu. Spatially resolved ground state atomic oxygen density during the mode transition of inductively coupled oxygen plasmas. *Vacuum*, 164:98, 2019. doi:10.1016/j.vacuum.2019.03.009.

[86] M. P. Blake. *Plasma dynamics at the surface interface in radio frequency discharges.* Ph.D. thesis, University of York, 2019.

[87] R. Peverall, S. D. A. Rogers, and G. A. D. Ritchie. Quantitative measurements of oxygen atom and negative ion densities in a low pressure oxygen plasma by cavity ringdown spectroscopy. *Plasma Sources Science and Technology*, 29(4):045004, 2020. doi:10.1088/1361-6595/ab7840.

[88] C. Drag, F. Marmuse, and C. Blondel. Measurement of the two-photon excitation cross-section of the $6p'[3/2]_2$ and $6p'[1/2]_0$ levels of Xe I at the wavelengths 224.3 and 222.6 nm. *Plasma Sources Science and Technology*, 30(7):075026, 2021. doi:10.1088/1361-6595/abfbeb.

[89] M. G. H. Boogaarts, S. Mazouffre, G. J. Brinkman, H. W. P. van der Heijden, P. Vankan, J. A. M. van der Mullen, D. C. Schram, and H. F. Döbele. Quantitative two-photon laser-induced fluorescence measurements of atomic hydrogen densities, temperatures, and velocities in an expanding thermal plasma. *Review of Scientific Instruments*, 73(1):73, 2002. doi:10.1063/1.1425777.

[90] J. P. Booth, D. Marinov, M. Foucher, O. Guaitella, D. Bresteau, L. Cabaret, and C. Drag. Gas temperature measurements in oxygen plasmas by high-resolution Two-Photon Absorption Laser-induced Fluorescence. *Journal of Instrumentation*, 10(11):C11003, 2015. doi:10.1088/1748-0221/10/11/C11003.

[91] C. Jiang and C. Carter. Absolute atomic oxygen density measurements for nanosecond-pulsed atmospheric-pressure plasma jets using two-photon absorption laser-induced fluorescence spectroscopy. *Plasma Sources Science and Technology*, 23(6):065006, 2014. doi:10.1088/0963-0252/23/6/065006.

[92] D. N. Meehan, K. Niemi, and E. Wagenaars. Gas temperature measurements in a pulsed, low-pressure inductively coupled plasma in oxygen. *Japanese Journal of Applied Physics*, 59(SH):SHHB03, 2020. doi:10.35848/1347-4065/ab7313.

[93] K. J. Taylor and G. R. Tynan. Control of dissociation by varying oxygen pressure in noble gas admixtures for plasma processing. *Journal of Vacuum Science & Technology A: Vacuum, Surfaces, and Films*, 23(4):643, 2005. doi:10.1116/1.1931682.

[94] T. H. Chung, H. R. Kang, and M. K. Bae. Optical emission diagnostics with electric probe measurements of inductively coupled Ar/O_2/Ar-O_2 plasmas. *Physics of Plasmas*, 19(11):113502, 2012. doi:10.1063/1.4765357.

[95] L. Liu, S. Sridhar, W. Zhu, V. M. Donnelly, D. J. Economou, M. D. Logue, and M. J. Kushner. External control of electron energy distributions in a dual tandem inductively coupled plasma . *Journal of Applied Physics*, 118(8):083303, 2015. doi:10.1063/1.4928870.

[96] W. Liu, D. Q. Wen, S. X. Zhao, F. Gao, and Y. N. Wang. Characterization of O2 /Ar inductively coupled plasma studied by using a Langmuir probe and global model. *Plasma Sources Science and Technology*, 24(2), 2015. doi:10.1088/0963-0252/24/2/025035.

[97] T. Gans, C. C. Lin, V. Schulz-von der Gathen, and H. F. Döbele. Phase-resolved emission spectroscopy of a hydrogen rf discharge for the determination of quenching coefficients. *Physical Review A*, 67(1):012707, 2003. doi:10.1103/PhysRevA.67.012707.

[98] J. W. Coburn and M. Chen. Optical emission spectroscopy of reactive plasmas: A method for correlating emission intensities to reactive particle density. *Journal of Applied Physics*, 51(6):3134, 1980. doi:10.1063/1.328060.

[99] D. V. Lopaev, A. V. Volynets, S. M. Zyryanov, A. I. Zotovich, and A. T. Rakhimov. Actinometry of O, N and F atoms. *Journal of Physics D: Applied Physics*, 50(7):075202, 2017. doi:10.1088/1361-6463/50/7/075202.

[100] M. V. Malyshev and V. M. Donnelly. Trace rare gases optical emission spectroscopy: Nonintrusive method for measuring electron temperatures in low-pressure, low-temperature plasmas. *Physical Review E*, 60(5):6016, 1999. doi:10.1103/PhysRevE.60.6016.

[101] M. Fuller, M. V. Malyshev, V. M. Donnelly, and I. P. Herman. Characterization of transformer coupled oxygen plasmas by trace rare gases-optical emission spectroscopy and Langmuir probe analysis. *Plasma Sources Science and Technology*, 9(2):116, 2000. doi:10.1088/0963-0252/9/2/304.

[102] Q. Algwari. *Plasma jet formation and interactions between atmospheric pressure dielectric barrier discharge jets*. Ph.D. thesis, Queen's University of Belfast, 2011.

[103] U. Fantz. Basics of plasma spectroscopy. *Plasma Sources Science and Technology*, 15(4):S137, 2006. doi:10.1088/0963-0252/15/4/S01.

[104] A. Goehlich, T. Kawetzki, and H. F. Döbele. On absolute calibration with xenon of laser diagnostic methods based on two-photon absorption. *Journal of Chemical Physics*, 108(22):9362, 1998. doi:10.1063/1.476388.

[105] K. Niemi, V. Schulz-von der Gathen, and H. F. Döbele. Absolute calibration of atomic density measurements by laser-induced fluorescence spectroscopy with two-photon excitation. *Journal of Physics D: Applied Physics*, 34(15):2330, 2001. doi:10.1088/0022-3727/34/15/312.

[106] L. Thorne, Anne Patricia and A. P. Thorne. *Spectrophysics.* Chapman and Hall, London, 1974.

[107] A. Kramida, Y. Ralchenko, J. Reader, and NIST ASD Team. NIST Atomic Spectra Database, Version 5.9, 2022. (Accessed: 2022-05-02), <`https://www.nist.gov/pml/atomic-spectra-database`>.

[108] S. Schröter. *Reactive oxygen and hydrogen species generation in radio-frequency atmospheric pressure plasmas.* Ph.D. thesis, University of York, 2017.

[109] S. Gomez, P. G. Steen, and W. G. Graham. Atomic oxygen surface loss coefficient measurements in a capacitive/inductive radio-frequency plasma. *Appl. Phys. Lett*, 81:19, 2002. doi:10.1063/1.1490630.

[110] Y.-L. Huang and R. J. Gordon. The multiplet state distribution of O(^3P_J) produced in the 193 nm photodissociation of SO_2. *Journal of Chemical Physics*, 93(1):868, 1990. doi:10.1063/1.459462.

[111] R. P. Saxon and J. Eichler. Theoretical calculation of two-photon absorption cross sections in atomic oxygen. *Physical Review A*, 34(1):199, 1986. doi:10.1103/PhysRevA.34.199.

[112] M. Tadokoro, A. Itoh, N. Nakano, Z. L. Petrović, and T. Makabe. Diagnostics of an inductively coupled plasma in oxygen. *IEEE Transactions on Plasma Science*, 26(6):1724 , 1998. doi:10.1109/27.747892.

[113] M. Zaka-Ul-Islam, K. Niemi, T. Gans, and D. O'Connell. Energetic electron avalanches and mode transitions in planar inductively coupled radio-frequency driven plasmas operated in oxygen. *Applied Physics Letters*, 99(4):041501, 2011. doi:10.1063/1.3612914.

[114] M. Fiebrandt, N. Bibinov, and P. Awakowicz. Determination of atomic oxygen state densities in a double inductively coupled plasma using optical emission and absorption spectroscopy and probe measurements. *Plasma Sources Science and Technology*, 29(4):045018, 2020. doi:10.1088/1361-6595/ab7cbe.

[115] S. Rauf and M. J. Kushner. Argon metastable densities in radio frequency Ar, Ar/O_2 and Ar/CF_4 electrical discharges. *Journal of Applied Physics*, 82(6):2805, 1997. doi:10.1063/1.366111.

[116] J. Ma and Y.-K. Pu. Tuning the electron temperature of a nitrogen plasma by adding helium and argon. *Physics of Plasmas*, 10(10):4118, 2003. doi:10.1063/1.1605950.

[117] M. H. Lee, H. C. Lee, and C. W. Chung. Comparison of pressure dependence of electron energy distributions in oxygen capacitively and inductively coupled plasmas. *Physical Review E*, 81(4):046402, 2010. doi:10.1103/PhysRevE.81.046402.

[118] H. C. Lee and C. W. Chung. Electron heating and control of electron energy distribution for the enhancement of the plasma ashing processing. *Plasma Sources Science and Technology*, 24(2):024001, 2015. doi:10.1088/0963-0252/24/2/024001.

[119] E. W. Weisstein. Gamma Function, 2022. (Accessed: 2022-05-02), <`https://mathworld.wolfram.com/GammaFunction.html`>.

[120] T. Wegner, C. Küllig, and J. Meichsner. On the E-H transition in inductively coupled radio frequency oxygen plasmas: I. Density and temperature of electrons, ground state and singlet metastable molecular oxygen. *Plasma Sources Science and Technology*, 26(2):025006, 2017. doi:10.1088/1361-6595/26/2/025006.

[121] H.-C. Lee, J.-K. Lee, and C.-W. Chung. Evolution of the electron energy distribution and E-H mode transition in inductively coupled nitrogen plasma. *Physics of Plasmas*, 17(3):033506, 2010. doi:10.1063/1.3361199.

[122] M. S. Barnes, J. C. Forster, and J. H. Keller. Electron energy distribution function measurements in a planar inductive oxygen radio frequency glow discharge. *Applied Physics Letters*, 62(21):2622, 1993. doi:10.1063/1.109265.

[123] V. M. Donnelly. Plasma electron temperatures and electron energy distributions measured by trace rare gases optical emission spectroscopy. *Journal of Physics D: Applied Physics*, 37:217, 2004. doi:10.1088/0022-3727/37/19/R01.

[124] A. Schwabedissen, E. C. Benck, and J. R. Roberts. Langmuir probe measurements in an inductively coupled plasma source. 1997.

[125] Y. W. Lee, H. L. Lee, and T. H. Chung. E-H mode transition in low-pressure inductively coupled nitrogen-argon and oxygen-argon plasmas. *Journal of Applied Physics*, 109(11), 2011. doi:10.1063/1.3587156.

[126] J. T. Gudmundsson, A. M. Marakhtanov, K. K. Patel, V. P. Gopinath, and M. A. Lieberman. On the plasma parameters of a planar inductive oxygen discharge. *Journal of Physics D: Applied Physics*, 33(11):1323, 2000. doi:10.1088/0022-3727/33/11/311.

[127] J. E. Chilton, J. B. Boffard, R. S. Schappe, and C. C. Lin. Measurement of electron-impact excitation into the $3p^5 4p$ levels of argon using Fourier-transform spectroscopy. *Physical Review A*, 57(1):267, 1998. doi:10.1103/PhysRevA.57.267.

[128] E. G. Thorsteinsson and J. T. Gudmundsson. A global (volume averaged) model of a nitrogen discharge: I. Steady state. *Plasma Sources Science and Technology*, 18(4):045001, 2009. doi:10.1088/0963-0252/18/4/045001.

[129] D. A. Toneli, R. S. Pessoa, M. Roberto, and J. T. Gudmundsson. A volume averaged global model study of the influence of the electron energy distribution and the wall material on an oxygen discharge. *Journal of Physics D: Applied Physics*, 48(49):495203, 2015. doi:10.1088/0022-3727/48/49/495203.

[130] C. S. Corr, P. G. Steen, and W. G. Graham. Instabilities in an inductively coupled oxygen plasma. *Plasma Sources Science and Technology*, 12(2):265, 2003. doi:10.1088/0963-0252/12/2/318.

[131] S.-H. Seo, C.-W. Chung, J.-I. Hong, and H.-Y. Chang. Nonlocal electron kinetics in a planar inductive helium discharge. *Physical Review E*, 62(5):7155, 2000. doi:10.1103/physreve.62.7155.

[132] J. Schulze, E. Schüngel, Z. Donkó, D. Luggenhölscher, and U. Czarnetzki. Phase resolved optical emission spectroscopy: a non-intrusive diagnostic to study electron dynamics in capacitive radio frequency discharges. *Journal of Physics D: Applied Physics*, 43(12):124016, 2010. doi:10.1088/0022-3727/43/12/124016.

[133] Y. Hayashi, S. Hirao, Y. Zhang, T. Gans, D. O'Connell, Z. Petrović, and T. Makabe. Argon metastable state densities in inductively coupled plasma in mixtures of Ar and O_2. *Journal of Physics D: Applied Physics*, 42(14):145206, 2009. doi:10.1088/0022-3727/42/14/145206.

[134] J. B. Boffard, C. C. Lin, and C. A. Dejoseph Jr. Application of excitation cross sections to optical plasma diagnostics. *Journal of Physics D: Applied Physics*, 37(12):R143, 2004. doi:10.1088/0022-3727/37/12/R01.

[135] C. Bowman, J. R. Harrison, B. Lipschultz, S. Orchard, K. J. Gibson, M. Carr, K. Verhaegh, and O. Myatra. Development and simulation of multi-diagnostic Bayesian analysis for 2D inference of divertor plasma characteristics. *Plasma Physics and Controlled Fusion*, 62(4):045014, 2020. doi:10.1088/1361-6587/ab759b.

[136] H. Dreier, A. Dinklage, R. Fischer, M. Hirsch, and P. Kornejew. Bayesian design of plasma diagnostics. *Review of Scientific Instruments*, 77(10):10F323, 2006. doi:10.1063/1.2336457.

[137] S. Jalas, M. Kirchen, P. Messner, P. Winkler, L. Hübner, J. Dirkwinkel, M. Schnepp, R. Lehe, and A. R. Maier. Bayesian Optimization of a Laser-Plasma Accelerator. *Physical Review Letters*, 126(10):104801, 2021. doi:10.1103/PhysRevLett.126.104801.

[138] N. Kang, S. G. Oh, and A. Ricard. Determination of the electron temperature in a planar inductive argon plasma with emission spectroscopy and electrostatic probe. *Journal of Physics D: Applied Physics*, 41(15):155203, 2008. doi:10.1088/0022-3727/41/15/155203.

[139] J. K. Kruschke. *Doing bayesian data analysis : a tutorial with R and BUGS*. Academic Press, Burlington, MA ; Oxford, 2011.

[140] H. Horiguchi, R. S. F. Chang, and D. W. Setser. Radiative lifetimes and two-body collisional deactivation rate constants in Ar for Xe($5p^5 6p$), Xe($5p^5 6p$), and Xe($5p^5 7p$) states. *Journal of Chemical Physics*, 75(3):1207, 1981. doi:10.1063/1.442169.

[141] A. Greb. *Dynamics of the Plasma-Surface Interface in Capacitively Coupled Radio-Frequency Oxygen Plasmas: Coupling Numerical Simulations with Optical Diagnostics*. Ph.D. thesis, University of York, 2013.

[142] A. T. West. *Optical and Electrical Diagnosis of Atmospheric Pressure Plasma Jets*. Ph.D. thesis, University of York, 2016.

[143] Oxford Instruments. iStar CCD series Intensified CCDs for Time-resolved Spectroscopy Specifications.

[144] E. J. H. Collart, J. A. G. Baggerman, and R. J. Visser. Excitation mechanisms of oxygen atoms in a low pressure O_2 radio-frequency plasma. *Journal of Applied Physics*, 70(10):5278, 1991. doi:10.1063/1.350237.

[145] J. Bromander, N. Duric, P. Erman, and M. Larsson. Lifetimes of Some Levels in Neutral Carbon, Nitrogen and Oxygen. *Physica Scripta*, 17(2):119, 1978. doi:10.1088/0031-8949/17/2/010.

[146] J. Bittner, K. Kohse-höinghaus, U. Meier, and T. Just. Quenching of two-photon-excited H(3s, 3d) and O(3p 3P2,1,0) atoms by rare gases and small molecules. *Chemical Physics Letters*, 143(6):571, 1988. doi:10.1016/0009-2614(88)87068-4.

[147] S. Kröll, H. Lundberg, A. Persson, and S. Svanberg. Time-resolved laser spectroscopy on high-lying states in neutral oxygen. *Physical Review Letters*, 55(3):284, 1985. doi:10.1103/PhysRevLett.55.284.

[148] W. K. Bischel, B. E. Perry, and D. R. Crosley. Detection of fluorescence from O and N atoms induced by two-photon absorption. *Applied optics*, 21(8):1419, 1982. doi:10.1364/AO.21.001419.

[149] C. Hsu, M. A. Nierode, J. W. Coburn, and D. B. Graves. Comparison of model and experiment for Ar, Ar/O_2 and Ar/O_2/Cl_2 inductively coupled plasmas. *Journal of Physics D: Applied Physics*, 39:3272, 2006. doi:10.1088/0022-3727/39/15/009.

[150] T. Sato and T. Makabe. A numerical investigation of atomic oxygen density in an inductively coupled plasma in O_2/Ar mixture. *Journal of Physics D: Applied Physics*, 41(3):035211, 2008. doi:10.1088/0022-3727/41/3/035211.

[151] S. Reuter, K. Niemi, V. Schulz-Von Der Gathen, and H. F. Döbele. Generation of atomic oxygen in the effluent of an atmospheric pressure plasma jet. *Plasma Sources Science and Technology*, 18(1):015006, 2009. doi:10.1088/0963-0252/18/1/015006.

[152] Y.-L. Huang and R. J. Gordon. The multiplet state distribution of $O(^3P_J)$ produced in the photodissociation of O_2 at 157 nm. *Journal of Chemical Physics*, 94(4):2640, 1991. doi:10.1063/1.460709.

[153] M. Abe, Y. Sato, and Y. Inagaki. Collisional relaxation of translational energy and fine-structure levels of the $O(^3P_j)$ atom created in the photodissociation of SO_2 at 193 nm. *Journal of Chemical Physics*, 101(7):5647, 1994. doi:10.1063/1.467350.

[154] Y. Matsumi, Y. Inagaki, and G. P. Morley. Fine structure branching ratios and translational energies of $O(^3P_j)$ atoms produced from collision induced intersystem crossing of $O(^1D)$ atoms. *Journal of Chemical Physics*, 100(1):315, 1994. doi:10.1063/1.467000.

[155] H. C. Lee, B. H. Seo, D. C. Kwon, J. H. Kim, D. J. Seong, S. J. Oh, C. W. Chung, K. H. You, and C. Shin. Evolution of electron temperature in inductively coupled plasma. *Applied Physics Letters*, 110(1):014106, 2017. doi:10.1063/1.4971980.

[156] J. E. Caplinger and G. P. Perram. The importance of cascade emission and metastable excitation in modeling strong atomic oxygen lines in laboratory plasmas. *Plasma Sources Science and Technology*, 29(1):015011, 2020. doi:10.1088/1361-6595/ab5e5f.

[157] D. O'Connell, K. Niemi, M. Zaka-Ul-Islam, and T. Gans. Space and phase resolved optical emission in mode transitions of radio-frequency inductively coupled plasmas. *Journal of Physics: Conference Series*, 162:012011, 2009. doi:10.1088/1742-6596/162/1/012011.

[158] P. S. Barklem. Electron-impact excitation of neutral oxygen. *Astronomy and Astrophysics*, 462(2):781 , 2007. doi:10.1051/0004-6361:20066341.

[159] P. J. Dagdigian, B. E. Forch, and A. W. Miziole. Collisional transfer between and quenching of the 3p ^{3}P and ^{5}P states of the oxygen atom. *Chemical Physics Letters*, 148(4):299, 1988. doi:10.1016/0009-2614(88)87276-2.

[160] E. E. Gulcicek, J. P. Doering, and S. O. Vaughan. Absolute differential and integral electron excitation cross sections for atomic oxygen, 6, the $^3\mathrm{P} \rightarrow {}^3\mathrm{P}$ and $^3\mathrm{P} \rightarrow {}^5\mathrm{P}$ transitions from 13.87 to 100 eV. *Journal of Geophysical Research*, 93(A6):5885–5889, 1988. doi:10.1029/ja093ia06p05885.

[161] T. Sawada and P. S. Ganas. Distorted-Wave Calculation of Electron-Impact Excitation of Atomic Oxygen. *Physical Review A*, 7(2):617, 1973. doi:10.1103/PhysRevA.7.617.

[162] Y. Ralchenko, R. K. Janev, T. Kato, D. V. Fursa, I. Bray, and F. J. De Heer. Electron-impact excitation and ionization cross sections for ground state and excited helium atoms. *Atomic Data and Nuclear Data Tables*, 94(4):603, 2008. doi:10.1016/j.adt.2007.11.003.

[163] A. Rohatgi. WebPlotDigitizer - Web Based Plot Digitizer, Version 4.5, 2022. (Accessed: 2022-05-02), <`https://apps.automeris.io/wpd/`>.

[164] Z. Anjum, M. Younus, and N. U. Rehman. Evolution of plasma parameters in capacitively coupled He-O$_2$/Ar mixture plasma generated at low pressure using 13.56 MHz generator. *Physica Scripta*, 95(4):045403, 2020. doi:10.1088/1402-4896/ab687f.

[165] J. B. Boffard, B. Chiaro, T. Weber, and C. C. Lin. Electron-impact excitation of argon : Optical emission cross sections in the range of 300 – 2500 nm. *Atomic Data and Nuclear Data Tables*, 93(6):831, 2007. doi:10.1016/j.adt.2007.06.004.

[166] D. C. Seo and T. H. Chung. Observation of the transition of operating regions in a low-pressure inductively coupled oxygen plasma by Langmuir probe measurement and optical emission spectroscopy. *Journal of Physics D: Applied Physics*, 34(18):2854, 2001. doi:10.1088/0022-3727/34/18/320.

[167] S. Siepa, S. Danko, T. V. Tsankov, T. Mussenbrock, and U. Czarnetzki. On the OES line-ratio technique in argon and argon-containing plasmas. *Journal of Physics D: Applied Physics*, 47(44):445201, 2014. doi:10.1088/0022-3727/47/44/445201.

[168] M. Younus, N. U. Rehman, M. Shafiq, M. Zakaullah, and M. Abrar. Evolution of plasma parameters in a He-N_2/Ar magnetic pole enhanced inductive plasma source. *Physics of Plasmas*, 23(2):023512, 2016. doi:10.1063/1.4942627.

[169] E. Kralkina, P. Nekludova, A. Nikonov, K. Vavilin, I. Zadiriev, and V. Tarakanov. Influence of external parameters on RF inductive discharge plasma characteristics. *Plasma Sources Science and Technology*, 30(11):115020, 2021. doi:10.1088/1361-6595/ac331a.